MONASH University

An investigation of geochemically enriched hotspots – an example from the Tasmantid Seamounts, the Azores and Hawai'i

Saskia Ruttor

(Master of Science, Geoscience)

A thesis submitted for the degree of *Doctor of Philosophy* at

Monash University in 2021

School of Earth, Atmosphere and Environment, Faculty of Science

Copyright notice

Abstract

Intraplate volcanism occurs due to the upwelling of hot mantle material, also known as mantle plumes. Analysing melting products of mantle plumes or ocean island basalts (OIB) in radiogenic isotopes has shown that the Earth's mantle is isotopically heterogeneous. It is assumed that this heterogeneity stems from the subduction, recycling and subsequent mixing of crustal material into the mantle.

The crustal material is generally assumed to show an enriched radiogenic isotopic signature and mixes with a mantle component that is less enriched in radiogenic isotopes. How these components coexist in the mantle and what kind of magmatic processes these components experience during partial melting is part of active research. A tool that could provide more insights into magmatic processes and mantle material due to their fractionation depending on oxidation state and bonding environment in mantle and minerals are stable iron (Fe) isotopes.

To explore the potential of Fe isotopes in understanding magmatic processes and source compositions of OIB that show an enriched radiogenic isotopic signature, I combine stable Fe isotopes with radiogenic isotopic ratios, and major and trace elements. I will focus on three locations, the Tasmantid Seamounts east of Australia, São Miguel on the Azores archipelago and the Big Island of Hawai'i, which is part of the Hawai'ian islands in the North Pacific. Ocean island lavas of these locations differ in alkalinity with the Tasmantid Seamounts showing both alkali and tholeiitic lavas, similar to Hawai'i. São Miguel is sourced by alkali lavas, which show a radiogenic isotopic heterogeneity on a small scale. Such isotopic heterogeneity on a small scale is also present on the Big Island of Hawai'i. This makes the three locations ideal to study the fractionation of Fe isotopes during magmatic processes such as mixing processes, melting conditions and source inheritance.

I can show that enriched (in radiogenic isotopes) components do not always melt at low melting degrees. Whereas alkalinity (high melting degree= tholeiitic lavas, low melting degree = alkali lavas) cannot be ascribed to enriched mantle components, the melting degree does fractionate Fe isotopes resulting in heavy Fe isotopes for lavas that experienced a low melting degree (alkali lavas) and light Fe isotopes for lavas that experienced a high melting degree (tholeiitic lavas). Additionally, the inherited source composition can influence the Fe isotopic

composition of OIB. However, enriched components cannot always be associated with a heavy Fe isotopic composition as shown with São Miguel. Multiple processes, like mixing processes between, for example, peridotite and metasomatising agents can affect the Fe isotopic composition to a large degree resulting in both light and heavy Fe isotopes. Such processes need to be considered when interpreting source dependency. Among other proxies (e.g., trace element ratios), Fe isotopes can identify mantle metasomatism by (1) deviating from trends that indicate olivine fractionation and accumulation and (2) using a three-isotope plot.

Immediate implications of the thesis are that Fe isotopes are a useful tracer to identify magmatic processes underneath ocean islands and mantle material including metasomatising agents involved in their generation.

Publications during enrolment

Ruttor, S., Nebel, O., Nebel-Jacobsen, Y., Cohen, B., Eggins, S. 2021. Alkalinity of ocean island lavas decoupled from source components: a case study from the EM1-PREMA Tasmantid mantle plume. *Geochimica et Cosmochimica Acta* **314**, 140-158.

Thesis including published works declaration

I hereby declare that this thesis contains no material which has been accepted for the award of any other degree or diploma at any university or equivalent institution and that, to the best of my knowledge and belief, this thesis contains no material previously published or written by another person, except where due reference is made in the text of the thesis.

This thesis includes one original paper published in the peer reviewed journal *Geochimica et Cosmochimica Acta* and two chapters formatted as papers that are not submitted yet. The core theme of the thesis is investigating geochemically enriched hotspots – examples from the Tasmantid Seamounts, the Azores and Hawai'i. The ideas, development and writing up of all the papers in the thesis were the principal responsibility of myself, the student, working within the School of Earth, Atmosphere and Environmental Science under the supervision of A/Prof. Dr. Oliver Nebel, Dr. Yona Nebel-Jacobsen and Dr. Mark Kendrick.

The inclusion of co-authors reflects the fact that the work came from active collaboration between researchers and acknowledges input into team-based research. This study is heavily laboratory-based, which is reflected in a contribution of ≤ 5% of some authors, who helped with experimental and instrumental set-up.

In the case of chapter 2, 3, and 4 my contribution to the work involved the following:

Thesis Chapter	**Publication Title**	**Status** *(published, in press, accepted or returned for revision, submitted)*	**Nature and % of student contribution**	**Co-author name(s) Nature and % of Co-author's contribution**	**Co-author(s), Monash student Y/N**
2	*Alkalinity of ocean island lavas decoupled from source components: a case study from the EM1-PREMA Tasmantid mantle plume*	*published*	*75%. Concept and collecting data and writing first draft*	***1) Oliver Nebel - input into manuscript 15 %*** ***2) Yona Nebel-Jacobsen - data analysis, manuscript review 5%***	*Yes* *Yes*

				3) Benjamin E.Cohen - manuscript review 3%	*No*
				4) Stephen Eggins - manuscript review 2%	*No*
3	*Influence of rifting and metasomatism on Fe isotopes in lavas from São Miguel, Azores*	*Returned for revision*	*72%. Concept and collecting data and writing first draft*	***1) Oliver Nebel -input into manuscript 10%*** ***2) Helen Williams – input into manuscript 3%*** ***3) Christoph Beier – input into manuscript 3%*** ***4) Marianne Richter - data analysis, manuscript review 3%*** ***5) Yona Nebel-Jacobsen, data analysis 3%*** ***6) René H.W. Romer, manuscript review 2%*** ***7) Simon P. Turner, manuscript review 2%*** ***8) Caroline R. Soderman, manuscript review 2%***	*Yes* *No* *No* *Yes* *Yes* *No* *No* *No*
4	*Iron isotopes on Kea- and Loa-trend lavas from*	*Not submitted*	*75%. Concept and collecting data and*	***1) Oliver Nebel input into***	*Yes*

	Hawai'i: an assessment of source inheritance vs magmatic processes in the Earth's largest plume		*writing first draft*	***manuscript 10 %*** ***2) Yona Nebel-Jacobsen, data analysis, manuscript review 4%*** ***3) Marc D. Norman, input into manuscript 4%*** ***4) Mark A. Kendrick, input into manuscript 4%*** ***5) Angus Rogers, input into manuscript 3%***	*Yes* *No* *No* *Yes*

During this study, three publications with co-authorship have been achieved:

Oliver Nebel, Paolo A. Sossi, Antoine Bénard, Richard J. Arculus, Gregory M. Yaxley, Jon D. Woodhead, D. Rhodri Davies, **Saskia Ruttor** (2019). Reconciling petrological and isotopic mixing mechanisms in the Pitcairn mantle plume using stable Fe isotopes, *Earth and Planetary Science Letters*, Volume 521, p. 60 – 67.

Ben R. Mather, R. Dietmar Mueller, Maria Seton, **Saskia Ruttor**, Oliver Nebel, Nick Mortimer (2020). Intraplate volcanism triggered by bursts in slab flux. *Science Advanced*, Volume 6/51.

Caroline R. Soderman, Simon Matthews, Oliver Shorttle, Matthew G. Jackson, **Saskia Ruttor**, Oliver Nebel, Simon Turner, Christoph Beier, Marc-Alban Millet, Elizabeth Wodim, Munir Humayun, Helen M. Williams (2021). Heavy δ57Fe in ocean island basalts: A non-unique signature of processes and source lithologies in the mantle, *Geochimica et Cosmochimica Acta*, Volume 292, p. 309 – 32.

Additionally, one manuscript with co-authorship is in review at *Nature Geoscience:*

Ben R. Mather, Maria Seton, Simon Williams, Joana Whittaker, Rebecca Carey, Maëlis Arnould, Nicholas Coltice, Angus Rogers, **Saskia Ruttor**, Oliver Nebel (2021). Parallel volcanic chains generated by plume-slab interaction.

I have renumbered sections of submitted or published papers in order to generate a consistent presentation within the thesis.

Student name: Saskia Ruttor

Student signature: **Date:** 22nd October, 2021

I hereby certify that the above declaration correctly reflects the nature and extent of the student's and co-authors' contributions to this work. In instances where I am not the responsible author I have consulted with the responsible author to agree on the respective contributions of the authors.

Main Supervisor name: Oliver Nebel

Main Supervisor signature: **Date:** 22nd October, 2021

Acknowledgements

First of all, I would like to thank my supervisor A./Prof. Dr. Oliver Nebel for the opportunity to become a Dr. and his support throughout the past three and a bit years. Not only did you give me insights into the plume and isotope world, but you also were there when I felt mentally drained during COVID-19. The discussions with you helped me to stay motivated and filled me with enthusiasm. Especially your use of analogies to explain topics etc., were always insightful (and funny)! Thank you also for the great field work on Aitutaki! I will never forget this!

Yona Nebel-Jacobsen, thank you for your co-supervision! Without your and Oliver's support on the mass spectrometer, I would have no data to write a PhD thesis about! No matter how long it took, you were there to get the mass spectrometer running, so I was able to produce good data. Thank you for your patience and stamina!

Thank you, Mark Kendrick, for your co-supervision, constructive feedback on my manuscripts and great discussions that helped me getting the most out of my data.

A big thanks also goes to my panel, Andrew Friedrich, Peter Cawood and Priyadarshi Chowdhury. Not only did you make me feel like I have done a great job in my milestones, but you also made me feel cared of. It is good to know that there are people you can go to in case you have a problem during the up and downs of a PhD!

I would also like to thank Maria Seton, who allowed me to join the RV Investigator on an expedition through the Tasman Sea. I never thought I would be a month on a ship, but there I was, enjoying every bit of it!

During my studies, I have met a lot of people but one of the most appreciated ones are definitely my office mates! Without you, Marianne Richter, Pablo Farias, Nathan Gardiner and Prasanna Gunawardana, my PhD experience would have been way less fun! Discussions in the office about research and life helped me through all kind of stages in my PhD, I loved the BBQ's outside of university and the workouts in the office and adventures and conferences we went on! Thank you all for filling this PhD journey with so much laughter!

A big thank you goes to my friend Fiona Couperthwaite for her support throughout my PhD! Countless of coffee breaks that brightened up my days in the office and daily zoom catch up/writing sessions that made me look forward to sitting on the computer each day! I'm

happy that I found such a good friend through Monash! Especially at the end of my PhD, my working days would have been much duller without you! Thank you mate, for always being there for me. The next coffee is on me!

I would also like to thank my family, Ingrid, Sven and Christian Ruttor. You have been and are always there for me and support me in whatever I'm doing. Without you, I would have never even gotten to the point of doing a PhD. You taught me to believe in myself and be confident. You are the best family and I love you and can't wait to see you again!

Last but not least, thank you so much Scott and Nala Jones to make me laugh and making me realise that down time is important! Thank you also for listening to my milestone talks 10 times a day. Scott, thank you for supporting me, organising dinner when I had to work long hours and never getting tired of me talking about research. It meant a lot to me and I'm very grateful to have you in my life. I can't wait what our future holds and I'm excited for it!

Finally, thank you Stephen Danczak for teaching me how to communicate science in a more effective way and giving constructive feedback on my introduction and conclusion! Thank you to all my co-authors for your contributions towards the journal papers! Thank you Monash EAE staff and PhD students of Monash for making the PhD an unforgettable and fun time!

Now it is time to close this chapter and start with a new challenge. Sassi out (mic drop)!

Table of Contents

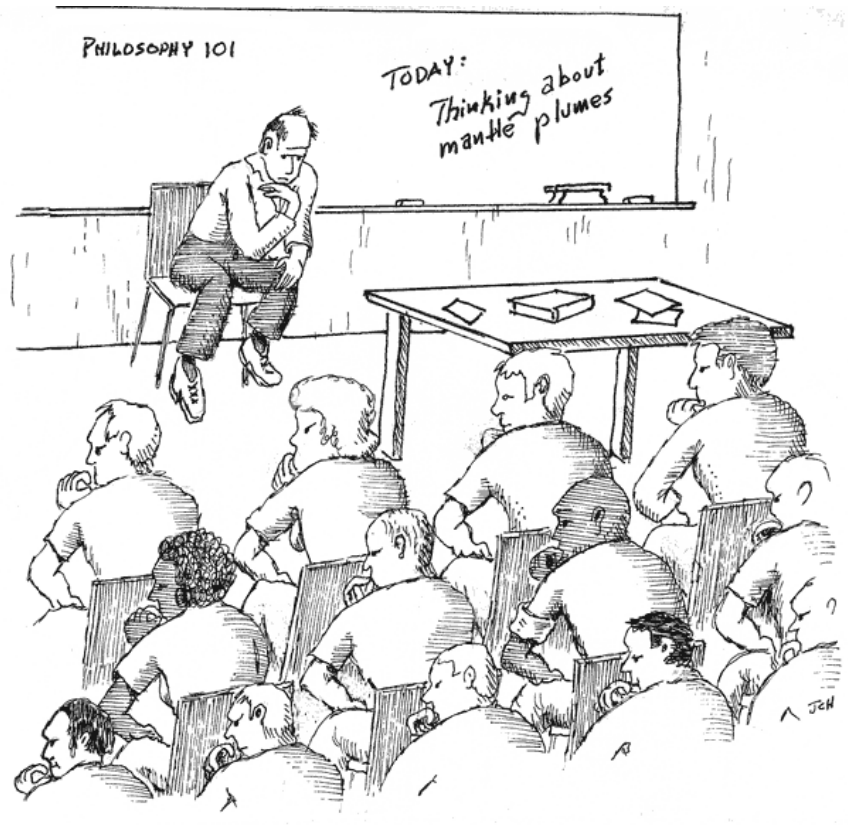

From Science Askew, mantleplumes.org

“If we knew what it was we were doing, it would not be called research, would it?”

(*Albert Einstein*)

CHAPTER 1

1. Introduction

1.1 Overview and research question

The Earth's mantle is an inaccessible reservoir, covered by a crust that can be up to 70 km thick. The deepest hole that has been drilled just scratches the surface, reaching a depth of 12.3 km (Kerr, 1984; Kozlovsky, 1984). But what happens underneath the crust? With a thickness of 2900 km and comprising 82% of the Earth's volume (Helffrich and Wood, 2001), the Earth's mantle is a reservoir that we know only little about. Several disciplines are trying to understand more about the evolution and composition of the mantle by using tomographic models (geophysics), material such as minerals and whole rocks (mineral physics) or element and isotope abundances (geochemists). This study will provide a geochemical perspective on the mantle by focusing on stable iron isotopes in combination with radiogenic isotopes in ocean island basalts (OIB), which are melting products that originate in the deep mantle (Morgan, 1971).

Radiogenic isotopes provide insights into the evolution and composition of the Earth's mantle, because the radiogenic isotopic composition of the mantle material, e.g., ambient mantle and subducted crustal material, does not change significantly after eruption (White, 2015; Hofmann, 1997; Zindler and Hart, 1986; Stracke et al., 2005). Analysing radiogenic isotopes in OIB has shown that the mantle is isotopically heterogeneous (Garapić et al., 2015; Hofmann, 1997; Jackson and Dasgupta, 2008; White, 2015; White, 1985; Stracke et al., 2005; Hart, 1984; Hart et al., 1992). This isotopic heterogeneity reflects the time-integrated subduction and recycling of crustal material, like oceanic or continental crust, into the Earth's mantle. In the mantle, the subducted and recycled material eventually mixes with the ambient mantle and thermal and chemical instabilities lead to the uprise of the mixed material back to the Earth's surface (Stracke et al., 2003; Workman et al., 2004; Niu and O' Hara, 2003; Hofmann, 2003; White, 2010). As the hot, buoyant mantle material approaches the lithosphere it starts melting and then erupts as an intraplate volcano, like Hawai'i. During the process of melting, magmatic processes such as fractional crystallisation and interaction with surrounding mantle material alter the geochemical composition of the magma. Such magmatic processes are difficult to reconstruct with radiogenic isotopes or common tracers, like major or trace elements, but important to understand to reconstruct processes that lead

to an isotopic heterogeneity (e.g., Yang et al., 2019; Sobolev et al., 2005; Niu and O' Hara, 2003; Lambart et al., 2013; Halliday et al., 1995; Kogiso et al., 2004; Sobolev et al., 2007; Jackson and Dasgupta, 2008).

Stable iron (Fe) isotopes are a relatively new geochemical tool that could provide more insights into mantle material and magmatic processes of ocean island lavas (e.g., Williams and Bizimis, 2014; Williams et al., 2009; Williams et al., 2005; Teng et al., 2008; Teng et al., 2013; Dauphas et al., 2009; Nebel et al., 2019; Gleeson et al., 2020). Fractionation of stable Fe isotopes as $1/T^2$ made low temperature processes the main application of stable isotope research as to the relatively large variation in natural systems. Recent analytical improvements have now achieved precisions sufficient to resolve high-temperature isotope fractionation (e.g., Beard and Johnson, 1999; Sossi et al., 2015; Millet and Dauphas, 2014; Cheng et al., 2014). For example, Williams and Bizimis (2014) suggest that Fe isotopes can be used to identify lithological units of the mantle and Nebel et al. (2019) and Konter et al. (2016) propose that mantle material can be distinguished by its Fe isotopic composition.

To explore the potential of Fe isotopes in characterising mantle material and magmatic processes, I will focus on OIB from the Tasmantid Seamounts (Chapter 2), São Miguel, Azores (Chapter 3), and Kīlauea and Mauna Loa on the Big Island of Hawai'i (Chapter 4). The Tasmantid Seamounts, an age progressive seamount chain in the Tasman and Coral Sea, show a dichotomy in alkalinity, similar to Hawai'i. This different alkalinity (alkali vs. tholeiitic lavas) suggests different melting conditions, e.g., degree of melting, temperature or/and pressure at time of melting. Assuming that stable Fe isotopes are affected by melting conditions, I expect to see a correlation of Fe isotopes with degrees of alkalinity. Furthermore, the Big Island of Hawai'i in the central Pacific Ocean shows a radiogenic isotopic heterogeneity on a km scale. Another island that shows such isotopic heterogeneity on a small scale is São Miguel, an island of the Azores in the northern Atlantic Ocean. Different mantle material is suggested to account for the isotopic trends confined to the location on the island, e.g., western São Miguel shows less radiogenic and eastern São Miguel more radiogenic isotopic compositions (e.g., Beier et al., 2007). Such differentiation is ideal to identify whether the mantle material and mixing processes influence the Fe isotopic composition of OIB. Contrary to the Tasmantid Seamounts and Hawai'i, São Miguel consists of alkali basalts only. Whether

alkalinity translates into different mantle material, and what kind of magmatic processes are causing a radiogenic isotopic heterogeneity, is not well constrained yet. For this study, samples from the three locations have been analysed in their stable Fe isotopes. Additionally, the Tasmantid Seamounts OIB have been analysed in their radiogenic strontium (Sr), neodymium (Nd), lead (Pb) and hafnium (Hf) and Hawai'ian OIB in their Hf isotopic ratios.

The thesis will address the following aims: (1) to identify the isotopic characteristics of OIB; (2) to identify petrogenetic processes that led to the formation of OIB. These are potentially recorded in the isotopic heterogeneity of OIB, stable Fe isotopes in particular, and may reveal conditions of partial melting or magma mixing in conjunction with radiogenic isotopes and trace elements; and (3) to distinguish whether enriched (subducted and recycled) and depleted mantle components remain as distinct lithological units (with different Fe isotopic composition) in the mantle.

1.2 Hot buoyant mantle material (or mantle plumes)

Understanding the formation of intraplate volcanoes is important to interpret the isotopic heterogeneity of mantle material. Because this thesis focuses on unravelling processes that cause this isotopic heterogeneity, a brief background on intraplate volcanism will be given here. The origin of oceanic islands, among them the Tasmantid Seamounts, Azores and Hawai'i, has been and still is under debate (Foulger, 2005; Foulger and Jurdy, 2007; Courtillot et al., 2003; Koppers, 2011) due to their occurrence in the middle of a tectonic plate. Wilson (1963) was the first to establish the theory of a deep, fixed source producing the Hawai'ian chain, the archetype of hotspots. Morgan (1971) introduced the model of mantle plumes, which is hot buoyant material rising from the deep mantle towards the surface, where hot rock starts to melt when reaching the lithosphere and then erupts as an intraplate volcano. The deep origin of mantle plumes is still under debate (e.g., Pilet et al., 2005; Humphreys & Niu, 2009). Geochemical (Doucet et al., 2020; Hofmann and White, 1982; White and Hofmann, 1982; Zindler and Hart, 1986) and seismological (Van der Meer et al., 2018; Ricard et al., 1993; Lithgow-Bertelloni and Richards, 1998; Van der Hilst et al., 1997) studies have shown that the material incorporated into mantle plumes has been subducted at convergent margins ranging in age from recent to hundreds of millions of years old material.

Current models propose that subducted and recycled material either sinks to the core-mantle boundary (CMB), ~2,900 km underneath the Earth's surface (Condie, 2005; Wang et al., 2018; French and Romanowicz, 2015; Garnero et al., 2016; Hahm et al., 2009; Courtillot et al., 2003) or stagnates at the mantle transition zone (MTZ) at 410 – 660 km depth (Dasgupta et al., 2004; Agrusta et al., 2017; Goes et al., 2008; van der Hist et al., 1991; Zhou, 1996). The stagnated slab, or fluids from the stagnated slab, can interact with upwelling mantle material (Dasgupta et al., 2006; Gerbode and Dasgupta, 2010) and may cause the generation of shallow mantle plumes at the MTZ (e.g., Anderson, 2000; Courtillot et al., 2003). At the CMB, instabilities of the thermal boundary layer lower the density of the accumulated material, which leads to its ascend towards the surface. The instabilities at the CMB occur mostly at the margins of two antipodal large low shear wave velocity provinces (LLSVPs), the African and Pacific LLSVPs (Dziewonski, 1984; Garnero et al., 2007; Burke et al., 2008; Montelli et al., 2004; Doucet et al., 2020). Geochemical studies suggest that mantle plumes transport subducted and recycled material as well as material from the LLSVPs towards the surface (Fig. 1a; Castillo, 1988; Doucet et al., 2020). Petrological models suggest that the plume material is about 100 - 250°C hotter than the surrounding mantle (Putirka, 2005), transporting heat towards the surface, which leads to the cooling of the Earth's core (Davies, 1993). The shape of mantle plumes has been described as a mushroom-like structure (Fig. 1b) based on laboratory and numerical models (Griffiths and Campbell 1990; Farnetani and Richards 1995; van Keken 1997). The centre of the plume head is hotter than the plume margins (Griffiths and Campbell, 1990). As the head of the plume approaches the lithosphere, its temperature exceeds the solidus and generates melts. This process, the transformation of solid rock into a liquid or melt, which represents a portion of the solid mantle, is called partial melting. Depending on the temperature and pressure as well as the lithospheric thickness (Niu et al., 2011; Frey et al., 1991), partial melting can take place under different melting conditions, which can result in a two-stage eruption, producing tholeiitic and alkali basalts. Tholeiitic and alkali basalts differ in their major element content (alkali ($Na_2O + K_2O$) vs silica (SiO_2) content) which is related to different degrees of melting, with alkali lavas melting at lower degrees than tholeiitic lavas (Green and Ringwood, 1967; Frey et al., 1991; Frey et al., 1978; Garcia et al., 1995; Naumann and Geist, 1999; O'Hara, 1965). Common proxies to evaluate the melting degree of lavas are crystal fractionation corrected major elements (Plank and Langmuir, 1992;

Taylor and Martinez, 2003) and primitive mantle normalised Rare Earth Elements (REE; O'Neill, 2016).

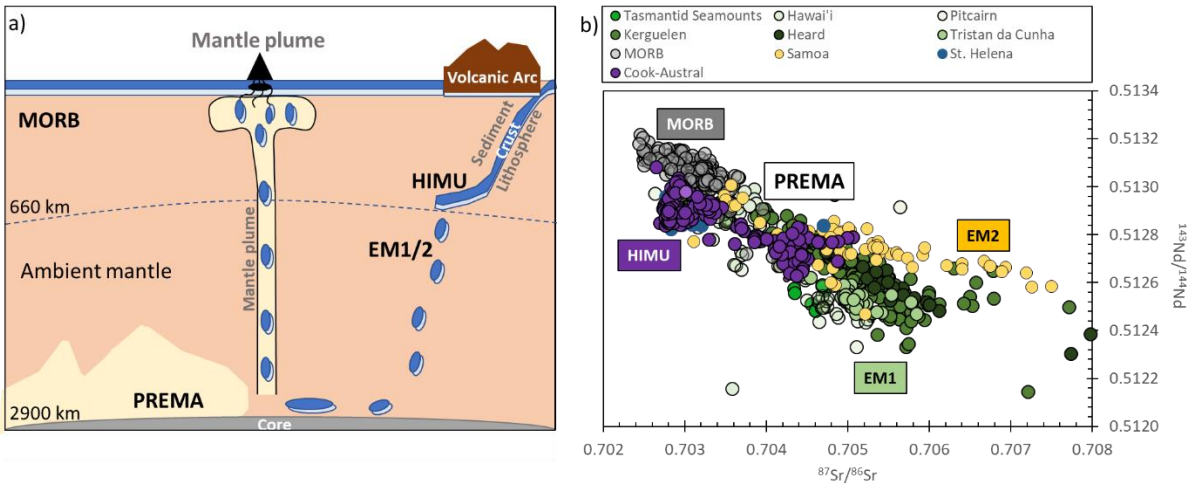

Figure 1. a) Cartoon of mantle plume rising towards the lithosphere, where the hot rock starts melting. Mantle plume can incorporate subducted oceanic crust (dark blue) and lithosphere (light blue) with pelagic or terrigenous sediments. Plume matrix consists of PREMA, which has been previously associated with large low shear wave velocity provinces (LLSVPs) residing at the CMB (Wang et al., 2013; Niu, 2018; Jackson et al., 2018). b) $^{87}Sr/^{86}Sr$ vs $^{143}Nd/^{144}Nd$, Pitcairn, Hawai'i, Kerguelen, Heard, Tristan da Cunha, Samoa, St. Helena, Cook-Austral from GEOROC (http://georoc.mpch-mainz.gwdg.de/georoc/), Tasmantid Seamount from Eggins et al. (1991) and Ruttor et al. (2021).

1.3 Source lithologies

Basaltic magmas (producing tholeiitic and alkali lavas) have been thought to derive only from mantle peridotite, which is an olivine-rich lithology (Yoder Jr and Tilley, 1962; O'Hara, 1968). However, the subduction and recycling of crustal material, which likely results in metasomatic lithologies like carbonated peridotite, pyroxenite and hornblendite, further add to their formation (Hirschmann et al., 2003; Kogiso et al., 2003; Gerbode and Dasgupta, 2010; Dasgupta et al., 2007; Dasgupta et al., 2004; Yang et al., 2019). To which extent these multiple lithologies contribute to the generation of OIB is part of active research (Lambart et al., 2016; Sobolev et al., 2007).

Several studies use major and trace elements in basalts and olivine phenocrysts in order to provide insights into source lithologies involved in generating OIB (Yang et al., 2019; Sobolev et al., 2007; Sobolev et al., 2005; Niu and O' Hara, 2003; Lambart et al., 2013; Halliday

et al., 1995; Kogiso et al., 2004; Matzen et al., 2017; Jackson and Dasgupta, 2008). However, the parameters used in those studies, especially incompatible elements, can be overprinted by mantle metasomatism (Niu and O' Hara, 2003) or strongly overlap (Fig. 2a, b), presenting a difficulty in interpreting the data. A new tool is needed to identify lithological units within the mantle and possible mixing processes that cause the heterogeneity in radiogenic isotopic spaces of OIB. Contrary to radiogenic isotopes, stable isotopes do not decay but fractionate during partial melting and fractional crystallisation and thus need to be considered as possible proxies to identify petrogenetic processes and source lithologies within the mantle.

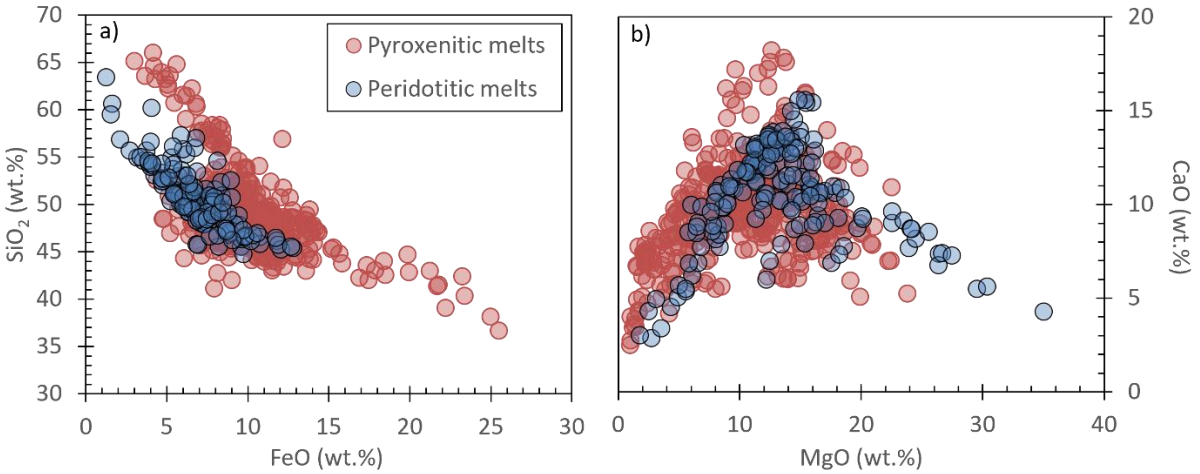

Figure 2. a) FeO vs SiO_2, b) MgO vs CaO. Data consists of experimental melts of peridotite and pyroxenite compiled from Yang et al. (2019) and references therein.

1.4 Mantle geochemistry

1.4.1 Radiogenic isotopes

Additional to providing insights into the evolution and composition of the Earth's mantle, radiogenic isotopes can be used to determine the age of crustal and mantle material. Here, I will discuss the overall concept of radiogenic isotopes and then focus on the evolution and composition of the Earth's mantle. For further information on geochronology the reader is referred to Patchett and Samson (2003) and Crossingham et al. (2017), and references therein.

As part of this study, radiogenic isotopes were analysed to characterise the nature of mantle components of the Tasmantid Seamounts and Hawai'i. Understanding the generation

of mantle components is important to interpret the different isotopic signatures of these OIB. A very simplified explanation is provided in the following: Igneous crust forms by partial melting processes of the primitive mantle (PM). The PM is a calculated value that represents the silicate Earth right after core separation and before crustal segregation (Sun and McDonough, 1989). Extracting material from the mantle results in a depletion in more incompatible elements (e.g., rubidium (Rb), neodymium (Nd)) over less incompatible elements (e.g., strontium (Sr), samarium (Sm)) of the mantle. Considering mantle convection and plate tectonics, the igneous crust eventually subducts back into the mantle. The radiogenic isotopic signatures of basalts (Fig. 1b) reflect the radiogenic isotopic parent-daughter ratio of crustal material at time of subduction (White, 1985). For example, ^{147}Sm decays into ^{143}Nd with a half-life of 106 Ga (Bizimis and Scher, 2016). With Nd being more incompatible than Sm, ^{147}Sm decaying into ^{143}Nd and ^{144}Nd being stable, a high ^{143}Nd/^{144}Nd indicates depletion in incompatible elements within a mantle source. The opposite holds true for ^{87}Rb decaying into ^{87}Sr. Here, Sr is more compatible than Rb, thus, a high ^{87}Sr/^{86}Sr shows an enrichment of the mantle source. Continuous formation of the crust at mid-ocean ridges means that the upper mantle experiences consistent depletion in incompatible elements. This depletion results, for example, in higher ^{143}Nd/^{144}Nd and lower ^{87}Sr/^{86}Sr values of the residue (Fig. 1b). Following the generation of mantle plumes (section 5.1.), the incorporation of the subducted material leads to a lower value in ^{143}Nd/^{144}Nd and higher value in ^{87}Sr/^{86}Sr (Fig. 1b). Because these fractionation processes happened a long time ago, we can detect isotopic decay. However, if the partial melting processes occurred recently, e.g., before eruption, not enough time has passed to detect changes in the radiogenic isotopic ratio. Thus, radiogenic isotopes give insights into the evolution and composition of the Earth's mantle.

By comparing these ratios, for example ^{87}Sr/^{86}Sr vs ^{143}Nd/^{144}Nd (Fig. 1b), of various hotspot locations isotopic trends have been identified, indicating an isotopic heterogeneity of the Earth's lower mantle (Garapić et al., 2015; Hart et al., 1973; Hofmann, 1997; White, 2015; White, 1985; Zindler and Hart, 1986; Stracke et al., 2005; Jackson et al., 2007). These trends in radiogenic isotopic systems describe a mixing between at least two endmembers, also termed mantle components. Mantle components range from depleted mid-ocean ridge

basalt mantle (DMM) to enriched mantle components (EM1, EM2) and HIMU (high $^{238}U/^{204}Pb$, Zindler and Hart, 1986).

Whereas the DMM is depleted in radiogenic Sr, Pb, Nd and Hf isotopes due to melt extraction events, which caused depletion of the upper mantle, EM1, EM2 and HIMU represent mantle endmembers with more radiogenic Sr, Nd, Pb and Hf isotopic signatures (Fig. 1b; Zindler and Hart, 1986). In radiogenic isotopic spaces, these mantle components intersect with the mantle plume matrix (Jackson et al., 2007), in the following referred to as the prevalent mantle "PREMA" (Zindler and Hart, 1986), but also known as the focal zone "FOZO" (Hart et al., 1992; Stracke et al., 2005), the primitive helium mantle "PHEM" (Farley et al., 1992) or the common component "C" (Hanan and Graham, 1996).

The intersection of EM1, EM2 and/or HIMU with PREMA is interpreted as a binary mixture of mantle components (Hart et al., 1992; Jackson et al., 2007; Castillo, 2015), where each mantle endmember "[…] represents a distinct, internally heterogeneous reservoir […]" (White, 1985). Representative hotspot locations for EM1 are, for example, Pitcairn, Hawai'i, the Tasmantid Seamounts, Tristan da Cunha, Kerguelen and Heard Island, EM2 representatives are Samoa and Society Islands and HIMU representatives are selective Cook-Austral Islands, e.g., Mangaia, and St. Helena (Fig. 1b). Additional to those "stereotypical" mantle components, São Miguel, for example, is an island that shows a unique radiogenic isotopic signature. We can decipher between a depleted and an enriched component with radiogenic isotopes, but another tool is needed to understand the material that causes São Miguel's unique radiogenic isotopic signature. I will show in Chapter 3 that stable Fe isotopes in combination with radiogenic isotopes and trace elements can trace metasomatized mantle material that is otherwise not detectable.

1.4.2 Stable iron isotopes

Light elements like hydrogen (H), carbon (C), nitrogen (N) and oxygen (O) have been traditionally studied in the field of stable isotope geochemistry. However, the introduction of new techniques like the multicollector-inductively coupled plasma-mass spectrometer (MC-ICP-MS) allowed expanding the analysis of stable isotopes to so called unconventional elements, like molybdenum (Mo), zinc (Zn) and iron (Fe) (e.g., Belshaw et al., 2000).

Iron is one of the most abundant elements in the Earth's mantle, existing in two oxidation states, ferrous (Fe^{2+}) and ferric iron (Fe^{3+}). During partial melting, the redox dependent partitioning of Fe between liquid and crystalline residue, with ferric iron being more incompatible than ferrous iron, leads to a heavy Fe isotopic signature in the melt, leaving behind a residue that is depleted in heavy Fe isotopes (Sossi and O'Neill, 2017; Teng et al., 2008; Williams et al., 2009). Additionally, differences in the bonding environment of Fe^{2+} and Fe^{3+} cause mass-dependent fractionation of stable iron isotopes between different phases during partial melting in the mantle (Weyer, 2008; Weyer and Ionov, 2007; Williams and Bizimis, 2014; Williams et al., 2005). For example, heavy Fe (i.e., ^{57}Fe) prefers short, strong Fe-O bonding environments as well as higher oxidation states, leading to isotopically heavy Fe in pyroxene-rich lithologies and light Fe isotopes in olivine-dominated lithologies with olivine having long, week Fe-O bonds, favouring ferrous iron and hence incorporating only light Fe isotopes into its structure (Sossi and O'Neill, 2017; Sossi et al., 2012; Schauble, 2004; Dauphas et al., 2014; Williams et al., 2005). This equilibrium inter-mineral fractionation leads to further enrichment of the melt during cooling through crystallisation of olivine and pyroxene (Sossi et al., 2012; Teng et al., 2008; Weyer, 2008). The behaviour of Fe during partial melting might thus be useful to identify lithological units like pyroxenite (pyroxene rich lithology) and peridotite (olivine-rich lithology) (e.g., Williams and Bizimis, 2014).

Iron has four stable isotopes: ^{54}Fe, ^{56}Fe, ^{57}Fe and ^{58}Fe, with the following natural abundances of 5.845, 91.754, 2.1191 and 0.2819%, respectively (Taylor et al., 1992). Iron isotopes are reported in delta (δ) notation to the IRMM-524a external standard, which is isotopically identical to IRMM-014 (Craddock and Dauphas, 2011) with ^{5x}Fe being either ^{56}Fe or ^{57}Fe, resulting in the permille deviation of the isotopic ratio $^{56}Fe/^{54}Fe$ or $^{57}Fe/^{54}Fe$:

$$\delta^{5x}Fe = \left[\frac{^{5x}Fe/^{54}Fe_{Sample}}{^{5x}Fe/^{54}Fe_{IRMM-524a}} - 1\right] x\ 1000 \quad (1)$$

Pristine lherzolites have been analysed to characterise the Fe isotopic composition of the ambient peridotitic mantle, or bulk silicate earth (BSE), with a $\delta^{57}Fe$ +0.05 ± 0.01‰ (2S.E; Sossi et al., 2016). Mid ocean ridge basalts (MORB) show a relatively homogenous Fe isotopic composition with $\delta^{57}Fe$ +0.15 ± 0.01‰ (Chen et al., 2019; Teng et al., 2013). The difference between BSE and MORB can be mostly explained by fractional crystallisation during partial

melting (Sossi et al., 2016; Richter et al., 2021). Compared to the BSE and MORB, OIB show a heterogeneous Fe isotopic composition (Fig. 3), ranging from -0.16 to +0.45‰ (Soderman et al., 2021; Konter et al., 2016; Nebel et al., 2019; Gleeson et al., 2020; Teng et al., 2013). The heavy Fe isotopic signature of OIB was thought to occur due to the contribution of pyroxenite (Williams and Bizimis, 2014). Williams and Bizimis (2014) present stable Fe isotopic compositions for garnet-pyroxenite (δ^{57}Fe +0.10 to +0.27‰) and peridotite (δ^{57}Fe -0.34 to +0.14‰) xenoliths from Oahu, Hawai'i, indicating that OIB generated from a pyroxenite show an on average heavier Fe isotopic composition than lavas associated with mantle peridotite. However, and because the heaviest Fe isotopic compositions in OIB exceed fractionation processes that occur during partial melting (Williams and Bizimis, 2014; Foden et al., 2018; Soderman et al., 2021), other processes need to be considered. The question is, what kind of processes or material can cause Fe isotopic compositions that cannot be explained by partial melting of peridotite or pyroxenite, i.e., heavy δ^{57}Fe > +0.15‰ or light δ^{57}Fe < +0.05‰?

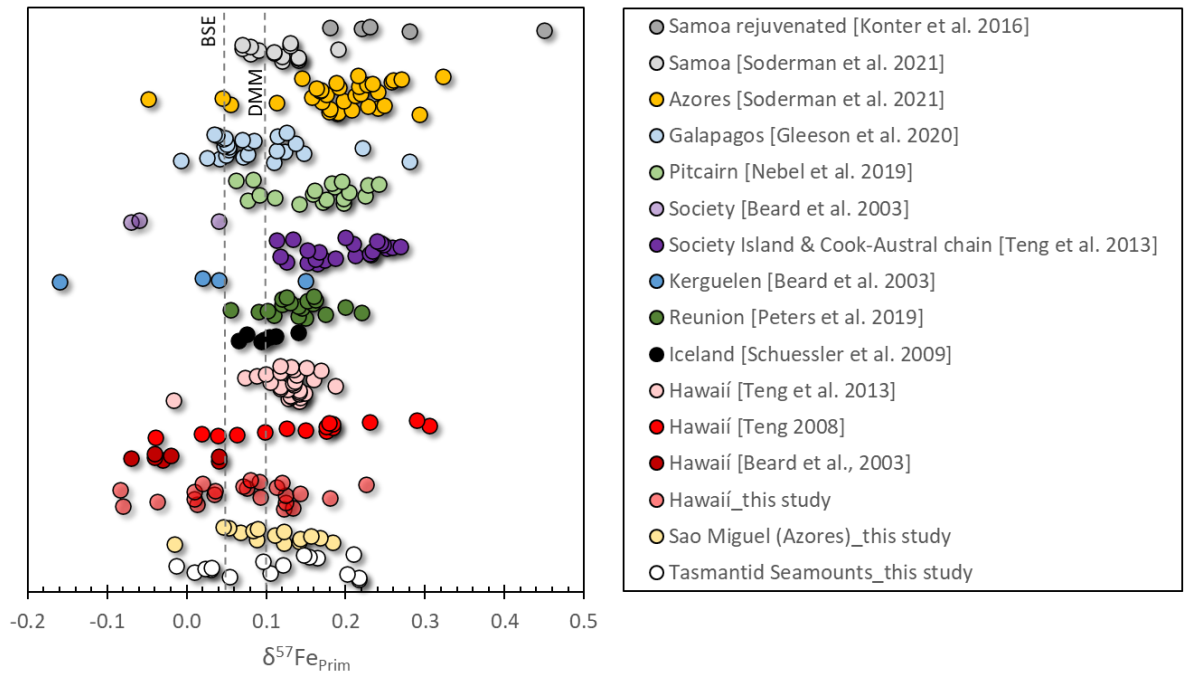

Figure 3. Compilation of primary melt Fe isotope variations ($\delta^{57}Fe_{Prim}$) in OIB. Data for DMM ($\delta^{57}Fe_{Prim}$ +0.10 ± 0.01‰; 2S.E) and BSE (δ^{57}Fe +0.05 ± 0.01‰; 2S.E) from Sossi et al. (2016).

1.4.2.1 Stable Fe isotope as a proxy for identifying petrogenetic processes

To evaluate processes that can fractionate Fe isotopes, we need to correct for crystal fractionation. This correction ensures that we can compare values of the primary melt, e.g.,

radiogenic isotopes and mantle normalised rare earth elements, to Fe isotope data. The above explained fractionation processes of Fe during partial melting are leading to a heavier measured $\delta^{57}Fe$ composition in OIB compared to the Fe isotopic composition of their primary melt ($\delta^{57}Fe_{prim}$; Sossi et al., 2012; Teng et al., 2008). We therefore correct the measured $\delta^{57}Fe$ for olivine fractionation. An olivine fractionation correction is outlined in Sossi et al. (2016) and in Chapter 2, 3, and 4. Recent studies show that comparisons of radiogenic Sr, Nd, Pb and Hf isotopic ratios with $\delta^{57}Fe_{prim}$ may provide insights into inherited Fe isotopic compositions of mantle components and may indicate source lithologies involved in melting and mixing processes (Nebel et al., 2019; Konter et al., 2016; Teng et al., 2013; Williams and Bizimis, 2014). At Pitcairn for example, PREMA is identified as one mixing endmember with a $\delta^{57}Fe_{prim}$ of +0.05‰, whereas the crustal component EM1 is showing a $\delta^{57}Fe_{prim}$ of +0.23‰. Due to the heavy $\delta^{57}Fe_{prim}$ signature of EM1, it has been suggested that a secondary pyroxenite mixes with peridotite. Mixing between peridotite and pyroxenite, may it be pyroxenite in the mantle or as veins in the lithosphere, is found to be a suitable scenario at mid-ocean ridges as well as ocean island settings to explain heavy Fe isotopes (Sun et al., 2020). However, some OIB, like the Azores and Samoa, exceed $\delta^{57}Fe_{prim}$ of +0.25‰ and cannot be explained by interaction of peridotite with eclogite or pyroxenite (Soderman et al., 2021).

In addition to the conundrum of how to explain heavy $\delta^{57}Fe_{prim}$, only few studies exist concentrating on OIB with light $\delta^{57}Fe_{prim}$ (Williams et al., 2005; Williams and Bizimis, 2014). So far, light $\delta^{57}Fe_{prim}$ have been documented in subduction zones as a result of carbonate-bearing fluids or melts (Debret et al., 2020) and intrusive carbonatites (Johnson et al., 2010). However, depending on several factors, i.e., the oxidation state of the mantle and the nature of the metasomatic agent, metasomatism can lead not only to light but also to heavy Fe isotopic signatures (Konter et al., 2016; Poitrasson et al., 2013; Sossi et al., 2012; Williams et al., 2005). Nonetheless, Fe isotopes are sensible to changes in oxygen fugacity within the mantle and may thus be a useful proxy to identify mantle metasomatism.

1.4.2.2 Reflection: Fe isotopes and formation of intraplate volcanoes

Figure 4 is a visual representation that brings the material and processes involved in generating OIB in context with Fe isotopes. Understanding the generation of OIB is crucial to comprehend the main chapters of this thesis and the potential Fe isotopes could have. The

full potential of Fe isotopes as a tracer for magmatic processes and mantle components is part of active research (e.g., McCoy-West et al., 2018; Williams et al., 2009; Soderman et al., 2021; Williams and Bizimis, 2014; Gleeson et al., 2020; Debret et al., 2020; Richter et al., 2021; Foden et al., 2018; Sossi et al., 2016; Nebel et al., 2013; Nebel et al., 2019; Nebel et al., 2015; Sossi and O'Neill, 2017; Schuessler et al., 2009; Johnson et al., 2010; Lesher et al., 2020; Teng et al., 2008; Chen et al., 2019; Sun et al., 2020).

We now know that mantle components can be differentiated in a less enriched (in radiogenic isotopes) endmember and an enriched endmember and can assume that the less enriched component shows lighter δ^{57}Fe than the enriched component. This is because the enriched component can be associated with crustal material. During subduction and recycling oceanic crust (δ^{57}Fe +0.15‰; Chen et al., 2019; Teng et al., 2013) and small amounts of sediment (Chase, 1981; Hofmann and White, 1982; Stracke et al., 2003; Weaver, 1991), which can show a heavy Fe isotopic signature (δ^{57}Fe < +0.9‰; Du et al., 2017), transform into eclogite under loss of fluids that contain light δ^{57}Fe (Fig. 4.; Debret et al., 2016; Turner et al., 2018). The loss of light δ^{57}Fe leads to the assumption that eclogite shows a heavier Fe isotopic composition of δ^{57}Fe ≥ +0.15‰ (Soderman et al., 2021) than oceanic crust with a δ^{57}Fe = +0.15‰ (Chen et al., 2019; Teng et al., 2013).

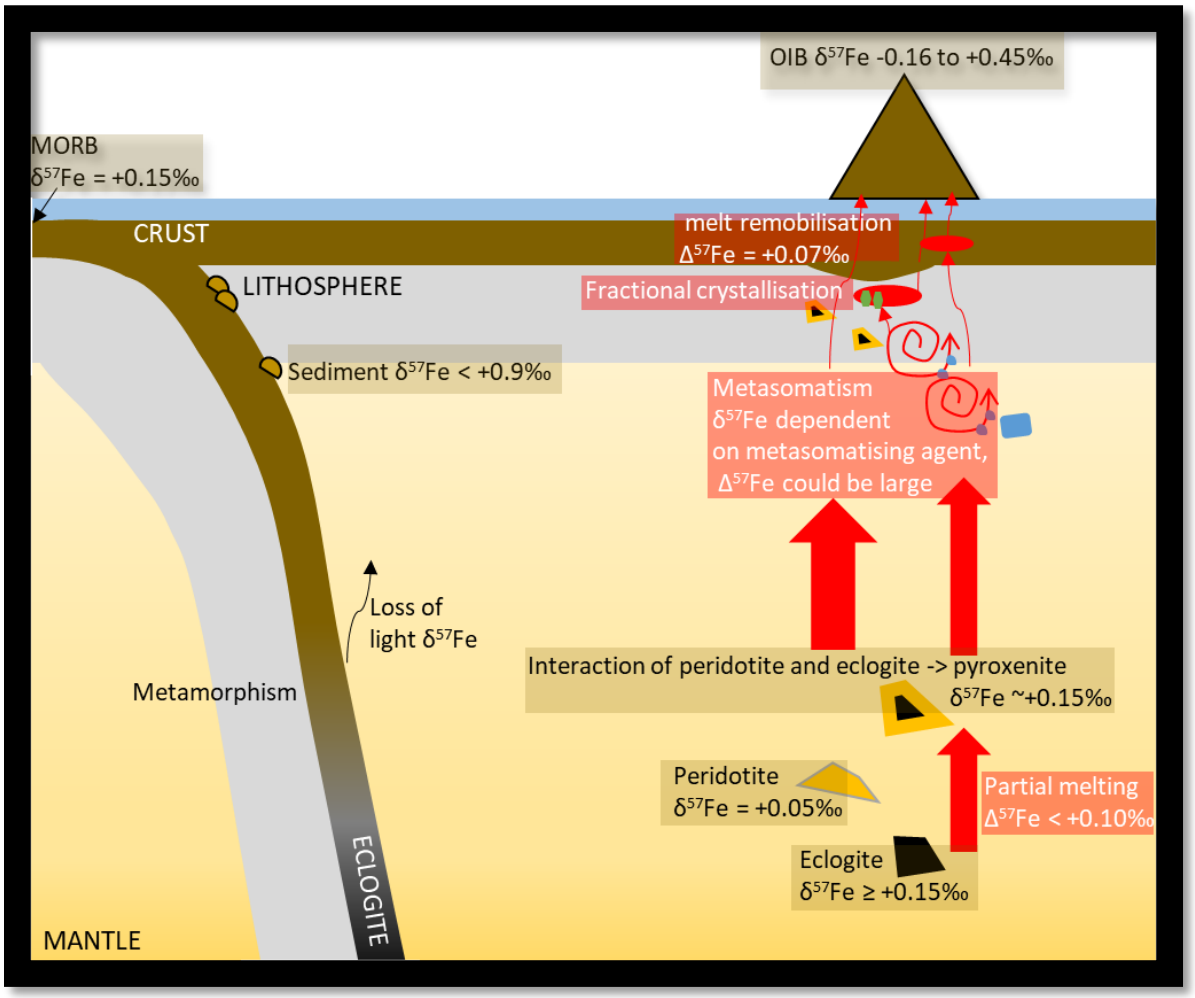

Figure 4. Schematic illustration of OIB generation, adapted from Soderman et al. (2021). Metamorphism (Debret et al., 2016) and hydrothermal alteration (El Korh et al., 2017) can lead to light Fe loss during subduction of oceanic crust (MORB = δ^{57}Fe +0.15‰; Chen et al., 2019; Teng et al., 2013). During upwelling, eclogite can interact with peridotite, leading to pyroxenite. Several processes can alter δ^{57}Fe during partial melting, e.g., metasomatism (Konter et al., 2016; Weyer and Ionov, 2007; Williams et al., 2004; Williams et al., 2005), fractional crystallisation (Sossi et al., 2016; Teng et al., 2008) and melt remobilisation (Soderman et al., 2021). Depending on melting degree (large melting degree = wide red arrow, low melting degree = thin red arrow), lithospheric thickness (Niu et al., 2011) and presence of pyroxenite (Sun et al., 2020) Fe isotopes can range between δ^{57}Fe -0.16 to+0.45‰.

Within the mantle, several processes can influence the Fe isotopic composition of subducted material: (1) Subducted, recycled material that reaches the CMB might experience contribution of heavy Fe isotopes from core liquids (Lesher et al., 2020); (2) Magmatic processes, like mixing processes, lead to a heterogeneity in Fe isotopes within the source material (Nebel et al., 2019; Konter et al., 2016); (3) melting conditions might influence the

Fe isotopic composition, with higher melting degrees leading to lighter Fe isotopes of the melt (Williams et al., 2005; Williams et al., 2004; Weyer and Ionov, 2007) and (4) alteration processes, i.e., diffusion or mantle metasomatism (Teng et al., 2011), might change the Fe isotopic composition of the source. Because the contribution of heavy Fe isotopes from the core is likely small, I concentrate on magmatic processes, melting conditions and source inheritance. Chapter 2 focuses on magmatic processes and melting conditions underneath the Tasmantid Seamounts and its effect on Fe isotopes, chapter 3 on magmatic processes and source heterogeneity underneath São Miguel and chapter 4 on magmatic processes and source heterogeneity underneath the Big Island of Hawai'i (Fig. 5). Understanding the petrogenesis of OIB is fundamental in order to constrain the cause of radiogenic isotopic heterogeneities.

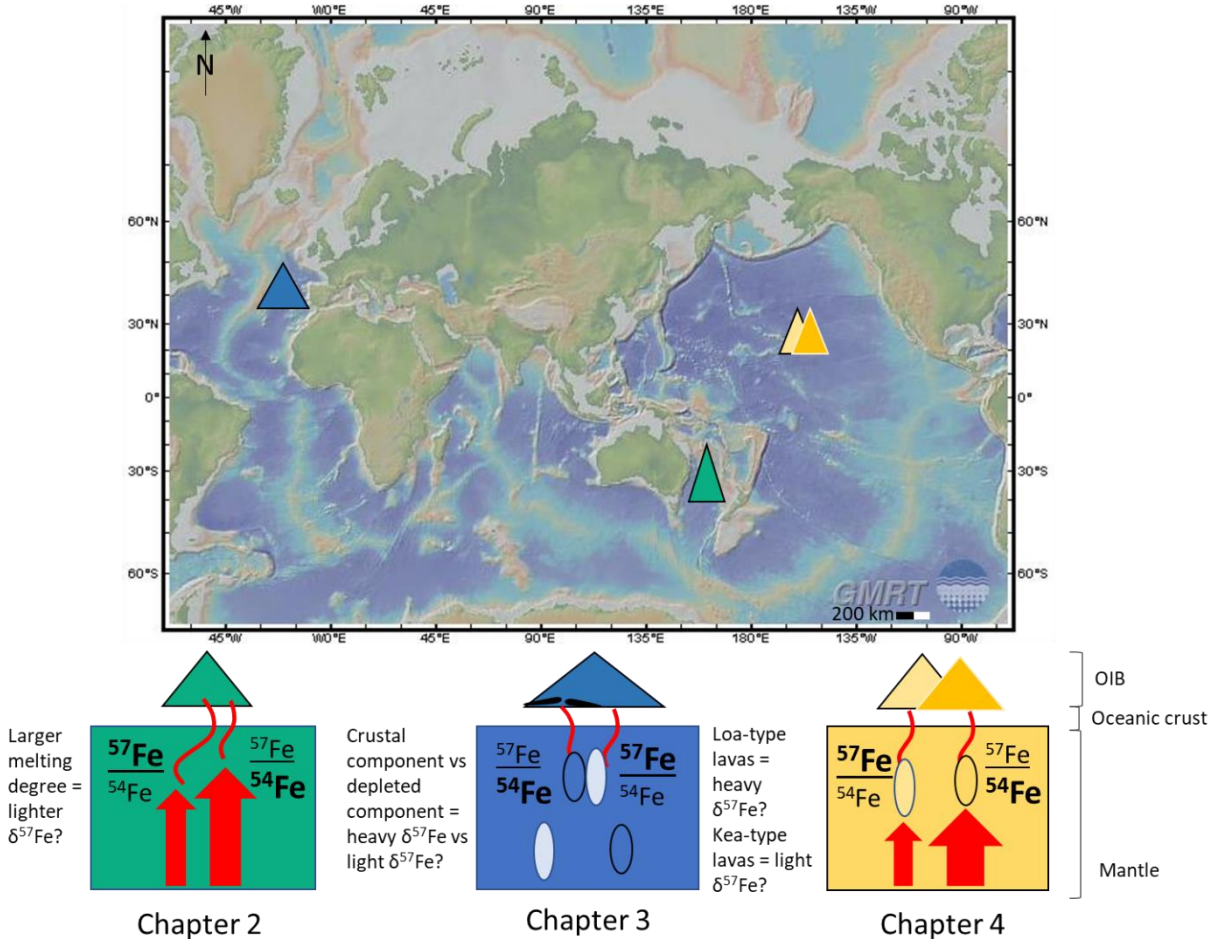

Figure 5. Schematic overview of location and focus of the three main chapters. Size of red arrow illustrates large vs small melting degree. Ovals illustrate different mantle components. Oceanic crust includes lithosphere. Map from www.geomapapp.org (Ryan et al., 2009).

1.5 Overview of manuscripts

Chapter 1 is introducing the theory around mantle plumes and the use of radiogenic and stable isotopes. The thesis comprises three main manuscripts: (1) "*Alkalinity of ocean island lavas decoupled from source components: a case study from the EM1-PREMA Tasmantid mantle plume"*, (2) "*The influence of mantle source composition and metasomatism on Fe isotopes in lavas from São Miguel, Azores*", (3) "*Iron isotope systematics during igneous differentiation in Kea- and Loa-trend lavas, Hawai'i*". Each of the manuscripts are stand-alone journal articles. This results in inevitable repetition of the methods section of each chapter. In brief, whole rock powder has been prepared for chromatographic extraction, a method that works with columns and acids to separate the element of interest. After chromatographic extraction, radiogenic and stable Fe isotopic ratios have been analysed with the multicollector-inductively coupled plasma-mass spectrometer (MC-ICP-MS) at Monash University, Australia, assuring high precision analysis. A summary of each manuscript including contribution is given in the following. Finally, Chapter 5 summarises the findings of Chapter 2, 3, and 4, and finishes on an outlook.Chapter 2, Manuscript 1: Alkalinity of ocean island lavas decoupled from source components: a case study from the EM1-PREMA Tasmantid mantle plume

Chapter 2 focuses on the radiogenic isotopic and stable Fe isotopic signature, and alkalinity of the Tasmantid Seamounts OIB. In total 26 samples have been prepared and analysed in their radiogenic Sr, Nd, Pb and Hf, and stable Fe isotopes in search for links between mantle components, alkalinity and possible mixing scenarios. Comparison of the Tasmantid Seamounts OIB to tholeiitic and alkali lavas from Pitcairn and Hawai'i, showed that the Tasmantid Seamounts are part of the EM1 plume family. Alkali and tholeiitic lavas of the Tasmantid Seamounts range in radiogenic isotopes between PREMA and EM1. The comparison confirms that there is no apparent systematic between alkalinity and mantle component, e.g., alkali lavas cannot always be ascribed to an enriched component. In stable Fe isotopes, alkali basalts of the Tasmantid Seamounts are isotopically heavier, ranging in $\delta^{57}Fe_{prim}$ (Fe isotopic composition calculated to primitive lavas along a liquid line of descent) from +0.10 to +0.21‰ with a median at +0.15‰, than tholeiitic lavas, which show a $\delta^{57}Fe_{prim}$ ranging from -0.01 to +0.22‰ with a median at +0.04‰. The difference in Fe isotopic

compositions between tholeiitic and alkali lavas cannot be ascribed to source inheritance but are solely of petrologic origin. The heavier Fe isotopic composition of alkali lavas can be explained by pressure dependency and melting in the garnet stability field. Tholeiitic lavas are derived from an ordinary depleted mantle, likely peridotite, with outliers towards heavy Fe isotopes of cryptic origin. We suggest that rather than depth, temperature differences are causing variable melting degrees between tholeiitic and alkali lavas of the Tasmantid Seamounts. We thus propose that tholeiitic lavas of the Tasmantid Seamounts likely represent melts from the centre of the plume, whereas alkali lavas form in peripheral areas. Chapter 2 has been published in the journal *Geochimica et Cosmochimica Acta*.

1.5.2 Chapter 3, Manuscript 2: The influence of mantle source composition and metasomatism on Fe isotopes in lavas from São Miguel, Azores

São Miguel, Azores, is subject of Chapter 3. Because radiogenic isotope data is available (Beier et al., 2007; Prytulak et al., 2014; Turner et al., 1997), we focused on analysing Fe isotopes of 18 samples. Previous studies have shown that eastern and western São Miguel show different radiogenic isotopic signatures and trace element compositions on a km scale (Beier et al., 2007; White et al., 1979; Widom et al., 1997; Turner et al., 1997; Elliott et al., 2007). We compare radiogenic Sr, Nd and Pb isotopic ratios, trace element and major element ratios with stable Fe isotopes to characterise the Fe isotopic composition of São Miguel's mantle source and possible mixing processes. The depleted (in radiogenic isotopes) component of western São Miguel shows a heavy Fe isotopic composition of $\delta^{57}Fe_{prim}$ (Fe isotopic composition calculated to primitive lavas along a liquid line of descent) from +0.09 to +0.18‰, whereas the enriched (in radiogenic isotopes) component of eastern São Miguel shows a lighter $\delta^{57}Fe_{prim}$ of +0.05 to +0.12‰. Covariations between radiogenic isotopes and $\delta^{57}Fe_{prim}$ suggest that the Fe isotopic composition is source related. However, crustal components with an enriched radiogenic isotopic composition have so far been associated with heavy Fe isotopic compositions. We discuss several processes, e.g., partial melting and mantle metasomatism to solve the conundrum as of why eastern São Miguel shows an enriched component with a light Fe isotopic composition. Elevated $^{78}Sr/^{86}Sr$, K_2O and Rb/Sr indicate the formation of phlogopite or high potassium hollandite, a mineral commonly associated with mantle metasomatism. We thus assume that a low degree silicic K-rich

metasomatising agent could explain the Fe isotopic composition of eastern São Miguel. The heavy Fe isotopic signature of western São Miguel is associated with melting at the ultraslow, active Terceira Rift and likely results from mixing between plume derived and rift drifted melts.

1.5.3 Chapter 4, Manuscript 3: Iron isotope systematics during igneous differentiation in Kea- and Loa-trend lavas, Hawai'i

In Chapter 4, we analysed 23 samples from the submarine Southwest Rift Zone of Mauna Loa and subaerial Pu'u 'Ō'ō, a vent on the East Rift Zone of Kīlauea, in stable Fe isotopes and complemented these with new radiogenic Hf isotopes. Mauna Loa is a representative of the 'Loa-' and Kīlauea a representative of the 'Kea-trend'. Because lavas that source Mauna Loa's Southwest Rift Zone and Pu'u 'Ō'ō are suggested to bypass the summit and do not undergo mixing processes therein, the aim is to investigate the nature and origin of the Fe isotopic composition of tholeiitic, shield building basalts. In Hf isotopic space, Mauna Loa lavas align with ε_{Hf} values of the Loa trend and Pu'u 'Ō'ō align with ε_{Hf} values of the Loa trend. Comparisons with Sr and Hf isotopic data as well as trace element ratios reveal that the Fe isotopic signature of both Mauna Loa and Pu'u 'Ō'ō cannot be ascribed to a source inheritance nor to melting degrees. Compared to a crystal fractionation trend represented by lavas from the Kīlauea Iki lava lake, basalts from Pu'u 'Ō'ō plot along the trend at MgO ~7.0 wt.% and an average δ^{57}Fe of +0.15‰. Basalts and picrites from Mauna Loa with MgO ~16.0 wt.% show lighter δ^{57}Fe of +0.06‰. The Fe isotopic composition of lavas that plot along this crystal fractionation trend can be explained by fractionation and accumulation of olivine. However, both Mauna Loa and Pu'u 'Ō'ō samples deviate towards lighter δ^{57}Fe. Based on a three-isotope plot, we suggest that these Mauna Loa and Pu'u 'Ō'ō samples result from a mixture or exchange of equilibrium and disequilibrium Fe isotope fractionation, possibly induced by re-charging events.

1.6 References

Agrusta, R., Goes, S. & van Hunen, J. (2017) Subducting-slab transition-zone interaction: Stagnation, penetration and mode switches. *Earth and Planetary Science Letters* **464**, 10-23.

Anderson, D. L. (2000) The thermal state of the upper mantle; no role for mantle plumes. *Geophysical Research Letters* **27**(22)**,** pp 3623-3626.

Beard, B. L. & Johnson, C. M. (1999) High precision iron isotope measurements of terrestrial and lunar materials. *Geochimica et Cosmochimica Acta* **63**(11-12)**,** pp 1653-1660.

Belshaw, N. S., Zhu, X. K., Guo, Y. & O'Nions, R. K. (2000) High precision measurement of iron isotopes by plasma source mass spectrometry. *International Journal of Mass Spectrometry* **197**(1)**,** pp 191-195.

Bizimis, M. & Scher, H. D. (2016) Neodymium Isotopes. *In:* White, W. M. (ed.) *Encyclopedia of Geochemistry: A Comprehensive Reference Source on the Chemistry of the Earth.* Cham: Springer International Publishing.

Burke, K., Steinberger, B., Torsvik, T. H. & Smethurst, M. A. (2008) Plume Generation Zones at the margins of Large Low Shear Velocity Provinces on the core–mantle boundary. *Earth and Planetary Science Letters* **265**(1)**,** pp 49-60.

Castillo, P. (1988) The Dupal anomaly as a trace of the upwelling lower mantle. *Nature* **336**(6200)**,** pp 667.

Castillo, P. R. (2015) The recycling of marine carbonates and sources of HIMU and FOZO ocean island basalts. *Lithos* **216-217**(C)**,** pp 254-263.

Chase, C. G. (1981) Oceanic island Pb: two-stage histories and mantle evolution. *Earth and Planetary Science Letters* **52**(2)**,** pp 277-284.

Chen, S., Niu, Y., Guo, P., Gong, H., Sun, P., Xue, Q., Duan, M. & Wang, X. (2019) Iron isotope fractionation during mid-ocean ridge basalt evolution: Evidence from lavas on the East

Pacific Rise at 10°30'N and its implications. *Geochimica et Cosmochimica Acta* **267**, p 227-239.

Cheng, T., Nebel, O., Sossi, P. A. & Chen, F. (2014) Refined separation of combined Fe–Hf from rock matrices for isotope analyses using AG-MP-1M and Ln-Spec chromatographic extraction resins. *MethodsX* **1**, 144-150.

Condie, K. C. (2005) *Earth As an Evolving Planetary System*, Burlington: Burlington: Elsevier Science & Technology.

Courtillot, V., Davaille, A., Besse, J. & Stock, J. (2003) Three distinct types of hotspots in the Earth's mantle. *Earth and Planetary Science Letters* **205**(3-4)**,** pp 295-308.

Craddock, P. R. & Dauphas, N. (2011) Iron isotopic compositions of geological reference materials and chondrites. *Geostandards and Geoanalytical Research* **35**(1)**,** pp 101-123.

Crossingham, T. J., Vasconcelos, P. M., Cunningham, T. & Knesel, K. M. (2017) 40Ar/39Ar geochronology and volume estimates of the Tasmantid Seamounts: Support for a change in the motion of the Australian plate. *Journal of Volcanology and Geothermal Research* **343**, pp 95-108.

Dasgupta, R., Hirschmann, M. M. & Smith, N. D. (2007) Partial Melting Experiments of Peridotite + CO 2 at 3 GPa and Genesis of Alkalic Ocean Island Basalts. *Journal of Petrology* **48**(11)**,** pp 2093-2124.

Dasgupta, R., Hirschmann, M. M. & Stalker, K. (2006) Immiscible Transition from Carbonate-rich to Silicate-rich Melts in the 3GPa Melting Interval of Eclogite CO 2 and Genesis of Silica-undersaturated Ocean Island Lavas. *Journal of Petrology* **47**(4)**,** pp 647-671.

Dasgupta, R., Hirschmann, M. M. & Withers, A. C. (2004) Deep global cycling of carbon constrained by the solidus of anhydrous, carbonated eclogite under upper mantle conditions. *Earth and Planetary Science Letters* **227**(1-2)**,** pp 73-85.

Dauphas, N., Craddock, P. R., Asimow, P. D., Bennett, V. C., Nutman, A. P. & Ohnenstetter, D. (2009) Iron isotopes may reveal the redox conditions of mantle melting from Archean to Present. *Earth and Planetary Science Letters* **288**(1-2)**,** pp 255-267.

Dauphas, N., Roskosz, M., Alp, E. E., Neuville, D. R., Hu, M. Y., Sio, C. K., Tissot, F. L. H., Zhao, J., Tissandier, L., Médard, E. & Cordier, C. (2014) Magma redox and structural controls on iron isotope variations in Earth's mantle and crust. *Earth and Planetary Science Letters* **398**(C)**,** pp 127-140.

Davies, G. F. (1993) Cooling the core and mantle by plume and plate flows. *Geophysical Journal International* **115**(1)**,** pp 132-146.

Debret, B., Millet, M. A., Pons, M. L., Bouilhol, P., Inglis, E. & Williams, H. (2016) Isotopic evidence for iron mobility during subduction. *Geology* **44**(3)**,** pp 215.

Debret, B., Reekie, C., Mattielli, N., Savov, I., Beunon, H., Ménez, B. & Williams, H. (2020) Redox transfer at subduction zones: insights from Fe isotopes in the Mariana forearc. *Geochemical Perspectives Letters* **12**, 46-51.

Doucet, L., Zheng-Xiang, L., Brendan, M., Collins, W., Spencer, C. & Mitchell, R. (2020) Distinct formation history for deep-mantle domains reflected in geochemical differences. *Nature Geoscience* **13**(7)**,** pp 511-515.

Du, D.-H., Wang, X.-L., Yang, T., Chen, X., Li, J.-Y. & Li, W. (2017) Origin of heavy Fe isotope compositions in high-silica igneous rocks: A rhyolite perspective. *Geochimica et Cosmochimica Acta* **218,** 58-72.

Dziewonski, A. M. (1984) Mapping the lower mantle: determination of lateral heterogeneity in P velocity up to degree and order 6. *Journal of Geophysical Research: Solid Earth* **89**(B7)**,** pp 5929-5952.

Eggins, S. M., Green, D. H. & Falloon, T. J. (1991) The Tasmantid Seamounts shallow melting and contamination of an EM1 mantle plume. *Earth and Planetary Science Letters* **107**(3)**,** pp 448-462.

El Korh, A., Luais, B., Deloule, E. & Cividini, D. (2017) Iron isotope fractionation in subduction-related high-pressure metabasites (Ile de Groix, France). *Contributions to Mineralogy and Petrology,* 172(6)**,** pp 1-19.

Farley, K. A., Natland, J. H. & Craig, H. (1992) Binary mixing of enriched and undegassed (primitive?) mantle components (He, Sr, Nd, Pb) in Samoan lavas. *Earth and Planetary Science Letters* **111**(1)**,** pp 183-199.

Farnetani, D. G. & Richards, M. A. (1995) Thermal entrainment and melting in mantle plumes. *Earth and Planetary Science Letters* **136**(3-4)**,** pp 251-267.

Foden, J., Sossi, P. A. & Nebel, O. (2018) Controls on the iron isotopic composition of global arc magmas. *Earth and Planetary Science Letters* **494**, 190-201.

Foulger, G. R. (2005) Mantle plumes: Why the current skepticism. *Chinese Science Bulletin* **50**(15)**,** pp 1555-1560.

Foulger, G. R. & Jurdy, D. M. (2007) Plates, plumes, and planetary processes: *Geological Society of America*.

French, S. W. & Romanowicz, B. (2015) Broad plumes rooted at the base of the Earth's mantle beneath major hotspots. *Nature* **525**(7567)**,** pp 95.

Frey, F., Green, D. & Roy, S. (1978) Integrated models of basalt petrogenesis: a study of quartz tholeiites to olivine melilitites from south eastern Australia utilizing geochemical and experimental petrological data. *Journal of Petrology* **19**(3)**,** pp 463-513.

Frey, F. A., Garcia, M. O., Wise, W. S., Kennedy, A., Gurriet, P. & Albarede, F. (1991) The evolution of Mauna Kea Volcano, Hawaii: Petrogenesis of tholeiitic and alkalic basalts. *Journal of Geophysical Research: Solid Earth* **96**(B9)**,** pp 14347-14375.

Garapić, G., Jackson, M., Hauri, E., Hart, S., Farley, K., Blusztajn, J. & Woodhead, J. (2015) A radiogenic isotopic (He-Sr-Nd-Pb-Os) study of lavas from the Pitcairn hotspot: Implications for the origin of EM-1 (enriched mantle 1). *Lithos* **228,** 1-11.

Garcia, M. O., Hulsebosch, T. P. & Rhodes, J. M. (1995) Olivine-rich submarine basalts from the southwest rift zone of Mauna Loa volcano: Implications for magmatic processes and geochemical evolution. *GMS* **92**, 219-239.

Garnero, E. J., Lay, T. & McNamara, A. (2007) Implications of lower-mantle structural heterogeneity for the existence and nature of whole-mantle plumes. *Special Papers-Geological Society of America* **430**, pp 79.

Garnero, E. J., Mcnamara, A. K. & Shim, S.-H. (2016) Continent-sized anomalous zones with low seismic velocity at the base of Earth's mantle. *Nature Geoscience* **9**(7)**,** pp. 481-489

Gerbode, C. & Dasgupta, R. (2010) Carbonate-fluxed Melting of MORB-like Pyroxenite at 2.9 GPa and Genesis of HIMU Ocean Island Basalts. *Journal of Petrology* **51**(10)**,** pp 2067-2088.

Gleeson, M. L. M., Gibson, S. A. & Williams, H. M. (2020) Novel insights from Fe-isotopes into the lithological heterogeneity of Ocean Island Basalts and plume-influenced MORBs. *Earth and Planetary Science Letters* **535**, 116114

Goes, S., Capitanio, F. A. & Morra, G. (2008) Evidence of lower-mantle slab penetration phases in plate motions. *Nature* **451**(7181)**,** pp 981-984.

Green, D. & Ringwood, A. (1967) The genesis of basaltic magmas. *Contributions to Mineralogy and Petrology* **15**(2)**,** pp 103-190.

Griffiths, R. W. & Campbell, I. H. (1990) Stirring and structure in mantle starting plumes. *Earth and Planetary Science Letters* **99**(1-2)**,** pp 66-78.

Hahm, D., Castillo, P. & Hilton, D. (2009) A deep mantle source for high 3He/4He ocean island basalts (OIB) inferred from Pacific near-ridge seamount lavas. *Geophysical Research Letters* **36**(20)**,** L20316.

Halliday, A. N., Lee, D.-C., Tommasini, S., Davies, G. R., Paslick, C. R., Godfrey Fitton, J. & James, D. E. (1995) Incompatible trace elements in OIB and MORB and source enrichment in the sub-oceanic mantle. *Earth and Planetary Science Letters* **133**(3-4)**,** pp 379-395.

Hanan, B. & Graham, D. (1996) Lead and helium isotope evidence from oceanic basalts for a common deep source of mantle plumes. *Science* **272**(5264)**,** pp 991-995.

Hart, S., Hauri, E., Oschmann, L. A. & Whitehead, J. A. (1992) Mantle Plumes and Entrainment: Isotopic Evidence. *Science* **256**(5056)**,** pp 517.

Hart, S., Schilling, J.-G. & Powell, J. (1973) Basalts from Iceland and along the Reykjanes Ridge: Sr isotope geochemistry. *Nature Physical Science* **246**(155)**,** pp 104-107.

Hart, S. R. (1984) A large-scale isotope anomaly in the Southern Hemisphere mantle. *Nature* **309**(5971)**,** pp 753.

Helffrich, G. R. & Wood, B. J. (2001) The Earth's mantle. *Nature* **412**(6846)**,** pp 501-507.

Hirschmann, M., Kogiso, T., Baker, M. & Stolper, E. (2003) Alkalic magmas generated by partial melting of garnet pyroxenite. *Geology* **31**(6)**,** pp 481.

Hofmann, A. W. (1997). Mantle geochemistry: the message from oceanic volcanism. *Nature* **385**(6613)**,** pp 219.

Hofmann, A. W. (2003) Sampling Mantle Heterogeneity through Oceanic Basalts: Isotopes and Trace Elements, in Treatise on Geochemistry: The Mantle and Core, edited by R. W. Carlson, H.D. Holland, and K.K. Turekian. Elsevier, New York.

Hofmann, A. W. & White, W. M. (1982) Mantle plumes from ancient oceanic crust. *Earth and Planetary Science Letters* **57**(2)**,** pp 421-436.

Humphreys, E. R. & Niu, Y. (2009) On the composition of ocean island basalts (OIB): The effects of lithospheric thickness variation and mantle metasomatism. Lithos, 112, pp 118-136.

Jackson, M. G., Becker, T. W. & Konter, J. G. (2018) Geochemistry and Distribution of Recycled Domains in the Mantle Inferred From Nd and Pb Isotopes in Oceanic Hot Spots:

Implications for Storage in the Large Low Shear Wave Velocity Provinces. *Geochemistry, Geophysics, Geosystems* **19**(9)**,** pp 3496-3519.

Jackson, M. G. & Dasgupta, R. (2008) Compositions of HIMU, EM1, and EM2 from global trends between radiogenic isotopes and major elements in ocean island basalts. *Earth and Planetary Science Letters* **276**(1)**,** pp 175-186.

Jackson, M. G., Kurz, M. D., Hart, S. R. & Workman, R. K. (2007) New Samoan lavas from Ofu Island reveal a hemispherically heterogeneous high 3He/ 4He mantle. *Earth and Planetary Science Letters* **264**(3)**,** pp 360-374.

Johnson, C., Bell, K., Beard, B. & Shultis, A. (2010) Iron isotope compositions of carbonatites record melt generation, crystallization, and late-stage volatile-transport processes. *Mineralogy and Petrology* **98**(1)**,** pp 91-110.

Kerr, R. A. (1984) The deepest hole in the world. *Science* **224,** 1420-1421.

Kogiso, T., Hirschmann, M. & Pertermann, M. (2004) High-pressure partial melting of mafic lithologies in the mantle. *Journal of Petrology* **45**(12)**,** pp 2407-2422.

Kogiso, T., Hirschmann, M. M. & Frost, D. J. (2003) High-pressure partial melting of garnet pyroxenite: possible mafic lithologies in the source of ocean island basalts. *Earth and Planetary Science Letters* **216**(4)**,** pp 603-617.

Konter, J. G., Pietruszka, A. J., Hanan, B. B., Finlayson, V. A., Craddock, P. R., Jackson, M. G. & Dauphas, N. (2016) Unusual δ56Fe values in Samoan rejuvenated lavas generated in the mantle. *Earth and Planetary Science Letters* **450**, 221-232.

Koppers, A. A. (2011) Mantle plumes persevere. *Nature Geoscience* **4**(12)**,** pp 816-817.

Kozlovsky, Y. A. (1984) The world's deepest well. *Scientific American* **251**(6)**,** pp 98-105.

Lambart, S., Baker, M. B. & Stolper, E. M. (2016) The role of pyroxenite in basalt genesis: Melt-PX, a melting parameterization for mantle pyroxenites between 0.9 and 5GPa. *Journal of Geophysical Research: Solid Earth* **121**(8)**,** pp 5708-5735.

Lambart, S., Laporte, D. & Schiano, P. (2013) Markers of the pyroxenite contribution in the major-element compositions of oceanic basalts: Review of the experimental constraints. *Lithos* **160-161**, pp. 14-36.

Lesher, C. E., Dannberg, J., Barfod, G. H., Bennett, N. R., Glessner, J. J., Lacks, D. J. & Brenan, J. M. (2020) Iron isotope fractionation at the core–mantle boundary by thermodiffusion. *Nature Geoscience* **13**(5)**,** pp 382-386.

Lithgow-Bertelloni, C. & Richards, M. A. (1998) The dynamics of Cenozoic and Mesozoic plate motions. *Reviews of Geophysics* **36**(1)**,** pp 27-78.

Matzen, A. K., Wood, B. J., Baker, M. B. & Stolper, E. M. (2017) The roles of pyroxenite and peridotite in the mantle sources of oceanic basalts. *Nature Geoscience* **10**(7)**,** pp 530-535.

McCoy-West, A. J., Fitton, J. G., Pons, M.-L., Inglis, E. C. & Williams, H. M. (2018) The Fe and Zn isotope composition of deep mantle source regions: Insights from Baffin Island picrites. *Geochimica et Cosmochimica Acta* **238,** 542-562.

Millet, M.-A. & Dauphas, N. (2014) Ultra-precise titanium stable isotope measurements by double-spike high resolution MC-ICP-MS. *Journal of Analytical Atomic Spectrometry* **29**(8)**,** pp 1444-1458.

Montelli, R., Nolet, G., Dahlen, F., Masters, G., Engdahl, E. R. & Hung, S.-H. (2004) Finite-frequency tomography reveals a variety of plumes in the mantle. *Science* **303**(5656)**,** pp 338-343.

Morgan, W. J. (1971) Convection plumes in the lower mantle. *Nature,* **230**(5288)**,** pp 42-43.

Naumann, T. R. & Geist, D. J. (1999) Generation of alkalic basalt by crystal fractionation of tholeiitic magma. *Geology* **27**(5)**,** pp 423-426.

Nebel, O., Arculus, R. J., Sossi, P. A., Jenner, F. E. & Whan, T. H. E. (2013) Iron isotopic evidence for convective resurfacing of recycled arc-front mantle beneath back-arc basins. *Geophysical Research Letters* **40**(22)**,** pp 5849-5853.

Nebel, O., Sossi, P. A., Bénard, A., Arculus, R. J., Yaxley, G. M., Woodhead, J. D., Rhodri Davies, D. & Ruttor, S. (2019) Reconciling petrological and isotopic mixing mechanisms in the Pitcairn mantle plume using stable Fe isotopes. *Earth and Planetary Science Letters* **521**, 60-67.

Nebel, O., Sossi, P. A., Bénard, A., Wille, M., Vroon, P. Z. & Arculus, R. J. (2015) Redox-variability and controls in subduction zones from an iron-isotope perspective. *Earth and Planetary Science Letters* **432,** 142-151.

Niu, Y. (2018) Origin of the LLSVPs at the base of the mantle is a consequence of plate tectonics – A petrological and geochemical perspective. *Geoscience Frontiers* **9**(5)**,** pp 1265-1278.

Niu, Y. & O' Hara, M. J. (2003) Origin of ocean island basalts: A new perspective from petrology, geochemistry, and mineral physics considerations. *Journal of Geophysical Research: Solid Earth* **108,** B4.

Niu, Y., Wilson, M., Humphreys, E. R. & O'Hara, M. J. (2011) The Origin of Intra-plate Ocean Island Basalts (OIB): the Lid Effect and its Geodynamic Implications. *Journal of Petrology* **52**(7-8)**,** pp 1443-1468.

O'Hara, M. (1968) The bearing of phase equilibria studies in synthetic and natural systems on the origin and evolution of basic and ultrabasic rocks. *Earth-Science Reviews* **4,** 69-133.

O'Neill, H. S. C. (2016) The Smoothness and Shapes of Chondrite-normalized Rare Earth Element Patterns in Basalts. *Journal of Petrology,* **57**(8)**,** pp 1463-1508.

O'Hara, M.(1965) Primary magmas and the origin of basalts. *Scottish Journal of Geology* **1**(1)**,** pp 19-40.

Patchett, P. & Samson, S. (2003) Ages and growth of the continental crust from radiogenic isotopes. *Treatise on geochemistry* **3**, pp. 659.

Pilet, S., Hernandez, J., Sylvester, P., Poujol, M. (2005) The metasomatic alternative for ocean island basalt chemical heterogeneity. Earth and Planetary ScienceLetters, 263, pp 148-166.

Plank, T. & Langmuir, C. H. (1992) Effects of the melting regime on the composition of the oceanic crust. *Journal of Geophysical Research: Solid Earth,* **97**(B13)**,** pp 19749-19770.

Poitrasson, F., Delpech, G. & Gregoire, M. (2013) On the iron isotope heterogeneity of lithospheric mantle xenoliths: implications for mantle metasomatism, the origin of basalts and the iron isotope composition of the Earth. *Contributions to Mineralogy and Petrology* **165**(6)**,** pp 1243-1258.

Putirka, K. D. (2005) Mantle potential temperatures at Hawaii, Iceland, and the mid-ocean ridge system, as inferred from olivine phenocrysts: Evidence for thermally driven mantle plumes. *Geochemistry, Geophysics, Geosystems* **6**(5)**,** Q05L08.

Ricard, Y., Richards, M., Lithgow-Bertelloni, C. & Le Stunff, Y. (1993) A geodynamic model of mantle density heterogeneity. *Journal of Geophysical Research: Solid Earth* **98**(B12)**,** pp 21895-21909.

Richter, M., Nebel, O., Schwindinger, M., Nebel-Jacobsen, Y. & Dick, H. J. (2021) Competing effects of spreading rate, crystal fractionation and source variability on Fe isotope systematics in mid-ocean ridge lavas. *Scientific Reports* **11**(1)**,** pp 1-15.

Ruttor, S., Nebel, O., Nebel-Jacobsen, Y., Cohen, B., Eggins, S. (2021) Alkalinity of ocean island lavas decoupled from source components: a case study from the EM1-PREMA Tasmantid mantle plume. *Geochmimica et Cosmochimica Acta* **314**, 140-158.

Ryan, W.B., Carbotte, S.M., Coplan, J.O., O'Hara, S., Melkonian, A., Arko, R., Weissel, R.A., Ferrini, V., Goodwillie, A. and Nitsche, F. (2009) Global multi-resolution topography synthesis. *Geochemistry, Geophysics, Geosystems* **10**.

Schauble, E. (2004) Applying stable isotope fractionation theory to new systems. *Rev. Mineral. Geochem.* **55,** 65-111.

Schuessler, J. A., Schoenberg, R. & Sigmarsson, O. (2009) Iron and lithium isotope systematics of the Hekla volcano, Iceland - Evidence for Fe isotope fractionation during magma differentiation. *Chemical Geology* **258**(1)**,** pp 78-91.

Sobolev, A. V., Hofmann, A. W., Kuzmin, D. V., Yaxley, G. M., Arndt, N. T., Chung, S. L., Danyushevsky, L. V., Elliott, T., Frey, F. A., Garcia, M. O., Gurenko, A. A., Kamenetsky, V. S., Kerr, A. C., Krivolutskaya, N. A., Matvienkov, V. V., Nikogosian, I. K., Rocholl, A., Sigurdsson, I. A., Sushchevskaya, N. M. & Teklay, M. (2007) The Amount of Recycled Crust in Sources of Mantle-Derived Melts. *Science* **316**(5823)**,** pp 412-417.

Sobolev, A. V., Hofmann, A. W., Sobolev, S. V. & Nikogosian, I. K. (2005) An olivine-free mantle source of Hawaiian shield basalts. *Nature* **434**(7033)**,** pp 590.

Soderman, C. R., Matthews, S., Shorttle, O., Jackson, M. G., Ruttor, S., Nebel, O., Turner, S., Beier, C., Millet, M.-A., Widom, E., Humayun, M. & Williams, H. M. (2021) Heavy δ57Fe in ocean island basalts: a non-unique signature of processes and source lithologies in the mantle. *Geochimica et Cosmochimica Acta* **292**, 309-332.

Sossi, P., Foden, J. & Halverson, G. (2012) Redox-controlled iron isotope fractionation during magmatic differentiation: an example from the Red Hill intrusion, S. Tasmania. *Contributions to Mineralogy and Petrology* **164**(5)**,** pp 757-772.

Sossi, P. A., Halverson, G. P., Nebel, O. & Eggins, S. M. (2015) Combined separation of Cu, Fe and Zn from rock matrices and improved analytical protocols for stable isotope determination. *Geostandards and Geoanalytical Research* **39**(2)**,** pp 129-149.

Sossi, P. A., Nebel, O. & Foden, J. (2016) Iron isotope systematics in planetary reservoirs. *Earth and Planetary Science Letters* **452**, 295-308.

Sossi, P. A. & O'Neill, H. S. C. (2017) The effect of bonding environment on iron isotope fractionation between minerals at high temperature. *Geochimica et Cosmochimica Acta* **196**, pp. 121.

Stracke, A., Bizimis, M. & Salters, V. J. M. (2003) Recycling oceanic crust: Quantitative constraints. *Geochemistry, Geophysics, Geosystems* **4**(3)**,** 8003.

Stracke, A., Hofmann, A. W. & Hart, S. R. (2005) FOZO, HIMU, and the rest of the mantle zoo. *Geochemistry, Geophysics, Geosystems* **6**(5)**,** Q05007.

Sun, P., Niu, Y., Guo, P., Duan, M., Chen, S., Gong, H., Wang, X. & Xiao, Y. (2020) Large iron isotope variation in the eastern Pacific mantle as a consequence of ancient low-degree melt metasomatism. *Geochimica et Cosmochimica Acta* **286**, 269-288.

Sun, S. S. & McDonough, W. F. (1989) Chemical and isotopic systematics of oceanic basalts: implications for mantle composition and processes. *Geological Society, London, Special Publications* **42**(1)**,** pp 313-345.

Taylor, B. & Martinez, F. (2003) Back-arc basin basalt systematics. *Earth and Planetary Science Letters* **210**(3-4)**,** pp 481-497.

Taylor, P., Maeck, R. & De Bièvre, P. (1992) Determination of the absolute isotopic composition and atomic weight of a reference sample of natural iron. *International Journal of Mass Spectrometry and Ion Processes* **121**(1-2)**,** pp 111-125.

Teng, F.-Z., Dauphas, N. & Helz, R. T. (2008) Iron isotope fractionation during magmatic differentiation in Kilauea Iki lava lake. *Science (New York, N.Y.)* **320**(5883)**,** pp 1620.

Teng, F.-Z., Dauphas, N., Helz, R. T., Gao, S. & Huang, S. (2011) Diffusion-driven magnesium and iron isotope fractionation in Hawaiian olivine. *Earth and Planetary Science Letters* **308**(3)**,** pp 317-324.

Teng, F.-Z., Dauphas, N., Huang, S. & Marty, B. (2013) Iron isotopic systematics of oceanic basalts. *Geochimica et Cosmochimica Acta* **107**(12-26).

Turner, S., Williams, H., Piazolo, S., Blichert-Toft, J., Gerdes, M., Adam, J., Liu, X.-M., Schaefer, B. & Maury, R. (2018) Sub-arc xenolith Fe-Li-Pb isotopes and textures tell tales of their journey through the mantle wedge and crust. *Geology* **46**(11)**,** pp 947-950.

Van der Hilst, R. D., Widiyantoro, S. & Engdahl, E. (1997) Evidence for deep mantle circulation from global tomography. *Nature* **386**(6625)**,** pp 578-584.

Van der Hist, R., Engdahl, R., Spakman, W. & Nolet, G. (1991) Tomographic imaging of subducted lithosphere below northwest Pacific island arcs. *Nature* **353**(6339)**,** pp 37-43.

Van der Meer, D. G., Van Hinsbergen, D. J. & Spakman, W. (2018) Atlas of the underworld: Slab remnants in the mantle, their sinking history, and a new outlook on lower mantle viscosity. *Tectonophysics* **723**, 309-448.

Van Keken, P. (1997) Evolution of starting mantle plumes: a comparison between numerical and laboratory models. *Earth and Planetary Science Letters* **148**(1-2)**,** pp 1-11.

Wang, X.-C., Li, Z.-X., Li, X.-H., Li, J., Xu, Y.-G. & Li, X.-H. (2013) Identification of an ancient mantle reservoir and young recycled materials in the source region of a young mantle plume: Implications for potential linkages between plume and plate tectonics. *Earth and Planetary Science Letters* **377-378**(C)**,** pp 248-259.

Wang, X.-J., Chen, L.-H., Hofmann, A. W., Hanyu, T., Kawabata, H., Zhong, Y., Xie, L.-W., Shi, J.-H., Miyazaki, T., Hirahara, Y., Takahashi, T., Senda, R., Chang, Q., Vaglarov, B. S. & Kimura, J.-I. (2018) Recycled ancient ghost carbonate in the Pitcairn mantle plume. *Proceedings of the National Academy of Sciences of the United States* **115**(35)**,** pp 8682.

Weaver, B. L. (1991) The origin of ocean island basalt end-member compositions: trace element and isotopic constraints. *Earth and Planetary Science Letters* **104**(2-4)**,** pp 381-397.

Weyer, S. (2008) Geochemistry. What drives iron isotope fractionation in magma? *Science (New York, N.Y.)* **320**(5883)**,** pp 1600.

Weyer, S. & Ionov, D. A. (2007) Partial melting and melt percolation in the mantle: The message from Fe isotopes. *Earth and Planetary Science Letters* **259**(1-2)**,** pp 119-133.

White, W. M. (1985) Sources of oceanic basalts: Radiogenic isotopic evidence. *Geology* **13**(2)**,** pp 115-118.

White, W. M. (2010) Oceanic island basalts and mantle plumes: the geochemical perspective. *Annual Review of Earth and Planetary Sciences* **38**, 133-160.

White, W. M. (2015) Isotopes, DUPAL, LLSVPs, and anekantavada. *Chemical Geology* **419**, 10-28.

White, W. M. & Hofmann, A. W. (1982) Sr and Nd isotope geochemistry of oceanic basalts and mantle evolution. *Nature* **296**, 821-825.

Williams, H. M. & Bizimis, M. (2014) Iron isotope tracing of mantle heterogeneity within the source regions of oceanic basalts. *Earth and Planetary Science Letters* **404**(C)**,** pp 396-407.

Williams, H. M., McCammon, C. A., Peslier, A. H., Halliday, A. N., Teutsch, N., Levasseur, S. & Burg, J.-P. (2004) Iron isotope fractionation and the oxygen fugacity of the mantle. *Science* **304**(5677)**,** pp 1656-1659.

Williams, H. M., Nielsen, S. G., Renac, C., Griffin, W. L., O'Reilly, S. Y., McCammon, C. A., Pearson, N., Viljoen, F., Alt, J. C. & Halliday, A. N. (2009) Fractionation of oxygen and iron isotopes by partial melting processes: Implications for the interpretation of stable isotope signatures in mafic rocks. *Earth and Planetary Science Letters* **283**(1)**,** pp 156-166.

Williams, H. M., Peslier, A. H., McCammon, C., Halliday, A. N., Levasseur, S., Teutsch, N. & Burg, J. P. (2005) Systematic iron isotope variations in mantle rocks and minerals: The effects of partial melting and oxygen fugacity. *Earth and Planetary Science Letters* **235**(1)**,** pp 435-452.

Wilson, J. T. (1963) A Possible Origin of the Hawaiian Islands. *Canadian Journal of Physics* **41**(3)**,** pp 863-870.

Workman, R. K., Hart, S. R., Jackson, M., Regelous, M., Farley, K. A., Blusztajn, J., Kurz, M. & Staudigel, H. (2004) Recycled metasomatized lithosphere as the origin of the Enriched Mantle II (EM2) end-member: Evidence from the Samoan Volcanic Chain. *Geochemistry, Geophysics, Geosystems* **5**(4), Q04008.

Yang, Z. F., Li, J., Jiang, Q. B., Xu, F., Guo, S. Y., Li, Y. & Zhang, J. (2019) Using major element logratios to recognize compositional patterns of basalt: Implications for source lithological and compositional heterogeneities. *Journal of Geophysical Research: Solid Earth* **124**(4)**,** pp 3458-3490.

Yoder Jr, H. & Tilley, C. E. (1962) Origin of basalt magmas: an experimental study of natural and synthetic rock systems. *Journal of Petrology* **3**(3)**,** pp 342-532.

Zhou, H. W. (1996) A high-resolution P wave model for the top 1200 km of the mantle. *Journal of Geophysical Research: Solid Earth* **101**(B12)**,** pp 27791-27810.

Zindler, A. & Hart, S. (1986) Chemical geodynamics. *Annual Review of Earth and Planetary Sciences* **14**, 493-571.

CHAPTER 2

Published in Geochmicia et Cosmochimica Acta

2. Alkalinity of ocean island lavas decoupled from enriched source components: a case study from the EM1-PREMA Tasmantid mantle plume

Saskia Ruttor[1*], Oliver Nebel[1], Yona Nebel-Yacobsen[1], Benjamin E. Cohen[2], Stephen Eggins[3]

[1] School of Earth, Atmosphere and Environment, Monash University, Melbourne, 3800 Clayton, Australia, saskia.ruttor@monash.edu

[2]School of GeoSciences, University of Edinburgh, Edinburgh EH9 3FE, United Kingdom

[3]Research School of Earth Sciences, Australian National University, Canberra ACT 0200, Australia

ABSTRACT

The alkalinity of ocean island basalts (OIB), which form by upwelling thermo-chemical instabilities in the mantle, is often associated with the degree of melting. Yet it remains to be tested if alkalinity and the degree of melting are systematically associated with enriched mantle components. The Tasmantid Seamounts, which are fossil remnants of the Tasmantid mantle plume, comprise a north-south age-progressive submarine volcanic chain in the Coral and Tasman Seas East of Australia. Dredged seafloor lavas from nine seamounts along the seamount chain, ranging in age from 50 – 6.5 Ma, show a dichotomy in alkalinity, similar to those observed in other hotspot areas such as Hawai'i or Pitcairn. In radiogenic Sr-Nd-Hf-Pb isotope systematics, Tasmantid Seamount lavas form a continuum between EM1 and PREMA and are thus part of the prevalent EM1-PREMA association in the Pacific. However, their radiogenic Pb isotope systematics mark the Tasmantid plume as an individuum with no resemblance to any other plume. In stable Fe isotopes (expressed as $\delta^{57}Fe_{Prim}$, which is the Fe isotopic composition calculated to primitive lavas along a liquid line of descent) alkali basalts are, on average, isotopically heavier than tholeiitic lavas, ranging in $\delta^{57}Fe_{Prim}$ from +0.10 to +0.21‰, unrelated to radiogenic isotope systematics, but with co-variations of $\delta^{57}Fe_{Prim}$ and Ti* (which is the primitive melt Ti content). These systematics point towards residual garnet as a key factor and thus indicate a solely petrologic relation between degrees of melting and Fe isotopes. Tholeiitic lavas exhibit a near-depleted mantle like isotopic composition (ranging in $\delta^{57}Fe_{Prim}$ from -0.01 to +0.22‰, median at $\delta^{57}Fe_{Prim}$ +0.04‰), yet with values of up to $\delta^{57}Fe_{Prim}$ +0.22‰ that require an isotopically heavy source of unknown origin.

The lack of systematics between alkalinity and radiogenic isotopic signatures indicates that temperature is the likely driving force for variable melting degrees in some samples over others. Based on these observations, we surmise that tholeiitic lavas form in the plume centre whereas alkaline lavas form at the cooler rim of the conduit. Mixing between melts and associated enriched components in the Tasmantid mantle plume may occur but, at least for alkaline lavas, only on a small scale.

2.1 Introduction

A defining feature of ocean island basalts (OIB), which belong to age-progressive chains of subaerial and submarine volcanoes, commonly associated with mantle plumes, is their broad range in chemical as well as radiogenic isotopic compositions. The combined radiogenic Sr-Nd-Hf-Pb isotopic compositions of global OIB reveal an isotopic heterogeneity of their mantle source(s) that requires the presence of recycled crustal components (Jackson and Dasgupta, 2008; Stracke et al., 2005; Garapić et al., 2015; White, 2015; Hart, 1988; Hofmann, 1997; Castillo, 1988). In addition to this diversity in radiogenic isotopic compositions, many OIB generated by mantle plumes in hotspot areas, such as Hawai'i, exhibit a dichotomy in alkalinity (Fig. 1), divided into alkaline and sub-alkaline/tholeiitic lavas. These two types of basaltic melts are mainly distinguishable through major element systematics of Na_2O+K_2O for a given SiO_2 content.

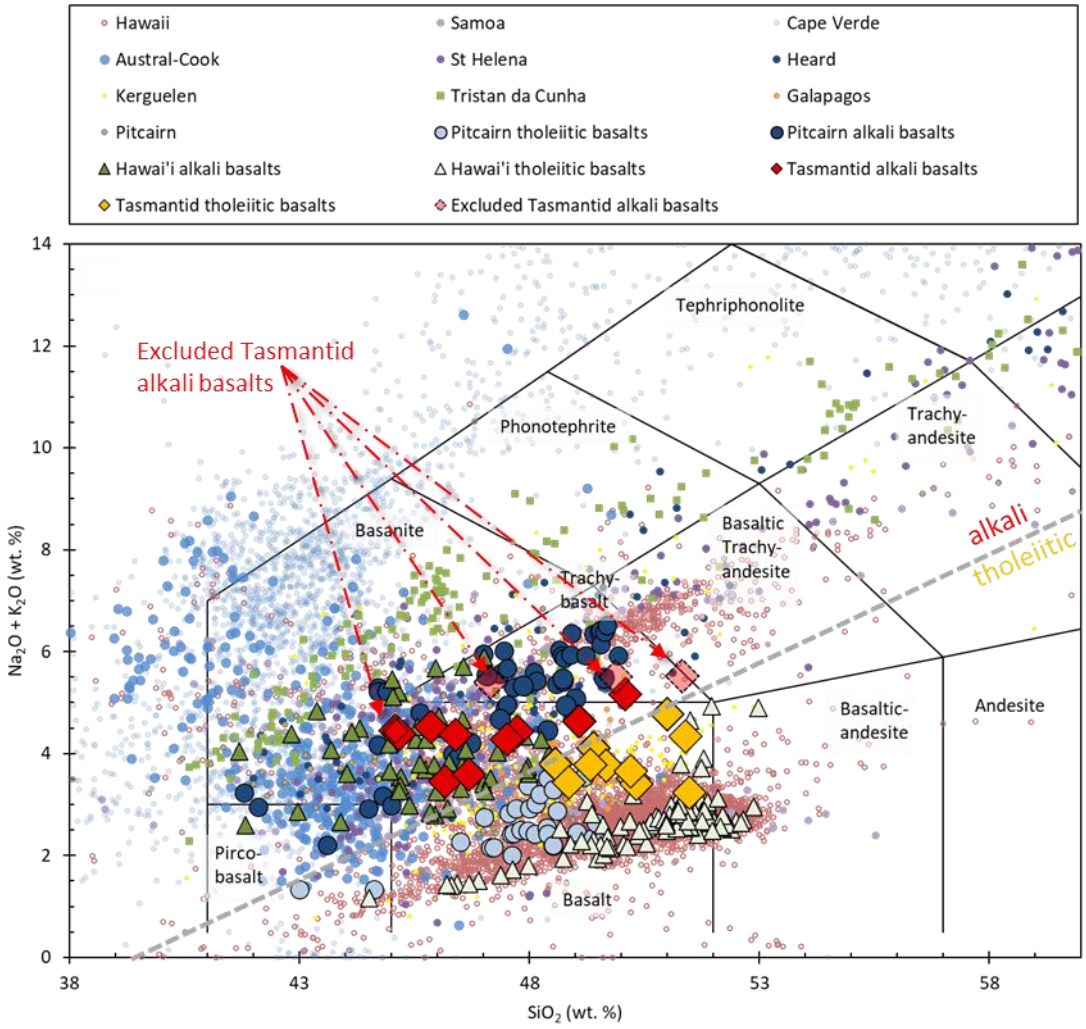

Figure 1. a) Total alkali-silica diagram (TAS diagram) after Le Bas et al. (1986) and division lines after Le Maître (1989) for classification of the whole rock suit of the Tasmantid Seamounts. In the following, the Tasmantid Seamounts will be compared to alkali and tholeiitic basalts of Hawai'i and Pitcairn (sample selection details in *section 5.1 Constraining and comparing enriched and depleted mantle components).* Data for Hawai'i, Pitcairn, Samoa, Cape Verde, Austral-Cook, St. Helena, Heard, Kerguelen, Tristan da Cunha, and Galapagos have been obtained from GEOROC (http://georoc.mpch-mainz.gwdg.de/georoc/). These locations represent hotspot areas all around the world and show that the bimodality of alkali and tholeiitic lavas at one location is common, however, some hotspots are restricted to alkali basalts, like Samoa, Cape Verde, Austral-Cook, Heard and Tristan da Cunha. Tasmantid Seamount samples that were screened out due to seawater alteration (four alkali basalts) have been highlighted in light red with dotted outlines.

The diversity of radiogenic isotopic compositions, divided into so-called enriched mantle components, suggests involvement of distinct parts of subducted oceanic lithosphere in the melting regime of OIB (Stracke et al., 2005; Lassiter and Hauri, 1998; Dupuy et al., 1989).

Consequently, this isotopic variability is likely to also involve lithological differences within the plume source, which, in turn, are associated with major element characteristics of plume-derived lavas (Jackson and Dasgupta, 2008). A clear connection between crustal character based on radiogenic isotopes and alkalinity has so far, however, not been established. The alkalinity of basalts (Na±K) at a given SiO_2 content can broadly be associated with their degree of melting: for tholeiitic basalts a higher melting degree at lower pressure is suggested (e.g., Garcia et al., 1993; Garcia et al., 1995; Green and Ringwood, 1967), whereas alkali basalts are associated with lower melting degrees at a higher pressure (e.g., Frey et al., 1978; Naumann and Geist, 1999; O'Hara, 1965; Green and Ringwood, 1967). For most OIB, this concept may hold true, yet it remains unclear if the presence of recycled crustal components adds to the degree of melting and with this to the alkaline character of erupted lavas. Based on experimental data, Mallik and Dasgupta (2012) outlined that major element systematics of alkali vs. tholeiitic lavas in OIB do not relate to melting regimes of respective lithologies, i.e., eclogite-facies crustal components vs peridotite melting. Instead, Jackson and Dasgupta (2008) and Jackson et al. (2012) highlight that major element systematics of OIB are related to specific enriched endmembers and source lithology (Si-poor to Si-rich), yet with the notable exception of Na. These contradictions spark the question as to what exactly controls alkalinity and how this relates to source lithology, which is arguably also related to mantle fertility, i.e., the pressure (*P*) - temperature (*T*) conditions at which these lithologies start to melt in the mantle. Alternative views suggest that the influence of lithospheric thickness dominates over mantle temperature in melting regimes of upwelling mantle (Niu et al., 2011). For individual plumes, and within their shield-building stage, lithospheric thickness is similar for all melts, and thus cannot be a defining factor for variations in the observed alkalinity.

In this paper, we seek to establish links between mantle components and alkalinity in OIB by using stable Fe isotopes in the Tasmantid Seamounts, an age-progressive chain of submarine volcanoes located east of Australia in the Tasman and Coral Seas. The Tasmantid Seamounts have been proposed to be plume-related, with unpublished isotopic data (radiogenic Sr and Nd isotopes from 18 samples) indicating an origin from a mixture of enriched and more primitive components of yet unidentified nature (McCulloch, 1988; Eggins et al., 1991). We analysed alkali and tholeiitic basalts from the Tasmantid Seamounts for stable Fe isotopes as well as major and trace elements and radiogenic Sr-Nd-Hf-Pb isotopic

compositions. Iron isotopes fractionate as a function of degree of melting (Williams and Bizimis, 2014; Soderman et al., 2021; Sossi and O'Neill, 2017; Foden et al., 2018), but also bear memory of potential crustal components (Nebel et al., 2019; Konter et al., 2016; Gleeson et al., 2020). By comparing radiogenic isotopic data with new stable Fe isotopic data of primary melts ($\delta^{57}Fe_{Prim}$ corrected for igneous differentiation), we aim to identify systematic variations between plume endmember components, degrees of melting and possible mixing scenarios.

2.2 Geological setting

The Tasmantid Seamounts are a chain of submarine volcanoes that extend from the Coral Sea in the north to the Tasman Sea in the south. The chain lies east of the Australian continent, and west of the Lord Howe Rise (Fig. 2). The Tasmantid Seamounts are one of three age-progressive volcanic chains in the region; with plume-related volcanic centres on the Australian continent to the west (Cohen et al., 2008; Wellman and McDougall, 1974; Cohen et al., 2013; Davies et al., 2015), and the Lord Howe plume track to the east (Fig. 2; Seton et al., 2019). The Tasmantid Seamount chain extends over more than 2500 km, with individual volcanoes rising to 4000 m above the surrounding seafloor. The oldest volcanoes (in the north of the chain) erupted ~50 Ma, with the volcanoes becoming progressively younger towards the south, consistent with plate motion in the region, with the youngest known volcano (Gascoyne) erupting ~6.5 Ma (McDougall and Duncan, 1988; Kalnins et al., 2015; Crossingham et al., 2017). The southward age progression is consistent with a volcanic hotspot that is supplied by a mantle plume beneath the northwards drifting Australian plate (Knesel et al., 2008). The Tasmantid Seamounts are located above an extinct mid-ocean ridge, which was active 82 - 52 Ma causing the opening of the Tasman Sea (Gaina et al., 1998).

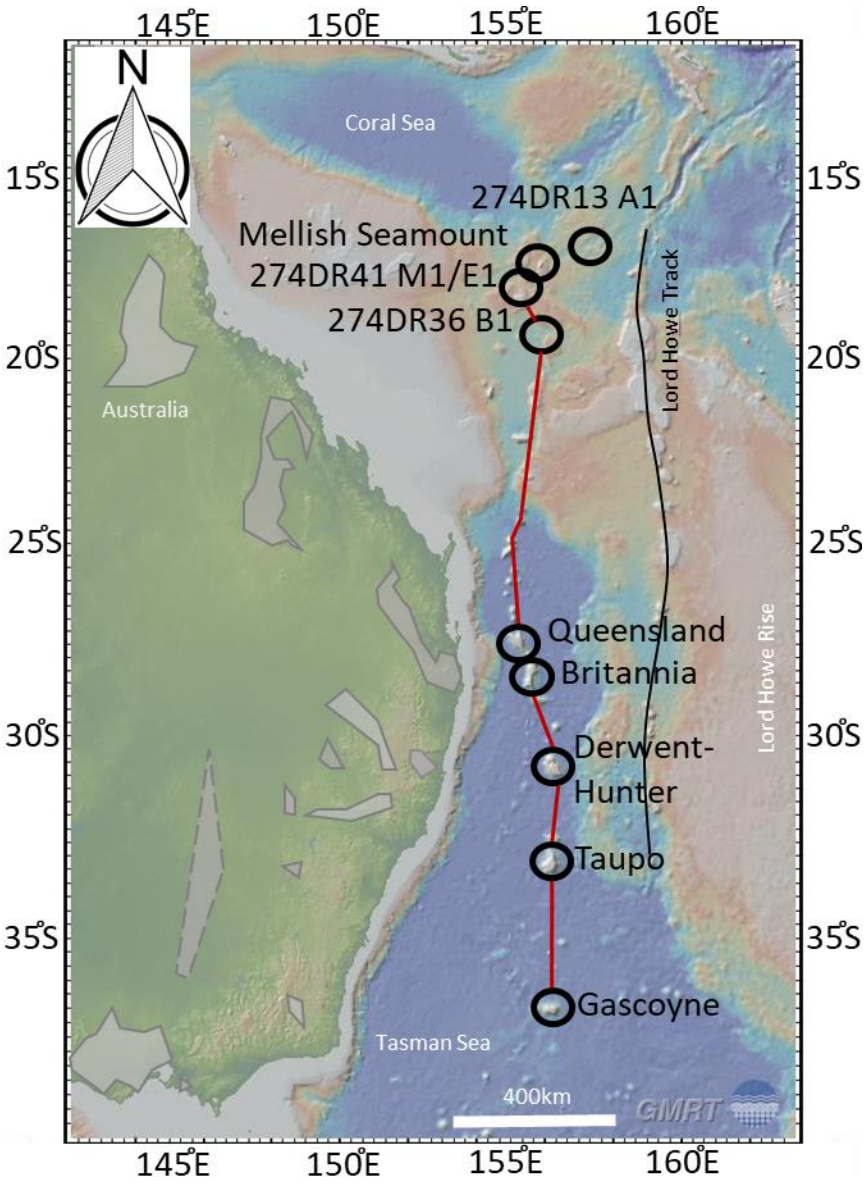

Figure 2. Location map of the Tasmantid Seamounts in the Tasman and Coral Seas (red line), with the Australian continent to the west, and Lord Howe Rise to the east. The figure was made with GeoMapApp (www.geomapapp.org; Ryan et al., 2009). The black circles show locations of rocks analysed in this study; samples 274SR13 A1, Mellish Seamount, 247DR41 M1, 247DR41 E1 and 274DR36 B1 are located in the Coral Sea, while rocks from Queensland, Britannia, Derwent-Hunter, Taupo, and Gascoyne are located in the Tasman Sea. Extinct spreading ridge is not drawn into figure to retain overview but follows the Tasmantid Seamounts. East Australian volcanoes in dark grey and lava fields in light grey following the classification of Wellman and McDougall (1974), leucites in dark grey with dashed outline (Cohen et al., 2008). The East Australian volcanoes (on the Australian continent) and the Lord Howe chain (on the Lord Howe Rise) are also chains of age progressive intraplate volcanoes.

2.3 Samples and methodology

The samples with the prefix `85` and `65` are the same as in Eggins et al. (1991) and McDougall and Duncan (1988) and cover the central and southern portions of the seamount trail (i.e., Queensland, Britannia, Derwent-Hunter, Taupo, and Gascoyne seamounts). They were obtained during dredging voyages on the RV *Franklin* in 1985 or 1986. Their petrography is described in Eggins et al. (1991). In short, rocks sampled from Gascoyne and Britannia have olivine and Cr-spinel phenocrysts, while rocks from Derwent-Hunter contain plagioclase and clinopyroxene phenocrysts. Taupo shows a variation of these phenocrysts. Fresh basalts show either altered rinds with cracks infilled with carbonate and zeolite or fresh glassy pillow margins. The sample with a prefix of 'TMD' is from Queensland, and was dredged on voyage SS2012_V07 of the RV *Southern Surveyor* (Cohen, 2012). Samples with a prefix of '274' are from the Coral Sea, from voyage SS2005_V02 of the RV *Southern Surveyor* (Exon et al., 2006). Exon et al. (2006) describe the whole rocks as fresh to slightly altered basalts with olivine, plagioclase and clinopyroxene in a fine-grained groundmass. The samples were chosen as being the freshest representatives from their respective seamounts, and to cover a wide latitudinal range of the Tasmantid Seamounts from north to south (Fig. 2).

2.3.1 Screening for alteration and fractionation

Submarine rocks often experience seawater alteration. In order to investigate the geochemistry of the magmatic processes, we have used four geochemical indicators to screen out the samples that have experienced seawater alteration: 1) $K_2O/P_2O_5 < 1$, as phosphorous is often precipitated by seawater (Frey et al., 1994; Hofmann and Feigenson, 1983), 2) P_2O_5/Nd, where decoupling indicates seawater alteration (Eggins et al., 1991); 3) negative cerium (Ce) anomalies, because seawater is depleted in Ce (O'Neill, 2016); and 4) MnO > 0.25 wt.%, because seawater alteration is often associated with precipitation of manganese oxide (Sofade, 2018).

Magnetite fractionation causes an increase in heavy Fe isotopes in the melt; corrections can be applied but become increasingly imprecise with increasing degrees of fractionation. For the discussion of Fe isotopes, we have therefore excluded samples that have undergone extensive fractional crystallization, using a cut-off value of MgO < 4.5 wt.% (Sossi

et al., 2012; Nebel et al., 2015). After using these geochemical indicators, 22 out of 26 samples are considered pristine; only four samples were excluded (further details in section *4. Results*).

2.3.2 Methodology

The major element and trace element data for samples with the prefix `85` and `65` were taken from Eggins et al. (1991) and McDougall and Duncan (1988). For samples TMD10-01 A4, 274DR41 M1, 274DR13 A1, 274DR22 A3, 274DR36 B1, and 274DR41 E1, major elements were analysed by quantitative XRF, with the Bruker-AXS S4 Pioneer X-ray fluorescence spectrometer, at the James Cook University, Townsville. Trace element data were analysed at the Isotopia Laboratory at Monash University, Clayton using a ThermoFisher ICap quadrupole mass spectrometer in solution mode. Sample aliquots for trace element analyses were taken from whole rock powders used for isotope analyse (see *3.2.1 Sample dissolution and purification procedures*). Data concentrations were calculated using a set of artificial standards for internal calibration, with absolute abundances accurate to within ± 5%, as determined by comparison against external, secondary rock standards.

2.3.2.1 Sample dissolution and purification procedures

Samples for Sr-Nd-Pb analyses were prepared following Pin et al. (2014). Approximately 100mg of rock powder was weighed into a Teflon® beaker. The rock powder was dissolved in a 1:1 mixture of concentrated double-distilled HF-HNO_3 in 15mL capped Savillex® beakers on a hotplate at 120°C for 24h. After evaporation to dryness the sample was treated three times with a drop of concentrated HNO_3 + 0.5M HCl and traces of HF to break down CaF bonds. For Sr-, and Pb-chemistry the chromatographic extraction resin Eichrom® Sr-Spec (100 – 150 µm) and for Nd-chemistry Eichrom® Tru-Spec resin were preconditioned with 0.1mL of 1M HNO_3 containing 50mg/mL of ascorbic acid. After introducing the sample solution onto the columns, both resins were rinsed with 0.5mL of 1M HNO_3 containing 50mg/mL of ascorbic acid. The Sr-Spec was washed with 7M HNO_3 to get rid of unwanted elements like Barium. Strontium elution was performed with 0.05M HNO_3. Subsequently, Pb was collected using 6M HCl. The Tru-Spec was rinsed with 1M HNO_3 (2mL), 0.05M HNO_3 (0.1mL) and 0.05M HCl (0.1mL) to wash out matrix elements. 0.05M HCl (1.5mL) was used to transfer Light Rare Earth Elements (LREE) from the TRU-Spec to the Ln-Spec. The Ln-Spec was treated with 0.05M HCl and 0.25M

HCl to elute lanthanides. Finally, with 0.25M HCl (2ml) Nd was collected. Samples were left on a hotplate at 55°C until dryness was achieved.

The analytical procedure used to extract Fe is published by Cheng et al. (2014) and Sossi et al. (2015). For complete dissolution ~25mg of rock powder was weighed into 15mL Savillex® beakers and treated with 2mL concentrated HF:HNO_3 (ratio 1:2). Samples were left capped on a hotplate at 120°C until completely dissolved. After evaporation, samples were treated with several drops of concentrated nitric acid (16M) to ensure the absence of fluoride bonds (Cheng et al., 2014). The AG-MP-1 anion resin was preconditioned with 9M HCl (Cheng et al., 2014). Samples were then taken up in 9M HCl and pipetted onto the resin. Column chromatographic extraction with 9M HCl and 5M HCl removed matrix elements as well as semi and transitional metals. The matrix was collected into a Teflon beaker for Hf analysis (see below *section 3.2.1*). The Fe fraction was eluted with 1M HCl. The collected Fe fraction was placed on a hotplate at 90°C. The dried samples were dissolved and taken up in 2% HNO_3.

For the chromatographic extraction of Hf the procedure of Nebel et al. (2009) and Cheng et al. (2014) was followed. For this method, the matrix was collected as explained above (removed matrix during chromatographic extraction of Fe) and dissolved in 3M HCl (10ml). The matrix was then loaded onto the Eichrom Ln spec resin. The resin was preconditioned with 3M HCl (10ml), 1M HF (10ml) and 3M HCl (3ml) before the samples were loaded onto the column. The resin was then rinsed with 3M HCl (10ml), 6M HCl (10ml) and MQ water (18mΩ). To elute Ti we used a mixture of citric acid and 0.4M HNO_3 and 1% H_2O_2 (60ml; Münker et al., 2001). Afterwards, Hf was extracted with 0.5M HF (10ml) and left on the hotplate to dry at 60°C.

2.3.2.2 Isotope analyses

The Sr-Nd-Pb-Hf-Fe isotope analyses were performed on a ThermoFisher™ Scientific Neptune*Plus* multi-collector inductively coupled plasma mass spectrometer (MC-ICP-MS) at the Isotopia Laboratory at the School of Earth, Atmosphere and Environment at Monash University, Australia. The samples were introduced via a low flow quartz cyclonic spray chamber and a PFA® nebuliser. Sr, Nd and Pb isotopes were measured in low resolution mode, whereas Fe was analysed in medium resolution mode. For Hf analysis, the samples were

introduced via a Teledyne Cetac® Technologies Aridus II to create dry plasma conditions. Hf isotopes were measured in low resolution mode.

To ensure data accuracy the reference materials BCR2, BHVO2 (USGS) and La Jolla (Nd reference material) were analysed (Table 1). Radiogenic Sr, Nd, Pb and Hf values are within analytical uncertainty of published literature values (Jweda et al., 2016; Weis et al., 2006; Weis et al., 2005).

For Fe, the data are reported in delta notation relative to the IRMM-524a external standard, which is isotopically identical to IRMM-014 (Craddock and Dauphas, 2011) with ^{5x}Fe being either ^{56}Fe or ^{57}Fe:

$$\delta^{5x}Fe = \left[\frac{^{5x}Fe/^{54}Fe_{Sample}}{^{5x}Fe/^{54}Fe_{IRMM-524a}} - 1\right] x\ 1000 \quad (1)$$

Each sample was analysed two to three times from a single dissolution batch using standard-sample-bracketing to ensure precision and accuracy. The average of these three individual analyses is presented as the result of the isotopic ratios for each sample. A Ni standard solution was added to each dissolution batch to correct for instrumental mass bias effects (Sossi et al., 2015). To ensure reliability and comparability of our Fe isotope data, the basaltic reference material BCR2 and BHVO1 were analysed three times (Table 2 shows the average of the three analyses). Our analyses are in agreement with previously published values (BCR2: δ^{56}Fe = +0.09 ± 0.01‰, δ^{57}Fe = +0.13 ± 0.02‰ in Craddock and Dauphas (2011) and δ^{57}Fe = +0.14 ± 0.02‰ in Sossi et al. (2015); BHVO1: δ^{56}Fe = +0.11 ± 0.01‰, δ^{57}Fe = +0.16 ± 0.01‰ in Craddock and Dauphas (2011)). The reproducibility of the method is ±0.02‰ (as a two-standard deviation) in ^{57}Fe/^{54}Fe relative to the IRMM-524a external standard based on repeated analyses of standard reference materials. At the end of the analysis a blank has been analysed and showed values below detection level and is thus negligible (<25 ng Fe).

2.4 Results

2.4.1 Major and trace elements

The Tasmantid Seamount samples range from alkali to tholeiitic basalts (Eggins et al., 1991; Fig. 1). Based on a compilation of other global hotspot areas (Fig. 1), the coexistence of alkali and tholeiitic basalts within a single volcanic hotspot centre is common. There is no apparent time-space variation along the Tasmantid Seamounts; tholeiitic basalts are found at

Gascoyne, Taupo, Derwent-Hunter, Britannia, Queensland, 274DR13 A1 and 274DR41 M1, while alkali basalts are found at Gascoyne, Taupo, Derwent-Hunter, Queensland, Mellish, 274DR36 B1 and 274DR41 E1 (Table 1). Given the low numbers of one to five samples analysed per seamount, it is highly likely that most seamounts have both tholeiitic and alkali lavas.

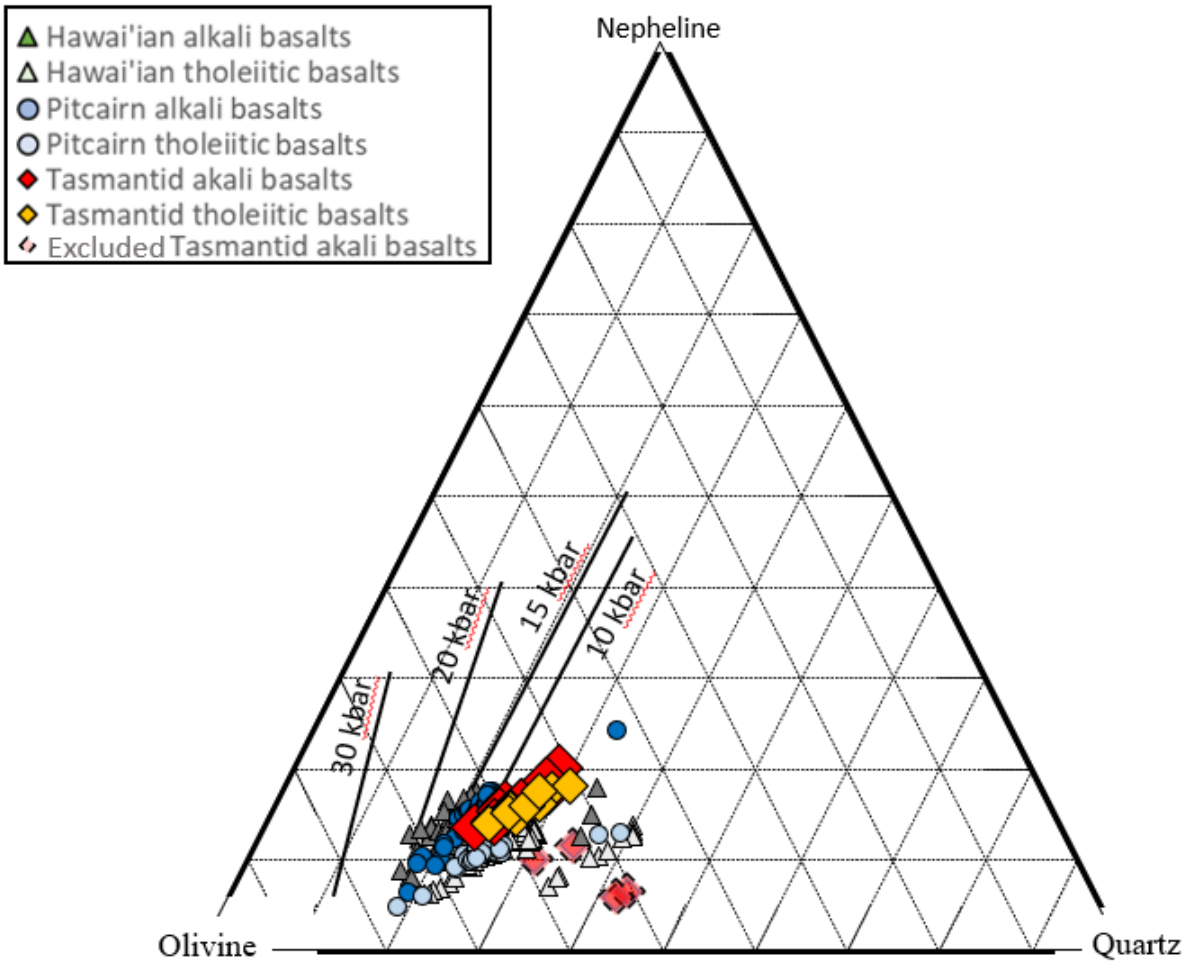

Figure 3. Olivine – nepheline – quartz plot after Irvine and Baragar (1971) (nepheline = nepheline + 0.6 * albite; quartz = quartz + 0.4 * albite + 0.25 * orthopyroxene; olivine = olivine + 0.75 * orthopyroxene). Melting pressure adapted from Hirose and Kushiro (1993). Excluded Tasmantid alkali basalts in red diamonds and dotted outline are deviating from the rest of the alkali lavas, strengthening the exclusion of these samples. Data for Hawai'i and Pitcairn from GEOROC (http://georoc.mpch-mainz.gwdg.de/georoc/).

On a Ne*-Ol*-Qtz* projection (Fig. 3), the tholeiitic basalts of the Tasmantid Seamounts show slightly more normative quartz with SiO_2 ranging from 48.58 – 51.48 wt.%. Alkali basalts range in SiO_2 from 45.17 – 50.08 wt.% and are, by definition, silica deficient compared to the tholeiitic basalts. Notably, samples that have been marked as altered through other trace

element systematics also plot off the igneous trend here. Alkali and tholeiitic lavas show increasing values of MnO and decreasing Al_2O_3 and P_2O_5 vs increasing MgO (4.8 wt.% < MgO < 11.4 wt.%; Fig. 4b, c, d and Supplementary data I, Fig. S1). Both alkali and tholeiitic basalts show a slight increase in CaO with increasing MgO. At a given degree of fractionation, alkali basalts have higher TiO_2, K_2O and Na_2O (Fig. 3 & 4) compared to tholeiitic basalts (Supplementary data I, Fig. S1).

As is expected for evolving lavas, MgO correlates positively with compatible elements such as Ni and Cr (Fig. 4e and Supplementary data I, Fig. S2). There is, however, no correlation between MgO and incompatible elements like Th and La (Fig. 4f). Chromium and La have not been included in Fig. 4, because Cr shows the same trend as Ni, and Th the same scatter as La. Alkali basalts are slightly more enriched in incompatible elements, showing an average in, for example, Th of 2.06 ppm, whereas tholeiitic basalts show an average in Th of 1.34 ppm (Fig. 4 & 5).

Three of the excluded alkali basalts show MgO < 4.5 wt.% with low FeO_T, Ni and Th. Sample 85177 has been excluded due to high Ni values (Fig. 4e; further explained below in section *4.3. Stable Fe isotope data*). The major and trace element data indicate that, for the Tasmantid samples analysed, fractional crystallization occurred via removal of olivine and clinopyroxene, given the increasing MgO value of alkali and tholeiitic basalts with increasing CaO/Al_2O_3 (Fig. 4c). There was little to no plagioclase fractionation (Fig. 4c), as is common for high-pressure melts.

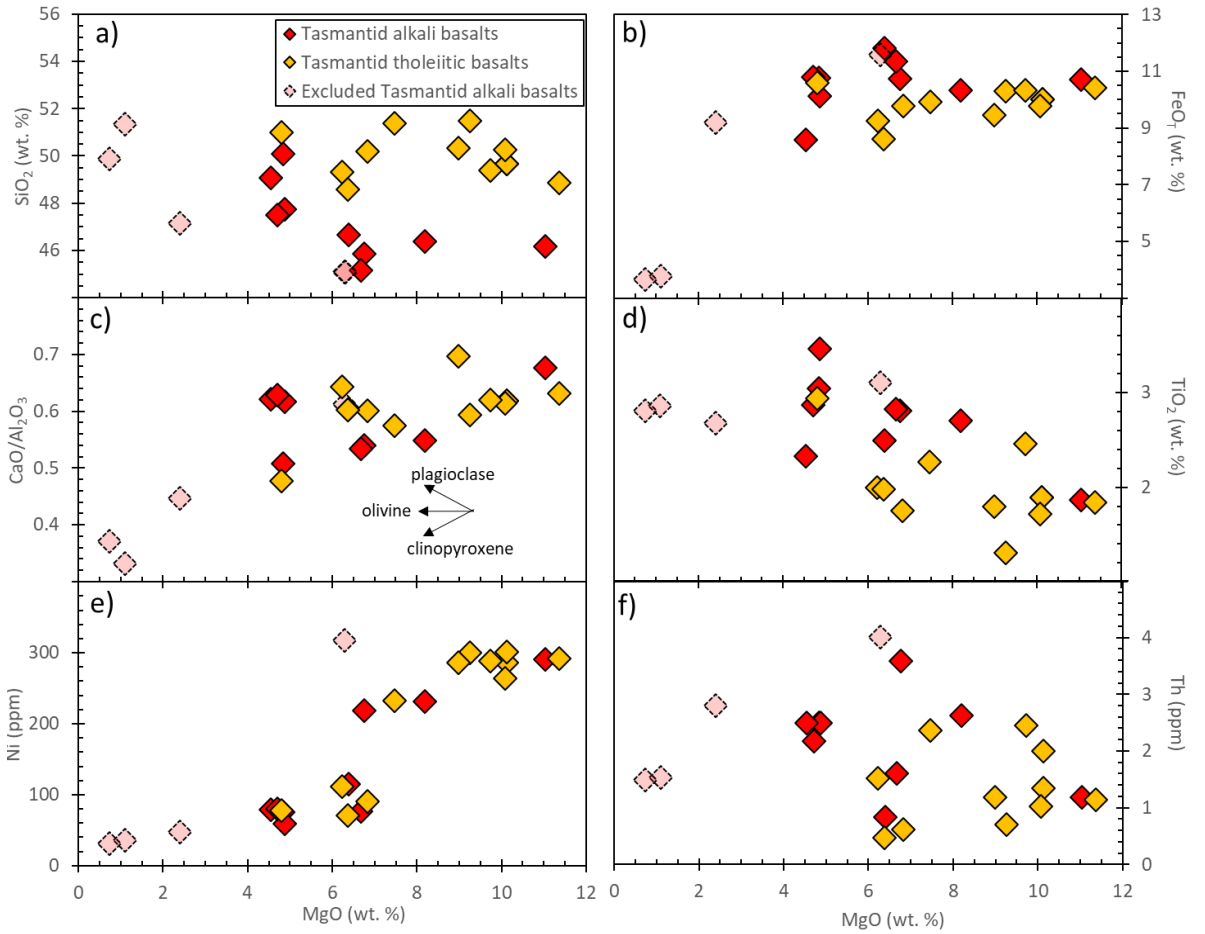

Figure 4. Variation diagrams for a) SiO_2, b) FeO_T, c) CaO/Al_2O_3, d) TiO_2, e) Ni, f) Th vs MgO for the Tasmantid Seamounts. Yellow squares represent tholeiitic basalts, red squares represent alkali basalts. Tholeiitic samples have lower FeO_T, TiO_2, Th than alkali basalts, whereas alkali basalts have lower SiO_2, CaO/Al_2O_3, Ni than the tholeiitic basalts. The light red highlighted samples have been excluded from the discussion, because they have undergone considerable fractional crystallization with MgO < 4.5 wt.% or show Ni > 300ppm.

Tasmantid samples show a positive Eu-anomaly (Fig. 5). One alkali basalt, sample 85167, shows a negative Cs anomaly but is not different to the rest of the samples in major elements and radiogenic Sr, Nd, Pb, and Hf, and stable Fe isotopes and is thus included here. Both basalt groups are depleted in Pb and enriched in Nb. Alkali basalts are enriched in incompatible trace elements (e.g., Y, Zr, Ba, Hf; Supplementary data I, Fig. S2) compared to tholeiitic basalts, which show higher values in compatible elements like Cr and Ni (Fig. 4 and Supplementary data I, Fig. S2).

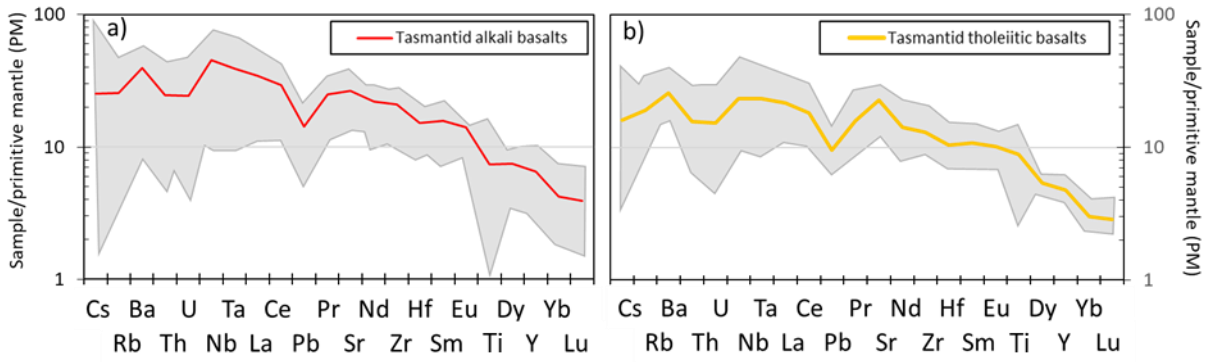

Figure 5. Primitive mantle-normalised trace element spider diagram. a) Red and b) yellow line show average values, grey background shows highest and lowest value. Normalising values are from McDonough and Sun (1995). Excluded samples are not included (for details online version: Research data). Note, only one alkali basalt, sample 65810 from Gascoyne, shows a strong depletion in Ti.

2.4.2 Radiogenic isotope data

Radiogenic isotope data is listed in Table 1. Compared to tholeiitic basalts, alkali lavas have less radiogenic $^{87}Sr/^{86}Sr$ and $^{143}Nd/^{144}Nd$ values, and more radiogenic Pb isotope values (Table 1). Alkali basalts show higher $^{176}Hf/^{177}Hf$ values than tholeiitic basalts.

Table 1a. Radiogenic Sr, Nd, Pb and Hf isotopic ratios for the Tasmantid Seamounts tholeiitic lavas. Samples starting with '65' or '68' are from Eggins et al. (1991). Samples starting with '85' are from McDougall and Duncan (1988). The sample with the prefix 'TMD' is from Cohen (2012). Samples with a prefix of '274' are from the Coral Sea from Exon et al. (2006). Nd data partly from McCulloch (1988), indicated with "§".

Rock Type	Seamount	Sample	$^{176}Hf/^{177}Hf$	±1S.E.	$^{87}Sr/^{86}Sr$	±1S.E.	$^{143}Nd/^{144}Nd$	±1S.E.	$^{206}Pb/^{204}Pb$	±1S.E.	$^{207}Pb/^{204}Pb$	±1S.E.	$^{208}Pb/^{204}Pb$	±1S.E.
tholeiitic	Gascoyne	65808	0.282689	0.000004	0.704598	0.000009	0.512483§	0.000006	17.8330	0.0008	15.5320	0.0007	37.9050	0.0018
tholeiitic	Gascoyne	65809	0.282689	0.000004	0.704598	0.000009	0.512483§	0.000007	17.8330	0.0008	15.5320	0.0007	37.9050	0.0018
tholeiitic	Gascoyne	65811	0.282721	0.000002	0.704638	0.000011	n.d.	n.d.	18.1954	0.0012	15.5853	0.0011	37.8654	0.0027
tholeiitic	Gascoyne	65821	0.282760	0.000004	0.704336	0.000009	0.512575§	0.000009	n.d.	n.d.	n.d.	n.d.	n.d.	n.d.
tholeiitic	Gascoyne	85170	0.282852	0.000004	0.704443	0.000009	0.512667	0.000014	18.1760	0.0008	15.5500	0.0007	38.3220	0.0018
tholeiitic	Gascoyne	85169	0.282842	0.000004	0.704440	0.000009	0.512693	0.000014	18.2240	0.0008	15.5640	0.0007	38.4470	0.0018
tholeiitic	Taupo	85174A	0.282823	0.000003	0.704211	0.000009	0.512705	0.000014	18.2563	0.0009	15.5986	0.0008	38.2463	0.0022
tholeiitic	Derwent-Hunter	65828	0.282842	0.000004	0.704716	0.000009	0.512567§	0.000005	n.d.	n.d.	n.d.	n.d.	n.d.	n.d.
tholeiitic	Britannia	68644	0.282756	0.000007	0.704548	0.000009	0.512512§	0.000009	18.1850	0.0012	15.6438	0.0011	38.0519	0.0029
tholeiitic	Queensland	TMD10-01 A4	0.282816	0.000004	0.705086	0.000009	0.512569	0.000009	18.1000	0.0021	15.5557	0.0017	38.2359	0.0047
tholeiitic	Unnamed seamount	274DR13 A1	0.282798	0.000004	0.705322	0.000010	0.512507	0.000005	17.5239	0.0017	15.5131	0.0015	37.7039	0.0035
tholeiitic	Unnamed seamount	274DR41 M1	0.282627	0.000004	0.705009	0.000007	0.512273	0.000005	17.3244	0.0018	15.5188	0.0016	37.7723	0.0039

Table 2b. Radiogenic Sr, Nd, Pb and Hf isotopic ratios for the Tasmantid Seamounts alkali lavas. Samples starting with '65' or '68' are from Eggins et al. (1991). Samples starting with '85' are from McDougall and Duncan (1988). The sample with the prefix 'TMD' is from Cohen (2012). Samples with a prefix of '274' are from the Coral Sea from Exon et al. (2006). Nd data partly from McCulloch (1988), indicated with "§".

Rock Type	Seamount	Sample	$^{176}Hf/^{177}Hf$	±1S.E.	$^{87}Sr/^{86}Sr$	±1S.E.	$^{143}Nd/^{144}Nd$	±1S.E.	$^{206}Pb/^{204}Pb$	±1S.E.	$^{207}Pb/^{204}Pb$	±1S.E.	$^{208}Pb/^{204}Pb$	±1S.E.
alkali	Gascoyne	65810	0.282756	0.000004	0.704348	0.000009	0.512558§	0.000010	17.8330	0.0008	15.5320	0.0007	37.9050	0.0018
alkali	Taupo	65839	n.d.	n.d.	0.70422	0.000009	0.512738§	0.000008	n.d.	n.d.	n.d.	n.d.	n.d.	n.d.
alkali	Taupo	85-175	0.282917	0.000004	0.704049	0.000009	0.512802	0.000014	18.4510	0.0008	15.5340	0.0007	38.4580	0.0018
alkali	Taupo	85-176	0.282908	0.000004	0.704047	0.000009	0.512777	0.000014	18.5170	0.0008	15.5560	0.0007	38.5680	0.0018
alkali	Derwent-Hunter	65835	n.d.	n.d.	0.704687	0.000009	0.512586§	0.000011	n.d.	n.d.	n.d.	n.d.	n.d.	n.d.
alkali	Queensland	85162	0.282897	0.000003	0.703792	0.000008	0.512777	0.000007	18.1386	0.0009	15.5889	0.0008	38.1143	0.0021
alkali	Derwent-Hunter	85183	0.282716	0.000004	0.704717	0.000011	0.512544	0.000006	18.7577	0.0011	15.6358	0.0009	38.1255	0.0022
alkali	Mellish Seamount	274DR22 A3	0.282702	0.000004	0.705742	0.000009	0.512416	0.000007	17.6169	0.0018	15.5515	0.0015	37.8760	0.0038
alkali	Unnamed seamount	274DR36 B1	0.282956	0.000005	0.705508	0.000008	0.512801	0.000005	18.7186	0.0016	15.5934	0.0013	38.6581	0.0035
alkali	Unnamed seamount	274DR41 E1	0.282725	0.000003	0.704169	0.000009	0.512361	0.000005	17.3803	0.0007	15.5302	0.0005	37.8216	0.0014
Reference		BCR2	0.282845	0.000004	0.705024	0.000012	0.512536	0.000008	18.7842	0.0005	15.6201	0.0004	38.7072	0.0013
		BHVO2	0.283099	0.000003	0.703472	0.000005	n.d.	n.d.	18.5953	0.0023	16.4761	0.0011	38.4261	0.0027
		La Jolla	n.d.	n.d.	n.d.	n.d.	0.511896	0.000014	n.d.	n.d.	n.d.	n.d.	n.d.	n.d.

317 **Table 2**. Measured stable Fe isotope data and primary melt Fe isotope data for the Tasmantid
318 Seamounts. 2 standard error calculated as follows: 2S.E. = 2S.D. / √n, with *n* being the number of
319 analyses, after Sossi et al. (2015). Samples starting with '65' or '68' are from Eggins et al. (1991).
320 Samples starting with '85' are from McDougall and Duncan (1988). The sample with the prefix 'TMD'
321 is from Cohen (2012). Samples with a prefix of '274' are from the Coral Sea from Exon et al. (2006).

Rock Type	Seamount	Sample	$\delta^{56}Fe$	±2S.E.	$\delta^{57}Fe$	±2S.E.	$\delta^{57}Fe_{Prim}$	n
tholeiitic	Gascoyne	65808	+0.15	0.02	+0.25	0.02	0.22	3
tholeiitic	Gascoyne	65809	+0.15	0.02	+0.25	0.02	0.13	3
tholeiitic	Gascoyne	65811	+0.05	0.02	+0.08	0.02	0.05	3
tholeiitic	Gascoyne	65821	n.d.	n.d.	n.d.	n.d.	n.d.	n.d.
tholeiitic	Gascoyne	85170	+0.11	0.01	+0.16	0.02	0.11	3
tholeiitic	Gascoyne	85169	+0.14	0.02	+0.24	0.02	0.20	3
tholeiitic	Taupo	85174A	+0.07	0.01	+0.11	0.01	0.01	3
tholeiitic	Derwent-Hunter	65828	n.d.	n.d.	n.d.	n.d.	n.d.	n.d.
tholeiitic	Britannia	68644	+0.03	0.02	+0.07	0.02	0.03	3
tholeiitic	Queensland	TMD10-01 A4	+0.04	0.01	+0.09	0.01	0.02	3
tholeiitic	Unnamed seamount	274DR13 A1	+0.03	0.01	+0.09	0.02	0.03	2
tholeiitic	Unnamed seamount	274DR41 M1	+0.04	0.01	+0.05	0.01	-0.01	3
alkali	Gascoyne	65810	+0.08	0.01	+0.15	0.02	0.12	3
alkali	Taupo	65839	n.d.	n.d.	n.d.	n.d.	n.d.	n.d.
alkali	Taupo	85175	n.d.	n.d.	n.d.	n.d.	n.d.	n.d.
alkali	Taupo	85176	+0.09	0.01	+0.15	0.03	0.10	3
alkali	Derwent-Hunter	65835	n.d.	n.d.	n.d.	n.d.	n.d.	n.d.
alkali	Queensland	85162	+0.18	0.02	+0.31	0.03	n.d.	3
alkali	Derwent-Hunter	85183	+0.17	0.03	+0.29	0.02	0.21	3
alkali	Mellish Seamount	274DR22 A3	+0.17	0.01	+0.24	0.05	0.16	3
alkali	Unnamed seamount	274DR36 B1	+0.17	0.02	+0.26	0.03	0.15	3
alkali	Unnamed seamount	274DR41 E1	+0.18	0.02	+0.23	0.03	0.15	3
Reference		BCR2	+0.11	0.01	+0.19	0.02	n.d.	3
		BHVO1	+0.09	0.03	+0.11	0.02	n.d.	3

322

2.4.3 Stable Fe isotope data

In stable Fe isotopes, alkali basalts of the Tasmantid Seamounts show on average a heavier measured $\delta^{57}Fe$ with +0.15 to +0.31‰ (Table 2 and Research data) compared to tholeiitic basalts, which range from +0.05 to +0.25‰ in $\delta^{57}Fe$ (Table 2 and Research data). Compared to the $\delta^{57}Fe$ composition of mid-ocean ridge basalts (MORB; $\delta^{57}Fe$ +0.07 to +0.25‰; Chen et al., 2019, Teng et al., 2013), alkali as well as tholeiitic basalts of the Tasmantid Seamounts display a wider range and an overall similar to heavier $\delta^{57}Fe$ signature.

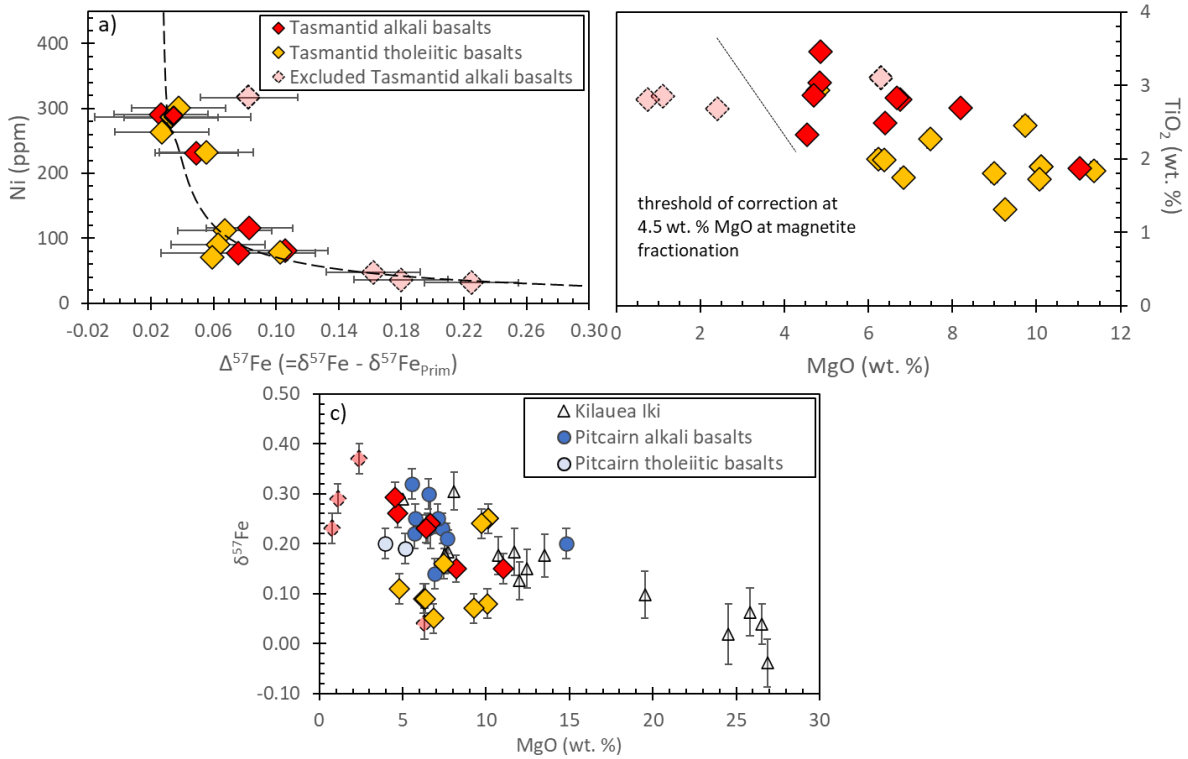

Figure 6. a) Degree of Fe isotope correction ($\Delta^{57}Fe$) vs Ni, an independent indicator for olivine fractionation. Sample 85177 is marked as light red, deviates from exponential average (curve in dotted grey) and has been excluded due to Ni > 300ppm. The other three excluded samples (274DR41 F2, 274DR39 A1 and 247DR41 F1) show a high fractionation factor and have been excluded due to MgO < 4.5 wt.%. b) Major element MgO vs TiO_2 to test for magnetite fractionation. A threshold at 4.5 wt.% was used to exclude samples that show magnetite fractionation. The studies of Nebel et al. (2015) and Sossi et al. (2012) show that at lower MgO magnetite is the primary host of iron. The highlighted sample 85177 does not show any sign of magnetite alteration, however, does show the highest Ni (ppm) value, deviating from the rest of the samples. c) MgO vs $\delta^{57}Fe$ including basalts from Kilauea Iki lava lake, which represent a fractional crystallization trend (Teng et al., 2008) and Pitcairn (Nebel et al.,

2019). Sample 65808 and 65809 at 10.12 MgO wt.% and δ^{57}Fe +0.25‰. For two tholeiitic basalts (65821 and 65828) and three alkali basalts (samples 65835, 65839 and 85175) stable Fe isotopes were not analysed due to lack of available sample. No MgO available for one alkali basalt (sample 85162).

Cooling of ascending magma involves the crystallization of olivine and pyroxene (Wagner and Grove, 1998). This crystallization is critical for the interpretation of Fe isotopes, because preferential incorporation of light Fe isotopes into olivine leads to an isotopically heavier Fe isotopic composition of the residual melt and elevated δ^{57}Fe (Teng et al., 2008; Dauphas et al., 2009; Schuessler et al., 2009; Sossi et al., 2012). We thus attempt to correct the measured δ^{57}Fe for crystal fractionation of olivine following a procedure outlined in Sossi et al. (2016) in order to compare primitive-mantle-normalised rare earth element (REE) ratios (which are not affected by olivine fractionation) with stable Fe isotopic compositions of calculated primary melts ($\delta^{57}Fe_{Prim}$). The validity of the applied olivine correction is illustrated by ppm Ni vs the degree of correction Δ^{57}Fe ($\Delta^{57}Fe = \delta^{57}Fe - \delta^{57}Fe_{Prim}$, Fig. 6a), with Ni being compatible in olivine and thus equally affected by olivine crystallisation but independent of our crystal fractionation correction. Combined with major element data, both the fractionation of olivine and pyroxene have been identified for alkali and tholeiitic basalts (Fig. 4c). Relative to olivine, pyroxene fractionation has a small effect on Fe isotope systematics (Weyer and Ionov, 2007; Williams and Bizimis, 2014). Because the applied olivine fractionation correction for Fe isotopes provides an upper limit on the fractional crystallisation correction, correction for pyroxene is obsolete (Soderman et al., 2021). Notably, the applied correction is an approximation of the source and should be treated as a model only. For the olivine fractionation correction, we add olivine (light Fe isotopes) to our starting melt composition with $Fe^{3+}/\sum Fe = 0.15$ until we reach a primary melt with Mg#=74 by using a $\Delta^{57}Fe_{Ol\text{-}melt}*10^6/T^2 = -0.4$ (Nebel et al., 2019; Sossi et al., 2016). Considering an exchange coefficient for Fe and Mg between olivine and melt $K_D^{Fe-Mg}_{Ol-Melt} > 0.3$ (Roeder and Emslie, 1970), the Mg# = 74 is in chemical equilibrium with the primitive mantle Mg# = 90 (Palme and O'Neill, 2014). Using the value of $\Delta^{57}Fe_{Ol\text{-}}melt*10^6/T^2 = -0.4$ provides results with the largest fractionation correction (correction with $\Delta^{57}Fe_{Ol\text{-}melt}*10^6/T^2 = -0.1$ shown in Supplementary data I, Fig. S3). It must be noted that the corrected values are modelled compositions that are suitable to identify processes relevant to the petrogenesis of the basalts but may slightly differ (estimated here

in the order of ±0.03, dependent on variations of the model parameters) from true values. After correction, the following $\delta^{57}Fe_{Prim}$ values have been calculated: the alkali basalts range from +0.10 to +0.21‰ and tholeiitic basalts from -0.01 to +0.22‰ (Fig. 7). In general, the correction for the alkali samples is larger than those for the tholeiitic basalts. The excluded alkali basalts range in $\delta^{57}Fe_{Prim}$ from -0.04 to +0.21‰ (highlighted in Fig. 7, Research data).

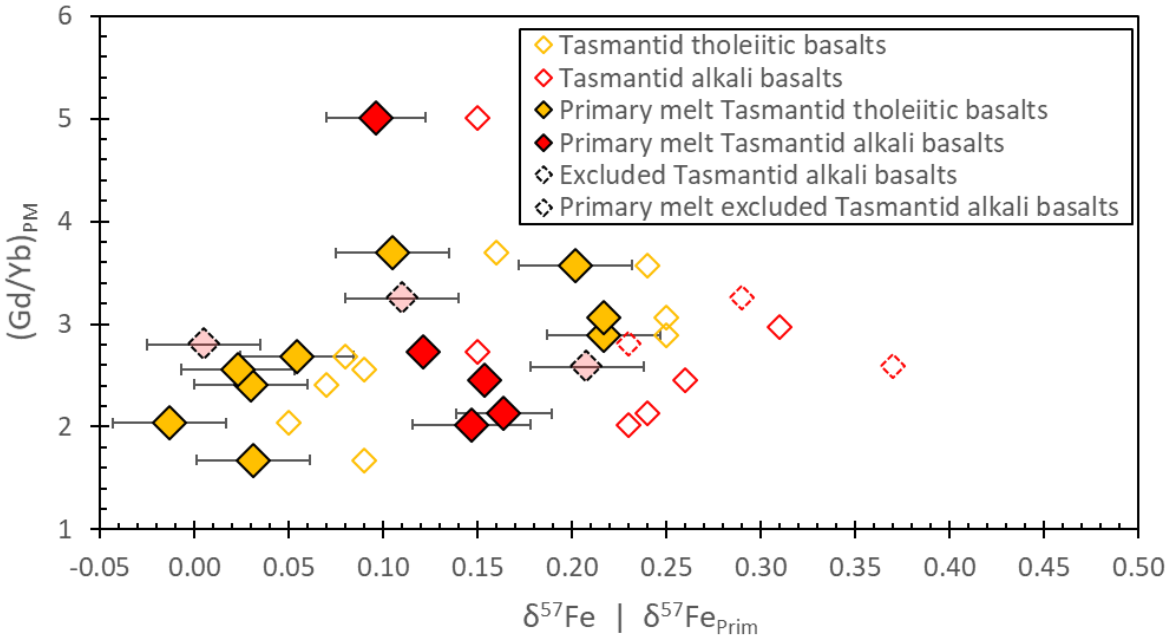

Figure 7. $(Gd/Yb)_{PM}$ vs $\delta^{57}Fe$ and $\delta^{57}Fe_{Prim}$. $\delta^{57}Fe_{Prim}$ values are crystal fractionation corrected following Nebel et al. (2019) and Sossi et al. (2016). Measured $\delta^{57}Fe$ values in open symbols show a heavier Fe isotopic signature compared to calculated $\delta^{57}Fe_{Prim}$ values. Alkali and tholeiitic basalts show similar Gd/Yb values. Both Gd and Yb are heavy rare earth elements (HREE) and have been normalized to primitive mantle using Sun and McDonough (1989b). For one alkali basalts (sample 85162; $\delta^{57}Fe$ = +0.31‰) major elements have not been analysed previously, thus $\delta^{57}Fe_{Prim}$ has not been calculated. For two alkali basalts, sample 85183 and 85177 (85177 highlighted in Fig. 2, 3 & 5 and excluded from discussion) no Gd and Yb values have been analysed previously, thus these samples are not shown here. For sample 85183 the $\delta^{57}Fe$ is +0.29‰ and its calculated $\delta^{57}Fe_{Prim}$ is +0.21‰. For sample 85177 the $\delta^{57}Fe$ is +0.04‰ and its calculated $\delta^{57}Fe_{Prim}$ is -0.04‰.

2.5 Discussion

In the following, we will compare Sr, Nd, Hf and Pb isotopic ratios of alkali and tholeiitic basalts from Pitcairn and Hawai'i to the Tasmantid Seamounts to characterise the Tasmantid Seamounts mantle endmembers. Then, we will discuss if alkali and tholeiitic basalts can be

associated with a mantle endmember, i.e., if alkali basalts can be ascribed to enriched (in radiogenic isotopes) mantle components. To evaluate petrogenetic processes, we compare trace element ratios to radiogenic isotopic ratios and introduce stable Fe isotopes. With stable Fe isotopes, we assess melting regimes of the Tasmantid Seamounts alkali and tholeiitic basalts and possible source variability.

2.5.1 Enriched vs. depleted mantle component in the Tasmantid plume

Ocean island basalts are categorised by broadly defined isotope clusters in multiple isotope diagrams (Hofmann, 1997; Zindler and Hart, 1986; Hart, 1988). These clusters are defined as reservoirs and are: DMM (depleted MORB mantle; high $^{143}Nd/^{144}Nd$, low $^{87}Sr/^{86}Sr$, low $^{206}Pb/^{204}Pb$, high $^{176}Hf/^{177}Hf$), HIMU (high U/Pb-ratio mantle; high $^{206}Pb/^{204}Pb$, intermediate $^{143}Nd/^{144}Nd$, low $^{87}Sr/^{86}Sr$, intermediate $^{176}Hf/^{177}Hf$), EM1 (enriched mantle 1; intermediate $^{87}Sr/^{86}Sr$, low $^{143}Nd/^{144}Nd$, low $^{206}Pb/^{204}Pb$, low $^{176}Hf/^{177}Hf$) and EM2 (enriched mantle 2; low $^{143}Nd/^{144}Nd$, intermediate $^{206}Pb/^{204}Pb$, high $^{87}Sr/^{86}Sr$, low $^{176}Hf/^{177}Hf$; Hofmann, 2003). A striking feature of these trajectories is their convergence in a zone termed PREMA (Prevalent Mantle; White, 2015; Zindler and Hart, 1986), also known as FOZO (Focus Zone; Hart et al., 1992; Hauri et al., 1994; Stracke et al., 2005), PHEM (Primitive Helium Mantle; Farley et al., 1992) or C (Common component; Hanan and Graham, 1996). Throughout this publication, we will be using 'PREMA'.

Based on radiogenic isotope data from 18 samples (McCulloch, 1988), Eggins et al. (1991) identified the Tasmantid basalts as being generated from two distinct mantle components, one of which being enriched and the other one depleted relative to each other. Coupled Sr-Nd-Pb-Hf isotope data strongly suggest that the "depleted" component identified by Eggins et al. (1991) is likely a PREMA component and the enriched component coincides with EM1 (Fig. 8).

Several studies (Abouchami et al., 2005; Hofmann and Farnetani, 2013; Jackson et al., 2012; White, 2015; Hart et al., 1992; Phillips et al., 2016; Roden et al., 1984) identified PREMA and EM1 as mantle endmembers in Hawai'ian tholeiitic and alkali OIB. The Pitcairn-Gambier Chain also represents a mixing trend of PREMA and EM1 (Garapić et al., 2015; Delavault et al., 2015; Hart et al., 1992), but with a lower heat flux compared to Hawai'i, which is a possible

driving force for the surfacing of deep mantle components. In the following, we will compare the Tasmantid Seamount samples with lavas from Hawai'i and Pitcairn to make assumptions about the mantle components that contributed to the Tasmantid Seamounts.

For both Hawai'i and Pitcairn, Fe isotope data is available (Nebel et al., 2019; Teng et al., 2008). Low MgO lavas (< 4.0 wt.%) have been excluded due to the strong effects of magnetite fractionation on Fe isotopic compositions of Pitcairn lavas (Rhodes et al., 2012; Nebel et al., 2019), and in analogy also for Hawai'i (Teng et al., 2008). All other geochemical data for Hawai'i and Pitcairn-Gambier Chain were taken from the GEOROC database (georoc.mpch-mainz.gwdg.de/georoc/). Additionally, we include MORB data from Gale et al. (2013), representative for the modern depleted upper mantle (Fig. 8). All samples that are marked as *rejuvenated (post shield-stage), slightly* to *heavily altered* or have less than two of the radiogenic isotope ratios of $^{87}Sr/^{86}Sr$, $^{143}Nd/^{144}Nd$, $^{208}Pb/^{204}Pb$ and $^{206}Pb/^{204}Pb$ listed, have been excluded. To further exclude altered samples, we filtered data with $K_2O/P_2O_5 < 1$ (Frey et al., 1994; Hofmann and Feigenson, 1983). The data from Hawai'i and Pitcairn (Supplementary data II) have been divided into tholeiitic and alkali basalts according to the TAS diagram.

In radiogenic Sr, Nd, Pb and Hf space, alkali and tholeiitic lavas of the Tasmantid Seamounts strongly overlap, showing a potential mixing trend between PREMA and EM1 endmembers (Fig. 8a, b, c, d). However, on average, alkali basalts of the Tasmantid Seamounts show more radiogenic Sr, Pb and less radiogenic (higher) Hf and Nd isotope ratios. Two outliers (274DR22 A3 and 274DR36 B1) of alkali basalts show more radiogenic $^{87}Sr/^{86}Sr$ values (Fig. 8a, c), deviating from the mixing trend between PREMA and EM1 of the Tasmantid Seamounts. Even though the applied seawater alteration proxies do not indicate seawater alteration of those two samples (section *3.1. Alteration*), we suggest that the two outliers might have suffered from addition of secondary seawater Sr (Bach et al., 2003; Hess et al., 1986). In contrast, in fluid-immobile radiogenic elements (Nd, Pb and Hf), these two outliers are not distinguishable from the other alkali basalts and are thus included in the interpretation.

While showing the classic EM1 isotope characteristics (Zindler and Hart, 1986), which are considered to be a remnant of subducted lithosphere *sensu lato* (White, 2015), the Tasmantid Seamounts EM1 signature is clearly not identical in all radiogenic isotopes to Hawai'i or

Pitcairn sources, in particular in its radiogenic Pb isotopes. It appears that EM1 components evolved with similar U-Th/Pb parent-daughter ratios but likely formed at different times, allowing for variable radiogenic ingrowth (time of formation further discussed in Supplementary data I, Fig. S4 & S5). The Tasmantid Seamount plume can thus be classified as an individual plume source in the EM1 family.

In $^{87}Sr/^{86}Sr$ and $^{143}Nd/^{144}Nd$ isotopic space the Tasmantid alkali basalts show a more enriched signature than Hawai'ian and Pitcairn basalts, plotting into the more enriched part of the PREMA area (Fig. 8a, b). In $^{206}Pb/^{204}Pb$ vs $^{208}Pb/^{204}Pb$ space, Hawai'ian and Tasmantid Seamount alkali lavas show radiogenic Pb isotope ratios that plot into the less radiogenic $^{206}Pb/^{204}Pb$ and $^{208}Pb/^{204}Pb$ of the PREMA field, whereas tholeiitic as well as alkali basalts of Pitcairn plot into the more radiogenic $^{206}Pb/^{204}Pb$ and $^{208}Pb/^{204}Pb$ PREMA field. In $^{176}Hf/^{177}Hf$ space, Pitcairn's tholeiitic and Tasmantid Seamount's alkali basalts plot within the PREMA area (Fig. 8c, d), whereas Hawai'ian alkali basalts plot between DMM and PREMA. The latter, however, may be a function of the limited Hf data available for plumes in general (Stracke et al., 2005). Based on the sum of observations, it is plausible to ascribe a PREMA association to the Tasmantid alkali basalts.

In summary, radiogenic isotopic signatures of Hawai'ian, Pitcairn and Tasmantid Seamounts' indicate that the PREMA component in each of these three plumes shows a different radiogenic isotopic composition. This can be explained by the different nature of primitive components in global OIB (Doucet et al., 2020; Jackson et al., 2007), so that 'primitive' relates to less radiogenic isotopic signatures in Sr, Nd and Hf and to a more radiogenic $^{206}Pb/^{204}Pb$ signature. Considering the petrogenesis of tholeiitic vs alkali basalts, a *direct* comparison of radiogenic with stable isotopes within different plumes is thus not suitable. However, a relative comparison of respective enriched vs primitive components of each plume in relation to its alkalinity still holds true. The individuality of each plume may thus mask systematic trends in global compilations.

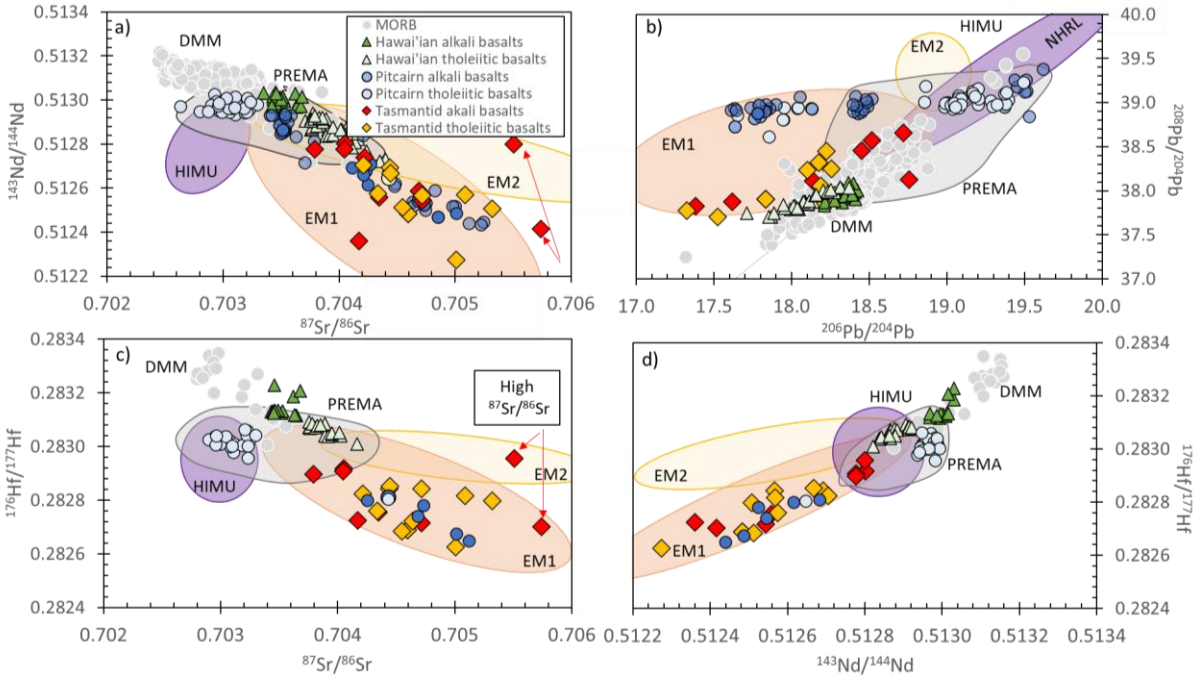

Figure 8. a) $^{87}Sr/^{86}Sr$ vs $^{143}Nd/^{144}Nd$, b) $^{206}Pb/^{204}Pb$ vs $^{208}Pb/^{204}Pb$, c) $^{87}Sr/^{86}Sr$ vs $^{176}Hf/^{177}Hf$, and d) $^{143}Nd/^{144}Nd$ vs $^{176}Hf/^{177}Hf$. Note that for one tholeiitic (sample 65811) Nd, for two tholeiitic basalts (sample 65821 and 65828) Pb and for two alkali basalts (samples 65835 and 65839) Pb and Hf isotopes were not analysed due to lack of available sample. The light grey circle indicates PREMA after Hauri et al. (1994), Jackson et al. (2007), Stracke et al. (2005) and White (2015). MORB has been plotted to show differences between MORB and OIB. The Northern Hemisphere Reference Line (NHRL) is adapted from Hart (1984). The areas of EM1, EM2 and HIMU, Hawai'i and Pitcairn were assembled from the GEOROC database. MORB data is from Gale et al. (2013). Two of the Tasmantid alkali basalts (samples 274DR22 A3 and 274DR36 B1, specified by red arrows) show extremely radiogenic $^{87}Sr/^{86}Sr$ ratios, which can be explained by the addition of secondary radiogenic Sr, presumably from seawater (present day seawater $^{87}Sr/^{86}Sr \sim 0.709$; Bach et al., 2003). Except for $^{87}Sr/^{86}Sr$, these two samples do not deviate from the rest of the alkali basalts in radiogenic Nd, Pb and Hf isotopes.

2.5.2 Petrogenetic considerations

2.5.2.1 Melting regimes and source variability

The majority of ocean islands are formed during the shield-building stage with production of both tholeiitic and alkali basalts (e.g., Naumann and Geist, 1999; Tilley and Scoon, 1961; Moore, 1966). For the shield-building stage of the Hawai'ian ocean islands, the largest one of its kind, the predominant mantle components identified by radiogenic isotope systematics are

EM1 and PREMA (Hart et al., 1992; White, 2015; Jackson et al., 2012; Hofmann and Farnetani, 2013; Abouchami et al., 2005). However, the radiogenic isotope trajectories of possible endmembers in alkali and tholeiitic OIB of Hawai'i indicate that the melting processes underlying these oceanic islands appear to be complex. By comparing Hawai'i, Pitcairn, and the Tasmantid Seamounts in radiogenic isotope spaces, it is apparent that alkali basalts cannot always be associated with a crustal component like EM1. Whereas Hawai'ian alkali basalts can be ascribed to PREMA and tholeiitic lavas to EM1, Pitcairn's alkali basalts can be ascribed to EM1 and tholeiitic basalts to PREMA. It appears that the Tasmantid Seamounts' tholeiitic basalts can be associated with a more pronounced EM1 signature and alkali basalts with a more pronounced PREMA signature (Fig. 8). Even though there is considerable overlap between tholeiitic vs. alkali basalts in radiogenic isotopes for the Tasmantid Seamounts, a bimodal distinction based on petrologic grounds (and not enriched components) is indicated in Fig. 9. Below we first explore the depth and degrees of melting of the respective alkaline vs tholeiite suites and then test if two component mixing can be responsible for the observed variability.

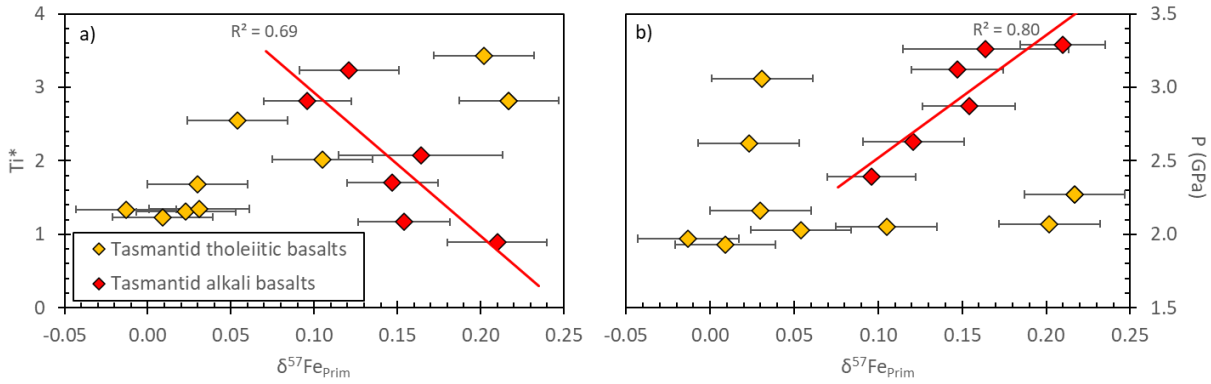

Figure 9. a) $\delta^{57}Fe_{Prim}$ vs Ti* and b) $\delta^{57}Fe_{Prim}$ vs pressure *P* (GPa). Ti* = $(TiO_2)(MgO)^{1.7}/34.3$ calculated following Taylor and Martinez (2003). Pressure calculated following Putirka (2016) (Research data). R^2 reflects correlation coefficient of the best fit.

An increase in $(Gd/Yb)_{PM}$ can indicate melting at greater depth, associated with the presence of residual garnet (Lassiter and DePaolo, 1997). Both Tasmantid tholeiitic and alkali basalts show a similar range in this so called "garnet signature" (Eggins et al., 1991; Fig. 10). Eggins et al. (1991) interpreted that the garnet signature of the tholeiitic basalts can be explained by mixing small melt fractions that derived from deeper regions of the plume with the tholeiitic magma. In this scenario, only the trace element signatures are overprinted by

this mixture whereas major elements remain pristine. These authors further suggest different melting degrees between the two Tasmantid Seamount magma series based on incompatible element variations (e.g., Zr/Nb and La/Sm). They conclude that the centre of the Tasmantid Seamount plume is represented by tholeiitic, high melting degree magma, formed at low pressure of ~1GPa and that alkali, low melting degree magma formed at greater depth, at ~2.5GPa, representing the edge of the conduit.

With our new, additional data presented in this study, we use $(La/Sm)_{PM}$ as a proxy for identifying differences in melting degrees (Pearce, 2008) between the Tasmantid Seamounts, and compare these with Hawai'ian and Pitcairn's alkali and tholeiitic basalts. Importantly, this ratio is not compromised by olivine fractionation, so that the ratio in erupting lavas allows direct constraints on the melting source. The Tasmantid Seamounts, on average, show slightly higher $(La/Sm)_{PM}$ values with 2.16 (average) and $(Gd/Yb)_{PM}$ values of 3.18 (average) in alkali lavas relative to tholeiitic basalts ($(La/Sm)_{PM}$ = 1.92, $(Gd/Yb)_{PM}$ = 2.73, average). The enrichment in incompatible elements (Research data and Supplementary data I, Fig. S2) and the slightly higher $(La/Sm)_{PM}$ ratio suggest that alkali basalts represent marginally lower degrees of melting compared to the tholeiites. This observation is also reflected in the Tasmantid trace element patterns (Fig. 4 & 5), as both alkali and tholeiitic basalts show similar yet not identical distributions, with tholeiitic basalts showing a sharper decrease in incompatible elements. However, the overlap of tholeiitic and alkali basalts in trace element ratios suggests that both basalt suits must have originated in the garnet stability field.

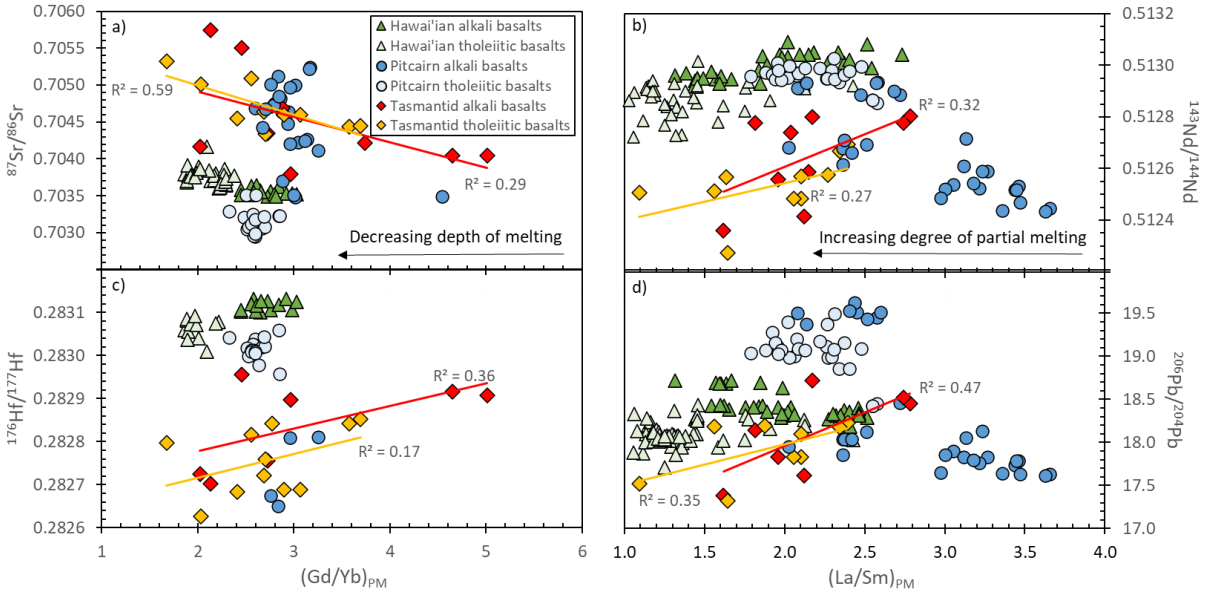

Figure 10. a) $(Gd/Yb)_{PM}$ vs $^{87}Sr/^{86}Sr$, b) $(La/Sm)_{PM}$ vs $^{143}Nd/^{144}Nd$, c) $(Gd/Yb)_{PM}$ vs $^{176}Hf/^{177}Hf$ and d) $(La/Sm)_{PM}$ vs $^{206}Pb/^{204}Pb$. Tholeiitic basalts: sample 65811 no radiogenic Nd isotopic ratio available, samples 65821 and 65828 no radiogenic Pb isotopic ratio available. Alkali basalts: sample 85183 no Gd, Sm or Yb available, samples 65835 and 65835 no Hf or radiogenic Pb isotopic ratio available. Red trendline represents trend produced by alkali basalts and yellow trendline represents the trend formed by tholeiitic lavas. R^2 reflects correlation coefficient of the best fit.

Radiogenic isotope ratios of Sr, Nd, Pb and Hf show a weak co-variation with trace element ratios of $(La/Sm)_{PM}$ and $(Gd/Yb)_{PM}$ (Fig. 10, R-values) in the Tasmantid samples. There is, however, a strong overlap of alkali and tholeiitic lavas (Fig. 10), which indicates that both melt types originated from a continuum of melting degrees. With both alkali and tholeiitic melts forming in the garnet stability field and no clear systematic radiogenic isotope distinction, we surmise that the enriched mantle component coexists with the depleted mantle component in close proximity within the plume. In other words, there is no depth-related systematic distribution of mantle components. This, however, still leaves the question open as to why some samples form at lower melting degrees than others.

With all factors, such as fertility/composition (radiogenic isotopes) and depth/pressure (trace element ratios) being similar or marginally different, the only viable alternative is temperature (*T).* In this, concentric temperature zoning in the rising plume conduit could account for differences in degrees of melting. Such interpretation would coincide with Eggins et al. (1991). Below, we will examine if melting degree influenced through differences in temperature or source variability affects the Fe isotopic signature of the Tasmantid Seamount basalts. For this, we compare trace element ratios of $(Gd/Yb)_{PM}$ and $(La/Sm)_{PM}$ as well as radiogenic Sr, Nd, Pb and Hf isotope ratios with our calculated primary melt iron isotopic composition $\delta^{57}Fe_{Prim}$.

2.5.2.2 Melting regimes and stable Fe isotopes

Based on the decoupling of radiogenic isotope ratios and element chemistry (Fig. 10), we suggest, as outlined above, that both depleted and enriched components melt in a similar depth in close proximity (Fig. 3; Hirschmann and Stolper, 1996). Even though tholeiitic and alkali basalts overlap in Fe isotopes, alkali basalts show, on average, heavier primary melt Fe isotope values of averaged +0.15‰ $\delta^{57}Fe_{Prim}$. Accordingly, tholeiitic basalts show, on average,

a lighter primary melt Fe isotopic composition of +0.09‰ $\delta^{57}Fe_{Prim}$. The co-variation of $(Gd/Yb)_{PM}$ with $\delta^{57}Fe_{Prim}$ for alkali basalts suggests a small dependency of Fe isotopes on the melting depth (Fig. 11a). It has to be noted here that, as stated above, the depth of melting is assumed to be similar for tholeiitic and alkali basalts (also shown by the similar $(Gd/Yb)_{PM}$ values, Fig. 10a & 11a).

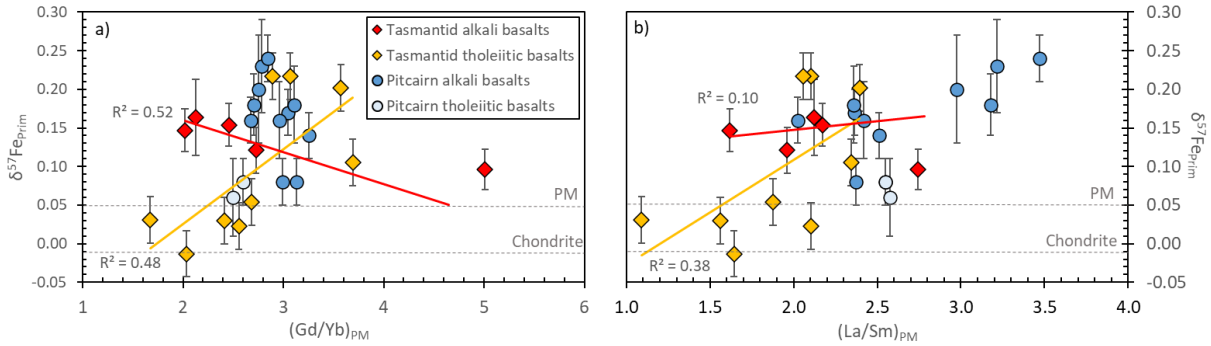

Figure 11. a) $(Gd/Yb)_{PM}$, b) $(La/Sm)_{PM}$ vs $\delta^{57}Fe_{Prim}$. Gd is not available for the tholeiitic basalts 85174A with $\delta^{57}Fe_{Prim}$ = +0.01‰ and for the alkali basalt 85183 with $\delta^{57}Fe_{Prim}$ = +0.21‰. R^2 reflects correlation coefficient of the best fit. Red trendline for alkali basalts and yellow for tholeiitic basalts. Alkali basalt with highest $(Gd/Yb)_{PM}$ and $(La/Sm)_{PM}$ not included in calculating R^2. $\delta^{57}Fe_{Prim}$ for chondritic material of -0.01 ± 0.01‰ (2S.E.; Craddock and Dauphas, 2011; Needham et al., 2009; Wang et al., 2014; Schoenberg and von Blanckenburg, 2006; Sossi et al., 2016). $\delta^{57}Fe_{Prim}$ = +0.05 ± 0.01‰ (2S.E.) of primitive mantle (PM) from Sossi et al. (2016).

Because a comparison of Ti* and P (GPa) with $\delta^{57}Fe_{Prim}$ suggests a bimodal distinction between tholeiitic and alkali lavas of the Tasmantid Seamounts (Fig. 9), we suggest that alkali and tholeiitic lavas could sample two distinct, isolated regions within the plume. If the alkaline lavas are taken as an entity (or mix of components yet in isolation) and are considered to be derived straight from their mantle source without any disturbance, their Fe isotope systematics can be explained through a pressure-related partial melting fractionation. When plotted against Ti* (parental melt Ti) and calculated pressure of melting, a trend is apparent in which the heaviest Fe isotopic composition is related to the highest pressure but also to a lower Ti* content (Fig. 9). With garnet being a key host and the highest D value for Ti being in the garnet stability field in peridotite (Prytulak and Elliott, 2007), retention of Ti in garnet is a possible explanation for the observed trend. If correct, then low degree, high-pressure melts produce heavier Fe isotopes through the retention of light Fe isotopes in garnet (Ye et al.,

2020), whereas higher melting degrees, equivalent to lower Ti* content and lower pressures dilute this effect.

The Ti* compositional variability is here solely explained through degrees of melting but may also reflect source enrichment (Prytulak and Elliott, 2007), which in turn may affect partial melting modes through differences in fertility, and with this again depth of melting. Iron isotopic compositions of $\delta^{57}Fe_{Prim}$ ~ +0.24‰ at Pitcairn have been explained with a second stage pyroxenite, which formed from the reaction of recycled, crustal eclogite with the ambient peridotite mantle. This can only be the case here for the deeper, low-degree component with $\delta^{57}Fe_{Prim}$ = +0.21‰.

The tholeiitic lavas do not follow any of these systematics and appear decoupled from the alkaline melts (e.g., Fig. 9). In either case, however, it is apparent that the Fe isotopic composition of the higher melting degree endmember approaches $\delta^{57}Fe_{Prim}$ = +0.04‰ (median of tholeiitic lavas), which is similar to the Fe isotopic composition of mantle peridotite (Craddock et al., 2013; Dauphas et al., 2009; Weyer and Ionov, 2007; Williams and Bizimis, 2014). Only one sample of the tholeiitic lavas (274DR41 M1) shows a value comparable to chondritic material with $\delta^{57}Fe_{Prim}$ = -0.01‰. The negative value is likely caused by our applied crystal fractionation correction, however, considering uncertainties, coincides with values documented for peridotitic mantle sources (Sossi et al., 2016). Melting of peridotite can explain the light Fe isotope data of tholeiitic basalts, but not some of the isotopically heavy Fe isotopic signature of the tholeiitic lava suite reaching $\delta^{57}Fe_{Prim}$ of up to +0.22‰ (Fig. 11b). The influence of melting degrees on Fe isotopic compositions has been discussed in several studies (Williams et al., 2005; Williams et al., 2004; Williams and Bizimis, 2014; Dauphas et al., 2009; Dauphas et al., 2014; Foden et al., 2018; Weyer and Ionov, 2007; Teng et al., 2013; Soderman et al., 2021), showing that lower degrees of melting result in elevated $\delta^{57}Fe$ values. Following modelling, partial melting of peridotite (i.e., fertile mantle with $\delta^{57}Fe$ = +0.05‰) does not exceed values of $\delta^{57}Fe$ = +0.15‰, even for a degree of melting (F) < 0.05 (Foden et al., 2018). Given that F for tholeiites is larger than for alkali basalts, another explanation is needed to generate heavy Fe isotopic compositions.

Although it is tempting to ascribe this isotopically heavy component to alkaline melts, the radiogenic isotope systematics or trace elements *and* Fe isotopes (e.g., Fig. 9) do not support

any such two-component mixing trends as to the absence of any co-variation. Instead, it appears that at least one more component needs to be considered. This is also important because tholeiites *do not* contain an admixed alkali component but could only reflect a larger degree of melting of the *same* source. With roughly similar depths of melting, it thus seems most plausible to assign the larger degree of melting of the tholeiites to elevated temperatures, likely in the centre of the plume (Supplementary data I, Fig. S6). This may also explain their larger abundance during the shield-building stage of ocean islands. A larger abundance and the mantle region sampled by these melts may also account for the presence of a component which is isotopically heavier in Fe and seemingly absent in the alkali lavas. In the following, we will discuss the possibility of the presence of an isotopically heavy component and its influence on the heavy Fe isotopic signature in tholeiitic basalts.

2.5.2.3 Heavy Fe isotopes in tholeiitic lavas

Stable Fe isotope variations in OIB depend on various factors which include melting degree (section *5.2.1 melting regimes and source variability* and *5.2.2 melting regimes and stable Fe isotopes*), but also source mineralogy or metasomatism and/or diffusion (Craddock et al., 2013; Dauphas et al., 2009; Weyer and Ionov, 2007; Williams and Bizimis, 2014). As partial melting has only a small influence on Fe isotopic compositions of tholeiitic lavas (e.g., Fig. 11), the variation of Fe isotopes in tholeiitic basalts of the Tasmantid Seamounts could result from an inherited Fe isotopic composition of the mantle source. Inherited Fe isotopic compositions have been proposed for OIB, e.g., Samoa (Konter et al., 2016) or Pitcairn (Nebel et al., 2019). Nebel et al. (2019) showed on Pitcairn basalts that PREMA can be associated with a BSE-like Fe isotopic composition of $\delta^{57}Fe_{Prim}$ = +0.05‰, whereas a crustal component (EM1 for Pitcairn) shows heavier Fe isotope values of up to $\delta^{57}Fe_{Prim}$ ~+0.24‰. However, comparing the Tasmantid Seamount basalts in radiogenic Sr, Nd, Pb and Hf isotope ratios with $\delta^{57}Fe_{Prim}$, co-variations can neither be observed for tholeiitic nor alkali basalts (Fig. 12). Thus, tholeiitic basalts of the Tasmantid Seamounts must have experienced additional alteration processes (Eggins et al., 1991), possibly in form of metasomatism or diffusion during metasomatism (Kang et al., 2020).

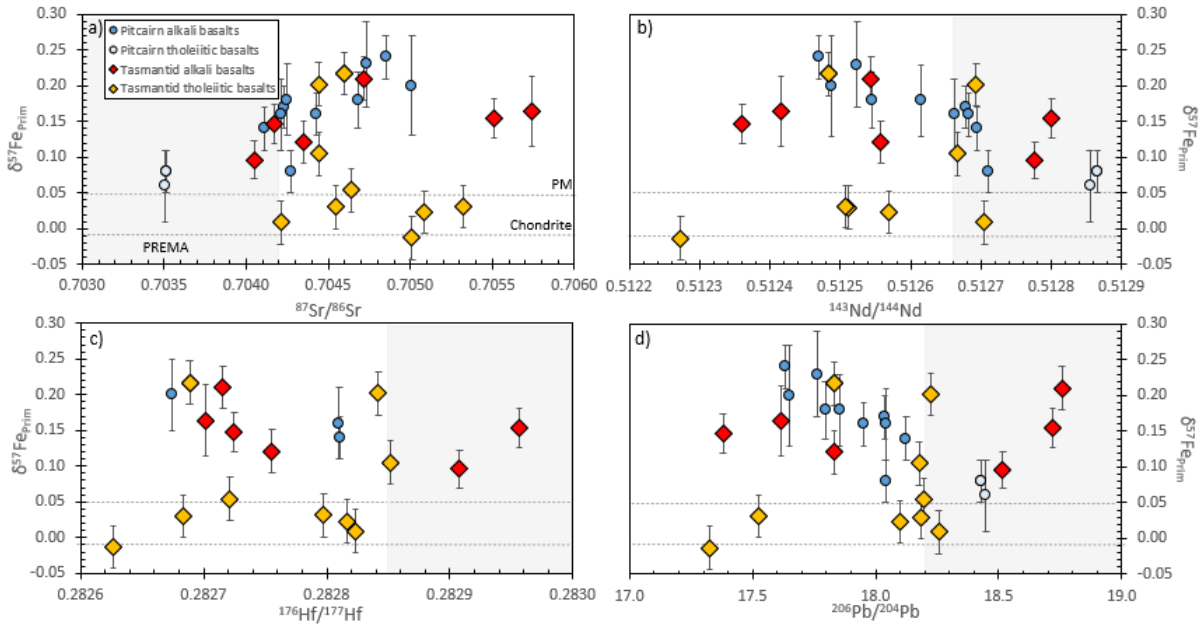

Figure 12. a) $^{87}Sr/^{86}Sr$, b) $^{143}Nd/^{144}Nd$, c) $^{176}Hf/^{177}Hf$, d) $^{206}Pb/^{204}Pb$ vs $\delta^{57}Fe_{Prim}$. For sample 6581 (tholeiitic basalts) no radiogenic Nd isotopic data available. Stable Fe isotopes show no co-variation with radiogenic isotopes. $\delta^{57}Fe_{Prim}$ for chondritic material of -0.01 ± 0.01‰ (2S.E.; Craddock and Dauphas, 2011; Needham et al., 2009; Wang et al., 2014; Schoenberg and von Blanckenburg, 2006; Sossi et al., 2016).Primitive mantle (PM) value of $\delta^{57}Fe_{Prim}$ = +0.05 ± 0.01‰ (2S.E.) from Sossi et al. (2016). PREMA field as in Fig. 8.

For Hawai'i, secondary pyroxenite was suggested as the source for low-pressure melting (Jones et al., 2017). Even though tholeiites have been produced during high pressure melting in the Tasmantid source, pyroxenite is a potential lithological unit that could produce heavier $\delta^{57}Fe_{Prim}$ values through petrogenesis (enriched mantle components; Konter et al., 2016; Nebel et al., 2019). In general, pyroxenite has an expected isotopically heavier Fe isotopic signature than peridotite, which is explained by Fe^{3+} being more incompatible than Fe^{2+} during the formation of pyroxenites, where partial melting goes in tandem with transport of heavier Fe isotopes in the melt (Williams and Bizimis, 2014; Williams et al., 2005; Dauphas et al., 2009; Williams et al., 2004; Nebel et al., 2019). With no clear two-component mixing between the endmember compositions, namely EM1 and PREMA, in radiogenic isotopes, the source of these pyroxenites remains enigmatic, similar to heavy Fe isotopes elsewhere in plumes (Soderman et al., 2021).

Considering that the Tasmantid Seamounts are located along an extinct mid-ocean ridge (Gaina et al., 1998), we surmise that pyroxenite veins formed at the lithosphere-asthenosphere boundary (Supplementary data I, Fig. S6; e.g., Hirschmann and Stolper, 1996). Low-degree metasomatized pyroxenite veins with heavy Fe isotopic signatures $\delta^{57}Fe \leq +0.54‰$ have been suggested for several mid-ocean ridge settings (e.g., Sun et al., 2020). During ascent of tholeiitic melts such signatures, even though extreme in nature, may interact with these lithologies, possibly through porous flow, whereas alkaline melts have surfaced through channelled flow in the mantle. Alternatively, serpentinite-derived, Fe-rich and isotopically heavy segments have been found in diamonds in the transition zone. Such a component, even though rare, may be responsible for such heavy Fe isotope excursions (Smith et al., 2021).

2.6 Conclusion

The Tasmantid Seamounts are generated by both alkali and tholeiitic melts present in one mantle plume. Radiogenic isotope systematics identify an EM1-PREMA connection in the plume, similar to many others in the greater Pacific regions. However, the isotopic signature of both enriched EM1 and PREMA, in radiogenic Pb isotopes in particular, are not identical to other plumes of similar mantle flavour. This makes the Tasmantid plume a unique part of the plume family.

Comparison with Hawai'ian and Pitcairn lavas, both with alkali and tholeiitic melts, confirms that there is no apparent systematic between the alkalinity and enriched components in this or other plumes. Based on major and trace element systematics, both, Tasmantid alkali and tholeiitic basalts originate in the garnet stability field, yet likely with different degrees of melting.

Stable Fe isotope data reveal that tholeiitic lavas of the Tasmantid Seamounts are derived from a mantle source with $\delta^{57}Fe$ similar to ordinary depleted or primitive mantle, likely peridotite, but with distinct outliers towards heavy Fe isotopic composition of cryptic origin. Alkali lavas show a more systematic variation in Fe isotopes dominated by a trend from isotopically lighter towards heavier Fe isotopes, ranging from $\delta^{57}Fe_{Prim}$ +0.10 to up to +0.21‰. The excursions towards heavier values can readily be explained by pressure dependency and

the presence of garnet, yet without any apparent relation to “enriched components” based on radiogenic isotopes.

Melting-induced or later mixing of depleted with enriched components and resulting varying amounts of either component in erupting lavas may explain some radiogenic and trace element systematics. However, because alkalinity is not affected by this, any such mixing must be of local character. Tholeiites are suggested to be a simple higher degree of melting equivalent to the alkali basalts. A viable scenario proposed here is an elevated temperature for the tholeiitic source, which likely places these melts into the centre of the plume, whereas the alkali melts form in peripheral areas. Further petrologic investigations are required to validate this hypothesis.

Acknowledgements

We thank the scientific and marine crews of the R/V *Franklin* and R/V *Southern Surveyor*, the Australian Marine National Facility, Ian McDougall and Neville Exon for the acquisition and provision of samples. Laboratory work was supported by the Monash Isotopia Laboratory and benefitted from the help provided by Rachelle Pierson and Massimo Raveggi. Fiona Couperthwaite, the reviewers and the editor are thanked for constructive feedback and comments on this manuscript. This study has been supported through a Discovery Australian Research Council grant No. DP180100580 awarded to Oliver Nebel.

2.7 References

Abouchami, W., Hofmann, A.W., Galer, S.J.G., Frey, F.A., Eisele, J. and Feigenson, M. (2005) Lead isotopes reveal bilateral asymmetry and vertical continuity in the Hawaiian mantle plume. *Nature* **434**, 851.

Bach, W., Peucker-Ehrenbrink, B., Hart, S.R. and Blusztajn, J.S. (2003) Geochemistry of hydrothermally altered oceanic crust: DSDP/ODP Hole 504B - Implications for seawater-crust exchange budgets and Sr-and Pb-isotopic evolution of the mantle. *Geochemistry, Geophysics, Geosystems* **4**, 8904.

Castillo, P. (1988) The Dupal anomaly as a trace of the upwelling lower mantle. *Nature* **336**,

667.

Chen, S., Niu, Y., Guo, P., Gong, H., Sun, P., Xue, Q., Duan, M. and Wang, X. (2019) Iron isotope fractionation during mid-ocean ridge basalt evolution: Evidence from lavas on the East Pacific Rise at 10°30'N and its implications. *Geochimica et Cosmochimica Acta* **267**, p 227-239.

Cheng, T., Nebel, O., Sossi, P.A. and Chen, F. (2014) Refined separation of combined Fe-Hf from rock matrices for isotope analyses using AG-MP-1M and Ln-Spec chromatographic extraction resins. *MethodsX* **1**, 144-150.

Cohen, B. (2012) Tasmantid Seamounts: Volcanic, Tectonic, and Carbonate Record Voyage Summary.

Cohen, B.E., Knesel, K.M., Vasconcelos, P.M. and Schellart, W.P. (2013) Tracking the Australian plate motion through the Cenozoic: Constraints from 40Ar/39Ar geochronology. *Tectonics* **32**, 1371-1383.

Cohen, B.E., Knesel, K.M., Vasconcelos, P.M., Thiede, D.S. and Hergt, J.M. (2008) 40Ar/39Ar constraints on the timing and origin of Miocene leucitite volcanism in southeastern Australia. *Australian Journal of Earth Sciences* **55**, 407-418.

Craddock, P.R. and Dauphas, N. (2011) Iron isotopic compositions of geological reference materials and chondrites. *Geostandards and Geoanalytical Research* **35**, 101-123.

Craddock, P.R., Warren, J.M. and Dauphas, N. (2013) Abyssal peridotites reveal the near-chondritic Fe isotopic composition of the Earth. *Earth and Planetary Science Letters* **365**, 63-76.

Crossingham, T.J., Vasconcelos, P.M., Cunningham, T. and Knesel, K.M. (2017) 40Ar/39Ar geochronology and volume estimates of the Tasmantid Seamounts: Support for a change in the motion of the Australian plate. *Journal of Volcanology and Geothermal research* **343**, 95-108.

Dauphas, N., Craddock, P.R., Asimow, P.D., Bennett, V.C., Nutman, A.P. and Ohnenstetter, D.

(2009) Iron isotopes may reveal the redox conditions of mantle melting from Archean to Present. *Earth and Planetary Science Letters* **288**, 255-267.

Dauphas, N., Roskosz, M., Alp, E.E., Neuville, D.R., Hu, M.Y., Sio, C.K., Tissot, F.L.H., Zhao, J., Tissandier, L., Médard, E. and Cordier, C. (2014) Magma redox and structural controls on iron isotope variations in Earth's mantle and crust. *Earth and Planetary Science letters* **398**, 127-140.

Davies, D.R., Rawlinson, N., Iaffaldano, G. and Campbell, I.H. (2015) Lithospheric controls on magma composition along Earth's longest continental hotspot track. *Nature* **525**, 511-514.

Delavault, H., Chauvel, C., Sobolev, A. and Batanova, V. (2015) Combined petrological, geochemical and isotopic modeling of a plume source: Example of Gambier Island, Pitcairn chain. *Earth and Planetary Science Letters* **426**, 23-35.

Doucet, L., Zheng-Xiang, L., Brendan, M., Collins, W., Spencer, C. and Mitchell, R. (2020) Distinct formation history for deep-mantle domains reflected in geochemical differences. *Nature Geoscience* **13**, 511-515.

Dupuy, C., Barsczus, H.G., Dostal, J., Vidal, P. and Liotard, J.-M. (1989) Subducted and recycled lithosphere as the mantle source of ocean island basalts from southern Polynesia, central Pacific. *Chemical Geology* **77**, 1-18.

Eggins, S.M., Green, D.H. and Falloon, T.J. (1991) The Tasmantid Seamounts shallow melting and contamination of an EM1 mantle plume. *Earth and Planetary Science Letters* **107**, 448-462.

Exon, N., Bernardel, G., Brown, J., Cortese, A., Findlay, C., Hoffmann, K., Howe, R. and Quilty, P. (2006) The geology of the Mellish Rise region off northeast Australia: a key piece in a tectonic puzzle. *Southern Survey Cruise SS02/2005* **Geoscience Australia Survey 274**, Geoscience Australia Record 2006/2008.

Farley, K.A., Natland, J.H. and Craig, H. (1992) Binary mixing of enriched and undegassed

(primitive?) mantle components (He, Sr, Nd, Pb) in Samoan lavas. *Earth and Planetary Science Letters* **111**, 183-199.

Foden, J., Sossi, P.A. and Nebel, O. (2018) Controls on the iron isotopic composition of global arc magmas. *Earth and Planetary Science Letters* **494**, 190-201.

Frey, F.A., Garcia, M.O. and Roden, M.F. (1994) Geochemical characteristics of Koolau Volcano: Implications of intershield geochemical differences among Hawaiian volcanoes. *Geochimica et Cosmochimica Acta* **58**, 1441-1462.

Frey, F.A., Green, D.H. and Roy, S.D. (1978) Integrated models of basalt petrogenesis a study of quartz tholeiites to olivine melilitites from South eastern Australia utilizing geochemical and experimental petrological data. *Journal of Petrology* **19**, 463-513.

Gaina, C., Müller, R., Roest, W. and Symonds, P. (1998) The opening of the Tasman Sea: a gravity anomaly animation. *Earth Interactions* **2**, 1-23.

Gale, A., Dalton, C.A., Langmuir, C.H., Su, Y. and Schilling, J. (2013) The mean composition of ocean ridge basalts. *Geochemistry, Geophysics, Geosystems* **14**, 489-518.

Garapić, G., Jackson, M.G., Hauri, E.H., Hart, S.R., Farley, K.A., Blusztajn, J.S. and Woodhead, J.D. (2015) A radiogenic isotopic (He-Sr-Nd-Pb-Os) study of lavas from the Pitcairn hotspot: Implications for the origin of EM-1 (enriched mantle 1). *Lithos* **228-228**, 1-11.

Garcia, M.O., Foss, D.J., West, H.B. and Mahoney, J.J. (1995) Geochemical and isotopic evolution of Loihi Volcano, Hawaii. *Journal of Petrology* **36**, 1647-1674.

Garcia, M.O., Jorgenson, B.A., Mahoney, J.J., Ito, E. and Irving, A.J. (1993) An evaluation of temporal geochemical evolution of Loihi Summit Lavas: Results from Alvin submersible dives. *Journal of Geophysical Research: Solid Earth* **98**, 537-550.

Gleeson, M.L.M., Gibson, S.A. and Williams, H.M. (2020) Novel insights from Fe-isotopes into the lithological heterogeneity of Ocean Island Basalts and plume-influenced MORBs. *Earth and Planetary Science Letters* **535**, 116114.

Green, D. and Ringwood, A. (1967) The genesis of basaltic magmas. *Contributions to Mineralogy and Petrology* **15**, 103-190.

Hanan, B. and Graham, D. (1996) Lead and helium isotope evidence from oceanic basalts for a common deep source of mantle plumes. *Science* **272**, 991-995.

Hart, S.R. (1984) A large-scale isotope anomaly in the Southern Hemisphere mantle. *Nature* **309**, 753-757.

Hart, S.R. (1988) Heterogeneous mantle domains: signatures, genesis and mixing chronologies. *Earth and Planetary Science Letters* **90**, 273-296.

Hart, S.R., Hauri, E., Oschmann, L.A. and Whitehead, J.A. (1992) Mantle Plumes and Entrainment: Isotopic Evidence. *Science* **256**, 517.

Hauri, E.H., Whitehead, J.A. and Hart, S.R. (1994) Fluid dynamic and geochemical aspects of entrainment in mantle plumes. *Journal of Geophysical Research: Solid Earth* **99**, 24275-24300.

Hess, J., Bender, M.L. and Schilling, J.G. (1986) Evolution of the ratio of strontium-87 to strontium-86 in seawater from cretaceous to present. *Science (New York, N.Y.)* **231**, 979.

Hirose, K. and Kushiro, I. (1993) Partial melting of dry peridotites at high pressures: determination of compositions of melts segregated from peridotite using aggregates of diamond. *Earth and Planetary Science Letters* **114**, 477-489.

Hirschmann, M.M. and Stolper, E.M. (1996) A possible role for garnet pyroxenite in the origin of the “garnet signature” in MORB. *Contributions to Mineralogy and Petrology* **124**, 185-208.

Hofmann, A. (1997) Mantle geochemistry: The message from oceanic volcanism. *Nature* **385**, 219-229.

Hofmann, A. and Feigenson, M. (1983) Case studies on the origin of basalt. *Contributions to*

Mineralogy and Petrology **84**, 382-389.

Hofmann, A.W. (2003) Sampling Mantle Heterogeneity through Oceanic Basalts: Isotopes and Trace Elements, in Treatise on Geochemistry: The Mantle and Core, edited by R. W. Carlson, H.D. Holland, and K.K. Turekian. Elsevier, New York, pp. 61-101.

Hofmann, A.W. and Farnetani, C.G. (2013) Two views of Hawaiian plume structure. *Geochemistry, Geophysics, Geosystems* **14**, 5308-5322.

Irvine, T. and Baragar, W. (1971) A guide to the chemical classification of the common volcanic rocks. *Canadian Journal of Earth Sciences* **8**, 523-548.

Jackson, M.G. and Dasgupta, R. (2008) Compositions of HIMU, EM1, and EM2 from global trends between radiogenic isotopes and major elements in ocean island basalts. *Earth and Planetary Science Letters* **276**, 175-186.

Jackson, M.G., Kurz, M.D., Hart, S.R. and Workman, R.K. (2007) New Samoan lavas from Ofu Island reveal a hemispherically heterogeneous high 3He/ 4He mantle. *Earth and Planetary Science Letters* **264**, 360-374.

Jackson, M.G., Weis, D. and Huang, S. (2012) Major element variations in Hawaiian shield lavas: Source features and perspectives from global ocean island basalt (OIB) systematics. *Geochemistry, Geophysics, Geosystems* **13**, Q09009.

Jones, T.D., Davies, D.R., Campbell, I.H., Iaffaldano, G., Yaxley, G., Kramer, S.C. and Wilson, C.R. (2017) The concurrent emergence and causes of double volcanic hotspot tracks on the Pacific plate. *Nature* **545**, 472-477.

Jweda, J., Bolge, L., Class, C. and Goldstein, S.L. (2016) High Precision Sr-Nd-Hf-Pb Isotopic Compositions of USGS Reference Material BCR-2. *Geostandards and Geoanalytical Research* **40**, 101-115.

Kalnins, L.M., Cohen, B.E., Fitton, J.G., Mark, D.F., Richards, F.D. and Barfod, D.N. (2015) The East Australian, Tasmantid, and Lord Howe Volcanic Chains: possible mechanisms behind a trio of hotspot trails, AGU Fall Meeting Abstracts.

Kang, J.-T., Zhou, C., Huang, J.-Y., Hao, Y.-T., Liu, F., Zhu, H.-L., Zhang, Z.-F. and Huang, F. (2020) Diffusion-driven Ca-Fe isotope fractionations in the upper mantle: Implications for mantle cooling and melt infiltration. *Geochimica et Cosmochimica Acta* **290**, 41-58.

Knesel, K., M., Cohen, B., E. , Vasconcelos, P., M. and Thiede, D., S. (2008) Rapid change in drift of the Australian plate records collision with Ontong Java plateau. *Nature* **454**, 754.

Konter, J.G., Pietruszka, A.J., Hanan, B.B., Finlayson, V.A., Craddock, P.R., Jackson, M.G. and Dauphas, N. (2016) Unusual δ56Fe values in Samoan rejuvenated lavas generated in the mantle. *Earth and Planetary Science Letters* **450**, 221-232.

Lassiter, J. and Hauri, E. (1998) Osmium-isotope variations in Hawaiian lavas: evidence for recycled oceanic lithosphere in the Hawaiian plume. *Earth and Planetary Science Letters* **164**, 483-496.

Lassiter, J.C. and DePaolo, D.J. (1997) Plume/lithosphere interaction in the generation of continental and oceanic flood basalts: chemical and isotopic constraints. *Geophysical Monograph-American Geophysical Union* **100**, 335-356.

Le Bas, M.J., Le Maitre, R.W., Streckeisen, A. and Zanettin, B.A. (1986) A Chemical Classification of Volcanic Rocks Based on the Total Alkali-Silica Diagram. *Journal of Petrology* **27**, 745-750.

Le Maître, R. (1989) A classification of igneous rocks and glossary of terms. Recommendations of the IUGS Subcommission on the Systematics of Igneous Rocks. Ed. IUGS. Blackwell Publications, 193p.

Mallik, A. and Dasgupta, R. (2012) Reaction between MORB-eclogite derived melts and fertile peridotite and generation of ocean island basalts. *Earth and Planetary Science Letters* **329**, 97-108.

McCulloch, M.T. (1988) Nd-Sr isotope geochemistry of the Tasmantid Seamounts - evolution of a hotspot trace. *Geological Society of Australia. Abstract.* **21**, 260-261.

McDonough, W.F. and Sun, S.S. (1995) The composition of the Earth. *Chemical Geology* **120**, 223-253.

McDougall, I. and Duncan, R.A. (1988) Age progressive volcanism in the Tasmantid Seamounts. *Earth and Planetary Science Letters* **89**, 207-220.

Moore, J.G. (1966) Rate of palagonitization of submarine basalt adjacent to Hawaii. *US Geological Survey Professional Paper* **550**, D163-D171.

Münker, C., Weyer, S., Scherer, E. and Mezger, K. (2001) Separation of high field strength elements (Nb, Ta, Zr, Hf) and Lu from rock samples for MC-ICPMS measurements. *Geochemistry, Geophysics, Geosystems* **2**, 2001GC000183.

Naumann, T. and Geist, D. (1999) Generation of alkalic basalt by crystal fractionation of tholeiitic magma. *Geology* **27**, 423-426.

Nebel, O., Morel, M.L.A. and Vroon, P.Z. (2009) Isotope Dilution Determinations of Lu, Hf, Zr, Ta and W, and Hf Isotope Compositions of NIST SRM 610 and 612 Glass Wafers. *Geostandards and Geoanalytical Research* **33**, 487-499.

Nebel, O., Sossi, P.A., Bénard, A., Arculus, R.J., Yaxley, G.M., Woodhead, J.D., Rhodri Davies, D. and Ruttor, S. (2019) Reconciling petrological and isotopic mixing mechanisms in the Pitcairn mantle plume using stable Fe isotopes. *Earth and Planetary Science Letters* **521**, 60-67.

Nebel, O., Sossi, P.A., Bénard, A., Wille, M., Vroon, P.Z. and Arculus, R.J. (2015) Redox-variability and controls in subduction zones from an iron-isotope perspective. *Earth and Planetary Science Letters* **432**, 142-151.

Needham, A., Porcelli, D. and Russell, S. (2009) An Fe isotope study of ordinary chondrites. *Geochimica et Cosmochimica Acta* **73**, 7399-7413.

Niu, Y., Wilson, M., Humphreys, E.R. and O'Hara, M.J. (2011) The Origin of Intra-plate Ocean Island Basalts (OIB): the Lid Effect and its Geodynamic Implications. *Journal of Petrology* **52**, 1443-1468.

O'Hara, M. (1965) Primary magmas and the origin of basalts. *Scottish Journal of Geology* **1**, 19-40.

O'Neill, H.S.C. (2016) The Smoothness and Shapes of Chondrite-normalized Rare Earth Element Patterns in Basalts. *Journal of Petrology* **57**, 1463-1508.

Palme, H. and O'Neill, H.S.C. (2014) Cosmochemical Estimates of Mantle Composition, in: Carlson, R.W.E. (Ed.), Treatise on Geochemistry. Elsevier B.V., Amsterdam, pp. 1-38.

Pearce, J.A. (2008) Geochemical fingerprinting of oceanic basalts with applications to ophiolite classification and the search for Archean oceanic crust. *Lithos* **100**, 14-48.

Phillips, E.H., Sims, K.W.W., Sherrod, D.R., Salters, V.J.M., Blusztajn, J. and Dulai, H. (2016) Isotopic constraints on the genesis and evolution of basanitic lavas at Haleakala, Island of Maui, Hawaii.(Report). *Geochimica et Cosmochimica Acta* **195**, 201.

Pin, C., Gannoun, A. and Dupont, A. (2014) Rapid, simultaneous separation of Sr, Pb, and Nd by extraction chromatography prior to isotope ratios determination by TIMS and MC-ICP-MS. *J. Anal. At. Spectrom.* **29**, 1858-1870.

Prytulak, J. and Elliott, T. (2007) TiO2 enrichment in ocean island basalts. *Earth and Planetary Science Letters* **263**, 388-403.

Putirka, K. (2016) Rates and styles of planetary cooling on Earth, Moon, Mars, and Vesta, using new models for oxygen fugacity, ferric-ferrous ratios, olivine-liquid Fe-Mg exchange, and mantle potential temperature. *American Mineralogist* **101**, 819-840.

Rhodes, J.M., Huang, S., Frey, F.A., Pringle, M. and Xu, G. (2012) Compositional diversity of Mauna Kea shield lavas recovered by the Hawaii Scientific Drilling Project: Inferences on source lithology, magma supply, and the role of multiple volcanoes. *Geochemistry, Geophysics, Geosystems* **13**, Q03014.

Roden, M.F., Frey, F.A. and Clague, D.A. (1984) Geochemistry of tholeiitic and alkalic lavas from the Koolau Range, Oahu, Hawaii: Implications for Hawaiian volcanism. *Earth and Planetary Science Letters* **69**, 141-158.

Roeder, P. and Emslie, R. (1970) Olivine-liquid equilibrium. *Contributions to Mineralogy and Petrology* **29**, 275-289.

Ryan, W.B., Carbotte, S.M., Coplan, J.O., O'Hara, S., Melkonian, A., Arko, R., Weissel, R.A., Ferrini, V., Goodwillie, A. and Nitsche, F. (2009) Global multi-resolution topography synthesis. *Geochemistry, Geophysics, Geosystems* **10**.

Schoenberg, R. and von Blanckenburg, F. (2006) Modes of planetary-scale Fe isotope fractionation. *Earth and Planetary Science Letters* **252**, 342-359.

Schuessler, J.A., Schoenberg, R. and Sigmarsson, O. (2009) Iron and lithium isotope systematics of the Hekla volcano, Iceland — Evidence for Fe isotope fractionation during magma differentiation. *Chemical Geology* **258**, 78-91.

Seton, M., Williams, S., Mortimer, N., Meffre, S., Micklethwaite, S. and Zahirovic, S. (2019) Magma production along the Lord Howe Seamount Chain, northern Zealandia. *Geological Magazine* **156**, 1605-1617.

Smith, E.M., Ni, P., Shirey, S.B., Richardson, S.H., Wang, W. and Shahar, A. (2021) Heavy iron in large gem diamonds traces deep subduction of serpentinized ocean floor. *Science Advances* **7**, eabe9773.

Soderman, C.R., Matthews, S., Shorttle, O., Jackson, M.G., Ruttor, S., Nebel, O., Turner, S., Beier, C., Millet, M.-A., Widom, E., Humayun, M. and Williams, H.M. (2021) Heavy δ57Fe in ocean island basalts: a non-unique signature of processes and source lithologies in the mantle. *Geochimica et Cosmochimica Acta* **292**, 309-332.

Sofade, A.O. (2018) Submarine Alteration of Seamount Rocks in the Canary Islands: Insights from Mineralogy, Trace Elements, and Stable Isotopes.

Sossi, P., Foden, J. and Halverson, G. (2012) Redox-controlled iron isotope fractionation during magmatic differentiation: an example from the Red Hill intrusion, S. Tasmania. *Contributions to Mineralogy and Petrology* **164**, 757-772.

Sossi, P.A., Halverson, G.P., Nebel, O. and Eggins, S.M. (2015) Combined Separation of Cu, Fe

and Zn from Rock Matrices and Improved Analytical Protocols for Stable Isotope Determination. *Geostand. Geoanal. Res.* **39**, 129-149.

Sossi, P.A., Nebel, O. and Foden, J. (2016) Iron isotope systematics in planetary reservoirs. *Earth and Planetary Science Letters* **452**, 295-308.

Sossi, P.A. and O'Neill, H.S.C. (2017) The effect of bonding environment on iron isotope fractionation between minerals at high temperature. *Geochimica et Cosmochimica Acta* **196**, 121.

Stracke, A., Hofmann, A.W. and Hart, S.R. (2005) FOZO, HIMU, and the rest of the mantle zoo. *Geochemistry, Geophysics, Geosystems* **6**, Q05007.

Sun, P., Niu, Y., Guo, P., Duan, M., Chen, S., Gong, H., Wang, X. and Xiao, Y. (2020) Large iron isotope variation in the eastern Pacific mantle as a consequence of ancient low-degree melt metasomatism. *Geochimica et Cosmochimica Acta* **286**, 269-288.

Sun, S.S. and McDonough, W.F. (1989) Chemical and isotopic systematics of oceanic basalts: implications for mantle composition and processes. *Geological Society, London, Special Publications* **42**, 313-345.

Taylor, B. and Martinez, F. (2003) Back-arc basin basalt systematics. *Earth and Planetary Science Letters* **210**, 481-497.

Teng, F.-Z., Dauphas, N. and Helz, R.T. (2008) Iron isotope fractionation during magmatic differentiation in Kilauea Iki lava lake. *Science (New York, N.Y.)* **320**, 1620.

Teng, F.-Z., Dauphas, N., Huang, S. and Marty, B. (2013) Iron isotopic systematics of oceanic basalts. *Geochimica et Cosmochimica Acta* **107**, 12-26.

Tilley, C.E. and Scoon, J.H. (1961) Differentiation of Hawaiian basalts trends of Mauna Loa and Kilauea historic magma. *American Journal of Science (1880)* **259**, 60-68.

Wagner, T.P. and Grove, T.L. (1998) Melt/harzburgite reaction in the petrogenesis of tholeiitic magma from Kilauea volcano, Hawaii. *Contributions to Mineralogy and Petrology* **131**,

1-12.

Wang, K., Savage, P.S. and Moynier, F. (2014) The iron isotope composition of enstatite meteorites: Implications for their origin and the metal/sulfide Fe isotopic fractionation factor. *Geochimica et Cosmochimica Acta* **142**, 149-165.

Weis, D., Kieffer, B., Maerschalk, C., Barling, J., De Jong, J., Williams, G.A., Hanano, D., Pretorius, W., Mattielli, N. and Scoates, J.S. (2006) High-precision isotopic characterization of USGS reference materials by TIMS and MC-ICP-MS. *Geochemistry, Geophysics, Geosystems* **7**, Q08006.

Weis, D., Kieffer, B., Maerschalk, C., Pretorius, W. and Barling, J. (2005) High-precision Pb-Sr-Nd-Hf isotopic characterization of USGS BHVO-1 and BHVO-2 reference materials. *Geochemistry, Geophysics, Geosystems* **6**, Q02002.

Wellman, P. and McDougall, I. (1974) Cainozoic igneous activity in eastern australia. *Tectonophysics* **23**, 49-65.

Weyer, S. and Ionov, D.A. (2007) Partial melting and melt percolation in the mantle: The message from Fe isotopes. *Earth and Planetary Science Letters* **259**, 119-133.

White, W.M. (2015) Isotopes, DUPAL, LLSVPs, and Anekantavada. *Chemical Geology* **419**, 10-28.

Williams, H.M. and Bizimis, M. (2014) Iron isotope tracing of mantle heterogeneity within the source regions of oceanic basalts. *Earth and Planetary Science Letters* **404**, 396-407.

Williams, H.M., McCammon, C.A., Peslier, A.H., Halliday, A.N., Teutsch, N., Levasseur, S. and Burg, J.-P. (2004) Iron isotope fractionation and the oxygen fugacity of the mantle. *Science* **304**, 1656-1659.

Williams, H.M., Peslier, A.H., McCammon, C., Halliday, A.N., Levasseur, S., Teutsch, N. and Burg, J.-P. (2005) Systematic iron isotope variations in mantle rocks and minerals: the effects of partial melting and oxygen fugacity. *Earth and Planetary Science Letters* **235**, 435-452.

Ye, H., Wu, C., Brzozowski, M.J., Yang, T., Zha, X., Zhao, S., Gao, B. and Li, W. (2020) Calibrating equilibrium Fe isotope fractionation factors between magnetite, garnet, amphibole, and biotite. *Geochimica et Cosmochimica Acta* **271**, 78-95.

Zindler, A. and Hart, S. (1986) Chemical geodynamics. *Annual Review of Earth and Planetary Sciences* **14**, 493-571.

SUPPLEMENTARY DATA

I. Supplementary data I

Major and trace element data

Alkali and tholeiitic lavas of the Tasmantid Seamounts show decreasing Al_2O_3, P_2O_5, K_2O and increasing MnO and Na_2O with increasing MgO (4.8 wt.% < MgO < 11.4 wt.%; Fig. S1). Alkali basalts are more enriched in incompatible trace elements (e.g., Y, Zr, Ba, Hf; Fig. S2) compared to tholeiitic basalts, which show higher values in compatible elements like Cr and Ni (Fig. S2).

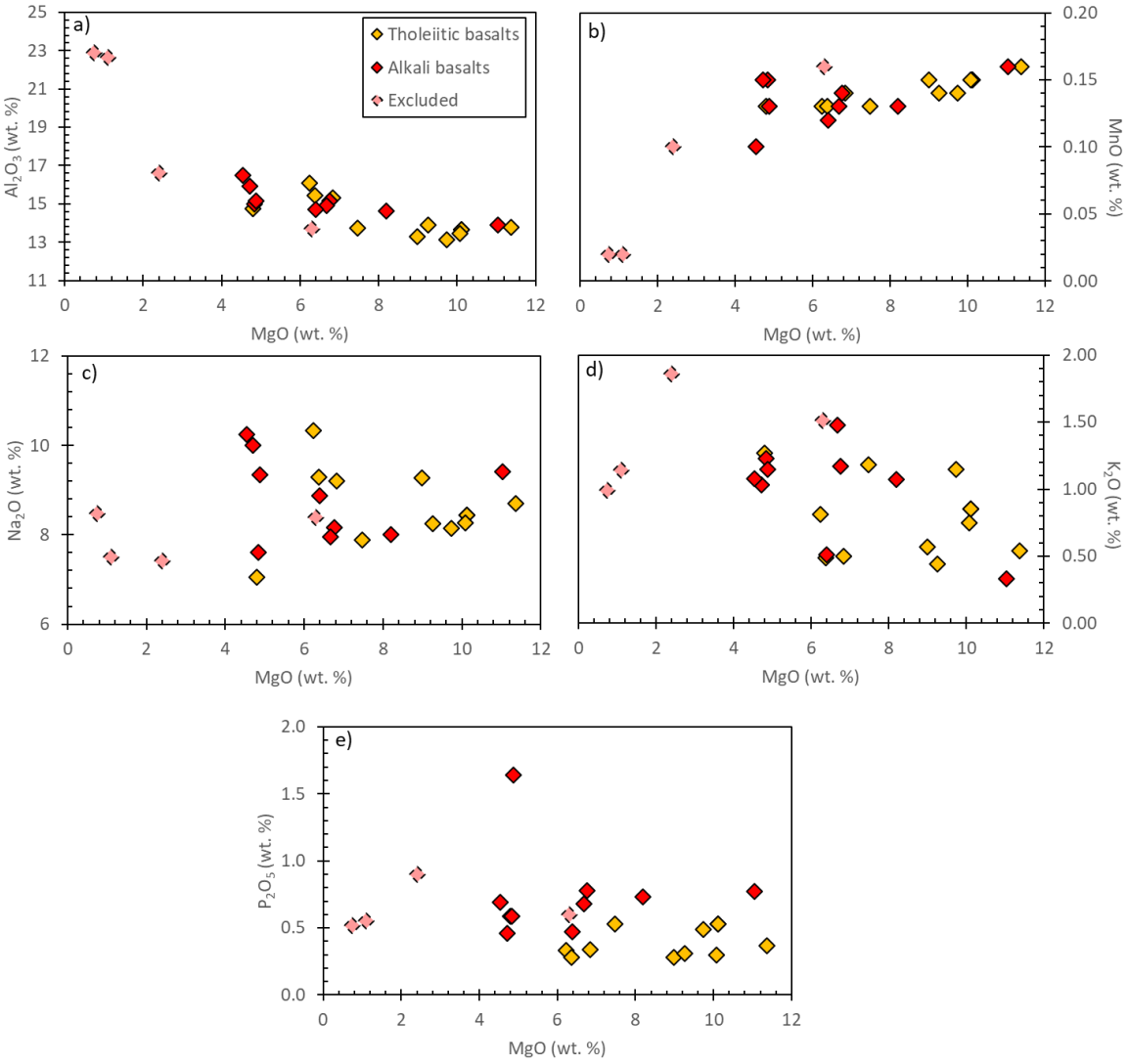

Figure S1. Variation diagrams for a) Al_2O_3, b) MnO, c) Na_2O, d) K_2O, e) P_2O_5 vs MgO for the Tasmantid Seamounts. Yellow squares represent tholeiitic basalts, red squares represent alkali basalts.

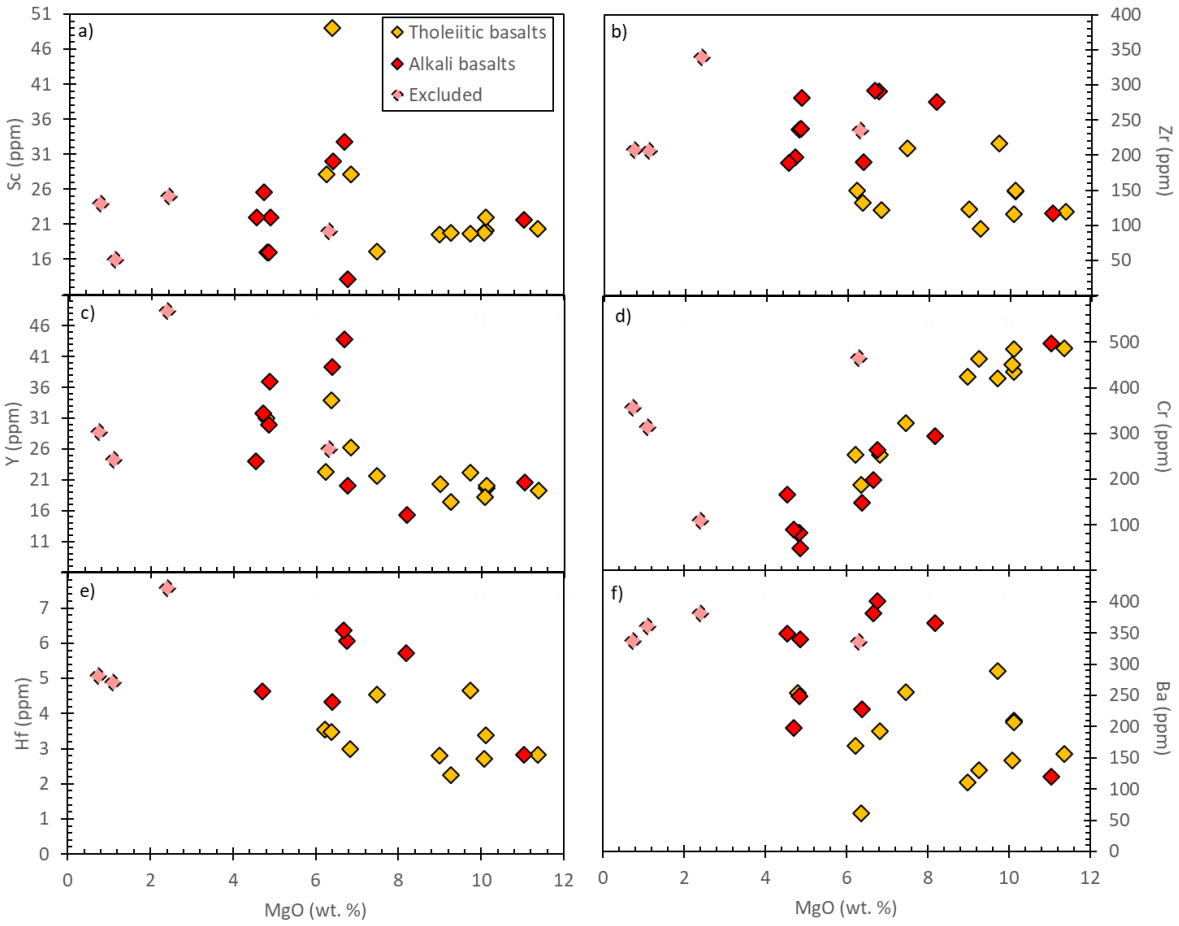

Figure S2. Selected trace elements with a) Sc, b) Zr, c) Y, d) Cr., e) Hf, f) Ba vs MgO of the Tasmantid Seamounts.

Olivine fractionation correction

The applied olivine fractionation is the maximum value to correct heavy Fe isotopes. Thus, we also corrected our data with $\Delta^{57}Fe_{ol\text{-}melt} = -0.1 \times 10^6$ (Fig. S3). The calculation is outlined in section *4.3. Stable Fe isotope data*, main manuscript. The interpretation of the data is not influenced by the applied correction factor.

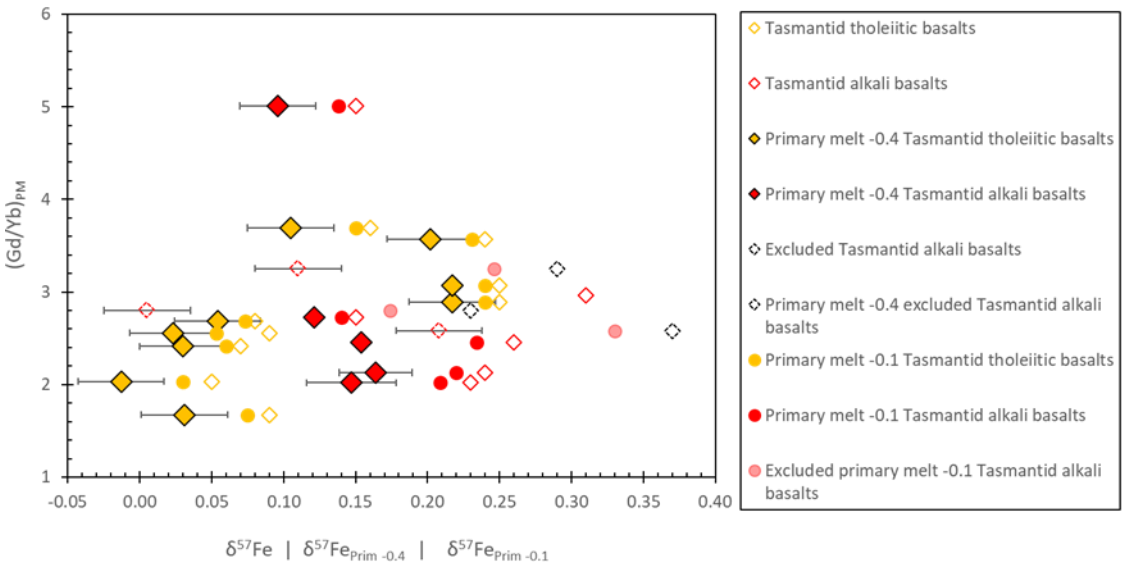

Figure S3. Measured $\delta^{57}Fe$ composition of Tasmantid Seamount basalts compared to calculated primary melt values $\delta^{57}Fe_{Prim}$ with $\Delta^{57}Fe_{ol\text{-}melt} = -0.1 \times 10^6/T^2$ and $\Delta^{57}Fe_{ol\text{-}melt} = -0.4 \times 10^6/T^2$ vs $(Gd/Yb)_{PM}$, fractionation crystallisation correction after Nebel et al. (2019); Sossi et al. (2016). Values of error bars shown with 2 S.E. Error bars in a) just shown for measured $\delta^{57}Fe$ to retain overview. For sample 85162 no major element data is available, thus the measured value $\delta^{57}Fe$ = +0.31‰ could not be corrected for olivine fractionation.

Discussion of age

In radiogenic Sr, Nd, Pb and Hf isotope space, the Tasmantid Seamount basalts identify as an individual member of the EM1-PREMA family. Most pronounced is its individual character in radiogenic Pb isotopic ratios, suggesting a similar U-Th/Pb parent-daughter ratio to EM1 components which likely formed at different times. In the following, we aim for a better understanding of the time of formation of the Tasmantid Seamount mantle component.

To explain the radiogenic Pb isotope ratio of the Tasmantid Seamounts we adapt an age model calculated by Frey et al. (2016) for Hawai'i and compare it to the Tasmantid Seamounts. The age model uses adcumulate gabbro with abundant cumulus plagioclase, common in the lower oceanic crust (i.e., Coogan et al., 2001) and formed from ancient mid-ocean ridge basalt (MORB), to explain trace element ratios and Pb isotopic ratios of Hawai'i. In radiogenic Pb isotopic ratios, Hawai'ian alkali as well as tholeiitic lavas overlap slightly, as is the case for the Tasmantid Seamount basalts (Fig. S4). Following the regression lines in Fig. S4, tholeiitic lavas (yellow line) of the Tasmantid Seamounts intersect at 3.50 Ga with the adcumulate gabbro.

Whereas alkali basalts intersect with the gabbro at 3.25 Ga (including outlier sample 85183 at 0.9153 $^{208}Pb^*/^{206}Pb^*$). Thus, to create the radiogenic Pb isotopic ratio of the Tasmantid tholeiitic and alkali basalts two different subduction times of their sources can be assumed.

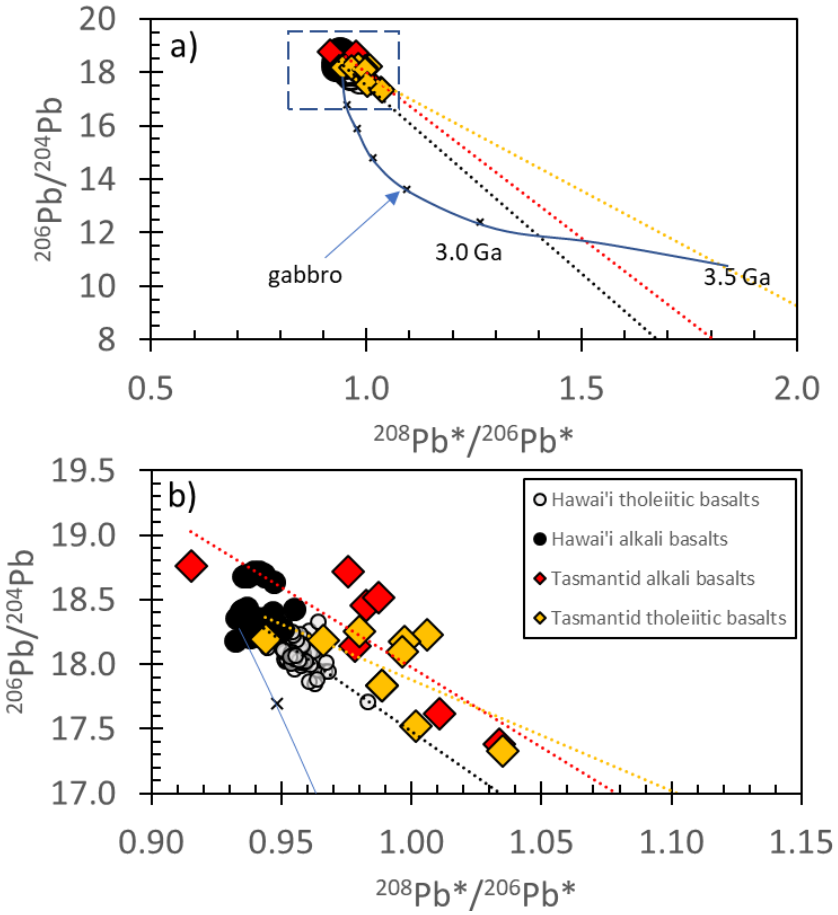

Figure S4. a) and b) $^{208}Pb^*/^{206}Pb^*$ vs $^{206}Pb/^{204}Pb$, dotted lines show trendlines of tholeiitic (yellow), alkali (red) Tasmantid Seamounts and Hawai'i (black). $^{208}Pb^*/^{206}Pb^*$ is a measure of time-integrated $^{132}Th/^{238}U$ ratio since earth formation and has been calculated with $^{208}Pb^*/^{206}Pb^*$ = ($^{208}Pb/^{204}Pb$ – 29.475)/($^{206}Pb/^{204}Pb$ – 9.307) following Galer and Nions (1985). Gabbro averaged from least altered gabbros in Hart et al. (1999). Evolution of $^{208}Pb^*/^{206}Pb^*$ and $^{206}Pb/^{204}Pb$ of the gabbro in incremental steps of 0.5 Ga from 0.5 to 3.5 GPa adapted from Frey et al. (2016). Th/U ratio of gabbro = 3.75. U/Pb ratio of gabbro = 0.033.

In $^{208}Pb^*/^{206}Pb^*$ vs $^{87}Sr/^{86}Sr$ tholeiitic and most of the alkali lavas plot within the same area. The two outliers (Fig. S5), alkali basalts of the Mellish Seamount and 274DR36 B1, were mentioned in the main text as being altered presumably by seawater. These two samples show $^{87}Sr/^{86}Sr$ ratios of 0.705742 and 0.705508, respectively. Another sample, sample 85183,

deviates from the majority of alkali basalts and shows a $^{208}Pb^*/^{206}Pb^*$ value of 0.9153 (Fig. S4). In radiogenic Sr, Nd and Hf space, this sample shows no deviation from the rest of the alkali basalts but plots underneath the NHRL line in radiogenic Pb-space (main text Fig. 8b). The radiogenic Pb isotopic ratio of the two samples with radiogenic $^{87}Sr/^{86}Sr$ are similar to the rest of the alkali basalts. We assume that only Sr has been affected by alteration in form of the addition of secondary Sr.

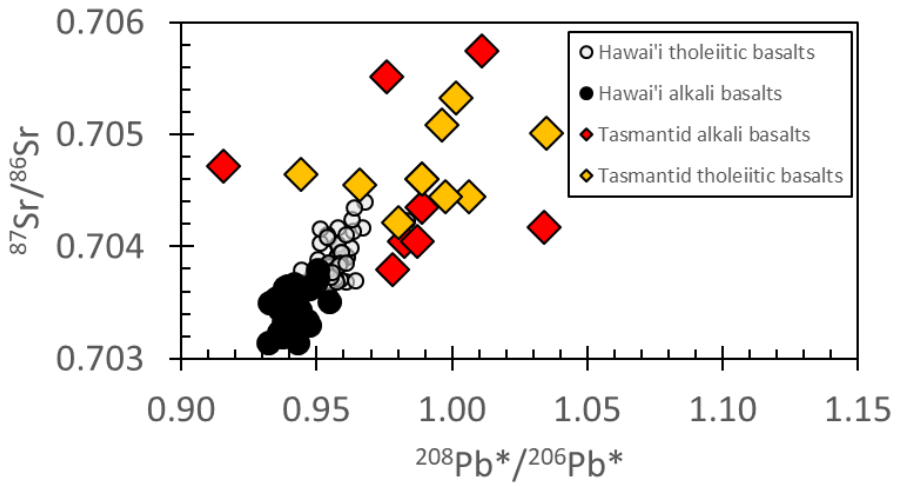

Figure S5. $^{208}Pb^*/^{206}Pb^*$ vs $^{87}Sr/^{86}Sr$ for Tasmantid Seamounts and alkali basalts. For $^{208}Pb^*/^{206}Pb^*$ calculation see Fig. S1.

Schematic illustration

Adiabatic upwelling of hot mantle material leads to melting of pyroxenite veins, which are enriched in incompatible elements and stable Fe isotope values. Melting induced at similar depth for alkali and tholeiitic melts. Pyroxenitic veins might be present and cause the heavy Fe isotopic signature of tholeiitic lavas (see main text).

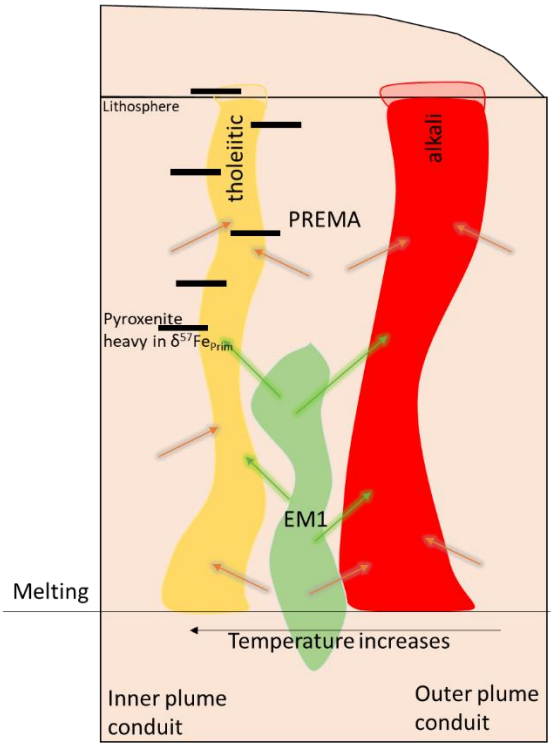

Figure S6. Schematic diagram of melting induced mixing of peridotite and pyroxenite beneath the Tasmantid Seamounts.

References

Coogan, L.A., Macleod, C.J., Dick, H.J.B., Edwards, S.J., Kvassnes, A., Natland, J.H., Robinson, P.T., Thompson, G. and O'Hara, M.J. (2001) Whole-rock geochemistry of gabbros from the Southwest Indian Ridge: constraints on geochemical fractionations between the upper and lower oceanic crust and magma chamber processes at (very) slow-spreading ridges. *Chemical Geology* **178**, 1-22.

Frey, F.A., Huang, S., Xu, G. and Jochum, K.P. (2016) The geochemical components that distinguish Loa- and Kea-trend Hawaiian shield lavas.(Report). *Geochimica et Cosmochimica Acta* **185**, 160.

Galer, S.J.G. and Nions, R.K.O. (1985) Residence time of thorium, uranium and lead in the mantle with implications for mantle convection. *Nature* **316**, 778.

Hart, S.R., Blusztajn, J., Dick, H.J.B., Meyer, P.S. and Muehlenbachs, K. (1999) The fingerprint of seawater circulation in a 500-meter section of ocean crust gabbros. *Geochimica et Cosmochimica Acta* **63**, 4059-4080.

Nebel, O., Sossi, P.A., Bénard, A., Arculus, R.J., Yaxley, G.M., Woodhead, J.D., Rhodri Davies, D. and Ruttor, S. (2019) Reconciling petrological and isotopic mixing mechanisms in the Pitcairn mantle plume using stable Fe isotopes. *Earth and Planetary Science Letters* **521**, 60-67.

Sossi, P.A., Nebel, O. and Foden, J. (2016) Iron isotope systematics in planetary reservoirs. *Earth and Planetary Science Letters* **452**, 295-308.

II. Supplementary data II

Table S1a. Major element data (wt. %) of alkali lavas from the Pitcairn Gambier Chain (GEOROC; http://georoc.mpch-mainz.gwdg.de/georoc/).

Sample No.	SIO_2	TIO_2	AL_2O_3	FEO_T	CAO	MGO	MNO	K_2O	NA_2O	P_2O_5
s_V479.2	41.80	3.88	12.59	12.69	10.90	8.64	0.17	0.83	2.40	0.63
s_V738.7	42.10	3.50	11.82	12.89	9.90	11.77	0.17	0.59	2.36	0.51
s_K6375.0/s_K6-375.0	43.60	2.93	9.39	12.46	9.40	16.24	0.18	0.76	1.44	0.30
s_V397.0	44.50	3.53	12.36	12.08	9.96	10.91	0.16	0.53	2.39	0.50
s_VI831.0	44.70	4.02	15.78	10.83	9.63	4.31	0.17	1.85	3.45	1.00
s_FR-635.5	44.70	4.80	15.00	12.53	9.80	5.30	0.15	1.26	2.90	0.75
s_V831.0	44.70	3.60	15.78	10.52	9.63	4.31	0.17	1.77	3.45	0.98
s_516	44.81	3.07	14.29	10.61	9.40	3.10	0.16	0.65	2.52	0.33
s_V850.2	44.90	3.51	15.57	11.16	9.37	4.99	0.17	1.73	3.49	0.96
s_K6-624.0	45.00	3.47	13.1	12.96	9.59	9.58	0.17	0.77	2.21	0.35
s_P20	45.61	4.77	15.58	13.69	8.84	4.57	0.19	1.10	3.71	0.47
s_PIT-8	46.32	2.77	13.35	11.52	8.31	11.91	0.17	0.98	3.02	0.43
s_PIT-11	46.45	2.74	13.24	11.53	8.21	12.03	0.17	0.99	2.94	0.42
s_VI359.2	47.00	3.46	16.79	10.56	7.34	3.79	0.14	2.10	3.85	1.00
s_V359.2	47.00	3.28	16.79	10.48	7.34	3.79	0.14	2.10	3.85	1.02
s_P12	47.08	3.85	15.42	13.01	7.62	5.15	0.18	1.64	3.88	0.69
s_P26	47.36	3.92	15.69	13.22	7.67	4.20	0.21	1.58	3.98	0.72
s_P9	47.37	3.57	15.06	11.41	8.82	7.09	0.17	1.43	3.24	0.53
s_P18	47.45	4.28	17.54	14.50	5.56	2.04	0.23	1.81	4.21	0.78
s_PIT-13	47.47	3.75	14.42	10.94	8.12	8.06	0.16	1.59	3.31	0.61
s_P11	47.51	3.86	15.69	13.08	7.85	3.96	0.20	1.63	4.05	0.72
s_P31	47.52	3.85	15.66	13.00	8.10	4.53	0.20	1.41	3.55	0.72
s_PI-376.0 / s_PI376.0	47.65	3.54	15.94	11.18	7.50	4.68	0.12	1.88	3.43	0.90
s_P7	47.88	3.75	14.93	10.99	8.44	6.54	0.17	1.64	3.68	0.57
s_PIT-1	48.10	3.50	14.30	9.99	7.20	7.10	0.15	1.70	3.90	0.90
s_PIT-7	48.15	3.55	15.28	10.52	8.69	6.39	0.16	1.59	3.84	0.60
s_P3	48.58	3.62	15.33	10.74	8.73	5.66	0.16	1.65	3.71	0.59
s_P28	48.65	3.67	16.07	12.64	7.02	3.44	0.30	1.77	4.27	0.78
s_PIT-16	48.71	4.08	15.82	10.46	8.45	4.45	0.17	2.00	3.92	0.79
s_PIT-3	48.73	3.27	14.76	10.39	7.82	7.77	0.15	1.70	3.71	0.62
s_P8	48.74	3.59	15.93	9.88	8.97	5.55	0.15	1.65	3.81	0.61
s_P5	48.76	4.27	15.36	11.25	8.29	3.86	0.18	2.26	3.62	0.88
s_P4	48.89	4.28	15.26	11.18	8.13	3.97	0.18	2.29	3.65	0.89
s_PIT-4A	48.91	4.34	14.97	10.68	8.53	4.25	0.17	2.13	4.23	0.82
s_PIT-12	49.22	3.34	15.14	10.31	7.87	6.27	0.16	1.88	4.04	0.73
s_FR-469.4	49.40	2.66	16.26	9.67	7.04	3.94	0.13	2.35	3.99	1.50
s_P30	49.52	3.26	15.69	11.70	7.49	3.67	0.20	1.84	4.55	0.77
s_PIT-6	49.54	2.99	15.96	11.35	7.50	3.83	0.21	2.00	4.42	1.17
s_P22	49.55	3.37	16.40	12.14	6.89	3.16	0.18	1.91	4.24	0.81
s_1	49.64	2.44	18.50	n.a.	6.88	2.80	0.15	1.66	4.73	0.19

Table S1b. Major element data (wt. %) of alkali lavas from the Pitcairn Gambier Chain (GEOROC; http://georoc.mpch-mainz.gwdg.de/georoc/).

Sample No.	SIO_2	TIO_2	AL_2O_3	FEO_T	CAO	MGO	MNO	K_2O	NA_2O	P_2O_5
s_P34	49.68	2.86	15.30	12.23	7.16	3.42	0.22	1.98	4.54	1.24
s_P10	49.92	3.95	16.17	9.72	8.54	3.82	0.15	1.93	3.99	0.71

Table S2a. Trace element data (ppm) and radiogenic isotopic data of alkali lavas from the Pitcairn Gambier Chain (GEOROC; http://georoc.mpch-mainz.gwdg.de/georoc/).

Sample No.	LA	SM	GD	YB	$^{143}Nd/^{144}Nd$	$^{87}Sr/^{86}Sr$	$^{206}Pb/^{204}Pb$	$^{207}Pb/^{204}Pb$	$^{208}Pb/^{204}Pb$
s_V479.2	37.4	9.7	n.d.	1.6	n.d.	n.d.	19.51	15.57	39.13
s_V738.7	29.9	7.8	n.d.	1.5	n.d.	n.d.	19.62	15.64	39.38
s_K6375.0/s_K6-375.0	20.7	6.3	5.4	1.0	0.5129	0.7035	19.50	15.55	39.12
s_V397.0	29.1	7.7	n.d.	1.3	n.d.	n.d.	19.53	15.57	38.84
s_VI831.0	53.0	13.1	n.d.	2.5	0.5129	0.7035	n.d.	n.d.	n.d.
s_FR-635.5	43.8	11.3	n.d.	2.0	0.5129	0.7035	n.d.	n.d.	n.d.
s_V831.0	53.0	13.1	n.d.	2.5	n.d.	n.d.	19.45	15.58	39.18
s_516	19.0	5.7	5.7	1.5	n.d.	n.d.	n.d.	n.d.	n.d.
s_V850.2	52.3	12.8	n.d.	2.4	n.d.	n.d.	19.51	15.58	39.26
s_K6-624.0	21.7	6.5	n.d.	1.3	0.5129	0.7036	19.37	15.54	38.95
s_P20	n.d.	n.d.	n.d.	n.d.	0.5128	0.7036	18.42	15.49	38.91
s_PIT-8	30.5	6.4	6.2	1.7	0.5125	0.7046	17.90	15.49	38.98
s_PIT-11	31.7	6.7	6.1	1.7	0.5125	0.7046	17.86	15.48	38.94
s_VI359.2	n.d.	n.d.	n.d.	n.d.	0.5129	0.7034	n.d.	n.d.	n.d.
s_V359.2	57.7	14.6	n.d.	2.8	n.d.	n.d.	19.44	15.61	39.26
s_P12	n.d.	n.d.	n.d.	n.d.	0.5129	0.7035	18.43	15.50	38.88
s_P26	n.d.	n.d.	n.d.	n.d.	0.5129	0.7035	18.49	15.50	38.96
s_P9	n.d.	n.d.	n.d.	n.d.	0.5125	0.7047	17.80	15.48	38.84
s_P18	n.d.	n.d.	n.d.	n.d.	0.5129	0.7035	18.52	15.52	39.05
s_PIT-13	50.9	9.4	8.2	2.2	0.5125	0.7050	17.74	15.47	38.94
s_P11	n.d.	n.d.	n.d.	n.d.	0.5129	0.7035	18.45	15.49	38.90
s_P31	43.1	10.1	8.1	2.2	0.5129	0.7035	18.46	15.49	38.92
s_PI-376.0 / s_PI376.0	50.8	12.6		2.2	0.5129	0.7034	n.d.	n.d.	n.d.
s_P7	n.d.	n.d.	n.d.	n.d.	0.5125	0.7047	17.76	15.46	38.82
s_PIT-1	51.1	8.9	8.5	2.2	0.5124	0.7052	17.63	15.46	38.94
s_PIT-7	46.7	9.1	8.2	2.3	0.5126	0.7048	17.83	15.49	38.98
s_P3	n.d.	n.d.	n.d.	n.d.	0.5125	0.7047	17.78	15.48	38.87
s_P28	n.d.	n.d.	n.d.	n.d.	0.5129	0.7035	18.48	15.50	39.01
s_PIT-16	62.2	12.2	11.4	3.6	0.5126	0.7047	18.13	15.52	38.93
s_PIT-3	52.2	9.2	8.8	2.3	0.5124	0.7052	17.61	15.46	38.91
s_P8	n.d.	n.d.	n.d.	n.d.	0.5125	0.7049	17.64	15.46	38.73
s_P5	n.d.	n.d.	n.d.	n.d.	0.5126	0.7045	17.83	15.48	38.91
s_P4	63.5	13.0	9.9	2.7	0.5126	0.7045	17.83	15.49	38.90
s_PIT-4A	62.1	11.4	10.4	3.0	0.5125	0.7047	17.79	15.49	38.97
s_PIT-12	56.1	10.4	9.3	2.6	0.5125	0.7050	17.79	15.49	38.98
s_FR-469.4	73.9	17.5		3.2	0.5129	0.7036	n.d.	n.d.	n.d.
s_P30	n.d.	n.d.	n.d.	n.d.	0.5129	0.7035	18.40	15.50	38.90
s_PIT-6	67.8	13.8	13.2	3.7	0.5127	0.7037	18.05	15.51	39.06
s_P22	n.d.	n.d.	n.d.	n.d.	0.5129	0.7035	18.48	15.52	39.04
s_1	n.d.	n.d.	n.d.	n.d.	n.d.	n.d.	n.d.	n.d.	n.d.

Table S2b. Trace element data (ppm) and radiogenic isotopic data of alkali lavas from the Pitcairn Gambier Chain (GEOROC; http://georoc.mpch-mainz.gwdg.de/georoc/).

Sample No.	LA	SM	GD	YB	$^{143}Nd/^{144}Nd$	$^{87}Sr/^{86}Sr$	$^{206}Pb/^{204}Pb$	$^{207}Pb/^{204}Pb$	$^{208}Pb/^{204}Pb$
s_P34	n.d.	n.d.	n.d.	n.d.	0.5129	0.70350	18.42	15.50	38.97
s_P10	57.71	10.93	8.54	2.46	0.5124	0.70512	17.64	15.46	38.91

Table S3. Major element data (wt. %) of tholeiitic lavas from the Pitcairn Gambier Chain (GEOROC; http://georoc.mpch-mainz.gwdg.de/georoc/).

Sample No.	SIO_2	TIO_2	AL_2O_3	FEO_T	CAO	MGO	MNO	K_2O	NA_2O	P_2O_5
s_GAG1 [19648]	43.00	1.31	8.35	10.98	6.31	20.30	0.17	0.18	1.16	0.18
s_GMD60	44.61	1.20	7.19	12.72	5.26	25.59	0.18	0.29	1.05	0.18
s_G38	46.05	2.05	15.35	n.d.	11.90	7.04	0.15	0.20	2.07	0.26
s_GMD71	47.02	2.45	13.40	11.03	10.47	9.29	0.18	0.76	1.99	0.39
s_GMD58	47.16	2.27	15.48	11.20	10.77	7.21	0.18	0.12	2.04	0.35
s_GMD64	47.22	2.05	13.26	11.41	9.76	11.35	0.17	0.40	1.76	0.26
s_GMP7	47.54	2.37	14.29	10.36	11.12	7.93	0.16	0.61	2.22	0.35
s_FA682.7	47.60	2.26	13.22	10.10	11.82	8.62	0.14	0.32	2.10	0.30
s_GMD76	47.62	1.97	14.06	9.68	11.23	7.85	0.14	0.25	1.76	0.27
s_GMD62	47.66	2.33	15.63	10.30	10.87	7.81	0.16	0.49	1.95	0.33
s_GKM31	47.70	2.28	14.32	10.42	10.60	9.39	0.15	0.70	2.23	0.31
s_GMD56	47.80	2.25	12.61	10.76	10.72	11.86	0.17	0.63	1.88	0.32
s_FA608	47.96	3.00	14.03	10.75	11.17	6.02	0.15	0.73	2.65	0.44
s_GMD67	47.97	2.38	14.79	10.65	12.42	7.12	0.17	0.40	2.08	0.35
s_TS730.5	48.00	2.90	14.78	10.93	11.95	6.15	0.16	0.42	2.50	0.35
s_GMD72	48.11	2.09	15.3	10.14	10.90	7.19	0.16	0.43	2.00	0.34
s_GMD59	48.13	2.53	14.88	10.27	11.23	7.07	0.17	0.79	2.22	0.37
s_AK34H	48.22	2.84	14.66	12.04	10.20	5.64	0.17	0.53	2.67	0.42
s_GMD70	48.37	2.25	15.37	10.07	11.38	7.29	0.16	0.41	2.14	0.35
s_GMD66	48.39	1.97	14.12	11.13	11.18	8.98	0.17	0.43	2.00	0.28
s_AG29D	48.40	2.50	15.00	10.04	9.54	7.45	0.14	0.82	2.70	0.45
s_MG10E	48.51	3.14	14.60	11.74	10.48	6.14	0.17	0.70	2.60	0.49
s_GMD74	48.51	1.69	14.90	11.00	10.81	9.13	0.17	0.29	1.90	0.24
s_GMD68	48.52	1.59	15.66	10.74	11.17	8.11	0.17	0.31	1.89	0.23
s_KM7L	48.60	2.52	14.17	10.80	11.47	6.78	0.17	0.56	2.32	0.40
s_GAK38	49.00	2.07	15.10	10.26	12.60	7.30	0.15	0.25	2.11	0.24
s_GMD61	49.03	2.07	14.09	10.82	10.47	9.91	0.20	0.45	2.00	0.28
s_TR14S	49.18	3.08	14.71	10.86	10.54	5.55	0.15	0.95	2.6	0.49
s_GMD52	49.38	1.74	15.07	9.60	11.52	7.40	0.15	0.32	2.02	0.22
s_G44*	49.45	2.31	15.15	n.d.	10.96	6.37	0.17	0.38	2.26	0.27
s_G-MD-73/ s_GMD73	49.52	1.97	15.18	10.00	11.44	7.84	0.15	0.27	1.99	0.29
s_GMD54	n.d.	n.d.	n.d.	n.d.	n.d.	n.d.	n.d.	n.d.	n.d.	n.d.
s_GMD64	n.d.	n.d.	n.d.	n.d.	n.d.	n.d.	n.d.	n.d.	n.d.	n.d.
s_GKM31	n.d.	n.d.	n.d.	n.d.	n.d.	n.d.	n.d.	n.d.	n.d.	n.d.
s_GMD62	n.d.	n.d.	n.d.	n.d.	n.d.	n.d.	n.d.	n.d.	n.d.	n.d.
s_GMD74	n.d.	n.d.	n.d.	n.d.	n.d.	n.d.	n.d.	n.d.	n.d.	n.d.

Table S4. Trace element data (ppm) and radiogenic isotopic data of tholeiitic lavas from the Pitcairn Gambier Chain (GEOROC; http://georoc.mpch-mainz.gwdg.de/georoc/).

Sample No.	LA	SM	GD	YB	$^{143}Nd/^{144}Nd$	$^{87}Sr/^{86}Sr$	$^{206}Pb/^{204}Pb$	$^{207}Pb/^{204}Pb$	$^{208}Pb/^{204}Pb$
s_GAG1]	10.0	3.1	2.8	0.9	0.5130	0.7030	19.20	15.56	38.98
s_GMD60	11.6	3.3	3.6	1.0	0.5130	0.7032	18.98	15.56	38.95
s_G38	13.9	4.5	5.0	1.6	0.5130	0.7032	19.12	15.55	39.03
s_GMD71	23.3	6.3	5.9	1.8	0.5129	0.7031	18.86	15.57	39.18
s_GMD58	16.7	5.2	4.8	1.5	0.5130	0.7030	19.01	15.55	39.00
s_GMD64	13.2	4.5	4.3	1.4	0.5130	0.7032	19.08	15.55	38.99
s_GMP7	19.5	5.5	5.3	1.6	0.5129	0.7031	19.11	15.56	39.05
s_FA682.7	14.8	4.7	n.d.	1.4	0.5130	0.7030	19.40	15.56	39.03
s_GMD76	13.1	4.3	4.2	1.3	0.5130	0.7030	19.28	15.56	39.02
s_GMD62	17.4	5.3	5.2	1.6	0.5130	0.7031	19.09	15.56	39.05
s_GKM31	18.5	5.3	4.9	1.6	0.5130	0.7030	19.18	15.56	39.08
s_GMD56	19.2	5.3	5.0	1.4	0.5130	0.7032	19.00	15.56	39.00
s_FA608	24.0	6.7	n.d.	1.7	0.5129	0.7028	19.38	15.54	38.98
s_GMD67	16.8	5.5	5.3	1.7	0.5129	0.7031	19.16	15.56	39.10
s_TS730.5	20.0	5.5	n.d.	1.8	0.5129	0.7030	19.49	15.60	39.23
s_GMD72	19.4	5.2	5.0	1.6	0.5130	0.7031	19.16	15.56	39.13
s_GMD59	25.6	6.8	6.3	2.0	0.5130	0.7031	18.85	15.54	39.01
s_AK34H	20.1	6.3	n.d.	2.2	0.5130	0.7031	18.99	15.57	38.99
s_GMD70	18.6	5.6	5.3	1.7	0.5130	0.7030	19.07	15.56	39.08
s_GMD66	13.8	4.4	4.4	1.4	0.5129	0.7032	19.07	15.56	39.05
s_AG29D	22.5	6.2	n.d.	1.8	0.5130	0.7029	19.08	15.55	38.95
s_MG10E	30.0	7.7	n.d.	2.3	0.5130	0.7029	19.09	15.55	39.05
s_GMD74	10.5	3.7	3.8	1.2	0.5130	0.7032	19.04	15.56	38.93
s_GMD68	11.4	3.7	3.9	1.4	0.5130	0.7033	19.03	15.56	38.98
s_KM7L	19.9	6.1	n.d.	1.8	0.5130	0.7031	19.20	15.55	39.05
s_GAK38	14.1	4.6	4.4	1.5	0.5130	0.7030	19.37	15.57	39.10
s_GMD61	16.8	5.0	4.9	1.6	0.5129	0.7032	19.20	15.57	39.16
s_TR14S	24.7	7.1	n.d.	2.1	0.5130	0.7032	19.17	15.56	39.11
s_GMD52	10.8	3.9	3.9	1.3	0.5130	0.7029	19.05	15.55	38.96
s_G44*	27.4	7.1	8.8	2.8	0.5130	0.7030	19.38	15.57	39.11
s_G-MD-73/ s_GMD73	12.8	4.4	4.3	1.4	0.5130	0.7030	19.05	15.55	38.99
s_GMD54	21.8	5.7	5.7	1.7	0.5130	0.7030	19.01	15.56	39.01
s_GMD64	13.3	4.5	4.4	1.3	0.5130	0.7032	n.d.	n.d.	n.d.
s_GKM31	n.d.	n.d.	n.d.	n.d.	n.d.	0.7030	19.18	15.56	39.07
s_GMD62	n.d.	n.d.	n.d.	n.d.	0.5130	0.7031	n.d.	n.d.	n.d.
s_GMD74	n.d.	n.d.	n.d.	n.d.	n.d.	n.d.	19.05	15.56	38.95

Table S5a. Major element data (wt. %) alkali lavas from Hawai'ian (GEOROC; http://georoc.mpch-mainz.gwdg.de/georoc/).

Sample No.	SIO_2	TIO_2	AL_2O_3	FEO_T	CAO	MGO	MNO	K_2O	NA_2O	P_2O_5
s_K208-2B	48.48	3.73	13.90	12.71	11.06	5.86	0.17	0.85	2.89	0.36
s_S709-5	47.49	4.10	14.77	11.90	10.87	5.66	0.18	0.92	3.29	0.51
s_K208-3	48.27	3.65	13.74	13.16	10.82	6.19	0.20	0.83	2.80	0.35
s_K208-7	46.53	4.03	14.52	13.81	10.48	6.36	0.17	0.89	2.87	0.34
s_S509-4B	43.38	5.77	14.97	15.54	8.17	6.46	0.20	1.27	3.57	0.68
s_S709-4	47.91	3.52	14.50	11.84	11.62	6.51	0.20	0.73	2.78	0.40
s_S709-9	45.39	4.81	14.17	13.49	11.71	6.93	0.20	0.54	2.45	0.31
s_K207-19	47.25	3.13	13.85	12.79	10.03	9.35	0.16	0.58	2.56	0.31
s_S505-10B	45.20	3.43	11.87	13.57	9.93	11.93	0.18	1.51	2.04	0.34
s_02AKA-7	48.42	3.32	14.04	12.00	9.85	4.78	0.17	0.85	3.15	0.50
s_02AKA-5	46.90	3.17	13.06	11.98	10.65	7.75	0.18	0.80	2.78	0.49
s_KH14	47.31	3.06	15.02	12.03	11.19	6.16	0.17	0.74	3.28	0.44
s_KH11	47.99	3.08	15.97	12.31	10.70	6.49	0.20	0.80	2.80	0.42
s_C-70	47.48	2.63	17.42	n.d.	8.54	6.74	0.18	1.20	3.12	0.36
s_MG1	47.89	3.75	14.77	12.25	9.47	5.18	0.19	0.98	3.36	0.61
s_MG1B	48.25	3.21	16.30	11.28	9.51	4.59	0.16	0.95	3.32	0.68
s_MG3B	47.00	2.90	15.69	11.96	10.82	6.39	0.18	0.71	2.70	0.39
s_02AMK-3	47.96	3.30	14.17	13.08	10.77	5.74	0.19	0.80	2.94	0.41
s_02AMK-13	47.15	2.96	15.11	12.19	11.46	5.80	0.18	0.75	2.76	0.36
s_02AMK-7	46.54	3.79	13.80	12.98	9.61	5.88	0.19	1.27	3.39	0.64
s_02AMK-2	47.92	3.17	14.09	12.37	10.85	5.92	0.18	0.81	2.88	0.38
s_MU-16	47.53	3.11	14.91	12.11	10.97	5.82	0.17	0.80	2.50	0.39
s_MU-5	45.93	3.28	14.32	12.14	10.18	7.93	0.17	0.88	2.80	0.41
s_C-78	41.83	3.16	14.32	n.d.	8.83	9.42	0.19	0.77	1.83	0.29
s_R164-1.55 / s_R164	46.25	3.88	14.65	12.63	10.70	6.25	0.19	0.74	3.09	0.35
s_R160-5.75 / s_R160	45.95	3.22	11.89	12.74	10.45	11.20	0.19	0.42	2.38	0.32
s_R166-5.25/ s_R166(WC) / s_R166	45.74	4.04	14.91	13.52	10.03	6.08	0.20	0.75	2.93	0.38
s_R167-1.30/ s_R167	45.92	3.98	14.63	13.26	10.29	6.30	0.19	0.77	3.01	0.38
s_R177-2.60/ s_R177	43.68	3.96	14.39	13.79	9.77	8.21	0.19	0.84	3.24	0.47
s_HK-58	42.97	3.09	11.58	13.34	12.30	11.27	0.18	0.75	2.11	0.43
s_H85-22	44.30	3.66	15.87	13.70	10.61	5.65	0.22	1.04	3.46	0.46
s_H85-23	44.14	3.65	15.70	13.71	10.64	5.78	0.23	1.01	3.41	0.45
s_H85-7	44.94	3.63	14.54	13.50	11.07	5.90	0.20	0.99	3.20	0.45
s_H85-8	44.97	3.55	14.56	13.21	11.35	5.92	0.20	0.91	2.74	0.42
s_H85-10	45.18	3.53	14.54	13.36	11.17	6.28	0.20	0.89	2.48	0.43

Table S5b. Major element data (wt. %) alkali lavas from Hawai'ian (GEOROC; http://georoc.mpch-mainz.gwdg.de/georoc/).

Sample No.	SIO_2	TIO_2	AL_2O_3	FEO_T	CAO	MGO	MNO	K_2O	NA_2O	P_2O_5
s_H85-14	45.61	3.41	15.61	12.22	10.73	6.44	0.20	1.02	2.77	0.44
s_H85-15	45.17	3.10	15.27	11.98	11.02	7.56	0.18	0.88	2.38	0.38
s_H85-21	43.90	3.23	14.55	13.90	11.35	8.40	0.22	0.76	1.90	0.41
s_H65-4	44.04	3.12	14.28	13.84	11.04	8.23	0.20	0.86	2.74	0.39
s_HK-50	41.68	3.82	14.63	14.19	12.90	6.16	0.20	0.96	3.08	0.43
s_HK-36	42.82	3.68	15.18	14.07	10.39	6.76	0.22	0.99	3.40	0.50
s_HK-29	47.02	3.59	16.19	11.94	7.85	4.68	0.22	1.32	4.57	0.60
s_HK-46	46.56	3.74	16.43	11.96	8.28	4.69	0.24	1.32	4.38	0.58
s_HK-1	45.54	3.94	14.47	14.03	10.38	5.16	0.21	1.04	3.23	0.48
s_H85-33	45.97	4.03	16.83	12.08	8.62	4.68	0.24	1.40	4.27	0.62
s_H85-11	45.16	4.30	15.62	13.53	8.60	4.95	0.21	1.51	3.70	0.71
s_H85-13	45.76	4.29	14.64	13.73	10.09	4.67	0.22	1.16	3.12	0.55
s_H85-12	45.57	4.03	14.74	13.46	10.09	5.18	0.22	1.23	3.29	0.56
s_H85-1	45.87	4.84	13.81	14.34	9.51	5.19	0.20	1.09	3.41	0.56
s_HK-31	45.02	3.68	15.63	13.37	9.66	4.82	0.22	1.23	4.23	0.54
s_HK-45	46.04	3.68	14.96	12.98	10.06	4.83	0.23	1.14	3.58	0.50
s_C-124	46.61	3.72	14.37	12.84	10.27	5.62	0.18	0.64	3.44	0.42
s_HO-20	46.22	3.11	14.76	12.32	9.88	7.99	0.19	0.35	2.58	0.35
s_HO-14	45.98	3.44	14.10	12.56	9.87	8.21	0.20	0.43	2.82	0.34
s_HO-19	47.04	3.76	14.71	12.92	10.12	5.61	0.21	0.45	2.82	0.45
s_HO-12	46.52	3.04	14.09	12.17	10.18	8.84	0.17	0.51	2.80	0.34
s_C-126	45.85	2.43	14.82	n.d.	10.27	9.36	0.18	0.40	2.45	0.40
s_HK-33	45.04	3.68	15.79	13.52	9.93	4.84	0.21	1.20	3.92	0.54

Table S6a. Trace element data (ppm) and radiogenic isotopic data of alkali lavas Hawai'ian (GEOROC; http://georoc.mpch-mainz.gwdg.de/georoc/).

Sample No.	LA	SM	GD	YB	$^{143}Nd/^{144}Nd$	$^{87}Sr/^{86}Sr$	$^{206}Pb/^{204}Pb$	$^{207}Pb/^{204}Pb$	$^{208}Pb/^{204}Pb$
s_K208-2B	18.1	7.0	7.3	2.3	n.d.	0.7035	18.68	15.50	38.26
s_S709-5	24.0	9.2	9.4	2.8	0.5129	0.7036	18.72	15.51	38.33
s_K208-3	18.2	7.4	7.7	2.6	0.5129	0.7036	18.70	15.51	38.33
s_K208-7	19.1	7.6	7.7	2.4	0.5130	0.7035	18.68	15.49	38.24
s_S509-4B	30.4	10.5	10.3	2.8	0.5129	0.7035	18.69	15.50	38.26
s_S709-4	19.2	7.7	8.1	2.5	0.5129	0.7036	18.69	15.51	38.32
s_S709-9	14.9	7.2	7.9	2.5	0.5130	0.7036	18.72	15.51	38.32
s_K207-19	14.3	5.9	6.2	2.1	0.5130	0.7035	18.43	15.48	38.18
s_S505-10B	20.6	6.6	6.5	1.9	0.5130	0.7036	18.64	15.50	38.31
s_02AKA-7	25.6	8.2	7.9	2.5	0.5130	0.7036	18.31	15.48	37.92
s_02AKA-5	25.3	8.1	7.9	2.5	0.5130	0.7036	18.29	15.48	37.90
s_KH14	n.d.	7.5	n.d.	2.3	0.5130	0.7036	n.d.	n.d.	n.d.
s_KH11	n.d.	8.2	n.d.	2.5	0.5130	0.7036	n.d.	n.d.	n.d.
s_C-70	n.d.	10.2	n.d.	n.d.	0.5130	0.7036	18.21	15.46	37.83
s_MG1	n.d.	10.0	n.d.	3.2	0.5130	0.7037	18.22	15.47	37.86
s_MG1B	n.d.	11.6	11.1	4.0	0.5130	0.7036	n.d.	n.d.	n.d.
s_MG3B	n.d.	7.5	7.5	2.4	0.5130	0.7036	n.d.	n.d.	n.d.
s_02AMK-3	22.4	7.3	6.9	2.1	0.5130	0.7035	18.41	15.48	37.99
s_02AMK-13	22.5	7.0	6.7	1.9	0.5130	0.7035	18.41	15.48	37.98
s_02AMK-7	36.1	9.7	9.0	2.4	0.5130	0.7035	18.38	15.48	37.97
s_02AMK-2	19.1	6.6	6.5	2.0	0.5130	0.7036	18.42	15.49	38.01
s_MU-16	21.5	6.8	n.d.	2.0	0.5130	0.7035	18.36	15.46	37.92
s_MU-5	23.7	8.1	n.d.	2.4	0.5130	0.7035	18.42	15.47	38.01
s_C-78	n.d.	n.d.	n.d.	n.d.	n.d.	n.d.	18.42	15.47	38.00
s_R164-1.55 / s_R164	20.6	7.9	8.1	2.4	n.d.	0.7035	18.38	15.48	37.97
s_R160-5.75 / s_R160	18.9	7.4	7.7	2.3	n.d.	n.d.	18.42	15.48	38.00
s_R166-5.25/ s_R166(WC) / s_R166	20.3	7.4	7.5	2.2	n.d.	0.7035	18.41	15.48	37.98
s_R167-1.30/ s_R167	21.2	7.5	n.d.	2.3	n.d.	0.7035	18.41	15.48	37.99
s_R177-2.60/ s_R177	26.1	10.4	10.6	2.8	n.d.	n.d.	18.44	15.48	38.02
s_HK-58	25.8	6.8	n.d.	1.3	n.d.	0.7031	18.18	15.45	37.75
s_H85-22	30.7	7.8	n.d.	2.1	0.5131	0.7033	18.29	15.46	37.90
s_H85-23	30.8	7.7	n.d.	2.2	0.5130	0.7032	n.d.	n.d.	n.d.
s_H85-7	25.5	8.2	n.d.	2.1	0.5130	0.7035	n.d.	n.d.	n.d.
s_H85-8	24.7	8.0	n.d.	2.2	0.5130	0.7034	n.d.	n.d.	n.d.
s_H85-10	24.9	8.0	n.d.	2.1	0.5130	0.7034	18.34	15.48	37.97

Table S6b. Trace element data (ppm) and radiogenic isotopic data of alkali lavas Hawai'ian (GEOROC; http://georoc.mpch-mainz.gwdg.de/georoc/).

Sample No.	LA	SM	GD	YB	$^{143}Nd/^{144}Nd$	$^{87}Sr/^{86}Sr$	$^{206}Pb/^{204}Pb$	$^{207}Pb/^{204}Pb$	$^{208}Pb/^{204}Pb$
s_H85-14	27.7	8.1	n.d.	2.0	0.5131	0.7034	n.d.	n.d.	n.d.
s_H85-15	24.5	7.3	n.d.	2.1	0.5130	0.7034	n.d.	n.d.	n.d.
s_H85-21	25.4	6.9	n.d.	1.9	0.5131	0.7033	n.d.	n.d.	n.d.
s_H65-4	25.9	6.9	n.d.	1.9	0.5130	0.7033	18.36	15.47	37.99
s_HK-50	27.4	7.7	n.d.	1.5	n.d.	0.7031	18.27	15.50	37.93
s_HK-36	28.9	7.9	n.d.	2.0	n.d.	0.7032	18.32	15.47	37.91
s_HK-29	38.1	9.9	n.d.	2.6	n.d.	0.7033	18.40	15.51	38.08
s_HK-46	36.9	9.5	n.d.	2.5	n.d.	0.7032	18.34	15.47	37.94
s_HK-1	29.6	9.1	n.d.	2.5	n.d.	0.7034	18.32	15.49	37.96
s_H85-33	39.5	9.2	n.d.	2.3	0.5130	0.7032	n.d.	n.d.	n.d.
s_H85-11	39.6	11.1	n.d.	2.8	0.5130	0.7034	n.d.	n.d.	n.d.
s_H85-13	32.6	10.3	n.d.	2.7	0.5131	0.7033	n.d.	n.d.	n.d.
s_H85-12	32.9	10.0	n.d.	2.6	0.5130	0.7034	n.d.	n.d.	n.d.
s_H85-1	27.7	9.3	n.d.	2.7	0.5130	0.7034	18.36	15.49	38.01
s_HK-31	35.4	9.6	n.d.	2.3	n.d.	0.7032	18.31	15.47	37.93
s_HK-45	33.3	9.2	n.d.	2.4	n.d.	0.7033	18.33	15.51	38.02
s_C-124	19.7	8.7	n.d.	2.7	0.5129	0.7037	18.27	15.48	37.99
s_HO-20	16.4	7.3	n.d.	2.3	0.5129	0.7038	n.d.	n.d.	n.d.
s_HO-14	15.5	7.1	n.d.	2.3	0.5130	0.7037	n.d.	n.d.	n.d.
s_HO-19	19.3	8.4	n.d.	2.5	0.5130	0.7038	18.28	15.48	38.00
s_HO-12	15.6	6.8	n.d.	2.1	0.5130	0.7036	18.31	15.46	37.93
s_C-126	15.4	6.6	n.d.	2.6	0.5130	0.7038	n.d.	n.d.	n.d.
s_HK-33	35.2	9.1	n.d.	2.4	n.d.	0.7033	18.31	15.48	37.94

Table S7a. Major element data (wt. %) tholeiitic lavas from Hawai'ian (GEOROC; http://georoc.mpch-mainz.gwdg.de/georoc/).

Sample No.	SIO_2	TIO_2	AL_2O_3	FEO_T	CAO	MGO	MNO	K_2O	NA_2O	P_2O_5
s_R185-3.95 / s_R185	49.25	2.89	13.22	11.59	10.92	7.43	0.18	0.56	2.51	0.31
s_K214-3	44.51	1.28	6.89	n.d.	6.07	26.22	0.18	0.17	0.99	0.14
s_S692-13	49.60	1.96	12.90	10.26	10.30	9.26	0.15	0.49	2.11	0.23
s_S692-15	49.70	1.89	12.50	10.71	9.91	11.10	0.17	0.35	2.02	0.22
s_S692-14	49.40	1.83	12.00	10.80	9.55	12.40	0.17	0.37	1.93	0.21
s_S690-1D	51.61	2.25	13.67	n.d.	10.58	6.33	0.16	0.63	2.48	0.26
s_K219-9	49.48	1.58	9.90	n.d.	8.01	17.95	0.17	0.25	1.70	0.15
s_S690-1B	48.73	1.59	9.30	n.d.	7.72	19.56	0.15	0.29	1.65	0.14
s_K218-5	46.42	1.18	7.15	n.d.	5.96	25.91	0.16	0.23	1.22	0.12
s_K218-1	46.30	1.15	6.99	n.d.	5.86	26.33	0.16	0.22	1.19	0.12
s_S690-3A	51.27	2.22	13.97	11.40	10.49	6.07	0.15	0.66	2.52	0.26
s_S690-3D	51.73	2.26	13.95	11.37	10.51	6.32	0.16	0.57	2.46	0.27
s_S690-2C	51.74	2.22	14.02	11.35	10.64	6.47	0.16	0.58	2.46	0.26
s_S690-4B	51.09	2.16	13.82	11.00	10.56	6.63	0.16	0.55	2.43	0.25
s_S690-8B	47.64	1.47	8.78	10.58	7.22	20.57	0.17	0.33	1.40	0.13
s_S690-7A	50.04	1.87	11.35	10.64	9.24	13.34	0.16	0.32	1.90	0.17
s_S690-8A	47.98	1.50	9.07	10.53	7.44	20.01	0.15	0.28	1.53	0.14
s_S690-6A	47.38	1.37	8.17	10.48	6.74	22.94	0.16	0.29	1.32	0.12
s_K219-R2/ s_K219-2	49.61	1.75	9.93	10.70	8.26	17.57	0.16	0.31	1.71	0.16
s_K218-R14	46.90	1.26	7.69	10.50	6.39	24.25	0.16	0.22	1.29	0.13
s_K218-13/ s_K218-R13	46.68	1.22	7.39	10.50	6.15	25.20	0.16	0.21	1.23	0.12
s_K219-R3/ s_K219-3	52.50	2.19	14.40	10.00	10.97	6.22	0.16	0.34	2.33	0.22
s_K218-R7 / s_K218-7	51.90	2.27	14.10	10.70	10.82	6.22	0.17	0.39	2.28	0.25
s_K218-R12/ s_K218-12	51.70	2.23	14.10	10.70	10.84	6.39	0.17	0.38	2.26	0.24
s_K218-R9A / s_K218-9A	51.90	2.20	14.10	10.60	10.90	6.39	0.16	0.38	2.27	0.24
s_K218-R8/ s_K218-8	52.00	2.20	14.20	10.60	10.93	6.40	0.16	0.37	2.29	0.25

Table S7b. Major element data (wt. %) tholeiitic lavas from Hawai'ian (GEOROC; http://georoc.mpch-mainz.gwdg.de/georoc/).

Sample No.	SIO_2	TIO_2	AL_2O_3	FEO_T	CAO	MGO	MNO	K_2O	NA_2O	P_2O_5
s_K218-R2A/ s_K218-2A	51.80	2.30	14.20	10.60	10.83	6.42	0.17	0.39	2.29	0.24
s_K219-R8/ s_K219-8	52.30	2.18	14.30	10.10	10.85	6.81	0.16	0.32	2.32	0.21
s_K219-R7/ s_K219-7	52.40	2.16	14.40	10.10	10.83	6.92	0.17	0.32	2.20	0.22
s_K219-R5/ s_K219-5	52.20	2.10	14.20	10.20	10.72	7.21	0.17	0.31	2.24	0.21
s_K219-R1/ s_K219-1	51.90	2.24	13.70	10.60	10.66	7.45	0.17	0.34	2.19	0.22
s_S507-1B	49.54	1.84	12.00	11.44	9.80	11.06	0.15	0.29	1.91	0.17
s_S507-5B	46.20	1.36	8.09	11.48	6.75	22.54	0.15	0.20	1.23	0.12
s_ML-52	51.34	2.11	13.72	10.64	10.24	7.33	0.16	0.44	2.12	0.26
s_ML-126	51.58	2.10	13.77	11.10	10.61	6.50	0.17	0.39	2.29	0.23
s_HW35	51.75	2.20	13.81	n.d.	10.57	6.81	0.17	0.47	2.41	0.27
s_HW33	52.03	2.07	13.81	n.d.	10.65	7.02	0.17	0.42	2.28	0.24
s_HW32	52.01	2.11	13.70	n.d.	10.67	7.20	0.17	0.37	2.30	0.22
s_HW31	51.87	2.10	13.69	n.d.	10.65	7.25	0.17	0.37	2.28	0.22
s_HW34	50.57	2.05	12.81	n.d.	10.02	9.58	0.17	0.40	2.15	0.23
s_HW30	49.76	1.88	10.96	n.d.	8.75	14.80	0.17	0.32	1.83	0.18
s_NE-45	51.88	2.23	13.68	10.85	10.37	6.31	0.17	0.47	2.57	0.27
s_L77-44	52.09	2.31	13.71	10.63	10.64	6.75	0.17	0.37	2.17	0.24
s_L00-520	51.89	2.05	13.74	10.79	10.55	6.85	0.18	0.38	2.29	0.23
s_L00-521	51.89	2.04	13.70	10.75	10.41	6.95	0.17	0.40	2.35	0.24
s_NE-19	52.31	2.14	14.09	10.30	10.67	6.96	0.17	0.44	2.18	0.28
s_L87-93A	51.51	2.05	13.74	10.99	10.28	7.05	0.17	0.40	2.18	0.25
s_NE-30	51.66	2.10	13.21	10.73	9.82	8.04	0.17	0.44	1.97	0.27
s_L80-90	51.52	2.01	13.12	10.55	10.26	8.51	0.17	0.45	2.10	0.26
s_L93-231	51.20	2.17	12.85	10.84	9.75	9.04	0.17	0.48	2.11	0.29
s_L88-29	50.35	1.98	12.08	10.82	9.59	11.26	0.17	0.30	2.09	0.19

Table S7c. Major element data (wt. %) tholeiitic lavas from Hawai'ian (GEOROC; http://georoc.mpch-mainz.gwdg.de/georoc/).

Sample No.	SIO_2	TIO_2	AL_2O_3	FEO_T	CAO	MGO	MNO	K_2O	NA_2O	P_2O_5
s_L00-05	50.54	1.92	11.98	10.81	9.46	11.80	0.17	0.30	1.93	0.20
s_SW-70	51.52	1.91	12.74	10.74	9.64	9.33	0.16	0.41	2.35	0.25
s_ML-07-KWWS-92/ s_ML-07	51.40	2.06	13.32	12.21	10.35	8.53	0.17	0.41	2.24	0.24
s_ML-61-KWWS-92 / s_ML-61	51.37	2.09	13.45	12.28	10.53	7.13	0.17	0.38	2.36	0.22
s_M27-11	51.60	2.45	13.40	11.54	10.75	6.25	0.17	0.44	2.41	0.28
s_ML-83	50.97	2.04	12.71	10.87	9.96	9.18	0.16	0.40	2.09	0.24
s_36 / s_KAH 36	51.44	2.09	14.24	10.39	11.14	7.25	0.17	0.25	2.39	0.24
s_61 / s_KAH 6	52.97	2.35	14.56	10.72	7.36	6.13	0.40	1.63	3.27	0.54
s_62 / s_KAH 62	51.49	2.45	14.93	10.99	7.32	6.74	0.16	1.38	3.27	0.47
s_114 / s_KAH 114	52.88	2.48	13.53	11.42	10.13	6.14	0.19	0.52	2.43	0.32
s_113/ s_KAH 113	52.65	2.21	13.92	10.59	10.68	6.62	0.16	0.39	2.31	0.23
s_39 / s_KAH 39	51.79	2.75	14.71	10.99	9.58	5.60	0.16	0.80	3.11	0.37
s_111 / s_KAH 111	51.29	2.71	14.86	10.80	9.38	5.65	0.16	0.75	3.04	0.34
s_KW-14	51.96	2.47	14.91	10.50	7.22	5.93	0.16	1.38	3.55	0.49
s_50 / s_KAH 50	51.73	2.81	13.52	11.95	9.47	5.43	0.17	0.71	3.00	0.29
s_127 / s_KAH 127	52.09	2.39	14.78	10.45	10.48	6.20	0.16	0.52	2.60	0.27
s_41/ s_KAH 41	51.22	2.51	14.53	10.88	10.22	6.48	0.17	0.30	2.63	0.28
s_N44 / s_KAH N44	51.80	2.74	13.78	11.85	9.45	6.88	0.16	0.39	2.48	0.26
s_158/ s_KAH 158	51.37	2.56	14.08	11.64	9.51	6.99	0.17	0.45	2.63	0.26
s_159/ s_KAH 159	51.25	2.53	13.86	11.53	9.65	7.02	0.17	0.48	2.44	0.27
s_126/ s_KAH 126	51.49	1.78	13.08	11.14	9.41	10.44	0.17	0.33	2.23	0.21
s_125 / s_KAH 125	51.37	1.83	13.07	11.38	9.16	10.63	0.17	0.34	2.22	0.19
s_KW-1	50.75	2.44	14.09	11.76	10.28	6.82	0.18	0.31	2.45	0.21
s_KW-5	49.35	2.53	14.44	11.33	11.13	7.52	0.17	0.28	2.54	0.23

Table S7d. Major element data (wt. %) tholeiitic lavas from Hawai'ian (GEOROC; http://georoc.mpch-mainz.gwdg.de/georoc/).

Sample No.	SIO_2	TIO_2	AL_2O_3	FEO_T	CAO	MGO	MNO	K_2O	NA_2O	P_2O_5
s_KW-25	49.69	1.84	10.75	11.87	8.38	15.27	0.17	0.34	1.83	0.19
s_KW-19	50.25	2.51	14.09	11.10	9.94	6.13	0.17	0.56	2.62	0.33
s_KW-23	49.98	1.77	12.04	12.42	8.50	11.15	0.18	0.39	2.18	0.24
s_0X078	51.46	2.28	15.00	10.70	9.70	5.40	0.17	0.41	2.47	0.26
s_0X067	51.21	2.38	14.30	10.70	9.90	6.90	0.19	0.47	2.42	0.28
s_0X068	50.64	2.22	14.50	10.80	9.50	7.60	0.19	0.35	2.25	0.25
s_0X069	50.19	1.76	14.60	10.30	9.00	8.50	0.18	0.32	2.36	0.20
s_88 / s_KSDPUNIT 88/ s_KSDP UNIT 88	48.89	1.80	12.60	11.21	8.19	13.02	0.26	0.19	2.03	0.17
s_27/ s_KSDPUNIT 27 / s_KSDP UNIT 27	51.76	2.22	14.09	10.20	10.55	6.88	0.17	0.32	2.35	0.24
s_41 / s_KSDPUNIT 41/ s_KSDP UNIT 41	50.63	2.39	13.41	11.10	10.72	7.38	0.18	0.32	2.34	0.23
s_34 / s_KSDPUNIT 34 / s_KSDP UNIT 34	50.48	2.14	12.96	10.91	10.07	9.64	0.18	0.28	2.22	0.20
s_38/ s_KSDPUNIT 38 / s_KSDP UNIT 38	51.21	2.32	13.50	10.90	10.59	7.60	0.18	0.31	2.23	0.22
s_68/ s_KSDPUNIT 68/ s_KSDP UNIT 68	50.80	1.98	12.84	10.52	9.39	10.09	0.17	0.26	2.48	0.18
s_76 / s_KSDPUNIT 76 / s_KSDP UNIT 76	48.66	2.32	13.25	11.19	10.68	9.62	0.19	0.18	2.34	0.12
s_1 / s_KSDPUNIT 1 / s_KSDP UNIT 1	49.34	1.59	11.32	10.55	8.20	15.42	0.17	0.27	1.94	0.18
s_9 / s_KSDPUNIT 9 / s_KSDP UNIT 9	52.60	1.70	13.22	10.20	9.18	9.19	0.17	0.26	2.38	0.17
s_57 / s_KSDPUNIT 57/ s_KSDP UNIT 57	51.05	2.35	13.77	10.70	10.60	7.37	0.18	0.36	2.44	0.23

Table S7e. Major element data (wt. %) tholeiitic lavas from Hawai'ian (GEOROC; http://georoc.mpch-mainz.gwdg.de/georoc/).

Sample No.	SIO_2	TIO_2	AL_2O_3	FEO_T	CAO	MGO	MNO	K_2O	NA_2O	P_2O_5
s_54 / s_KSDPUNIT 54/ s_KSDP UNIT 54	51.25	2.40	13.78	10.62	10.72	6.95	0.18	0.40	2.53	0.25
s_24 / s_KSDPUNIT 24 / s_KSDP UNIT 24	52.20	2.13	13.74	10.47	10.05	7.18	0.17	0.37	2.42	0.23
s_6 / s_KSDPUNIT 6 / s_KSDP UNIT 6	50.14	1.54	11.22	10.37	7.87	15.07	0.16	0.29	1.89	0.18
s_49 / s_KSDPUNIT 49 / s_KSDP UNIT 49	51.25	2.18	13.62	10.61	10.65	7.41	0.18	0.34	2.47	0.21
s_46/ s_KSDPUNIT 46/ s_KSDP UNIT 46	51.36	2.26	13.61	10.51	10.44	7.58	0.17	0.38	2.43	0.23
s_62/ s_KSDPUNIT 62 / s_KSDP UNIT 62	50.93	2.23	12.98	10.77	10.23	8.68	0.18	0.38	2.33	0.23
s_8 / s_KSDPUNIT 8 / s_KSDP UNIT 8	50.40	1.97	12.08	10.67	9.25	11.53	0.17	0.38	2.11	0.23
s_61 / s_KSDPUNIT 61 / s_KSDP UNIT 61	51.27	2.29	13.79	10.54	10.23	7.34	0.17	0.42	2.57	0.25
s_17/ s_KSDPUNIT 17/ s_KSDP UNIT 17	50.97	2.30	13.75	10.84	10.49	7.51	0.17	0.42	2.23	0.25
s_74 / s_KSDPUNIT 74 / s_KSDP UNIT 74	52.15	2.14	13.95	10.29	10.33	7.23	0.17	0.31	2.25	0.18
s_51 / s_KSDPUNIT 51 s_KSDP UNIT 51	51.45	2.25	13.77	10.47	10.40	7.56	0.17	0.36	2.31	0.20
s_15 / s_KSDPUNIT 15 / s_KSDP UNIT 15	50.97	2.02	12.86	11.05	9.62	9.49	0.17	0.40	2.20	0.22
s_66 / s_KSDPUNIT 66 / s_KSDP UNIT 66	51.23	2.09	13.03	10.33	9.92	8.60	0.17	0.42	2.46	0.22
s_20 / s_KSDPUNIT 20 / s_KSDP UNIT 20	49.13	1.94	11.47	11.05	8.95	13.66	0.17	0.44	1.85	0.22
s_71 / s_KSDPUNIT 71 / s_KSDP UNIT 71	51.97	2.06	13.71	10.40	10.02	8.17	0.18	0.31	2.17	0.15

Table S8a. Trace element data (ppm) and radiogenic isotopic data of tholeiitic lavas Hawai'ian (GEOROC; http://georoc.mpch-mainz.gwdg.de/georoc/).

Sample No.	LA	SM	GD	YB	$^{143}Nd/^{144}Nd$	$^{87}Sr/^{86}Sr$	$^{206}Pb/^{204}Pb$	$^{207}Pb/^{204}Pb$	$^{208}Pb/^{204}Pb$
s_R185-3.95 / s_R185	14.8	6.5	n.d.	2.2	0.5130	0.7035	18.43	15.49	38.01
s_K214-3	n.d.	n.d.	n.d.	n.d.	0.5130	0.7037	18.70	15.50	38.29
s_S692-13	11.0	n.d.	n.d.	n.d.	0.5129	0.7038	18.20	15.45	37.98
s_S692-15	11.0	n.d.	n.d.	n.d.	0.5129	0.7038	18.20	15.45	37.98
s_S692-14	10.0	n.d.	n.d.	n.d.	0.5129	0.7038	18.20	15.45	37.98
s_S690-1D	n.d.	n.d.	n.d.	n.d.	0.5129	0.7038	18.11	15.46	37.90
s_K219-9	n.d.	n.d.	n.d.	n.d.	0.5129	0.7037	18.18	15.46	37.95
s_S690-1B	n.d.	n.d.	n.d.	n.d.	0.5129	0.7037	18.23	15.46	37.99
s_K218-5	n.d.	n.d.	n.d.	n.d.	0.5129	0.7037	18.09	15.45	37.84
s_K218-1	n.d.	n.d.	n.d.	n.d.	0.5129	0.7038	18.08	15.45	37.84
s_S690-3A	13.9	6.1	6.1	2.7	0.5129	0.7038	18.10	15.45	37.85
s_S690-3D	n.d.	n.d.	n.d.	n.d.	0.5128	0.7038	18.10	15.46	37.89
s_S690-2C	13.5	6.0	6.2	2.7	0.5129	0.7038	18.10	15.46	37.88
s_S690-4B	n.d.	n.d.	n.d.	n.d.	0.5128	0.7038	18.10	15.46	37.87
s_S690-8B	n.d.	n.d.	n.d.	n.d.	0.5129	0.7037	18.26	15.48	38.08
s_S690-7A	7.6	4.2	4.2	1.8	0.5129	0.7037	18.17	15.46	37.95
s_S690-8A	8.0	4.8	5.1	2.2	0.5129	0.7037	18.33	15.50	38.17
s_S690-6A	n.d.	n.d.	n.d.	n.d.	0.5129	0.7037	18.16	15.45	37.93
s_K219-R2/ s_K219-2	n.d.	n.d.	n.d.	n.d.	0.5129	0.7037	18.24	15.46	37.98
s_K218-R14	n.d.	n.d.	n.d.	n.d.	0.5129	0.7037	18.09	15.45	37.84
s_K218-13/ s_K218-R13	n.d.	n.d.	n.d.	n.d.	0.5129	0.7037	18.13	15.47	37.90
s_K219-R3/ s_K219-3	n.d.	n.d.	n.d.	n.d.	0.5129	0.7037	18.17	15.45	37.92
s_K218-R7 / s_K218-7	n.d.	n.d.	n.d.	n.d.	0.5129	0.7037	18.09	15.45	37.84
s_K218-R12/ s_K218-12	n.d.	n.d.	n.d.	n.d.	0.5129	0.7037	18.09	15.46	37.84
s_K218-R9A / s_K218-9A	n.d.	n.d.	n.d.	n.d.	0.5129	0.7037	18.09	15.45	37.84
s_K218-R8/ s_K218-8	n.d.	n.d.	n.d.	n.d.	0.5129	0.7037	18.09	15.45	37.84

Table S8b. Trace element data (ppm) and radiogenic isotopic data of tholeiitic lavas Hawai'ian (GEOROC; http://georoc.mpch-mainz.gwdg.de/georoc/).

Sample No.	LA	SM	GD	YB	$^{143}Nd/^{144}Nd$	$^{87}Sr/^{86}Sr$	$^{206}Pb/^{204}Pb$	$^{207}Pb/^{204}Pb$	$^{208}Pb/^{204}Pb$
s_K218-R2A/ s_K218-2A	n.d.	n.d.	n.d.	n.d.	0.5129	0.7037	18.09	15.46	37.84
s_K219-R8/ s_K219-8	n.d.	n.d.	n.d.	n.d.	0.5129	0.7037	18.17	15.45	37.92
s_K219-R7/ s_K219-7	n.d.	n.d.	n.d.	n.d.	n.d.	0.7037	18.16	15.45	37.92
s_K219-R5/ s_K219-5	n.d.	n.d.	n.d.	n.d.	0.5129	0.7037	n.d.	n.d.	n.d.
s_K219-R1/ s_K219-1	n.d.	n.d.	n.d.	n.d.	0.5129	0.7037	18.25	15.45	37.97
s_S507-1B	6.9	3.8	4.6	1.8	0.5129	0.7037	18.20	15.47	38.00
s_S507-5B	5.3	2.9	3.5	1.3	0.5129	0.7037	18.24	15.47	38.02
s_ML-52	10.3	5.0	n.d.	1.9	0.5129	0.7039	18.09	15.47	37.88
s_ML-126	9.1	n.d.	n.d.	n.d.	0.5129	0.7039	18.08	15.46	37.86
s_HW35	9.8	4.7	5.0	2.0	0.5128	0.7039	18.07	15.46	37.87
s_HW33	9.1	4.6	4.9	2.1	0.5128	0.7039	18.08	15.46	37.88
s_HW32	8.1	4.4	4.8	2.0	0.5129	0.7038	18.11	15.46	37.85
s_HW31	7.9	4.4	4.7	2.0	0.5129	0.7038	18.10	15.46	37.86
s_HW34	8.7	4.7	4.9	2.0	0.5129	0.7038	18.10	15.46	37.85
s_HW30	7.1	3.9	4.3	1.8	0.5129	0.7038	18.28	15.48	37.98
s_NE-45	n.d.	n.d.	n.d.	n.d.	0.5128	0.7039	18.08	15.46	37.90
s_L77-44	n.d.	n.d.	n.d.	n.d.	0.5129	0.7037	18.19	15.47	37.88
s_L00-520	n.d.	n.d.	n.d.	n.d.	0.5129	0.7039	18.10	15.46	37.88
s_L00-521	n.d.	n.d.	n.d.	n.d.	0.5129	0.7039	18.08	15.46	37.88
s_NE-19	n.d.	n.d.	n.d.	n.d.	0.5128	0.7039	18.09	15.46	37.91
s_L87-93A	n.d.	n.d.	n.d.	n.d.	0.5129	0.7039	18.09	15.46	37.88
s_NE-30	n.d.	n.d.	n.d.	n.d.	0.5128	0.7039	18.09	15.46	37.92
s_L80-90	n.d.	n.d.	n.d.	n.d.	0.5128	0.7040	18.09	15.47	37.89
s_L93-231	n.d.	n.d.	n.d.	n.d.	0.5128	0.7039	18.12	15.47	37.91
s_L88-29	n.d.	n.d.	n.d.	n.d.	0.5130	0.7037	18.25	15.46	37.92

Table S8c. Trace element data (ppm) and radiogenic isotopic data of tholeiitic lavas Hawai'ian (GEOROC; http://georoc.mpch-mainz.gwdg.de/georoc/).

Sample No.	LA	SM	GD	YB	$^{143}Nd/^{144}Nd$	$^{87}Sr/^{86}Sr$	$^{206}Pb/^{204}Pb$	$^{207}Pb/^{204}Pb$	$^{208}Pb/^{204}Pb$
s_L00-05	n.d.	n.d.	n.d.	n.d.	0.5130	0.7037	18.25	15.46	37.92
s_SW-70	n.d.	n.d.	n.d.	n.d.	0.5128	0.7040	18.11	15.46	37.95
s_ML-07-KWWS-92 / s_ML-07	10.2	4.7	5.3	1.9	0.5129	0.7036	n.d.	n.d.	n.d.
s_ML-61-KWWS-92 / s_ML-61	7.7	4.8	6.0	2.2	0.5129	0.7038	n.d.	n.d.	n.d.
s_M27-11	9.0	4.9	5.7	2.1	0.5129	0.7038	18.14	15.46	37.87
s_ML-83	9.1	4.9	n.d.	1.9	0.5129	0.7039	18.12	15.46	37.88
s_36 / s_KAH 36	9.8	4.6	5.1	2.0	0.5128	0.7042	17.99	15.43	37.79
s_61 / s_KAH 6	42.9	15.6	n.d.	6.9	0.5128	0.7041	18.03	15.47	37.80
s_62 / s_KAH 62	124.0	80.0	n.d.	26.6	0.5128	0.7041	18.03	15.47	37.79
s_114 / s_KAH 114	39.7	14.4	n.d.	5.7	0.5129	0.7039	18.31	15.47	38.03
s_113 / s_KAH 113	11.8	5.2	n.d.	2.2	0.5129	0.7038	18.31	15.47	38.04
s_39 / s_KAH 39	31.5	11.3	n.d.	4.4	0.5129	0.7037	18.27	15.47	37.99
s_111 / s_KAH 111	55.7	16.7	n.d.	9.9	0.5129	0.7037	18.26	15.47	37.97
s_KW-14	51.1	13.4	n.d.	5.4	0.5129	0.7040	18.03	15.47	37.77
s_50 / s_KAH 50	13.7	5.5	n.d.	2.1	0.5128	0.7042	17.95	15.45	37.83
s_127 / s_KAH 127	30.3	10.1	n.d.	4.4	0.5129	0.7040	18.16	15.46	37.95
s_41 / s_KAH 41	n.d.	n.d.	n.d.	n.d.	0.5129	0.7040	18.15	15.46	37.94
s_N44 / s_KAH N44	18.6	5.6	n.d.	2.0	0.5129	0.7038	18.19	15.46	37.97
s_158 / s_KAH 158	n.d.	n.d.	n.d.	n.d.	0.5129	0.7038	18.23	15.46	37.99
s_159 / s_KAH 159	13.5	5.9	n.d.	2.4	0.5129	0.7039	18.25	15.46	38.01
s_126 / s_KAH 126	13.9	5.5	n.d.	2.0	0.5128	0.7039	18.02	15.45	37.83
s_125 / s_KAH 125	8.1	4.4	n.d.	2.0	0.5129	0.7040	18.01	15.44	37.82
s_KW-1	9.5	4.7	n.d.	2.0	0.5128	0.7041	17.95	15.45	37.81
s_KW-5	10.9	5.3	n.d.	1.9	0.5129	0.7038	18.37	15.46	38.03

Table S8d. Trace element data (ppm) and radiogenic isotopic data of tholeiitic lavas Hawai'ian (GEOROC; http://georoc.mpch-mainz.gwdg.de/georoc/).

Sample No.	LA	SM	GD	YB	$^{143}Nd/^{144}Nd$	$^{87}Sr/^{86}Sr$	$^{206}Pb/^{204}Pb$	$^{207}Pb/^{204}Pb$	$^{208}Pb/^{204}Pb$
s_KW-25	7.6	3.9	n.d.	1.7	0.5128	0.7042	18.05	15.43	37.79
s_KW-19	13.7	6.4	n.d.	2.6	0.5127	0.7044	17.95	15.45	37.84
s_KW-23	9.7	5.2	n.d.	2.5	0.5129	0.7041	18.04	15.43	37.80
s_0X078	12.8	6.5	n.d.	2.3	0.5128	0.7042	17.71	15.43	37.74
s_0X067	12.1	5.8	n.d.	2.1	0.5127	0.7042	17.85	15.42	37.70
s_0X068	9.4	5.4	n.d.	2.0	0.5128	0.7041	17.87	15.44	37.70
s_0X069	7.5	4.5	n.d.	1.8	0.5127	0.7044	17.89	15.43	37.74
s_88 / s_KSDPUNIT 88/ s_KSDP UNIT 88	8.7	3.9	4.2	1.6	n.d.	n.d.	18.02	15.44	37.90
s_27/ s_KSDPUNIT 27 / s_KSDP UNIT 27	10.4	5.3	5.7	2.0	n.d.	0.7038	18.04	15.45	37.83
s_41 / s_KSDPUNIT 41/ s_KSDP UNIT 41	10.6	5.6	6.0	2.2	n.d.	0.7036	18.15	15.46	37.87
s_34 / s_KSDPUNIT 34 / s_KSDP UNIT 34	8.8	4.8	5.2	1.9	n.d.	n.d.	18.09	15.45	37.83
s_38/ s_KSDPUNIT 38 / s_KSDP UNIT 38	9.9	5.2	5.6	2.1	n.d.	n.d.	18.12	15.46	37.85
s_68/ s_KSDPUNIT 68/ s_KSDP UNIT 68	8.8	4.5	5.0	1.8	n.d.	0.7039	18.03	15.45	37.84
s_76 / s_KSDPUNIT 76 / s_KSDP UNIT 76	8.7	5.1	5.4	1.8	n.d.	n.d.	18.13	15.45	37.81
s_1 / s_KSDPUNIT 1 / s_KSDP UNIT 1	7.2	3.6	3.9	1.5	n.d.	0.7038	18.02	15.45	37.83
s_9 / s_KSDPUNIT 9 / s_KSDP UNIT 9	7.0	4.0	4.4	1.8	n.d.	0.7039	18.00	15.45	37.83
s_57 / s_KSDPUNIT 57/ s_KSDP UNIT 57	11.1	5.5	5.7	2.0	n.d.	0.7037	18.10	15.46	37.86

Table S8e. Trace element data (ppm) and radiogenic isotopic data of tholeiitic lavas Hawai'ian (GEOROC; http://georoc.mpch-mainz.gwdg.de/georoc/).

Sample No.	LA	SM	GD	YB	$^{143}Nd/^{144}Nd$	$^{87}Sr/^{86}Sr$	$^{206}Pb/^{204}Pb$	$^{207}Pb/^{204}Pb$	$^{208}Pb/^{204}Pb$
s_54 / s_KSDPUNIT 54/ s_KSDP UNIT 54	11.9	5.5	5.8	2.0	n.d.	n.d.	18.07	15.45	37.84
s_24 / s_KSDPUNIT 24 / s_KSDP UNIT 24	9.6	5.0	5.4	1.9	n.d.	0.7038	18.09	15.46	37.85
s_6 / s_KSDPUNIT 6 / s_KSDP UNIT 6	6.8	3.7	3.9	1.4	n.d.	n.d.	18.01	15.45	37.82
s_49 / s_KSDPUNIT 49 / s_KSDP UNIT 49	9.0	4.8	5.2	1.9	n.d.	0.7037	18.11	15.45	37.85
s_46/ s_KSDPUNIT 46/ s_KSDP UNIT 46	10.0	5.1	5.4	1.9	n.d.	0.7037	18.02	15.45	37.82
s_62/ s_KSDPUNIT 62 / s_KSDP UNIT 62	9.6	4.7	5.0	1.9	n.d.	n.d.	18.06	15.45	37.84
s_8 / s_KSDPUNIT 8 / s_KSDP UNIT 8	8.8	4.6	5.0	1.8	n.d.	n.d.	18.01	15.45	37.78
s_61 / s_KSDPUNIT 61 / s_KSDP UNIT 61	10.9	5.2	5.6	2.1	n.d.	n.d.	18.08	15.45	37.85
s_17/ s_KSDPUNIT 17/ s_KSDP UNIT 17	10.2	5.1	5.5	2.0	n.d.	n.d.	18.07	15.45	37.83
s_74 / s_KSDPUNIT 74 / s_KSDP UNIT 74	9.2	4.8	5.2	1.9	n.d.	n.d.	18.03	15.45	37.84
s_51 / s_KSDPUNIT 51 s_KSDP UNIT 51	9.8	5.1	5.5	2.0	n.d.	0.7037	18.05	15.45	37.82
s_15 / s_KSDPUNIT 15 / s_KSDP UNIT 15	9.3	4.6	5.0	1.9	n.d.	n.d.	18.07	15.46	37.84
s_66 / s_KSDPUNIT 66 / s_KSDP UNIT 66	9.2	4.7	5.1	1.9	n.d.	n.d.	18.04	15.45	37.82
s_20 / s_KSDPUNIT 20 / s_KSDP UNIT 20	9.7	4.6	4.8	1.7	n.d.	n.d.	18.07	15.46	37.82
s_71 / s_KSDPUNIT 71 / s_KSDP UNIT 71	9.6	4.9	5.4	1.8	n.d.	0.7038	18.07	15.45	37.85

III. Research data

Table S9. Major element data in wt. % of alkali lavas from the Tasmantid Seamounts.

Seamount	Gascoyne	Taupo	Taupo	Taupo	Derwent-Hunter	Queensland	Mellish Seamount	unnamed seamount	unnamed seamount	Derwent-Hunter
Sample No.	65810*	65839*	85175^{+}	85176^{+}	65835*	85162^{+}	274DR22 A3^{-}	274DR36 B1^{-}	274DR41 E1^{-}	85183^{+}
Longitude (East)	156.23	156.23	156.23	156.23	156.23	155.16	155.76	156.01	155.63	156.23
Latitude (South)	-36.65	-32.98	-32.98	-32.98	-30.93	-27.61	-17.60	-19.46	-18.18	-30.93
SiO_2	46.17	50.08	45.86	46.39	47.73	n.d.	45.17	47.51	46.68	49.09
TiO2	1.87	3.04	2.81	2.70	3.46	n.d.	2.83	2.87	2.49	2.33
Al2O3	13.91	14.98	15.14	14.62	15.15	n.d.	14.91	15.94	14.70	16.50
Fe2O3	11.91	11.97	11.93	11.48	11.26	n.d.	12.62	12.01	13.13	8.58
MnO	0.16	0.15	0.14	0.13	0.13	n.d.	0.13	0.15	0.12	0.10
MgO	11.04	4.84	6.76	8.19	4.87	n.d.	6.67	4.71	6.39	4.54
CaO	9.41	7.61	8.17	8.01	9.35	n.d.	7.96	10.01	8.88	10.24
Na2O	3.12	3.93	3.36	3.30	3.28	n.d.	2.90	3.25	3.08	3.55
K2O	0.33	1.23	1.17	1.07	1.15	n.d.	1.48	1.03	0.51	1.08
P2O5	0.77	0.59	0.78	0.73	1.64	n.d.	0.68	0.46	0.47	0.69
L.O.I.	1.34	1.22	3.68	3.79	1.84	n.d.	4.11	2.00	3.32	3.30
Ti8	3.23	1.29	2.11	2.81	1.49	n.d.	2.08	1.17	1.70	0.89

Table S10. Major element data in wt. % of tholeiitic lavas from the Tasmantid Seamounts.

Seamount	Gascoyne	Gascoyne	Gascoyne	Gascoyne	Gascoyne	Gascoyne	Taupo	Derwent-Hunter	Britannia	Queensland	unnamed seamount	unnamed seamount
Sample No.	65808*	65809*	65811*	65821*	85169^{+}	85170^{+}	85174A^{+}	65828*	68644*	TMD10-01 A4$^{\#}$	274DR13 A1^{-}	274DR41 M1^{-}
Longitude (East)	156.23	156.23	156.23	156.23	156.23	156.23	156.29	156.23	155.45	155.15	157.49	155.63
Latitude (South)	-36.65	-36.65	-36.65	-36.65	-36.65	-36.65	-33.1	-30.93	-28.63	-27.695	-16.85	-18.18
SiO_2	49.67	49.67	50.25	48.85	49.40	51.39	51.01	50.32	51.48	49.33	48.58	50.2
TiO_2	1.89	1.89	1.72	1.84	2.46	2.27	2.94	1.80	1.31	2.00	1.98	1.75
Al_2O_3	13.66	13.66	13.46	13.79	13.14	13.74	14.76	13.30	13.90	16.07	15.44	15.31
Fe_2O_3	11.13	11.13	10.87	11.57	11.47	11.02	11.78	10.51	11.44	10.28	9.56	10.86
MnO	0.15	0.15	0.15	0.16	0.14	0.13	0.13	0.15	0.14	0.13	0.13	0.14
MgO	10.12	10.12	10.08	11.37	9.73	7.47	4.80	8.99	9.26	6.23	6.37	6.83
CaO	8.44	8.44	8.26	8.70	8.15	7.89	7.05	9.27	8.25	10.33	9.29	9.21
Na_2O	2.92	2.92	2.77	2.89	2.94	3.16	3.50	2.84	2.80	2.97	3.29	3.15
K_2O	0.85	0.85	0.75	0.54	1.15	1.18	1.27	0.57	0.44	0.81	0.49	0.50
P_2O_5	0.53	0.53	0.30	0.37	0.49	0.53	0.59	0.28	0.31	0.33	0.28	0.34
L.O.I.	0.50	0.50	0.77	0.56	0.57	0.68	1.98	2.21	0.39	1.78	3.98	1.70
Ti8	2.82	2.821	2.55	3.35	3.43	2.02	1.23	2.20	1.68	1.31	1.34	1.34

Table S11a. Trace element data in ppm of alkali lavas from the Tasmantid Seamounts.

Seamount	Gascoyne	Taupo	Taupo	Taupo	Derwent-Hunter	Queensland	Mellish Seamount	unnamed seamount	unnamed seamount	Derwent-Hunter
Sample No.	65810*	65839*	85175^{+}	85176^{+}	65835*	85162^{+}	274DR22 A3^{-}	274DR36 B1^{-}	274DR41 E1^{-}	85183^{+}
Li	11.57		15.95	23.83	n.d.	21.16	60.46	27.03	6.20	n.d.
Be	0.82		2.09	2.06	n.d.	1.32	1.43	1.29	0.90	n.d.
Sc	21.62	17.00	13.13	9.39	22.00	22.29	32.80	25.57	29.97	22.00
Ti	10982.76		18461.69	17955.03	n.d.	13855.69	n.d.	n.d.	n.d.	n.d.
V	184.06	168.00	188.56	172.19	266.00	228.18	299.10	262.70	280.40	202.00
Cr	497.25	83.00	264.68	294.54	49.00	310.58	198.21	89.32	148.80	166.00
Co	79.03	n.d.	40.71	43.32	n.d.	40.46	42.54	46.81	51.08	n.d.
Ni	290.95	76.00	218.73	231.63	59.00	139.54	77.04	80.63	115.37	79.00
Cu	33.77	n.d.	49.55	48.02	n.d.	62.77	40.90	51.99	47.36	37.00
Zn	113.38	n.d.	112.00	104.79	n.d.	109.71	106.20	96.76	104.50	n.d.
Ga	17.52	n.d.	21.33	20.01	n.d.	22.04	21.41	21.93	20.96	n.d.
Se	0.04	n.d.	n.d.	n.d.	n.d.	n.d.	n.d.	n.d.	n.d.	n.d.
Rb	1.80	20.00	8.23	3.90	34.00	12.18	23.44	20.91	3.27	11.50
Sr	486.27	538.00	775.41	660.10	609.00	549.70	352.46	545.52	323.32	705.00
Y	20.59	30.00	20.09	15.25	37.00	14.84	43.81	31.74	39.39	24.00
Zr	116.95	238.00	291.15	275.76	282.00	148.09	291.79	196.49	189.80	189.00
Nb	15.59	31.00	49.66	46.67	39.00	29.05	24.66	30.95	13.01	23.00
Mo	0.74	n.d.	2.20	1.84	n.d.	1.50	0.95	1.26	0.39	n.d.
Ag	0.03	n.d.	n.d.	n.d.	n.d.	n.d.	n.d.	n.d.	n.d.	n.d.
Cd	0.07	n.d.	0.11	0.12	n.d.	0.08	0.12	0.11	0.12	n.d.
Sn(2.3/2.1)	1.22	n.d.	3.74	3.14	n.d.	2.98	1.73	1.78	1.25	n.d.
Sb	0.30	n.d.	0.86	0.41	n.d.	0.74	0.21	0.10	-0.01	n.d.
Cs	0.01	n.d.	0.03	0.03	n.d.	0.33	1.65	1.43	0.17	n.d.

Table S11b. Trace element data in ppm of alkali lavas from the Tasmantid Seamounts.

Seamount	Gascoyne	Taupo	Taupo	Taupo	Derwent-Hunter	Queensland	Mellish Seamount	unnamed seamount	unnamed seamount	Derwent-Hunter
Sample No.	65810*	65839*	85175^{+}	85176^{+}	65835*	85162^{+}	274DR22 A3^{-}	274DR36 B1^{-}	274DR41 E1^{-}	85183^{+}
Ba	119.22	249.00	400.80	366.20	340.00	314.60	381.71	198.00	228.02	349.00
La	13.97	26.30	35.44	30.54	32.60	10.47	29.66	22.65	17.76	21.00
Ce	29.24	51.10	74.00	64.58	71.80	23.44	68.38	50.35	41.23	50.00
Pr	3.96	7.36	9.20	8.01	9.32	3.19	9.04	6.59	5.78	n.d.
Nd	17.74	32.30	37.72	33.01	41.80	14.43	39.05	28.44	26.77	33.00
Sm	4.53	8.20	8.10	7.08	9.64	3.67	8.89	6.64	6.98	n.d.
Eu	1.65	2.84	2.64	2.27	3.41	1.46	2.84	2.30	2.41	n.d.
Gd	4.60	8.66	6.97	5.92	9.65	3.73	8.89	6.76	7.40	n.d.
Tb	0.69	n.d.	0.98	0.81	n.d.	0.58	1.34	1.01	1.15	n.d.
Dy	3.70	6.45	4.61	3.76	7.46	2.96	7.66	5.66	6.72	n.d.
Ho	0.70	n.d.	0.76	0.62	n.d.	0.54	1.52	1.10	1.35	n.d.
Er	1.79	2.71	1.82	1.44	3.75	1.32	4.09	2.85	3.62	n.d.
Yb	1.38	1.89	1.22	0.96	2.73	1.02	3.41	2.24	2.99	n.d.
Lu	0.19	n.d.	0.16	0.13	n.d.	0.15	0.50	0.32	0.43	n.d.
Hf	2.83	n.d.	6.06	5.72	n.d.	3.33	6.36	4.62	4.34	n.d.
Ta	1.06	n.d.	2.96	2.81	n.d.	1.75	1.42	1.90	0.76	n.d.
W	197.28	n.d.	0.52	0.44	n.d.	0.34	n.d.	n.d.	n.d.	n.d.
Ti	0.01	n.d.	n.d.	n.d.	n.d.	n.d.	0.04	0.07	0.02	n.d.
Pb	1.54	4.00	2.90	2.69	4.00	2.16	2.91	1.64	2.16	2.50
Th	1.19	2.50	3.59	2.62	2.50	1.10	1.61	2.18	0.83	2.50
U	0.80	n.d.	1.10	0.84	n.d.	0.30	0.30	0.59	0.11	n.d.

Table S12a. Trace element data in wt. % of tholeiitic lavas from the Tasmantid Seamounts.

Seamount	Gascoyne	Gascoyne	Gascoyne	Gascoyne	Gascoyne	Gascoyne	Taupo	Derwent-Hunter	Britannia	Queensland	unnamed seamount	unnamed seamount
Sample No.	65808*	65809*	65811*	65821*	85169[+]	85170[+]	85174A[+]	65828*	68644*	TMD10-01 A4[#]	274DR13 A1[-]	274DR41 M1[-]
Li	13.77	n.d.	14.87	15.08	8.32	8.85	n.d.	40.87	6.94	17.84	56.01	25.22
Be	1.14	n.d.	0.92	0.97	1.66	1.70	n.d.	0.99	0.70	1.01	0.49	0.62
Sc	20.14	22.00	19.73	20.38	19.61	17.06	17.00	19.55	19.73	28.14	49.01	28.18
Ti	11097.75	n.d.	9922.20	10367.49	15630.98	14737.19	n.d.	11931.93	7877.62	n.d.	n.d.	n.d.
V	163.33	174.00	160.65	171.61	189.23	161.58	166.00	187.99	160.66	205.50	293.00	220.60
Cr	434.67	484.00	450.04	486.57	421.41	323.44	83.00	425.02	463.32	253.16	188.46	253.07
Co	108.04	n.d.	68.58	113.45	50.52	44.59	n.d.	68.45	51.54	38.79	43.69	43.39
Ni	285.67	301.00	263.88	291.90	288.38	232.48	78.00	286.57	300.65	111.58	70.74	90.16
Cu	51.44	n.d.	45.61	48.51	61.29	50.79	28.00	52.85	62.53	55.67	203.49	47.72
Zn	114.14	n.d.	107.14	113.16	113.10	113.41	n.d.	111.97	94.52	74.08	85.90	81.67
Ga	18.61	n.d.	18.56	18.41	20.20	20.89	n.d.	18.64	17.86	19.58	19.82	19.07
Se	0.05	n.d.	0.04	0.04	n.d.	n.d.	n.d.	n.d.	n.d.	n.d.	n.d.	n.d.
Rb	13.23	13.50	11.99	6.86	18.50	18.71	21.00	9.37	8.94	15.15	5.77	4.86
Sr	532.24	551.00	425.01	442.87	616.20	576.10	531.00	390.06	272.10	497.28	290.30	367.35
Y	19.64	20.00	18.16	19.32	22.15	21.69	31.00	20.28	17.35	22.30	33.90	26.31
Zr	148.39	149.00	116.44	119.92	216.82	209.62	236.00	123.29	95.72	149.97	131.88	121.95
Nb	16.99	17.00	12.68	14.87	34.16	28.24	29.00	14.09	6.70	19.07	7.00	7.89
Mo	1.12	n.d.	0.96	0.99	1.97	1.74	n.d.	0.90	0.65	0.91	0.27	0.26
Ag	0.15	n.d.	0.03	0.04	n.d.	n.d.	n.d.	n.d.	n.d.	n.d.	n.d.	n.d.
Cd	0.06	n.d.	0.06	0.06	0.08	0.09	n.d.	0.08	0.05	0.08	0.07	0.07
Sn(2.3/2.1)	1.50	n.d.	1.18	1.71	2.34	2.53	n.d.	1.38	1.48	1.28	1.11	0.91
Sb	0.08	n.d.	0.05	0.07	0.07	0.09	n.d.	0.05	0.03	0.16	0.31	0.02
Cs	0.32	n.d.	0.31	0.07	0.18	0.19	n.d.	0.30	0.09	0.69	0.27	0.35

Table S12b. Trace element data in wt. % of tholeiitic lavas from the Tasmantid Seamounts.

Seamount	Gascoyne	Gascoyne	Gascoyne	Gascoyne	Gascoyne	Gascoyne	Taupo	Derwent-Hunter	Britannia	Queensland	unnamed seamount	unnamed seamount
Sample No.	65808*	65809*	65811*	65821*	85169[+]	85170[+]	85174A[+]	65828*	68644*	TMD10-01 A4[#]	274DR13 A1[-]	274DR41 M1[-]
Ba	210.03	207.00	146.03	155.75	288.60	254.70	254.00	110.69	130.18	169.55	61.40	192.64
La	16.01	16.20	11.97	15.24	25.78	23.92	n.d.	11.64	8.25	16.51	8.51	12.55
Ce	35.04	36.60	25.97	28.18	55.44	50.66	n.d.	25.99	18.27	37.46	22.27	28.87
Pr	4.62	4.55	3.49	3.81	7.12	6.58	n.d.	3.56	2.48	4.90	3.44	4.07
Nd	20.21	22.00	15.61	16.88	30.19	27.88	n.d.	16.28	11.54	21.16	17.15	18.90
Sm	4.84	5.01	4.06	4.27	6.85	6.49	n.d.	4.53	3.36	4.99	4.96	4.86
Eu	1.68	1.92	1.48	1.55	2.19	2.13	n.d.	1.61	1.26	1.76	1.76	1.80
Gd	4.64	5.19	4.14	4.32	6.15	6.03	n.d.	4.70	3.80	5.05	5.73	5.15
Tb	0.70	n.d.	0.63	0.66	0.90	0.88	n.d.	0.71	0.61	0.75	0.95	0.79
Dy	3.67	4.08	3.40	3.52	4.47	4.38	n.d.	3.85	3.28	4.18	5.79	4.61
Ho	0.69	n.d.	0.64	0.67	0.79	0.76	n.d.	0.72	0.62	0.80	1.20	0.93
Er	1.73	1.85	1.63	1.69	1.91	1.83	n.d.	1.82	1.60	2.04	3.28	2.50
Yb	1.31	1.38	1.26	1.30	1.40	1.33	n.d.	1.38	1.28	1.61	2.79	2.06
Lu	0.18	n.d.	0.18	0.18	0.19	0.18	n.d.	0.19	0.18	0.23	0.40	0.30
Hf	3.38	n.d.	2.70	2.82	4.65	4.54	n.d.	2.81	2.25	3.55	3.48	2.98
Ta	1.15	n.d.	0.89	1.20	2.03	1.70	n.d.	0.95	0.39	1.19	0.46	0.50
W	248.49	n.d.	199.62	464.97	0.58	0.51	n.d.	158.17	0.18	n.d.	n.d.	n.d.
Ti	0.04	n.d.	0.04	0.03	n.d.	n.d.	n.d.	0.06	n.d.	0.05	0.02	0.01
Pb	1.97	2.00	1.56	1.62	2.38	2.30	n.d.	1.82	1.23	1.60	1.12	1.68
Th	1.34	2.00	1.02	1.14	2.46	2.37	n.d.	1.19	0.71	1.52	0.47	0.61
U	0.37	n.d.	0.28	0.43	0.65	0.64	n.d.	0.39	0.18	0.39	0.35	0.12

Table S13. Major element data in wt. % of alkali lavas from the Tasmantid Seamounts that have been excluded.

Seamount	unnamed seamount	unnamed seamount	unnamed seamount	Derwent-Hunter
Sample No.	274DR41 F2^{-}	274DR39 A1^{-}	274DR41 F1^{-}	85177^{+}
SiO_2	51.34	47.16	49.89	45.09
TiO_2	2.86	2.68	2.81	3.10
Al_2O_3	22.63	16.60	22.88	13.71
Fe_2O_3	4.21	10.21	4.08	12.84
MnO	0.02	0.10	0.02	0.16
MgO	1.10	2.40	0.74	6.30
CaO	7.50	7.42	8.48	8.38
Na_2O	4.38	3.53	4.50	2.93
K_2O	1.14	1.86	0.99	1.51
P_2O_5	0.55	0.90	0.52	0.60
L.O.I.	4.00	6.74	3.84	4.74
Ti8	0.10	0.35	0.05	2.07

Table S14a. Trace element data in ppm of alkali lavas from the Tasmantid Seamounts that have been excluded.

Seamount	unnamed seamount	unnamed seamount	unnamed seamount	Derwent-Hunter
Sample No.	274DR41 F2^{-}	274DR39 A1^{-}	274DR41 F1^{-}	85177^{+}
Li	12.10	32.16	14.28	n.d.
Be	0.75	1.89	0.73	n.d.
Sc	15.92	24.97	23.97	20
Ti	n.d.	n.d.	n.d.	n.d.
V	252.80	188.60	299.50	299
Cr	313.28	109.90	356.09	465
Co	22.38	29.94	24.19	n.d.
Ni	36.36	47.84	31.52	317
Cu	63.51	43.05	79.82	79
Zn	49.97	122.70	40.60	n.d.
Ga	25.91	23.45	29.21	n.d.
Se	n.d.	n.d.	n.d.	n.d.
Rb	7.66	29.17	6.65	27
Sr	456.60	543.04	528.47	566
Y	24.33	48.45	28.76	26
Zr	206.40	338.80	207.51	235
Nb	17.40	25.98	17.33	39
Mo	0.69	0.82	0.53	n.d.
Ag	n.d.	n.d.	n.d.	n.d.
Cd	0.06	0.15	0.09	n.d.
Sn(2.3/2.1)	1.81	2.23	1.79	n.d.
Sb	0.42	0.55	0.30	n.d.
Cs	0.05	0.73	0.06	n.d.

Table S14b. Trace element data in ppm of alkali lavas from the Tasmantid Seamounts that have been excluded.

Seamount	unnamed seamount	unnamed seamount	unnamed seamount	Derwent-Hunter
Sample No.	274DR41 F2^{-}	274DR39 A1^{-}	274DR41 F1^{-}	85177^{+}
Ba	360.40	381.92	337.31	336
La	20.83	45.06	21.07	28
Ce	46.18	94.08	47.75	67
Pr	6.19	12.29	6.43	n.d.
Nd	26.93	51.57	28.27	38
Sm	6.10	11.02	6.68	n.d.
Eu	2.34	3.44	2.49	n.d.
Gd	5.89	10.71	6.49	n.d.
Tb	0.84	1.52	0.95	n.d.
Dy	4.45	8.33	5.19	n.d.
Ho	0.83	1.61	1.00	n.d.
Er	2.10	4.21	2.55	n.d.
Yb	1.48	3.38	1.89	n.d.
Lu	0.20	0.50	0.26	n.d.
Hf	4.89	7.58	5.08	n.d.
Ta	1.03	1.47	1.00	n.d.
W	n.d.	n.d.	n.d.	n.d.
Ti	0.06	0.26	0.03	n.d.
Pb	3.25	4.61	3.14	4
Th	1.53	2.79	1.49	4
U	0.72	0.67	0.46	n.d.

Table S15. Calculated pressure (P) and temperature (T) as well as major elements (wt. %) of parental magma of alkali lavas from the Tasmantid Seamounts.

Seamount	Gascoyne	Taupo	Taupo	Taupo	Derwent-Hunter	Derwent-Hunter	Mellish Seamount	unnamed seamount	unnamed seamount
Sample No.	65810*	65839*	85175^{+}	85176^{+}	65835*	85-183^{+}	274DR22 A3^{-}	274-DR36 B1^{-}	274DR41 E1^{-}
SiO_2	46.71	46.09	48.47	46.81	45.94	49.37	45.84	46.52	46.46
TiO_2	2.15	1.55	2.00	2.55	2.28	2.00	2.11	2.05	1.80
Al_2O_3	11.66	11.54	10.68	11.15	10.10	14.18	11.12	11.38	10.61
FeO	10.59	10.77	10.40	10.28	11.59	8.37	11.40	10.76	11.61
MnO	0.10	0.13	0.11	0.10	0.12	0.09	0.10	0.11	0.09
MgO	18.26	18.56	17.93	17.68	19.98	12.57	19.63	18.57	20.00
CaO	6.46	7.86	6.69	6.97	6.27	8.85	6.03	7.23	6.50
Na_2O	2.63	2.59	2.39	2.41	2.16	3.05	2.16	2.32	2.22
K_2O	0.85	0.27	0.93	0.85	1.11	0.93	1.10	0.74	0.37
P_2O_5	0.58	0.64	0.40	1.21	0.44	0.59	0.51	0.33	0.34
T(°C)	1592.00	1612.00	1580.00	1569.00	1561.00	1624.00	1612.00	1578.00	1639.00
P(GPa)	2.63	3.09	2.87	2.39	2.64	3.29	3.26	2.87	3.12
$\delta^{57}Fe_{Prim}$	0.12	n.d.	n.d.	0.10	n.d.	0.21	0.16	0.15	0.15

Table S16. Calculated pressure (P) and temperature (T) as well as major elements (wt. %) of parental magma of tholeiitic lavas from the Tasmantid Seamounts.

Seamount	Gascoyne	Gascoyne	Gascoyne	Gascoyne	Gascoyne	Gascoyne	Taupo	Derwent-Hunter	Britannia	Queensland	unnamed seamount	unnamed seamount
Sample No.	65808*	65809*	65811*	65821*	85169[+]	85170[+]	85174A[+]	65828*	68644*	TMD10-01 A4[#]	274DR13 A1[-]	274-DR41 M1[-]
SiO_2	48.76	48.76	49.62	47.90	49.82	49.96	49.77	48.29	49.01	48.23	49.13	46.21
TiO_2	1.57	1.58	1.45	1.54	1.78	1.05	1.50	1.57	1.37	2.17	2.12	2.14
Al_2O_3	11.36	11.36	11.36	11.54	10.77	11.16	11.11	12.60	11.94	10.72	10.65	11.52
FeO	10.13	10.12	10.00	10.41	10.08	10.35	9.77	9.57	10.00	10.70	10.63	10.90
MnO	0.12	0.12	0.13	0.13	0.10	0.11	0.13	0.10	0.11	0.11	0.09	0.11
MgO	17.41	17.41	17.20	17.97	17.38	17.83	16.85	16.49	17.20	18.42	18.34	18.80
CaO	7.07	7.07	7.02	7.33	6.25	6.69	7.80	8.17	7.26	5.53	5.18	6.30
Na_2O	2.43	2.43	2.34	2.42	2.48	2.25	2.37	2.33	2.46	2.81	2.52	2.56
K_2O	0.71	0.71	0.63	0.45	0.92	0.35	0.48	0.63	0.39	0.88	0.92	0.89
P_2O_5	0.44	0.44	0.25	0.31	0.42	0.25	0.23	0.26	0.27	0.42	0.43	0.59
T(°C)	1567.00	1567.00	1558.00	1595.00	1559.00	1591.00	1550.00	1530.00	1569.00	1602.00	1603.00	1512.00
P(GPa)	2.27	2.27	2.03	2.50	2.07	2.05	1.93	2.16	2.16	2.62	3.06	1.97
$\delta^{57}Fe_{Prim}$	0.22	0.22	0.05	n.d.	0.20	0.11	0.01	n.d.	0.03	0.02	0.03	-0.01

CHAPTER 3

3. The influence of mantle source composition and metasomatism on Fe isotopes in lavas from São Miguel, Azores

Saskia Ruttor[1]*, Oliver Nebel[1], Helen Williams[2], Christoph Beier[3], Marianne Richter[1], Yona Nebel-Jacobsen[1], René H.W. Romer[4] and Simon P. Turner[5], Caroline R. Soderman[2]

1 School of Earth, Atmosphere and Environment, Monash University, Melbourne, Australia, saskia.ruttor@monash.edu

2 Department of Earth Sciences, University of Cambridge, Cambridge, CB2 3EQ, UK

3 Department of Geoscience and Geography, University of Helsinki, P.O. Box 64, FIN-00014 Helsinki, Finland

4 GeoZentrum Nordbayern, Friedrich-Alexander-Universität Erlangen-Nürnberg (FAU), Schlossgarten 5, D-91054 Erlangen, Germany

5 Department of Earth and Environmental Sciences, Macquarie University, Australia

Key words: Fe isotopes, Azores, melting, rift, peridotite, metasomatism

Abstract

Ocean island basalts (OIB) display a wide range in radiogenic Sr-Nd-Pb ratios but also exhibit a large variability in stable iron (Fe) isotopes. This Fe isotopic heterogeneity can be inherited from mixing or melting of various exotic mantle components of enriched crustal origin, i.e., oceanic or continental crust, lithosphere and sediments. The extent to which the inherited Fe isotopic signature of the subducted and recycled material influences the Fe isotopic composition of OIB and which role secondary processes accompanied with partial melting play is, however, not well understood. The eastern Azores island of São Miguel displays a systematic change from a less radiogenic mantle source in the West to a highly enriched source in the East. The latter is unique amongst global OIB in that it has both, extremely radiogenic $^{206}Pb/^{204}Pb$ and $^{87}Sr/^{86}Sr$ isotopic ratios. The regional distribution, complexity and uniqueness of these isotopic source characteristics are ideally suited to gain insights into the spatial distribution of mantle components and their controls on Fe isotope systematics. Comparing $\delta^{57}Fe_{prim}$, which is the isotopic composition calculated to primitive lavas along a liquid line of descent, with $^{87}Sr/^{86}Sr$, $^{143}Nd/^{144}Nd$, $^{206}Pb/^{204}Pb$ and $^{208}Pb/^{204}Pb$ reveals that the depleted component of western São Miguel shows a heavy Fe isotopic composition ranging

from $\delta^{57}Fe_{prim}$ = +0.09 to +0.18‰ (excluding one outlier at -0.02‰ $\delta^{57}Fe_{prim}$), whereas the enriched component of eastern São Miguel shows lighter $\delta^{57}Fe_{prim}$ = +0.05 to +0.12‰. The light Fe isotopic signature of eastern São Miguel is striking because crustal material has previously been associated with heavier Fe isotopic compositions. Among the metasomatising agents discussed, we can show by mass balance calculations that a carbonatitic metasomatising agent cannot account for the light Fe isotopic composition of eastern São Miguel. Strong deviation of eastern São Miguel lavas from other Azores islands in K_2O and Rb/Sr vs $\delta^{57}Fe_{prim}$ indicate silicic K-rich mantle metasomatism, resulting in the $\delta^{57}Fe_{prim}$ observed for eastern São Miguel. The heavy Fe isotopic composition of western São Miguel's lavas are likely related to the active Terceira Rift and represent low degree melting of a less enriched component at the ultraslow spreading ridge. Two scenarios are needed to explain the Fe isotopic composition of eastern and western São Miguel, which indicates a separate plumbing system underneath eastern and western São Miguel. The dominance of light Fe isotopes associated with mantle metasomatism may be a distinctive feature of this type of plume source elsewhere.

3.1 Introduction

The subduction and recycling of crustal material over hundreds of millions of years has introduced crustal signatures in an otherwise predominantly depleted upper mantle. These crustal signatures are composed of oceanic or continental crust and their lithospheric mantles, accompanied by small amounts of sediments, and are best traced through radiogenic Sr-Nd-Pb-Hf isotopic ratios of mantle-derived lavas (Zindler and Hart, 1986; Hofmann, 1997; Hofmann and Farnetani, 2013; Lassiter and Hauri, 1998; Hart et al., 1992; Stracke, 2012; Koppers et al., 2021; Salters and White, 1998). Ocean island basalts (OIB) away from plate margins record complex patterns of radiogenic Sr-Nd-Pb-Hf isotopes with distinct combinations in individual OIB locations (e.g., Stracke et al., 2005; White, 2015; Hofmann, 2003). Mass balance considerations for these trace elements suggest that these lavas sample isotopically enriched sources as remnants of crustal recycling in conjunction with more primitive mantle plume material (Pietruszka et al., 2013; Stracke et al., 2003; Lassiter and Hauri, 1998; Zindler and Hart, 1986). Diversity in radiogenic isotopes within single plumes indicate that both, plume sources and processes during ascend create mixing patterns of depleted prevalent mantle (PREMA) and recycled, crustal material termed enriched mantle component 1 and 2 (EM1/2), and HIMU (high $^{238}U/^{204}Pb$; Zindler and Hart 1986). These OIB radiogenic isotopic signatures of so-called mantle components are well documented, yet their complex distribution even within single plume regions (e.g., Hawai'i, Iceland, Azores) indicate petrologic complexities superimposed on simple source component distribution patterns (Kurz et al., 1990; Blichert-Toft and Albarede, 1998; Weis et al., 2011; Fitton et al., 2003).

São Miguel, an island of the Azores in the Atlantic Ocean, displays a wide range of radiogenic isotopic compositions, extending from a less enriched source at western São Miguel (radiogenic isotopic composition similar to PREMA as well as enriched mid-ocean ridge basalts (MORB); see discussion in Beier et al., 2007; Beier et al., 2018) to a source composition unique in elevated radiogenic Sr, Nd and Pb isotopic signatures at eastern São Miguel (Beier et al., 2007; Turner et al., 2007; Beier et al., 2018; Elliott et al., 2007). The sources are geographically separated but generally tend to show an increasing degree of enrichment in radiogenic isotopes and trace element compositions from West to East (Turner et al., 1997; Widom et al., 1997; Elliott et al., 2007; Beier et al., 2007). The distribution of geochemical

signatures is directly linked to individual fault systems related to the slow spreading Terceira Rift axis (Haase and Beier, 2003). The melting processes and the mantle source(s) that cause eastern São Miguel's unique enriched and western São Miguel's less enriched radiogenic isotopic signature is still under debate (e.g., Beier et al., 2006; Beier et al., 2007; Elliott et al., 2007; Haase and Beier, 2003; Kurz et al., 1990; Widom et al., 1997; Widom and Farquhar, 2003). A prevalent problem in resolving isotopic heterogeneity in plume sources like the ones feeding São Miguel is elusive and complex petrogenetic mixing during (i) plume ascent, (ii) partial melting and (iii) potential magma reservoir dynamics (e.g., mush reservoirs) *en route* to the surface may contribute to heterogenous isotopic signatures of erupting lavas.

To understand magmatic processes and mantle material that generate OIB at São Miguel, we use new stable Fe isotopes in conjunction with traditional radiogenic isotopes. Over the past decade, stable Fe isotopes have been established as a tool to identify the lithology of mantle components that generate OIB (Williams and Bizimis, 2014; Konter et al., 2016; Nebel et al., 2019). Furthermore, due to its sensitivity to Fe redox state and associated bonding in crystal lattices or melts (Sossi and O'Neill, 2017), Fe isotopes are a useful tracer for magmatic processes such as partial melting, crystal fractionation and mantle metasomatism (Beard and Johnson, 2004; Poitrasson et al., 2013; Williams et al., 2005; Weyer and Ionov, 2007).

The variance in radiogenic isotopes on a km-scale and the uniqueness of the eastern source composition renders lavas from São Miguel suitable to resolve potential magmatic processes that add to the diversity in radiogenic isotopic signatures in OIB. Our data reveal a heavy Fe isotopic signature for western São Miguel's lavas and a relatively light Fe isotopic composition for eastern São Miguel's lavas. The differences in Fe isotopes between eastern and western São Miguel can be ascribed to a source dependency given the good correlations between stable Fe isotopes and radiogenic Sr, Nd and Pb ratios. Crustal material is generally ascribed to heavier Fe isotopic compositions than analysed for São Miguel. Several processes, among other long degree mantle metasomatism, will be discussed in the following. The heavy Fe isotopic composition of western São Miguel's lavas might be result from rift-related metasomatism associated with the ultraslow Terceira Rift.

3.2 Geological Setting

The Azores archipelago consists of nine volcanic islands where the islands of São Miguel, Terceira and Graciosa and the submarine seamount João de Castro (Romer et al., 2021 ; Fig. 1a) are located along the ultraslow spreading Terceira Rift (extension rates of 2 – 4 mm/year; Vogt and Jung, 2004; Searle, 1980). São Miguel consists of four stratovolcanoes, which are from West to East, Sete Cidades, Agua de Pau, Furnas and Nordeste (Fig. 1b). The western part of São Miguel is dominated by the central volcano Sete Cidades (Beier et al., 2006). To the East of Sete Cidades, the so-called Waist Zone consists of a series of scoria cones (Booth et al., 1978; Fig. 1b). The Sr isotopic signatures of the southern scoria cones imply mixing with a source underneath Sete Cidades, whereas the northern scoria cones display Sr isotopic signatures indicating mixing with the eastern volcano of Agua de Pau (Haase and Beier, 2003). Sete Cidades and the western Waist Zone scoria cones are situated along the NW-SE striking Terceira Rift axis (Fig. 1b). In contrast, the eastern part of São Miguel consists of three central volcanoes Agua de Pau, Furnas (not sampled for this study) and Nordeste, aligned in an EW direction. The eastern volcano of Nordeste is inactive and dated to be ~800 kyrs (Johnson et al., 1998). With the exception of Nordeste, all volcanoes on São Miguel are active (Duncan et al., 2015).

From the western islands (Graciosa, Faial, Pico and São Jorge) of the Azores, located closest to the neighbouring mid-Atlantic Ridge, to the eastern islands (Terceira, São Miguel and Santa Maria), the thickness of lithosphere increases (Beier et al., 2008; Béguelin et al., 2017). São Miguel lavas erupted on lithosphere with ~70-80 km thickness and have been generated from melts that form in the garnet stability field as evident by elevated Middle Rare Earth Element (REE) relative to the Heavy REE Ytterbium (Yb, Beier et al., 2007; Spieker et al., 2018).

As part of the Azores, São Miguel is situated near the northern Atlantic Large Low Shear Velocity Province (LLSVP), which could be considered to be an indicator for a deep mantle plume origin, also suggested by tomographic models (French and Romanowicz, 2015; Lekic et al., 2012; King and Adam, 2014). However, a deep origin of the Azores mantle plume is a matter of active debate due to elevated volatile contents (Beier et al., 2012; Métrich et al.,

2014; Asimow et al., 2004) and noble gas isotope data from São Miguel, which are comparable to MORB values (Moreira et al., 2018; Moreira et al., 2012; Kurz et al., 1990).

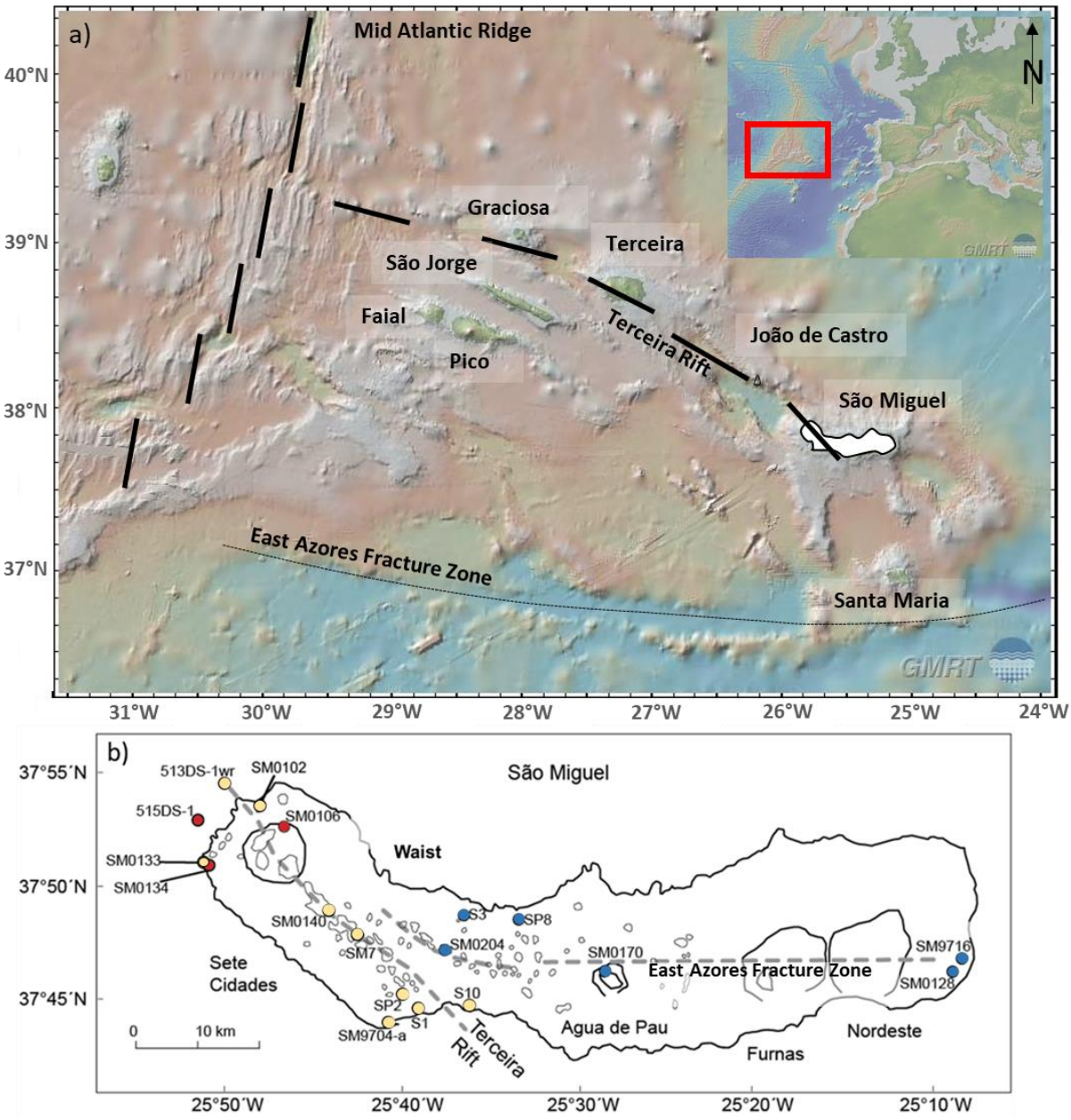

Figure 1. a) The map shows the Azores with João de Castro, Terceira, Graciosa and north-west of São Miguel located on the Terceira Rift. Maps are from the GeoMapApp by Ryan et al. (2009); http://www.geomapapp.org/. b) Map modified after Beier et al. (2007) showing the sample localities. At the volcanic *Waist Zone* (Booth et al., 1978), São Miguel is divided into western (yellow circle) and eastern (blue circle) area, samples in red circles have been excluded from the discussion, because samples have been affected by magnetite fractionation (see 4.1). The main tectonic features are highlighted by grey dotted lines (adopted from Forjaz, 1986), with Sete Cidades being located on the

active Terceira Rift and the eastern volcanoes being located parallel to the inactive East Azores Fracture Zone.

3.3 Sample selection and analytical methods

3.3.1 Sample selection

We have selected 18 fresh, well-characterised alkali basalts from São Miguel (TAS diagram Supplementary data I) and divided them into western (basalts) and eastern (trachybasalts) São Miguel based on their geological features (Haase and Beier, 2003; Forjaz, 1986) and published Sr, Nd and Pb isotopic compositions (Beier et al., 2007; Elliott et al., 2007; Turner et al., 1997; Prytulak et al., 2014). Lavas from western São Miguel include four samples from Sete Cidades and five samples from the southern rift zone of the Waist Zone; eastern São Miguel lavas are those from the northern rift zone of the Waist Zone with three samples, one sample from the Agua de Pau and two samples from Nordeste (Beier et al., 2018; Fig. 1b). The samples SM0133, SM0102, 513DS-1wr, SM0170, SM0128, SM9716, SM0204 have been described by Beier et al. (2006) and Beier et al. (2007) as "*optically fresh and lack of alteration of olivine crystals and vesicle fillings"*. According to Beier et al. (2006) other samples show iddingsitized olivine rims and clay filling in cracks and vesicles. For the whole rock analyses "*fresh cores of these whole rocks were cut, coarse crushed and washed in ionized water and then fine crushed in an agate ball mill"* (Beier et al., 2006; p. 1379). Sample SM07 is described by Elliott et al. (2007) as a basalt that shows olivine and clinopyroxene phenocrysts, and by Prytulak et al. (2014) as a sample that is displaying *"little petrographic or geochemical evidence for contamination*". Turner et al. (1997) described the samples S1, S10, SP2, S3 and SP8, which contain olivine as the main phenocryst phase. A more detailed description of the samples and the Azores chemistry is given in Beier et al. (2007) and Beier et al. (2008) and summarised in Larrea et al. (2018) and Beier et al. (2018). Major and trace element as well as radiogenic isotope data for all samples analysed in this study are summarised in the Supplementary data II.

3.3.2 Analytical methods

We analysed well characterised samples previously published for their major, trace element and Sr-Nd-Pb isotopic compositions by Beier et al. (2007), Prytulak et al. (2014),

Turner et al. (1997), and Elliott et al. (2007) for their stable Fe isotopic compositions. For rock dissolution, ~25 mg of rock powder has been weighed into PFA Teflon beakers and treated with 2 mL concentrated HF:HNO_3 (ratio 1:2). Samples were dissolved for a maximum of three days on a hotplate at 120°C. After evaporation, samples were re-dissolved with small volumes of concentrated nitric acid and a drop of per-oxide to ensure the breakdown of fluoride bonds (Cheng et al., 2014), and finally taken up in 9M HCl (Monash University) or 6M HCl (Durham University) and pipetted onto the AG-MP-1 (Monash University) or AG1-X4 (Durham University) anionic resin (Cheng et al., 2014), which was preconditioned with 9M HCl (Monash University) or 6M HCl (Durham University). Column chromatographic extraction with 9M HCl, 6M HCl and 5M HCl removed matrix elements as well as semi and transitional metals. The Fe fraction was eluted with 1M HCl. The collected Fe fraction was placed on a hotplate at 90°C. The dried samples were dissolved and taken up in 2% HNO_3. The detailed chromatographic extraction procedure for Fe purification used at Monash University has been reported by Cheng et al. (2014) and Sossi et al. (2015).

The Fe isotope analyses were performed on ThermoFisher™ Scientific Neptune plus multi-collector inductively coupled plasma mass spectrometers (MC-ICP-MS) at the Isotopia Laboratory at the School of Earth, Atmosphere and Environment at Monash University, Australia and Durham University. The samples were introduced via a low flow quartz cyclonic spray chamber and a PFA nebuliser. In medium-resolution mode (Sossi et al., 2015), data were collected in per mille notation relative to the IRMM-014 (Durham University) or IRMM-524a (Monash University) bracketing standards, the latter being isotopically identical to IRMM-014 (Craddock and Dauphas, 2010), and with ^{5x}Fe being either ^{56}Fe or ^{57}Fe, respectively:

$$\delta^{5x}Fe = \left[\frac{^{5x}Fe/^{54}Fe_{Sample}}{^{5x}Fe/^{54}Fe_{IRMM-524a}} - 1\right] x\ 1000 \quad (1)$$

Each sample was analysed two to three times from a single dissolution batch to ensure precision and accuracy, and isotope ratios for each sample represent averaged values (Table 1). Each single dissolution batch was mixed with an in-house Ni standard solution to correct for instrumental mass bias effects (Sossi et al., 2015). To ensure reliability and comparability of our Fe isotope data, the basaltic reference materials BCR2, BHVO1, BIR-1 and $FeCl_3$ were analysed (Table 1). The latter is an in-house standard and coincides with analyses at Cambridge University with δ^{56}Fe = -0.69 ± 0.03‰ (two-standard deviation 2 S.D.) and δ^{57}Fe =

-1.03 ± 0.05‰ (Soderman et al., 2021). The basaltic reference materials BCR2, BHVO1, BIR-1 are in agreement with previously published analysis (BCR2: $\delta^{56}Fe$ = +0.09 ± 0.01‰ (2S.D.) , $\delta^{57}Fe$ = +0.13 ± 0.02‰ in Craddock and Dauphas (2010) and $\delta^{57}Fe$ = +0.14 ± 0.02‰ in Sossi et al. (2015); BHVO1: $\delta^{56}Fe$ = +0.10 ± 0.01‰, $\delta^{57}Fe$ = +0.16 ± 0.01‰ in Craddock and Dauphas (2010); BIR-1: $\delta^{56}Fe$ = +0.05 ± 0.02‰, $\delta^{57}Fe$ = +0.09 ± 0.02‰ in Craddock and Dauphas (2010)). The reproducibility of the method is ±0.03‰ (2S.D.) in $^{57}Fe/^{54}Fe$ relative to the IRMM-524a external standard based on repeated analyses of standard reference materials. The reproducibility of each sample was calculated as the standard deviation from 2-3 repeated analyses and we always use the larger error (external vs. sample-averaged error). At the end of the analysis a procedural blank was analysed and generally showed values below detection level and is thus negligible.

Ascending mantle melts experience significant olivine and minor pyroxene fractionation, which results in the preferential removal of Fe^{2+} (relative to Fe^{3+}) and also affects the Fe isotopic composition of the melts (Sossi et al., 2012; Williams et al., 2005), driving residual melts toward isotopically heavy values (Teng et al., 2008). Correcting the measured $\delta^{57}Fe$ for crystal fractionation is thus essential to ensure a meaningful comparison between stable and radiogenic isotopic compositions of primary melts from OIB. In order to assess the primary melt compositions, termed $\delta^{57}Fe_{prim}$, we apply an olivine fractionation correction to the measured $\delta^{57}Fe$ isotope values (Sossi et al., 2016). By using a temperature dependent fractionation factor $\Delta^{57}Fe_{Min\text{-}Melt}*10^6/T^2$ = -0.4 (further outlined in Sossi et al., 2016) and assuming a starting melt composition with $Fe^{3+}/\sum Fe$ = 0.15 (Nebel et al., 2019), we are adding olivine (isotopically light Fe) to our sample lavas until a primary melt composition with Mg# = 74 was reached. Considering an exchange coefficient for Fe and Mg between olivine and melt $K_{D\,Ol-Melt}^{Fe-Mg}$ > 0.3 (Roeder and Emslie, 1970), the Mg# = 74 is in chemical equilibrium with a primitive mantle Mg# = 90 (Palme and O'Neill, 2014). The term $\Delta^{57}Fe_{Min\text{-}Melt}$ describes the difference between the melt $\delta^{57}Fe_{Melt}$ value and the mineral $\delta^{57}Fe_{Min}$ isotope value (i.e., olivine):

$$\Delta^{57}Fe = \delta^{57}Fe_{Min} - \delta^{57}Fe_{Melt} \quad (2)$$

The starting melt composition with $Fe^{3+}/\sum Fe$ = 0.15 is higher than global MORB values of $Fe^{3+}/\sum Fe$ = +0.12 ± 0.02 (Bézos and Humler, 2005) and used for primary melt stable Fe isotope

calculations in OIB (Nebel et al., 2019; Soderman et al., 2021) and back-arc basalts (Nebel et al., 2018). OIB glasses from São Miguel have not been analysed for their redox-state rendering this approach a best-estimate.

The main uncertainties of the fractionation correction model lie in the variability of the initial mantle source composition at Mg# = 90 and the fractionation factor between mineral species applied. However, even though the São Miguel mantle source may be heterogeneous, i.e., peridotite and pyroxenite lithologies may variably contribute to the melting regime, a pyroxenitic source deviates by only ± 2 Mg# relative to a peridotite source region (Herzberg, 2011), which is negligible for the approach applied here (Nebel et al., 2019). Variations in the inter-mineral correction factor of $-0.4*10^6/T^2$ equate to $\delta^{57}Fe_{prim}$ 0.03‰ variations per 0.1 unit in the correction factor, with smaller correction factors leading to apparently less pronounced corrections. It needs to be stated here that our applied fractionation factor of $-0.4*10^6/T^2$ is a large extent of correction for basalts ranging from 4.0 – 14.3 wt.% MgO (Soderman et al., 2021). A test for the magnitude of the applied correction using $\Delta^{57}Fe_{Min-Melt} = -0.4*10^6/T^2$, is further illustrated in Figure 3, where we compare $\delta^{57}Fe_{prim-0.1}$ corrected with a $\Delta^{57}Fe_{Min-Melt} = -0.1*10^6/T^2$. Throughout the manuscript, $\delta^{57}Fe_{prim}$ is shown with a correction factor of $\Delta^{57}Fe_{Min-Melt} = -0.4*10^6/T^2$, because we will compare our data with other Azores islands (São Jorge, Pico, Faial, Terceira, João de Castro and Graciosa) from Soderman et al. (2021), who used a fractionation factors of $-0.4*10^6/T^2$.

The São Miguel whole rock Fe isotope values are presented both as measured $\delta^{57}Fe$ and as calculated primary melt $\delta^{57}Fe_{prim}$. Errors for $\delta^{57}Fe$ and $\delta^{57}Fe_{prim}$ are reported as the standard deviation of repeated analyses of each sample aliquot from the IRMM-524a (Monash University) or IRMM-014 (Durham University) Fe standards (or ±0.03‰ in case this value is lower). The $\delta^{57}Fe_{prim}$ do not include error propagations of the correction method.

3.4 Results

3.4.1 Filtering for wall rock assimilation and magnetite fractionation

We scanned our new data for potential secondary effects by excluding: (1) Samples exceeding a Ba/Rb value of 12 ± 2 (Hofmann and White, 1983), indicative for country rock assimilation. Exceptions are samples SM9704A and SM0140 with a Ba/Rb of 15.9 and 22.7, respectively, due to their high MgO content of 12.67 and 9.81 wt.%, which precludes

assimilation of quartz syenite country rock; (2) Samples with MgO < 4.0 wt.% and TiO_2 < 2.5 wt.% (Fig. 2) due to the influence of magnetite fractionation on the Fe isotopic composition of the remaining melt by preferentially removing isotopically heavy Fe (Nebel et al., 2019; Sossi et al., 2012; Nebel et al., 2015); a feature that cannot adequately be corrected for. For the latter, the excluded samples (SM0106, SM0134, 515DS-1) show high $\Delta^{57}Fe$ (= $\delta^{57}Fe$ – $\delta^{57}Fe_{prim}$) of 0.14 to 0.26‰ (Fig. 3) and are not discussed in detail. Two samples of eastern São Miguel with a MgO < 5.0 wt.% plot arguably close to the threshold defined by Nebel et al. (2019) and Sossi et al. (2012). These samples, however, show a $\Delta^{57}Fe$ of 0.10 and 0.12‰, in line with Ni contents of 18 and 21 ppm (Supplementary data II), and are interpreted as not being affected by the fractionation of magnetite.

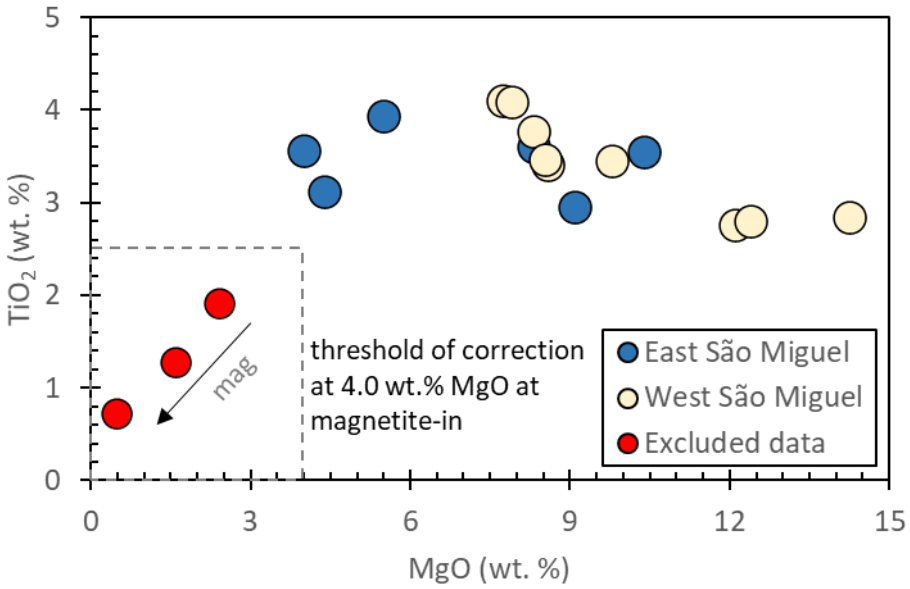

Figure 2. MgO vs TiO_2 to illustrate potential magnetite saturation of samples. Our threshold at 4.0 wt.% MgO ensures the exclusion of samples affected by magnetite fractionation. Several studies, e.g., Nebel et al. (2015) and Sossi et al. (2012) show that at low MgO values magnetite is the primary host of Fe. Red circles highlight the samples that have been excluded from the discussion.

3.4.2 Stable Fe isotopes

Samples from São Miguel have measured $\delta^{57}Fe$ signatures comparable to or heavier than mean MORB (+0.15 ± 0.01‰ $\delta^{57}Fe$ (2S.D.); Chen et al., 2019, Teng et al., 2013) with a single outlier at western São Miguel (SM0133) which has a lighter Fe isotopic composition than MORB with $\delta^{57}Fe$ = +0.03‰. Generally, $\delta^{57}Fe$ values range from +0.09 to +0.24‰ for eastern São Miguel and from +0.13 to +0.22‰ for western São Miguel lavas, if SM0133 is excluded.

The primary magma shows a value of ~12.0 wt.% MgO for lavas from São Miguel. We therefore correct lavas <12.0 wt. MgO for olivine fractionation. SM0140 with 12.41 wt.% MgO can be left uncorrected. SM0102 with 14.26 wt.% shows presumably olivine accumulation rather than fractionation. Olivine accumulation can only be corrected for when olivine is in equilibrium with the final bulk composition (McCoy-West et al., 2018), which is unlikely in this case. Due to the lack of a statistical difference between high and low MgO lavas, we include SM0102 in the following. Following correction for olivine crystal fractionation ($\Delta^{57}Fe_{Min\text{-}Melt} = -0.4*10^6/T^2$), the following, slightly lighter melt $\delta^{57}Fe_{prim}$ compositions are obtained for eastern and western São Miguel lavas: $\delta^{57}Fe_{prim}$ +0.05 to +0.12‰ and +0.09 to +0.18‰ (excluding outlier SM0170 at -0.2‰), respectively. Samples from western São Miguel display the lowest values in both $\delta^{57}Fe$ and $\delta^{57}Fe_{prim}$ (Fig. 3). The crystal fractionation correction factor ($\Delta^{57}Fe$) is largest for eastern São Miguel ranging from $\Delta^{57}Fe$ = 0.04 to 0.12‰, whereas western São Miguel shows lower values with $\Delta^{57}Fe$ = 0.00 to 0.07‰. We note here that this correction is only an approximation of the exact likely liquid line of descent and thus should be treated as such. Nonetheless, even though the effect is minor (Fig. 3), it better approaches the true nature of primitive melts prior to crystal fractionation.

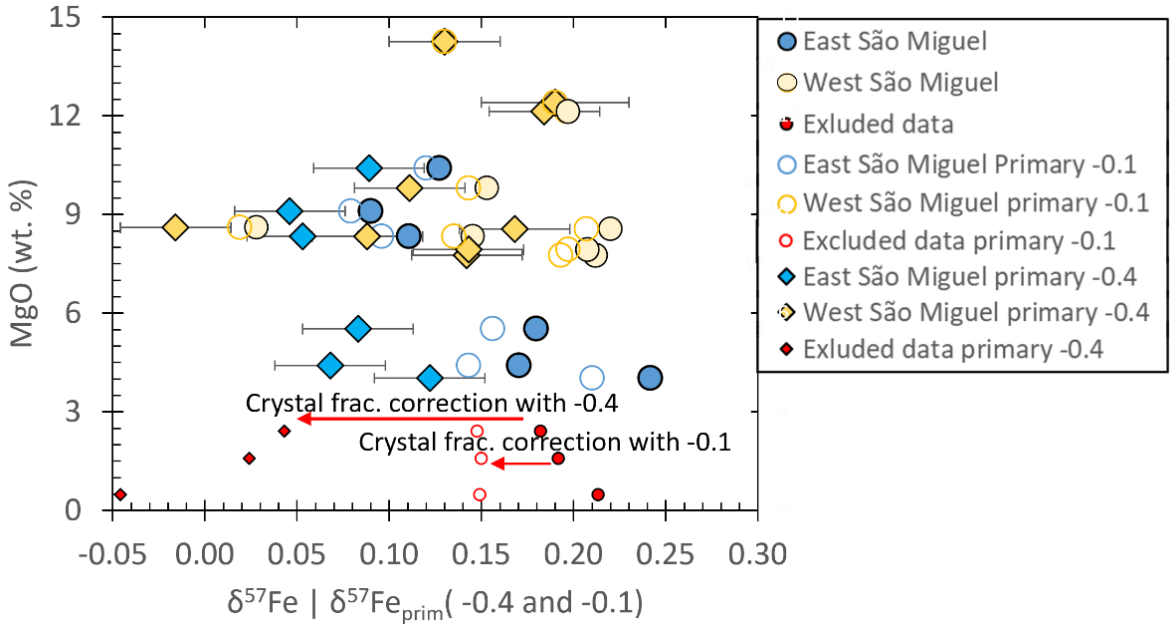

Figure 3. a) Analysed $\delta^{57}Fe$ compositions of eastern and western São Miguel lavas are illustrated as circles and compared to calculated primary melt values $\delta^{57}Fe_{prim}$ (calculated with a fractionation factor

of $\Delta^{57}Fe_{ol\text{-}melt}$ = -0.1*$10^6/T^2$, illustrated as empty circles) and $\delta^{57}Fe_{prim}$ (calculated with a fractionation factor of $\Delta^{57}Fe_{ol\text{-}melt}$ = -0.4*$10^6/T^2$, illustrated as diamonds) vs MgO. Crystal fractionation correction after Nebel et al. (2019); Sossi et al. (2016). Values of error bars shown with ±2 S.E. Error bars just shown for measured $\delta^{57}Fe$ to retain overview. Analysed $\delta^{57}Fe$ of eastern São Miguel samples co-variate with MgO with a MSWD of 1.19.

Table 1. Iron isotope values for São Miguel lavas. Samples with "*" have been analysed at the Durham University. 2 standard error calculated as follows: 2 S.E. = 2 S.D. / $\sqrt{n}$, with *n* being the number of analyses, after Sossi et al. (2015). Each sample has been analysed 2-3 times (n=2-3). $\Delta^{57}Fe_{prim}$ calculated with $\Delta^{57}Fe_{ol\text{-}melt}$ = -0.4*$10^6/T^2$. For major, trace and radiogenic isotope values see Supplementary data II.

Sample	Location	MgO (wt.%)	$\delta^{56}Fe$	±2 S.E.	$\delta^{57}Fe$	±2 S.E.	$\delta^{57}Fe_{prim}$	$\Delta^{57}Fe$	n
SM0140	Sete Cidades	12.41	+0.13	0.02	+0.19	0.04	+0.19	0	2
SM0133	Sete Cidades	8.60	+0.03	0.01	+0.03	0.03	-0.02	0.04	3
SM0102	Sete Cidades	14.26	+0.07	0.03	+0.13	0.01	+0.13	0	3
513DS-1 wr	Sete Cidades	12.13	+0.14	0.01	+0.20	0.02	+0.18	0.01	3
SM9704A	Waist Zone	9.81	+0.04	0.01	+0.15	0.01	+0.11	0.04	2
S1*	Waist Zone	7.76	+0.12	0.02	+0.21	0.03	+0.14	0.07	3
SM7	Waist Zone	8.56	+0.15	0.03	+0.22	0.02	+0.17	0.05	3
S10*	Waist Zone	8.33	+0.10	0.02	+0.15	0.03	+0.09	0.05	2
SP2*	Waist Zone	7.93	+0.13	0.01	+0.21	0.02	+0.14	0.06	2
SM0170	Agua de Pau	4.41	+0.13	0.02	+0.17	0.02	+0.07	0.10	3
SM0128	Nordeste	4.03	+0.16	0.01	+0.24	0.01	+0.12	0.12	3
SM9716	Nordeste	5.52	+0.11	0.01	+0.18	0.01	+0.08	0.10	3
SM0204	Waist Zone	10.41	+0.10	0.01	+0.13	0.02	+0.09	0.04	3
S3*	Waist Zone	8.34	+0.13	0.00	+0.11	0.03	+0.05	0.06	2
SP8*	Waist Zone	9.10	+0.06	0.02	+0.09	0.03	+0.05	0.04	2
Excluded data									
SM0106	Sete Cidades	0.48	+0.15	0.01	+0.21	0.02	-0.05	0.26	3
SM0134	Sete Cidades	2.41	+0.14	0.01	+0.18	0.01	+0.04	0.14	3
515DS-1	Submarine W Sete Cidades	1.58	+0.15	0.01	+0.19	0.02	+0.02	0.17	3
BCR2			+0.10	0.00	+0.13	0.01			3

BHVO1		+0.09	0.03	+0.11	0.02	2
BIR-1*		+0.06	0.01	+0.08	0.01	2
$FeCl_3$*		-0.69	0.01	-1.03	0.01	25

3.5 Discussion

Various factors such as fractionation during partial melting and crystallisation (Teng et al., 2008; Williams et al., 2009; Teng et al., 2013), source mineralogy (Dauphas et al., 2009; Weyer and Ionov, 2007; Williams and Bizimis, 2014; Craddock et al., 2013), source inheritance (Nebel et al., 2019; Konter et al., 2016), mixing process of source lithologies (Nebel et al., 2019) and metasomatism or diffusion (Teng et al., 2011; Sun et al., 2020) influence Fe isotopic compositions of OIB. In the following, we will compare $\delta^{57}Fe_{prim}$ with radiogenic isotope data, major elements and trace elements to evaluate if (5.1) mantle source and mixing processes, (5.2) source mineralogy and melting degree, (5.3) metasomatism and/or (5.4) tectonic setting (e.g., mixing of rift related melt with plume-related mantle material) can explain the Fe isotopic signature of western and eastern São Miguel lavas.

3.5.1 Source dependency of the Fe isotopic signature of primary melts for eastern and western São Miguel

To evaluate the geochemical source dependency of stable Fe isotopes and to elucidate if potential melt mixing processes are causing the variation in radiogenic isotopic systems and stable Fe isotopic signatures, we compare the published $^{208}Pb/^{204}Pb$, $^{206}Pb/^{204}Pb$, $^{87}Sr/^{86}Sr$, $^{143}Nd/^{144}Nd$ values (Beier et al., 2007; Turner et al., 1997; Prytulak et al., 2014) with our new $\delta^{57}Fe_{prim}$ data from western and eastern São Miguel (Fig. 4). Western and eastern São Miguel lavas exhibit very different radiogenic isotope systematics, and our Fe isotope data needs to be placed into this complex context:

The unique radiogenic isotopic signature of eastern São Miguel is characterised by radiogenic Pb and radiogenic Sr and Nd isotopic compositions. To explain the deviation of eastern São Miguel from commonly observed OIB sources in radiogenic isotopic systems, various mantle sources have been proposed over the last decades (Beier et al., 2007; Davies et al., 1989; Elliott et al., 2007; Moreira et al., 2018). Beier et al. (2007), Davies et al. (1989), Genske et al. (2013), Turner et al. (1997), and Widom and Farquhar (2003) have based their

models on mantle source components created from ancient recycled oceanic crust based on $\delta^{18}O$ combined with radiogenic Sr-Nd-Pb isotopic systematics. Furthermore, thick lithospheric roots (infused by metasomatism) or ancient recycled oceanic lithosphere (variably influenced by metasomatism and/or distinct mantle sources) have been suggested for causing the enrichment in radiogenic isotopes (Turner et al., 2007; Elliott et al., 2007; Beier et al., 2007; Widom and Farquhar, 2003). On the basis of radiogenic isotopic compositions and eastern São Miguel's low ^{3}He signature (R/Ra of 0.4-5.55, lower than MORB with R/Ra 8 ± 1), it has been suggested that the source of eastern São Miguel is comprised of ancient, recycled material, subducted at ca. 3 Ga (Moreira et al., 2012; Elliott et al., 2007). Contrary to eastern São Miguel, western São Miguel lavas show a less radiogenic isotopic signature in $^{208}Pb/^{204}Pb$, $^{206}Pb/^{204}Pb$, $^{87}Sr/^{86}Sr$ and $^{143}Nd/^{144}Nd$ (Fig. 4), which has been proposed to represent a common Azores source component (e.g., Beier et al., 2007; Beier et al., 2018). Additionally, He isotopic signatures of western São Miguel are comparable to MORB (Kurz, 1991; Kurz et al., 1990).

When combining radiogenic Sr-Nd-Pb isotopic ratios with stable Fe isotopes, lavas from São Miguel show a positive covariation between $^{143}Nd/^{144}Nd$ and $\delta^{57}Fe_{prim}$ and negative trends between $^{208}Pb/^{204}Pb$, $^{206}Pb/^{204}Pb$ and $^{87}Sr/^{86}Sr$ vs. $\delta^{57}Fe_{prim}$ (Fig. 4c-f). Firstly, these trends between radiogenic isotopes and stable isotopic compositions demonstrate that Fe isotope systematics of São Miguel's lavas are dominated by mantle source variations. As expected, the one outlier, sample SM0133 with $\delta^{57}Fe_{prim}$ -0.02‰, deviates from the correlation, yet shows radiogenic isotopic values in line with the rest of the western São Miguel lavas. The outlier will be discussed further in section 5.4. Source dependency of Fe isotopes, or "inherited Fe isotopic compositions from crustal precursors" have been proposed for MORB as well as other OIB (Konter et al., 2016; Nebel et al., 2019; Sun et al., 2020). It is thus plausible, especially considering that trace element ratios and radiogenic isotopic ratios are source dependent (Elliott et al., 2007; Beier et al., 2007; Widom et al., 1997; Turner et al., 1997; White et al., 1979) that the São Miguel's Fe isotopic variations, at least to a large degree, reflect an inherited Fe isotopic signature from the source as well.

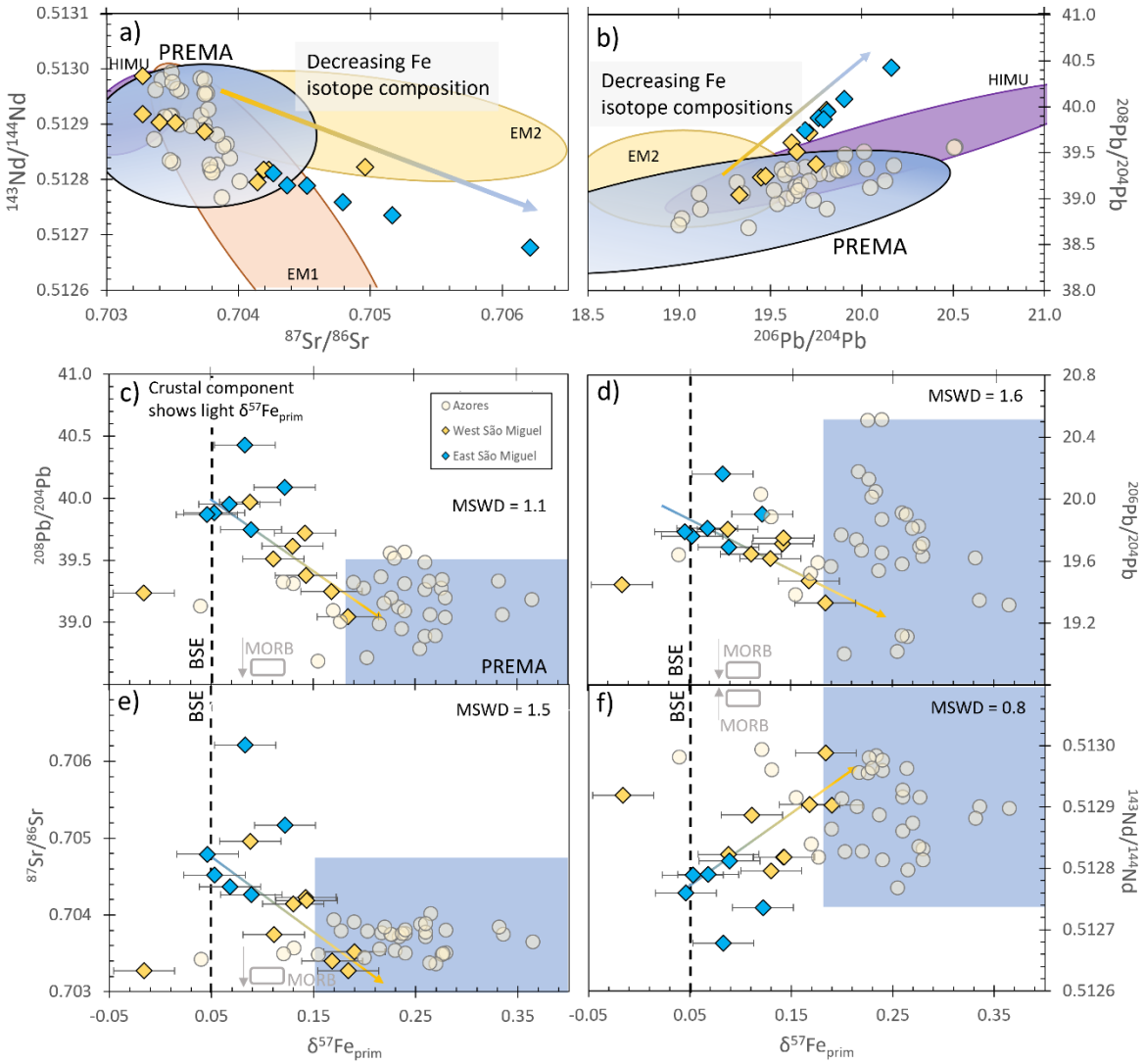

Figure 4. a) $^{87}Sr/^{86}Sr$ vs $^{143}Nd/^{144}Nd$, b) $^{206}Pb/^{204}Pb$ vs $^{208}Pb/^{204}Pb$, and $\delta^{57}Fe_{prim}$ vs c) $^{208}Pb/^{204}Pb$, d) $^{206}Pb/^{204}Pb$, e) $^{87}Sr/^{86}Sr$, f) $^{143}Nd/^{144}Nd$ for eastern and western São Miguel. PREMA area after Hauri et al. (1994), Jackson et al. (2007), Stracke et al. (2005) and White (2015). MORB +0.10 ± 0.01‰ $\delta^{57}Fe_{prim}$ and bulk silicate earth (BSE) +0.05 ± 0.01‰ $\delta^{57}Fe$ are from Sossi et al. (2016). Azores (São Jorge, Pico, Faial, Terceira, João de Castro and Graciosa) are from Soderman et al. (2021). Mean squared weighted deviation (MSWD) calculated after Wendt and Carl (1991).

Enriched radiogenic isotopic signatures in OIB (e.g., EM1) are commonly associated with recycled crustal material, which can be accompanied by small amounts of sediment (Hofmann and White, 1982; Chase, 1981; Stracke et al., 2003; Weaver, 1991). In the mantle, this recycled crustal material is present as eclogite, presumably interacting with the ambient peridotite to form pyroxenite (Sobolev et al., 2007), which can be heavy in Fe isotopes (Nebel et al., 2019; Konter et al., 2016; Soderman et al., 2021). However, eastern São Miguel's lavas, which can

be associated with recycled crustal material due to the enriched radiogenic isotopic signature, show lighter $\delta^{57}Fe_{prim}$ values than western São Miguel ranging from +0.05 to +0.12‰. Western São Miguel lavas with a less enriched radiogenic isotopic signature show heavier $\delta^{57}Fe_{prim}$ values of up to +0.18‰.

Importantly, in all cases, the assigned trends of the combined stable Fe isotopes and radiogenic Sr-Nd-Pb isotopic ratios of eastern and western São Miguel are surprising. One would expect the more enriched radiogenic isotopic signatures to be associated with heavy $\delta^{57}Fe_{prim}$, if the latter is considered to represent a recycled crustal component (Nebel et al., 2019; Konter et al., 2016) or pyroxenite formed from recycled crustal protoliths (Williams and Bizimis, 2014). The less enriched radiogenic Sr-Nd-Pb isotopic component of western São Miguel coincides with samples from other Azores islands and shows a slightly heavier Fe isotopic signature than eastern São Miguel (Fig. 4a-f). If this 'less enriched isotopic signature' is indeed related to a peridotite source, as opposed to eclogite/pyroxenite, it is in contradiction to the widely accepted view that the isotopically less enriched mantle, which is represented by peridotite (Boyet and Carlson, 2006; Hofmann, 1997; Salters and Stracke, 2004; Zindler and Hart, 1986), is associated with an Fe isotopic composition of $\delta^{57}Fe$ = +0.05 ± 0.01‰ (2S.E.; Sossi et al., 2016). To solve this conundrum, we will discuss magmatic processes that could lead to the light Fe isotopic signature of eastern and to the heavy Fe isotopic signature of western São Miguel.

3.5.2 Light Fe isotopes of eastern São Miguel – degree of melting

Isotope fractionation during partial mantle melting, and subsequent crystal fractionation can account for a small variation in Fe isotopes (Teng et al., 2008; Teng et al., 2013; Williams et al., 2009). During partial melting, the crystal bonding dependent partitioning of Fe between liquid and crystalline residue, with ferric iron (Fe^{3+}) being more incompatible than ferrous iron (Fe^{2+}) (Woodland and Koch, 2003), leads to a heavy Fe isotopic signature in the melt. With larger degrees of melting, more olivine enters the melt phase, which leads to a relatively lighter Fe isotopic composition compared to melts that experienced low melting degrees (Williams and Bizimis, 2014).

Beier et al. (2007) and Elliott et al. (2007) compared major elements and trace element ratios to show that Azores islands of São Jorge, Pico, Faial, Terceira, João de Castro and

Graciosa have melting degrees (F) ranging between 4 and 6% (Beier et al., 2013), and are subtly larger than those suggested for São Miguel. Subsequently, Beier et al. (2013) showed that the melting degree of São Miguel lavas on average is similar to that of Santa Maria, an Azores island southeast of São Miguel, with an estimation of ca. F = 2 – 3%. The changes in degree of partial melting may be associated with changes in lithospheric thickness from west to east of the Azores archipelago (Standish et al., 2008; Prytulak and Elliott, 2007). Although there are no apparent differences in melting degrees between and within eastern and western São Miguel (Beier et al., 2013), source compositional variability may be affecting calculations on subtle differences in degrees of melting. Nonetheless, the decoupling of REE, major element systematics and $\delta^{57}Fe_{prim}$ (e.g., $\delta^{57}Fe_{prim}$ vs $(Sm/Yb)_{PM}$ and Ti_8; see Supplementary data I Fig. S1) indicates that the variation in Fe isotopes *between* eastern and western São Miguel is not a function of the degree of partial melting in the São Miguel mantle source. It is, however, intriguing that the low melting degree of eastern and western São Miguel results in lighter Fe isotopic compositions compared to the Azores islands of São Jorge, Pico, Faial, Terceira, João de Castro and Graciosa (Fig. 4). Melting at higher melt degrees results for the Azores lavas in low Ba/Nb, Rb/Nb and La/Nb at heavier $\delta^{57}Fe_{prim}$, whereas western São Miguel lavas show lighter $\delta^{57}Fe_{prim}$ at similar trace element ratios. Eastern São Miguel lavas, showing the lightest $\delta^{57}Fe_{prim}$, deviate towards elevated Rb/Nb and La/Nb ratios. Such enrichment in incompatible elements, here pronounced deviation of eastern São Miguel in $\delta^{57}Fe_{prim}$ vs Rb and La (Fig. 4c, e), combined with light $\delta^{57}Fe_{prim}$ suggests that the otherwise enriched component of eastern São Miguel might have experienced fractionation processes other than crystal fractionation, that lead to a light Fe isotopic signature (e.g., mantle metasomatism in Fig. 4).

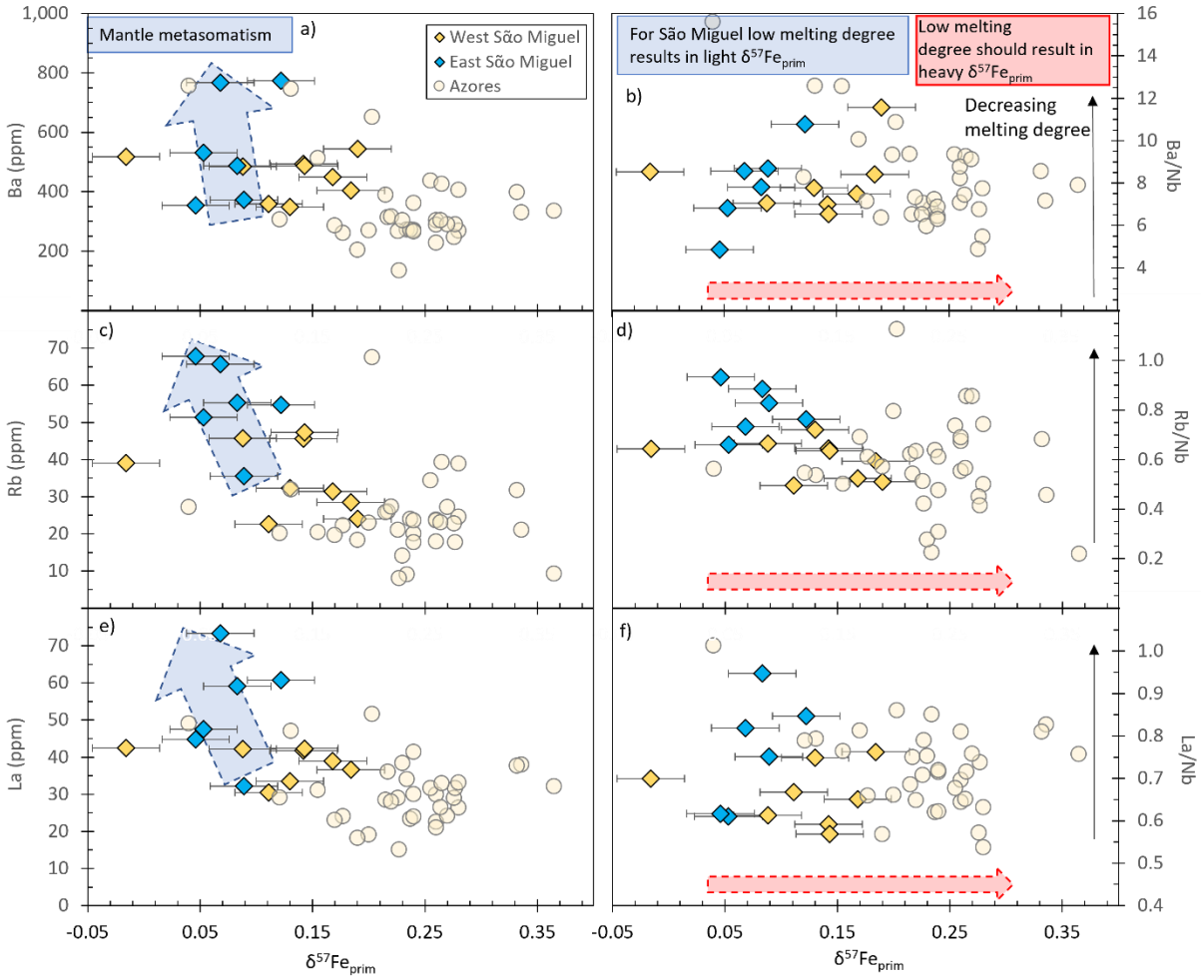

Figure 4. a) Ba, b) Ba/Nb, c) Rb, d) Rb/Nd, e) La, f) La/Nb vs $\delta^{57}Fe_{prim}$. Azores (São Jorge, Pico, Faial, Terceira, João de Castro and Graciosa) are from Soderman et al. (2021).

3.5.3 Light Fe isotopes of eastern São Miguel – mantle metasomatism

To characterise melts and fluids that can act as metasomatising agents in the mantle, it is crucial to understand the Fe isotopic composition of metasomatising agents and how such material alters the inherited Fe isotopic composition of upwelling mantle material. Considering the subduction of MORB and a small input of continental sediments, which show a wide range with $\delta^{57}Fe$ +0.08 to +0.90‰ (Du et al., 2017) or arc system sediments with $\delta^{57}Fe$ +0.17‰ (Nebel et al., 2015) and loss of light Fe isotopes during hydrothermal alteration (El Korh et al., 2017), most subducted recycled slab components are expected to show a heavy Fe isotopic signature of $\delta^{57}Fe$ > +0.15‰. However, in a model in which enriched mantle components (where enriched refers to radiogenic isotopes) are derived from subducted oceanic crust and/or lithosphere and sediments, a subduction component must exist that is

also isotopically light and not heavy in Fe isotopes. Light Fe isotope values have been associated with slab derived melts, subducted sediments, CO_2-rich fluids or carbonatitic melts (Beard and Johnson, 2004; Williams et al., 2005; Weyer and Ionov, 2007; Poitrasson et al., 2013; Zhao et al., 2010; Zhao et al., 2012; Johnson et al., 2010; Rouxel et al., 2003).

Mantle metasomatism involving such metasomatising agents has been described at several OIB locations, for example, Hawai'i, Pitcairn, Samoa, Fernando de Noronha Island, Kerguelen Island, and the Island of Santa Maria as part of the Azores (Hauri et al., 1993; Schiano et al., 1994; Mattielli et al., 1999; Kogarko et al., 2001; Beier et al., 2013; Wang et al., 2018; Sobolev et al., 2000; Weyer and Ionov, 2007; Poitrasson et al., 2013). Based on element ratios of Ti/Sm and K/La, Beier et al. (2013) show that mixing of carbonated peridotite with melts from a volatile free garnet peridotite (ratio 20:80) can explain the geochemical composition of Santa Maria. However, a carbonatite melt-mantle mixing model (Supplementary data I Fig S3) and mass balance calculations show that the carbonatitic melt must be unrealistically heavy to achieve the average Fe isotopic composition of eastern São Miguel's lavas: Considering mass balance calculations, 1% of a carbonatitic component cannot explain the Fe isotopic composition of eastern São Miguel's lavas: assuming that a carbonatite and anhydrous peridotite melt show equal proportions of Fe and considering a contribution of 1% carbonatitic component with $\delta^{57}Fe_{carbonatite}$ = -0.45‰ to a peridotite with $\delta^{57}Fe_{prim}$ = +0.05‰, by mass balance, a $\delta^{57}Fe_{prim}$ of ~ +0.05‰ (min. $\delta^{57}Fe_{prim}$ of eastern São Miguel lavas) can be achieved. The value of $\delta^{57}Fe_{carbonatite}$ = -0.45‰ is a reasonable estimation of carbonatite magmas that are in equilibrium with silicate melts (Johnson et al., 2010). To achieve the average $\delta^{57}Fe_{prim}$ of ~ +0.08‰ of eastern São Miguel's lavas, a mixture of peridotite with $\delta^{57}Fe_{prim}$ = +0.05‰ and $\delta^{57}Fe_{carbonatite}$ = +3.0‰ (ratio 99:1) is needed. Such heavy Fe isotopic compositions have not been analysed in carbonatites (Johnson et al., 2010). Irrespective of the true proportions and endmember compositions, considering simplified mass balance calculations, it is apparent that 1% of a carbonatitic component shows either no change between the Fe isotopic composition of the source and the melt or must be unrealistically heavy to achieve the average Fe isotopic composition of eastern São Miguel's lavas. Increasing the mixing ratio to 80:20 will result in $\delta^{57}Fe_{prim}$ < +0.05‰ and, additionally, contradicts our calculated carbonatite melt-mantle mixing model (Supplementary data I Fig

S3). Thus, we exclude the possibility of a carbonatitic melt as a metasomatising agent for eastern São Miguel's lavas.

A characterisitic that might indicate mantle metasoamtism is the enrichment in K_2O and Rb/Sr of eastern São Miguel compared to western São Miguel and other Azores islands (Fig. 5). This enrichment indicates the contribution of a potassium (K)-rich mineral, possibly amphibole, phlogopite or its high-pressure equivalent K-hollandite (LaTourrette et al., 1995). Phlogopite is a mineral associated with mantle metasomatism (Xiao et al., 2010; Zhao et al., 2012; Safonov et al., 2019) showing heavy $\delta^{57}Fe$ +0.32 to +0.49‰ (Zhao et al., 2012; Zhao et al., 2010). An interaction of phlogopite with the melt sourcing eastern São Miguel is expected to result in heavy Fe isotope values. Interestingly, with the enrichment in K and Rb/Sr, $\delta^{57}Fe_{prim}$ is decreasing (Fig. 6a, c) and $^{87}Sr/^{86}Sr$ is increasing (Fig. 6b, d). Solutions to this conundrum could be that (1) the metasomatic agent with a light Fe isotopic composition altered the Fe isotopic composition of eastern São Miguel's lavas to a larger degree than phlogopite; (2) phlogopite was produced at a later stage as a by-product of metasomatism (Zhao et al., 2017); (3) phlogopite is a cryptic residue, which would explain the covariation of Sr, Nd and Pb isotopes with K_2O and Rb/Sr (Fig. 5).

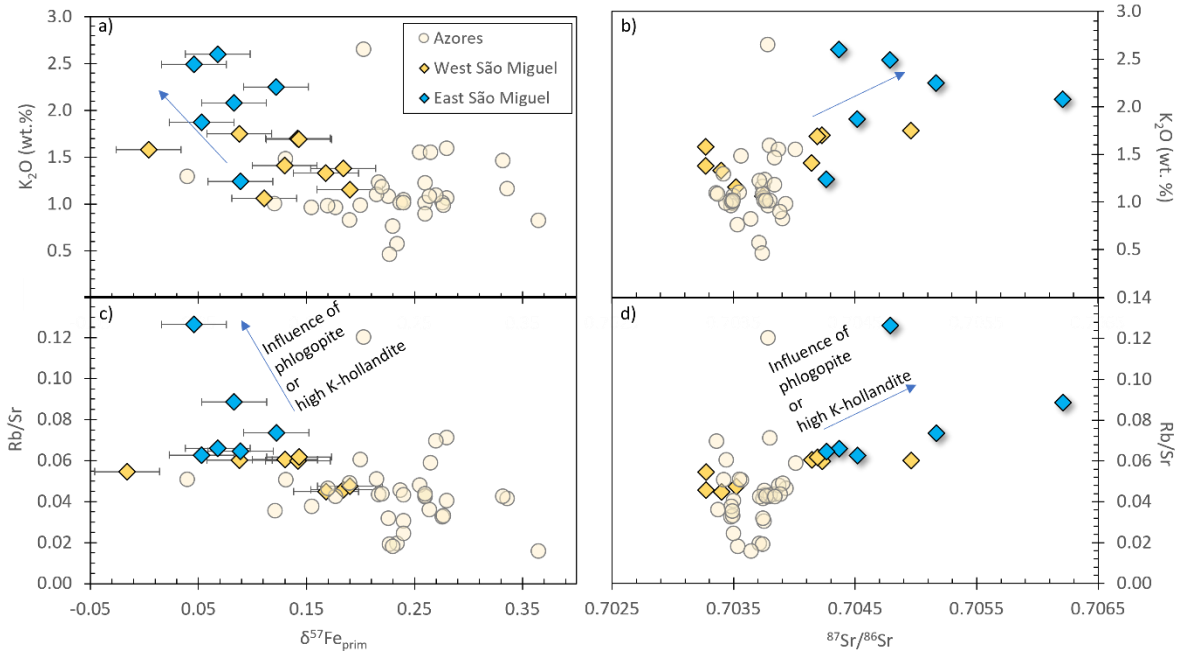

Figure 5. a) $\delta^{57}Fe_{prim}$ vs K_2O, b) $^{87}Sr/^{86}Sr$ vs K_2O, c) $\delta^{57}Fe_{prim}$ vs Rb/Sr, d) $^{87}Sr/^{86}Sr$ vs Rb/Sr. Increasing K_2O and Rb/Sr indicate the influence of phlogopite or K-rich hollandite. Azores (São Jorge, Pico, Faial, Terceira, João de Castro and Graciosa) from Soderman et al. (2021).

The sum of observations, including the low melting degree (Beier et al., 2013), indicate that a small volume of a hydrous silicic K-rich melt could act as a metasomatizing agent. This is further supported by covariations between K_2O and Rb/Sr and radiogenic isotopes (e.g., Fig. 6b, d and Supplementary data I Fig. S3). Considering that small amounts of such metasomatising agent mixes with peridotite, the range in $\delta^{57}Fe_{prim}$ of +0.05 to +0.12‰ can be reached, depending on the mixing ratio (e.g., ratios between 99:1 and 80:20) of eastern São Miguel's lavas.

Beier et al. (2007) discuss the possibility of a basaltic melt as a metasomatic agent but conclude that a basaltic melt as recycled oceanic crust, and not as a metasomatising agent, can explain trace element patterns and radiogenic isotope signatures of eastern São Miguel's lavas. Given the good co-variation between radiogenic isotopic ratios and $\delta^{57}Fe_{prim}$ we cannot exclude this possibility. However, if eastern São Miguel's lavas are sourced by a simple recycled oceanic crust, we would have expected an $\delta^{57}Fe_{prim} > +0.15$‰ (Williams and Bizimis, 2014). Furthermore, a "*basaltic under-plate within an ancient, recycled oceanic lithosphere*" has been suggested by Elliott et al. (2007). Such ancient lithosphere is presumably lighter than the BSE in its Fe isotopic composition (Nebel et al., 2014), because it has not experienced fractionation processes compared to an oceanic crust which has a $\delta^{57}Fe_{prim}$ of +0.10‰ (Sossi et al., 2016). The Fe isotopic composition of the underplated basalt can only be assumed. Expecting that this basalt has experienced fractionation process, we suggest that such underplated basalt shows a $\delta^{57}Fe_{prim} \geq +0.10$‰, which is equal to or heavier than MORB. Mixing of ancient lithosphere with $\delta^{57}Fe_{prim} < +0.05$‰, underplated basalts with $\delta^{57}Fe_{prim} \geq +0.10$‰, and peridotite with $\delta^{57}Fe_{prim} = +0.05$‰, results in lighter Fe isotopic compositions than observed for lavas from eastern São Miguel. Note, if the basaltic underplate iron isotopic compositions of $\delta^{57}Fe_{prim} \geq +0.3$‰ the Fe isotopic signature of eastern São Miguel lavas can be achieved.

The mantle material sourcing eastern São Miguel remains unresolved; however, it is striking that extreme radiogenic isotopic ratios show a light Fe isotopic composition. Western São Miguel lavas demand another explanation given their less enriched radiogenic isotopic signature and heavy Fe isotopes with $\delta^{57}Fe_{prim} \geq +0.09$‰. Thus, a different scenario is needed to explain the heavy Fe isotopic signature of western São Miguel's lavas.

3.5.4 The heavy Fe isotopic signature of western São Miguel – Influence of tectonic setting

Western São Miguel are isotopically too heavy (1) to be ascribed to metasomatism by silicic or carbonatitic melt with a light Fe isotopic composition and (2) to simply reflect partial mantle melting processes of peridotite, which, following modelling, do not exceed values of $d^{57}Fe$ +0.15‰ for a melt fraction < 0.1 (Foden et al., 2018).

A clue as to why western São Miguel samples are isotopically heavier is their geographic location, which argues for a crustal control on the geochemical signature of these lavas. When projected against the longitude and tectonic structure of São Miguel (Fig. 6), it becomes apparent that all lavas except the outlier sample SM0133 are located along the Terceira Rift, a tectonic structure that runs through the NW part of the island. Melting at a rift setting (Terceira Rift) may thus have a considerable influence on the Fe isotopic composition of western São Miguel's lavas, and in analogue also radiogenic isotopic systematics. More MORB-like radiogenic isotopic systematics in Sr-Nd-Pb isotopes indicate the presence of an upper mantle melting component, which is in line with low, MORB-like $^{3}He/^{4}He$ ratios associated with the Terceira Rift (Madureira et al., 2011; Kurz, 1991; Kurz et al., 1990).

Compared to OIB, MORB show a homogenous Fe isotopic signature of $\delta^{57}Fe$ +0.15 ± 0.01‰ (Chen et al., 2019; Teng et al., 2013) but can deviate towards heavier Fe isotopes with $\delta^{57}Fe \geq$ +0.15‰ (Sun et al., 2020). Such heavy Fe isotopic signatures at mid-ocean ridge settings have previously been associated with melting of pyroxenitic veins in the lithosphere (Sun et al., 2020). A contribution of a pyroxenitic source to explain heavy Fe isotopic signatures has been discussed for other Azores locations (São Jorge, Pico, Faial, Terceira, João de Castro and Graciosa; Soderman et al., 2021). If such Fe isotopic heterogeneities, tentatively coupled with a more fertile source, exist as "streaks" in the lithosphere, this may explain some of the heterogeneity observed in OIB.

Alternatively, ultraslow spreading ridge settings have recently been associated with heavy Fe isotopic compositions (Richter et al., 2021). Is has been argued that lavas erupting at ultraslow spreading ridges preserves the inherited Fe isotopic composition of the source (Richter et al., 2021), which aligns with our samples. Simple addition of a low-degree melt fraction of upper mantle peridotite, associated with the Terceira Rift, appears to be the most

plausible explanation for the observed variability in Fe and radiogenic isotopes. The most westerly samples (outlier excluded) in Figure 6b would therein reflect the most affected lavas through this process, whereas samples towards the east experienced a dilution effect through more plume melt components.

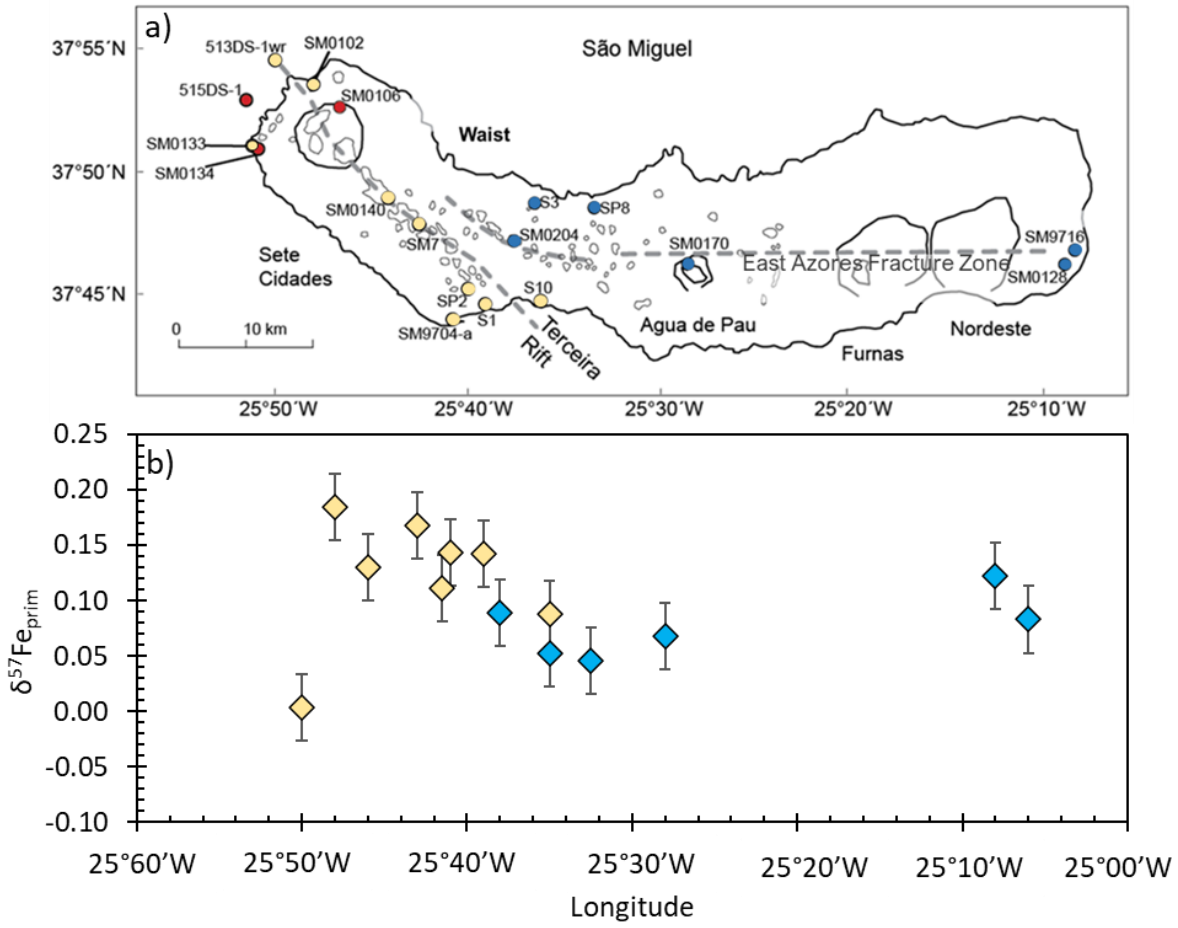

Figure 7. a) Map modified after Beier et al. (2007) showing the sample localities, detailed description in Fig. 1b. b) Longitude vs $\delta^{57}Fe_{prim}$ with western São Miguel samples along the Terceira Rift showing heavier Fe isotopes than eastern São Miguel. An overlap occurs for lavas on the Waist Zone. Agua de Pau and Nordeste show comparable Fe isotope data to the Waist Zone. One sample of western São Miguel deviates from eastern and western São Miguel by showing a $\delta^{57}Fe_{prim}$ of -0.02‰. This sample lies not on the Terceira Rift.

3.6 Geodynamic implications

The distinction of western and eastern São Miguel can be made based on their Fe isotope systematics, despite the binary mixing array in radiogenic isotopes. A separate plumbing system beneath eastern and western São Miguel has previously been describe by Haase and

Beier (2003) to explain the diverse radiogenic isotopic signature of eastern and western São Miguel. In the scenario advocated here, eastern São Miguel shows a lighter Fe isotopic composition with more radiogenic isotopic ratios than western São Miguel. Covariations between radiogenic isotopic ratios of Sr, Nd and Pb with stable Fe isotopes of the primary melt suggest two different sources for eastern and western São Miguel.

3.7 Conclusions

Combined radiogenic Sr-Nd-Pb mantle array proxies with stable Fe isotopic compositions of primary melts from western and eastern São Miguel reveal a complex mantle melting scenario. A correction for igneous differentiation only erases minor variability in Fe isotopic compositions. Consequently, the Fe isotope variability in lavas from São Miguel is not only dependent on differentiation processes occurring during magmatic cooling but also strongly depends on the initial Fe isotopic composition of mantle components. Based on co-variations of stable Fe and radiogenic Sr-Nd-Pb isotopes, the melting regime below São Miguel requires a scenario in which eastern São Miguel represents a component enriched in radiogenic isotopes and light in Fe isotopes. Mass balance calculations revealed that a carbonatitic component acting as a metasomatising agent cannot account for this light Fe isotopic composition. Rather, the mantle component is suggested to be derived from a source that might have experienced mantle metasomatism by a silicic K-rich melt. This indicates that other light Fe isotopes in OIB settings may also be related to mantle metasomatism, noting that this type of overprint can be very diverse in composition and associated radiogenic isotope systematics.

The heavy Fe isotopic signature of western São Miguel's lavas is likely influenced by melting at an ultraslow rift setting. Here, western São Miguel's lavas might have experienced enrichment in Fe isotopes and incompatible elements by partial melting of presumably peridotite of lower crustal assemblages. The superimposed addition of this component to the original São Miguel lavas creates a mixing trend in radiogenic isotopes, in parts obscuring the true nature of a common mantle source underneath the island.

Acknowledgements

We thank Edward Inglis and Geoff Nowell, who helped with the sample preparation and Fe isotope analyses at the Durham University. HMW acknowledges funding from a NERC Consortia Grant ("Deep Volatiles"; NE/M000303/1) and an ERC Consolidator Grants ("HabitablePlanet"; 306655). ON acknowledges funding from the Australian Research Council (DP180100852).

3.8 References

Asimow, P.D., Dixon, J. and Langmuir, C. (2004) A hydrous melting and fractionation model for mid-ocean ridge basalts: Application to the Mid-Atlantic Ridge near the Azores. *Geochemistry, Geophysics, Geosystems* **5**, Q01E16.

Beard, B.L. and Johnson, C.M. (2004) Inter-mineral Fe isotope variations in mantle-derived rocks and implications for the Fe geochemical cycle. *Geochimica et Cosmochimica Acta* **68**, 4727-4743.

Béguelin, P., Bizimis, M., Beier, C. and Turner, S. (2017) Rift-plume interaction reveals multiple generations of recycled oceanic crust in Azores lavas. *Geochimica et Cosmochimica Acta* **218**, 132-152.

Beier, C., Haase, K.M., Abouchami, W., Krienitz, M.S. and Hauff, F. (2008) Magma genesis by rifting of oceanic lithosphere above anomalous mantle: Terceira Rift, Azores. *Geochemistry, Geophysics, Geosystems* **9**, Q12013.

Beier, C., Haase, K.M. and Brandl, P.A. (2018) Melting and mantle sources in the Azores, Volcanoes of the Azores. Springer, pp. 251-280.

Beier, C., Haase, K.M. and Hansteen, T.H. (2006) Magma Evolution of the Sete Cidades Volcano, São Miguel, Azores. *Journal of Petrology* **47**, 1375-1411.

Beier, C., Haase, K.M. and Turner, S.P. (2012) Conditions of melting beneath the Azores. *Lithos* **144**, 1-11.

Beier, C., Mata, J., Stöckhert, F., Mattielli, N., Brandl, P., Madureira, P., Genske, F., Martins, S.,

Madeira, J. and Haase, K. (2013) Geochemical evidence for melting of carbonated peridotite on Santa Maria Island, Azores. *Contributions to Mineralogy and Petrology* **165**, 823-841.

Beier, C., Stracke, A. and Haase, K.M. (2007) The peculiar geochemical signatures of Sao Miguel (Azores) lavas: Metasomatised or recycled mantle sources? *Earth and Planetary Science Letters* **259**, 186-199.

Bézos, A. and Humler, E. (2005) The Fe3+/ΣFe ratios of MORB glasses and their implications for mantle melting. *Geochimica et Cosmochimica Acta* **69**, 711-725.

Blichert-Toft, J. and Albarede, F. (1998) Hafnium isotope stratigraphy of Mauna Loa and Mauna Kea lavas from the Hawaii Scientific Drilling Project core. *Mineralogical Magazine* **62**, 166-167.

Booth, B., Croasdale, R. and Walker, G.P.L. (1978) A Quantitative Study of Five Thousand Years of Volcanism on Sao Miguel, Azores. *Philosophical Transactions of the Royal Society of London. Series A, Mathematical and Physical Sciences (1934-1990)* **288**, 271-319.

Boyet, M. and Carlson, R.W. (2006) A new geochemical model for the Earth's mantle inferred from 146Sm– 142Nd systematics. *Earth and Planetary Science Letters* **250**, 254-268.

Chase, C.G. (1981) Oceanic island Pb: two-stage histories and mantle evolution. *Earth and Planetary Science Letters* **52**, 277-284.

Chen, S., Niu, Y., Guo, P., Gong, H., Sun, P., Xue, Q., Duan, M. and Wang, X. (2019) Iron isotope fractionation during mid-ocean ridge basalt evolution: Evidence from lavas on the East Pacific Rise at 10°30'N and its implications. *Geochimica et Cosmochimica Acta* **267**, p 227-239.

Cheng, T., Nebel, O., Sossi, P.A. and Chen, F. (2014) Refined separation of combined Fe-Hf from rock matrices for isotope analyses using AG-MP-1M and Ln-Spec chromatographic extraction resins. *MethodsX* **1**, 144-150.

Craddock, P.R. and Dauphas, N. (2010) Iron Isotopic Compositions of Geological Reference

Materials and Chondrites. *Geostandards and Geoanalytical Research* **35**, 101-123.

Craddock, P.R., Warren, J.M. and Dauphas, N. (2013) Abyssal peridotites reveal the near-chondritic Fe isotopic composition of the Earth. *Earth and Planetary Science Letters* **365**, 63-76.

Dauphas, N., Craddock, P.R., Asimow, P.D., Bennett, V.C., Nutman, A.P. and Ohnenstetter, D. (2009) Iron isotopes may reveal the redox conditions of mantle melting from Archean to Present. *Earth and Planetary Science Letters* **288**, 255-267.

Davies, G.R., Cliff, R.A., Norry, M.J. and Gerlach, D.C. (1989) A combined chemical and Pb-Sr-Nd isotope study of the Azores and Cape Verde hot-spots: The geodynamic implications. *Geological Society Special Publication* **42**, 231-255.

Du, D.-H., Wang, X.-L., Yang, T., Chen, X., Li, J.-Y. and Li, W. (2017) Origin of heavy Fe isotope compositions in high-silica igneous rocks: A rhyolite perspective. *Geochimica et Cosmochimica Acta* **218**, 58-72.

Duncan, A.M., Guest, J.E., Wallenstein, N. and Chester, D.K. (2015) The Older Volcanic Complexes of São Miguel, Azores: Nordeste and Povoação. *Geological Society, London, Memoirs* **44**, 147-153.

El Korh, A., Luais, B., Deloule, E. and Cividini, D. (2017) Iron isotope fractionation in subduction-related high-pressure metabasites (Ile de Groix, France). *Contributions to Mineralogy and Petrology* **172**, 1-19.

Elliott, T., Blichert-Toft, J., Heumann, A., Koetsier, G. and Forjaz, V. (2007) The origin of enriched mantle beneath São Miguel, Azores. *Geochimica et Cosmochimica Acta* **71**, 219-240.

Fitton, J.G., Saunders, A.D., Kempton, P.D. and Hardarson, B.S. (2003) Does depleted mantle form an intrinsic part of the Iceland plume? *Geochemistry, Geophysics, Geosystems* **4**, 1032.

Foden, J., Sossi, P.A. and Nebel, O. (2018) Controls on the iron isotopic composition of global arc magmas. *Earth and Planetary Science Letters* **494**, 190-201.

Forjaz, V.H. (1986) Ilha de S. Miguel (Acores)—Carta tectónica na escala 1: 50.000. *Doc. Int. CV/INIC* **9**, 86.

French, S.W. and Romanowicz, B. (2015) Broad plumes rooted at the base of the Earth's mantle beneath major hotspots. *Nature* **525**, 95.

Genske, F.S., Beier, C., Haase, K.M., Turner, S.P., Krumm, S. and Brandl, P.A. (2013) Oxygen isotopes in the Azores islands: Crustal assimilation recorded in olivine. *Geology* **41**, 491-494.

Haase, K.M. and Beier, C. (2003) Tectonic control of ocean island basalt sources on São Miguel, Azores? *Geophysical Research Letters* **30**, 1856.

Hart, S.R., Hauri, E., Oschmann, L.A. and Whitehead, J.A. (1992) Mantle Plumes and Entrainment: Isotopic Evidence. *Science* **256**, 517.

Hauri, E.H., Shimizu, N., Dieu, J.J. and Hart, S.R. (1993) Evidence for hotspot-related carbonatite metasomatism in the oceanic upper mantle. *Nature (London)* **365**, 221-227.

Hauri, E.H., Whitehead, J.A. and Hart, S.R. (1994) Fluid dynamic and geochemical aspects of entrainment in mantle plumes. *Journal of Geophysical Research: Solid Earth* **99**, 24275-24300.

Herzberg, C. (2011) Identification of Source Lithology in the Hawaiian and Canary Islands: Implications for Origins. *Journal of Petrology* **52**, 113-146.

Hofmann, A.W. (1997) Mantle geochemistry: the message from oceanic volcanism. *Nature* **385**, 219.

Hofmann, A.W. (2003) Sampling Mantle Heterogeneity through Oceanic Basalts: Isotopes and Trace Elements, in Treatise on Geochemistry: The Mantle and Core, edited by R. W. Carlson, H.D. Holland, and K.K. Turekian. Elsevier, New York, pp. 61-101.

Hofmann, A.W. and Farnetani, C.G. (2013) Two views of Hawaiian plume structure.

Geochemistry, Geophysics, Geosystems **14**, 5308-5322.

Hofmann, A.W. and White, W.M. (1982) Mantle plumes from ancient oceanic crust. *Earth and Planetary Science Letters* **57**, 421-436.

Hofmann, A.W. and White, W.M. (1983) Ba, Rb and Cs in the Earth's mantle. *Zeitschrift für Naturforschung A* **38**, 256-266.

Jackson, M.G., Kurz, M.D., Hart, S.R. and Workman, R.K. (2007) New Samoan lavas from Ofu Island reveal a hemispherically heterogeneous high 3He/ 4He mantle. *Earth and Planetary Science Letters* **264**, 360-374.

Johnson, C., Bell, K., Beard, B. and Shultis, A. (2010) Iron isotope compositions of carbonatites record melt generation, crystallization, and late-stage volatile-transport processes. *Mineralogy and Petrology* **98**, 91-110.

Johnson, C.L., Wijbrans, J.R., Constable, C.G., Gee, J., Staudigel, H., Tauxe, L., Forjaz, V.-H. and Salgueiro, M. (1998) 40Ar/39Ar ages and paleomagnetism of Sao Miguel lavas, Azores. *Earth and Planetary Science Letters* **160**, 637-649.

King, S.D. and Adam, C. (2014) Hotspot swells revisited. *Physics of the Earth and Planetary Interiors* **235**, 66.

Kogarko, L., Kurat, G. and Ntaflos, T. (2001) Carbonate metasomatism of the oceanic mantle beneath Fernando de Noronha Island, Brazil. *Contributions to Mineralogy and Petrology* **140**, 577-587.

Konter, J.G., Pietruszka, A.J., Hanan, B.B., Finlayson, V.A., Craddock, P.R., Jackson, M.G. and Dauphas, N. (2016) Unusual δ56Fe values in Samoan rejuvenated lavas generated in the mantle. *Earth and Planetary Science Letters* **450**, 221-232.

Koppers, A.A., Becker, T.W., Jackson, M.G., Konrad, K., Müller, R.D., Romanowicz, B., Steinberger, B. and Whittaker, J.M. (2021) Mantle plumes and their role in Earth processes. *Nature Reviews Earth & Environment*, 1-20.

Kurz, M. (1991) Noble gas isotopes in oceanic basalts: Controversial constraints on mantle models. *Applications of Radiogenic Isotope Systems to Problems in Geology*, 259-286.

Kurz, M., Kammer, D., Gulessarian, A. and Moore, R. (1990) Isotopic variations within oceanic islands: He, Sr and Pb isotopes in basalts from São Miguel, Azores. *Eos* **71**, 657.

Larrea, P., França, Z., Widom, E. and Lago, M. (2018) Petrology of the Azores Islands, Volcanoes of the Azores. Springer, pp. 197-249.

Lassiter, J. and Hauri, E. (1998) Osmium-isotope variations in Hawaiian lavas: evidence for recycled oceanic lithosphere in the Hawaiian plume. *Earth and Planetary Science Letters* **164**, 483-496.

LaTourrette, T., Hervig, R.L. and Holloway, J.R. (1995) Trace element partitioning between amphibole, phlogopite, and basanite melt. *Earth and Planetary Science Letters* **135**, 13-30.

Lekic, V., Cottaar, S., Dziewonski, A. and Romanowicz, B. (2012) Cluster analysis of global lower mantle tomography: A new class of structure and implications for chemical heterogeneity. *Earth and Planetary Science Letters* **357-358**, 68-77.

Madureira, P., Moreira, M., Nunes, J.C., Lourenço, N., Gautheron, C., Carvalho, M.d.R., Mata, J. and Pinto de Abreu, M. (2011) He and Ne isotopic ratios from the Terceira Rift (Azores): Constraints on the boundary between Eurasia and Nubia mantle sources.

Mattielli, N., Weis, D., Scoates, J.S., Shimizu, N., GreGoire, M., Mennessier, J.P., Cottin, J.Y. and Giret, A. (1999) Evolution of Heterogeneous Lithospheric Mantle in a Plume Environment Beneath the Kerguelen Archipelago. *Journal of Petrology* **40**, 1721-1744.

McCoy-West, A.J., Fitton, J.G., Pons, M.-L., Inglis, E.C., Williams, H.M., (2018) The Fe and Zn isotope composition of deep mantle source regions: Insights from Baffin Island picrites. *Geochimica et Cosmochimica Acta* **238,** 542-562. 10.1016/j.gca.2018.07.021.

Métrich, N., Zanon, V., Créon, L., Hildenbrand, A., Moreira, M. and Marques, F.O. (2014) Is the 'Azores hotspot'a wetspot? Insights from the geochemistry of fluid and melt inclusions

in olivine of Pico basalts. *Journal of Petrology* **55**, 377-393.

Moreira, M., Kanzari, A. and Madureira, P. (2012) Helium and neon isotopes in São Miguel island basalts, Azores Archipelago: New constraints on the "low 3He" hotspot origin. *Chemical Geology* **322-323**, 91-98.

Moreira, M.A., Madureira, P. and Mata, J. (2018) Noble gas constraints on the origin of the Azores hotspot, Volcanoes of the Azores. Springer, pp. 281-299.

Nebel, O., Campbell, I.H., Sossi, P.A. and Van Kranendonk, M.J. (2014) Hafnium and iron isotopes in early Archean komatiites record a plume-driven convection cycle in the Hadean Earth. *Earth and Planetary Science Letters* **397**, 111-120.

Nebel, O., Sossi, P.A., Bénard, A., Arculus, R.J., Yaxley, G.M., Woodhead, J.D., Rhodri Davies, D. and Ruttor, S. (2019) Reconciling petrological and isotopic mixing mechanisms in the Pitcairn mantle plume using stable Fe isotopes. *Earth and Planetary Science Letters* **521**, 60-67.

Nebel, O., Sossi, P.A., Bénard, A., Wille, M., Vroon, P.Z. and Arculus, R.J. (2015) Redox-variability and controls in subduction zones from an iron-isotope perspective. *Earth and Planetary Science Letters* **432**, 142-151.

Nebel, O., Sossi, P.A., Foden, J., Bénard, A., Brandl, P.A., Stammeier, J.A., Lupton, J., Richter, M. and Arculus, R.J. (2018) Iron isotope variability in ocean floor lavas and mantle sources in the Lau back-arc basin. *Geochimica et Cosmochimica Acta* **241**, 150-163.

Palme, H. and O'Neill, H.S.C. (2014) Cosmochemical Estimates of Mantle Composition, in: Carlson, R.W.E. (Ed.), Treatise on Geochemistry. Elsevier B.V., Amsterdam, pp. 1-38.

Pietruszka, A.J., Norman, M.D., Garcia, M.O., Marske, J.P. and Burns, D.H. (2013) Chemical heterogeneity in the Hawaiian mantle plume from the alteration and dehydration of recycled oceanic crust. *Earth and Planetary Science Letters* **361**, 298-309.

Poitrasson, F., Delpech, G. and Gregoire, M. (2013) On the iron isotope heterogeneity of lithospheric mantle xenoliths: implications for mantle metasomatism, the origin of

basalts and the iron isotope composition of the Earth. *Contributions to mMineralogy and Petrology* **165**, 1243-1258.

Prytulak, J., Avanzinelli, R., Koetsier, G., Kreissig, K., Beier, C. and Elliott, T. (2014) Melting versus contamination effects on U-238-Th-230-Ra-226 and U-235-Pa-231 disequilibria in lavas from Sao Miguel, Azores. *Chemical Geology* **381**, 94-109.

Prytulak, J. and Elliott, T. (2007) TiO2 enrichment in ocean island basalts. *Earth and Planetary Science Letters* **263**, 388-403.

Richter, M., Nebel, O., Schwindinger, M., Nebel-Jacobsen, Y. and Dick, H.J. (2021) Competing effects of spreading rate, crystal fractionation and source variability on Fe isotope systematics in mid-ocean ridge lavas. *Scientific Reports* **11**, 1-15.

Roeder, P. and Emslie, R. (1970) Olivine-liquid equilibrium. *Contributions to Mineralogy and Petrology* **29**, 275-289.

Romer, R.H., Beier, C., Haase, K.M., Eberts, A. and Hübscher, C. (2021) The evolution of central volcanoes in ultraslow rift systems: Constraints from D. João de Castro seamount, Azores. *Tectonics* **40**, e2020TC006663.

Rouxel, O., Dobbek, N., Ludden, J. and Fouquet, Y. (2003) Iron isotope fractionation during oceanic crust alteration. *Chemical Geology* **202**, 155-182.

Ryan, W.B., Carbotte, S.M., Coplan, J.O., O'Hara, S., Melkonian, A., Arko, R., Weissel, R.A., Ferrini, V., Goodwillie, A. and Nitsche, F. (2009) Global multi-resolution topography synthesis. *Geochemistry, Geophysics, Geosystems* **10**, Q03014.

Safonov, O., Butvina, V. and Limanov, E. (2019) Phlogopite-Forming Reactions as Indicators of Metasomatism in the Lithospheric Mantle. *Minerals* **9**, 685.

Salters, V.J. and White, W.M. (1998) Hf isotope constraints on mantle evolution. *Chemical Geology* **145**, 447-460.

Salters, V.J.M. and Stracke, A. (2004) Composition of the depleted mantle. *Geochemistry,*

Geophysics, Geosystems **5**, Q05B07.

Schiano, P., Clocchiatti, R., Shimizu, N., Weis, D. and Mattielli, N. (1994) Cogenetic silica-rich and carbonate-rich melts trapped in mantle minerals in Kerguelen ultramafic xenoliths: Implications for metasomatism in the oceanic upper mantle. *Earth and Planetary Science Letters* **123**, 167-178.

Searle, R. (1980) Tectonic pattern of the Azores spreading centre and triple junction. *Earth and Planetary Science Letters* **51**, 415-434.

Sobolev, A., V. , Hofmann, A., W. and Nikogosian, I., K. (2000) Recycled oceanic crust observed in 'ghost plagioclase' within the source of Mauna Loa lavas. *Nature* **404**, 986.

Sobolev, A.V., Hofmann, A.W., Kuzmin, D.V., Yaxley, G.M., Arndt, N.T., Chung, S.L., Danyushevsky, L.V., Elliott, T., Frey, F.A., Garcia, M.O., Gurenko, A.A., Kamenetsky, V.S., Kerr, A.C., Krivolutskaya, N.A., Matvienkov, V.V., Nikogosian, I.K., Rocholl, A., Sigurdsson, I.A., Sushchevskaya, N.M. and Teklay, M. (2007) The Amount of Recycled Crust in Sources of Mantle-Derived Melts. *Science* **316**, 412-417.

Soderman, C.R., Matthews, S., Shorttle, O., Jackson, M.G., Ruttor, S., Nebel, O., Turner, S., Beier, C., Millet, M.-A., Widom, E., Humayun, M. and Williams, H.M. (2021) Heavy δ57Fe in ocean island basalts: a non-unique signature of processes and source lithologies in the mantle. *Geochimica et Cosmochimica Acta* **292**, 309-332.

Sossi, P., Foden, J. and Halverson, G. (2012) Redox-controlled iron isotope fractionation during magmatic differentiation: an example from the Red Hill intrusion, S. Tasmania. *Contributions to Mineralogy and Petrology* **164**, 757-772.

Sossi, P.A., Halverson, G.P., Nebel, O. and Eggins, S.M. (2015) Combined Separation of Cu, Fe and Zn from Rock Matrices and Improved Analytical Protocols for Stable Isotope Determination. *Geostand. Geoanal. Res.* **39**, 129-149.

Sossi, P.A., Nebel, O. and Foden, J. (2016) Iron isotope systematics in planetary reservoirs. *Earth and Planetary Science Letters* **452**, 295-308.

Sossi, P.A. and O'Neill, H.S.C. (2017) The effect of bonding environment on iron isotope fractionation between minerals at high temperature. *Geochimica et Cosmochimica Acta* **196**, 121-143.

Spieker, K., Rondenay, S., Ramalho, R., Thomas, C. and Helffrich, G. (2018) Constraints on the structure of the crust and lithosphere beneath the Azores Islands from teleseismic receiver functions. *Geophysical Journal International* **213**, 824-835.

Standish, J.J., Dick, H.J., Michael, P.J., Melson, W.G. and O'Hearn, T. (2008) MORB generation beneath the ultraslow spreading Southwest Indian Ridge (9–25 E): Major element chemistry and the importance of process versus source. *Geochemistry, Geophysics, Geosystems* **9**, Q05004.

Stracke, A. (2012) Earth's heterogeneous mantle: A product of convection-driven interaction between crust and mantle. *Chemical Geology* **330**, 274-299.

Stracke, A., Bizimis, M. and Salters, V.J.M. (2003) Recycling oceanic crust: Quantitative constraints. *Geochemistry, Geophysics, Geosystems* **4**, 8003.

Stracke, A., Hofmann, A.W. and Hart, S.R. (2005) FOZO, HIMU, and the rest of the mantle zoo. *Geochemistry, Geophysics, Geosystems* **6**, Q05007.

Sun, P., Niu, Y., Guo, P., Duan, M., Chen, S., Gong, H., Wang, X. and Xiao, Y. (2020) Large iron isotope variation in the eastern Pacific mantle as a consequence of ancient low-degree melt metasomatism. *Geochimica et Cosmochimica Acta* **286**, 269-288.

Teng, F.-Z., Dauphas, N. and Helz, R.T. (2008) Iron isotope fractionation during magmatic differentiation in Kilauea Iki lava lake. *Science (New York, N.Y.)* **320**, 1620.

Teng, F.-Z., Dauphas, N., Helz, R.T., Gao, S. and Huang, S. (2011) Diffusion-driven magnesium and iron isotope fractionation in Hawaiian olivine. *Earth and Planetary Science Letters* **308**, 317-324.

Teng, F.-Z., Dauphas, N., Huang, S. and Marty, B. (2013) Iron isotopic systematics of oceanic basalts. *Geochimica et Cosmochimica Acta* **107**, 12-26.

Turner, S., Hawkesworth, C., Rogers, N. and King, P. (1997) U-Th isotope disequilibria and ocean island basalt generation in the Azores. *Chemical Geology* **139**, 145-164.

Turner, S., Tonarini, S., Bindeman, I., Leeman, W., P. and Schaefer, B., F. (2007) Boron and oxygen isotope evidence for recycling of subducted components over the past 2.5Gyr. *Nature* **447**, 702.

Vogt, P.R. and Jung, W.Y. (2004) The Terceira Rift as hyper-slow, hotspot-dominated oblique spreading axis: A comparison with other slow-spreading plate boundaries. *Earth and Planetary Science Letters* **218**, 77-90.

Wang, X.-J., Chen, L.-H., Hofmann, A.W., Hanyu, T., Kawabata, H., Zhong, Y., Xie, L.-W., Shi, J.-H., Miyazaki, T., Hirahara, Y., Takahashi, T., Senda, R., Chang, Q., Vaglarov, B.S. and Kimura, J.-I. (2018) Recycled ancient ghost carbonate in the Pitcairn mantle plume. *Proceedings of the National Academy of Sciences of the United States* **115**, 8682.

Weaver, B.L. (1991) The origin of ocean island basalt end-member compositions: trace element and isotopic constraints. *Earth and Planetary Science Letters* **104**, 381-397.

Weis, D., Garcia, M., O., Rhodes, J.M., Jellinek, M. and Scoates, J., S. (2011) Role of the deep mantle in generating the compositional asymmetry of the Hawaiian mantle plume. *Nature Geoscience* **4**, 831.

Wendt, I. and Carl, C. (1991) The statistical distribution of the mean squared weighted deviation. *Chemical Geology: Isotope Geoscience Section* **86**, 275-285.

Weyer, S. and Ionov, D.A. (2007) Partial melting and melt percolation in the mantle: The message from Fe isotopes. *Earth and Planetary Science Letters* **259**, 119-133.

White, W.M. (2015) Isotopes, DUPAL, LLSVPs, and anekantavada. *Chemical Geology* **419**, 10-28.

White, W.M., Tapia, M.D. and Schilling, J.-G. (1979) The petrology and geochemistry of the Azores Islands. *Contributions to Mineralogy and Petrology* **69**, 201-213.

Widom, E., Carlson, R.W., Gill, J.B. and Schmincke, H.U. (1997) Th–Sr–Nd–Pb isotope and trace element evidence for the origin of the São Miguel, Azores, enriched mantle source. *Chemical Geology* **140**, 49-68.

Widom, E. and Farquhar, J. (2003) Oxygen isotope signatures in olivines from São Miguel (Azores) basalts: implications for crustal and mantle processes. *Chemical Geology* **193**, 237-255.

Williams, H.M. and Bizimis, M. (2014) Iron isotope tracing of mantle heterogeneity within the source regions of oceanic basalts. *Earth and Planetary Science Letters* **404**, 396-407.

Williams, H.M., Nielsen, S.G., Renac, C., Griffin, W.L., O'Reilly, S.Y., McCammon, C.A., Pearson, N., Viljoen, F., Alt, J.C. and Halliday, A.N. (2009) Fractionation of oxygen and iron isotopes by partial melting processes: Implications for the interpretation of stable isotope signatures in mafic rocks. *Earth and Planetary Science Letters* **283**, 156-166.

Williams, H.M., Peslier, A.H., McCammon, C., Halliday, A.N., Levasseur, S., Teutsch, N. and Burg, J.P. (2005) Systematic iron isotope variations in mantle rocks and minerals: The effects of partial melting and oxygen fugacity. *Earth and Planetary Science Letters* **235**, 435-452.

Woodland, A.B. and Koch, M. (2003) Variation in oxygen fugacity with depth in the upper mantle beneath the Kaapvaal craton, Southern Africa. *Earth and Planetary Science letters* **214**, 295-310.

Xiao, Y., Zhang, H.-F., Fan, W.-M., Ying, J.-F., Zhang, J., Zhao, X.-M. and Su, B.-X. (2010) Evolution of lithospheric mantle beneath the Tan-Lu fault zone, eastern North China Craton: evidence from petrology and geochemistry of peridotite xenoliths. *Lithos* **117**, 229-246.

Zhao, X., Zhang, H., Zhu, X., Tang, S. and Tang, Y. (2010) Iron isotope variations in spinel peridotite xenoliths from North China Craton: implications for mantle metasomatism. *Contributions to Mineralogy and Petrology* **160**, 1-14.

Zhao, X., Zhang, H., Zhu, X., Tang, S. and Yan, B. (2012) Iron isotope evidence for multistage melt–peridotite interactions in the lithospheric mantle of eastern China. *Chemical Geology* **292**, 127-139.

Zhao, X.M., Cao, H.H., Mi, X., Evans, N.J., Qi, Y.H., Huang, F. and Zhang, H.F. (2017) Combined iron and magnesium isotope geochemistry of pyroxenite xenoliths from Hannuoba, North China Craton: implications for mantle metasomatism. *Contributions to Mineralogy and Petrology* **172**, 40.

Zindler, A. and Hart, S. (1986) Chemical geodynamics. *Annual Review of Earth and Planetary Sciences* **14**, 493-571.

SUPPLEMENTARY DATA

I. Supplementary data I

Sample selection

Ocean island basalts (OIB) can be divided into alkali and tholeiitic lavas through major element systematics of Na_2O+K_2O vs SiO_2 (Fig. S1). Eastern São Miguel lavas can be ascribed to Trachybasalts, with one outlier being identified as a basalt. Western São Miguel lavas have been identified as basalts.

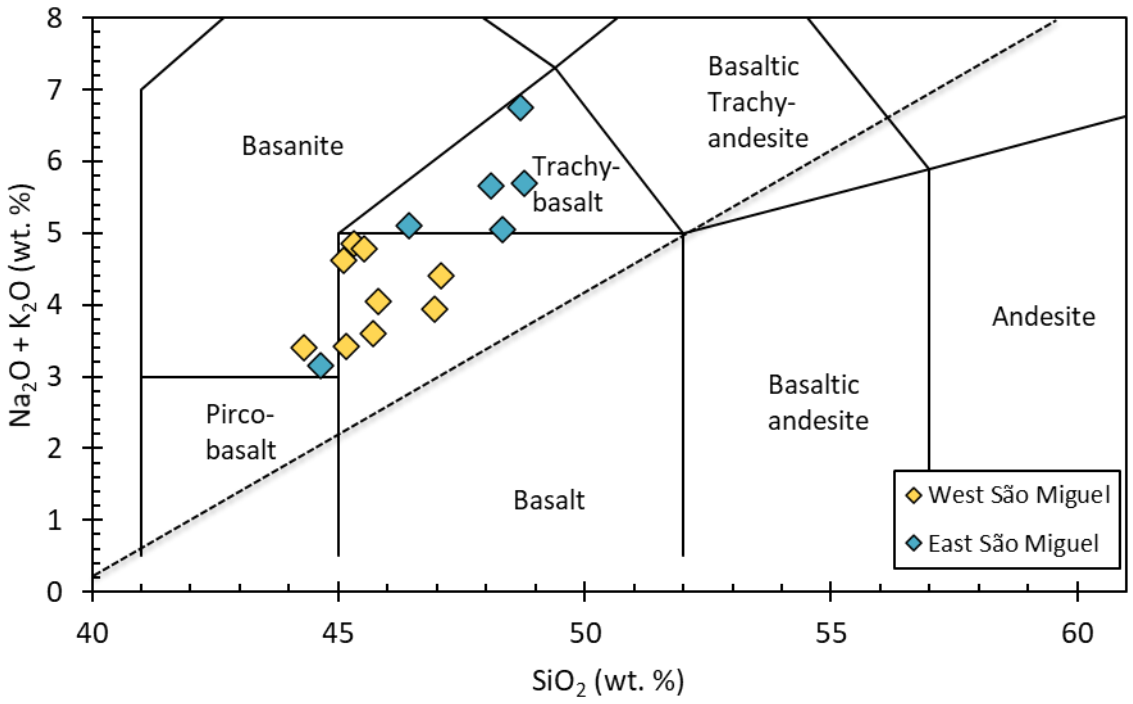

Figure S1. Total alkali-silica diagram (TAS diagram) after Le Bas et al. (1986b) and division lines after Le Maître (1989). São Miguel lavas can be ascribed to alkali basalts plotting above the division line, ranging from basalts to trachybasalts.

Discussion – melting degree

To assess the degree of partial melting in São Miguel's lavas, we compare REE ratios, FeO and TiO_2, both crystal fractionation-corrected to 8.0 wt. % MgO ($Fe_{8.0}$ and $Ti_{8.0}$; Plank and Langmuir, 1992; Taylor and Martinez, 2003), to $\delta^{57}Fe_{prim}$. To avoid error in correction we only corrected samples with 4.4 – 9.8 wt. % MgO (Taylor and Martinez, 2003; Plank and Langmuir, 1992). In ratios of light REE relative to middle REE $(La/Sm)_{PM}$, the lavas from western São Miguel range from 2.7 to 3.1 and lavas from eastern São Miguel from 2.8 to 3.6 (Fig. S2a). In ratios of middle REE relative to heavy REE with $(Sm/Yb)_{PM}$ the lavas are ranging from 4.7 to 5.0 for western São Miguel and from 3.8 to 4.9 for eastern São Miguel (Fig. S2b). Comparing

these ratios to $\delta^{57}Fe_{prim}$, we do not observe any correlation of the REE with $\delta^{57}Fe_{prim}$. Additionally, eastern São Miguel as well as western São Miguel show no co-variation with either $Fe_{8.0}$ or $Ti_{8.0}$ vs $\delta^{57}Fe_{prim}$ (Fig. S2c, d).

It can be argued that western and eastern São Miguel show a slightly lower melting degree than the other Azores islands (São Jorge, Pico, Faial, Terceira, João de Castro and Graciosa) when compared in $(La/Sm)_{PM}$ and $(Sm/Yb)_{PM}$.

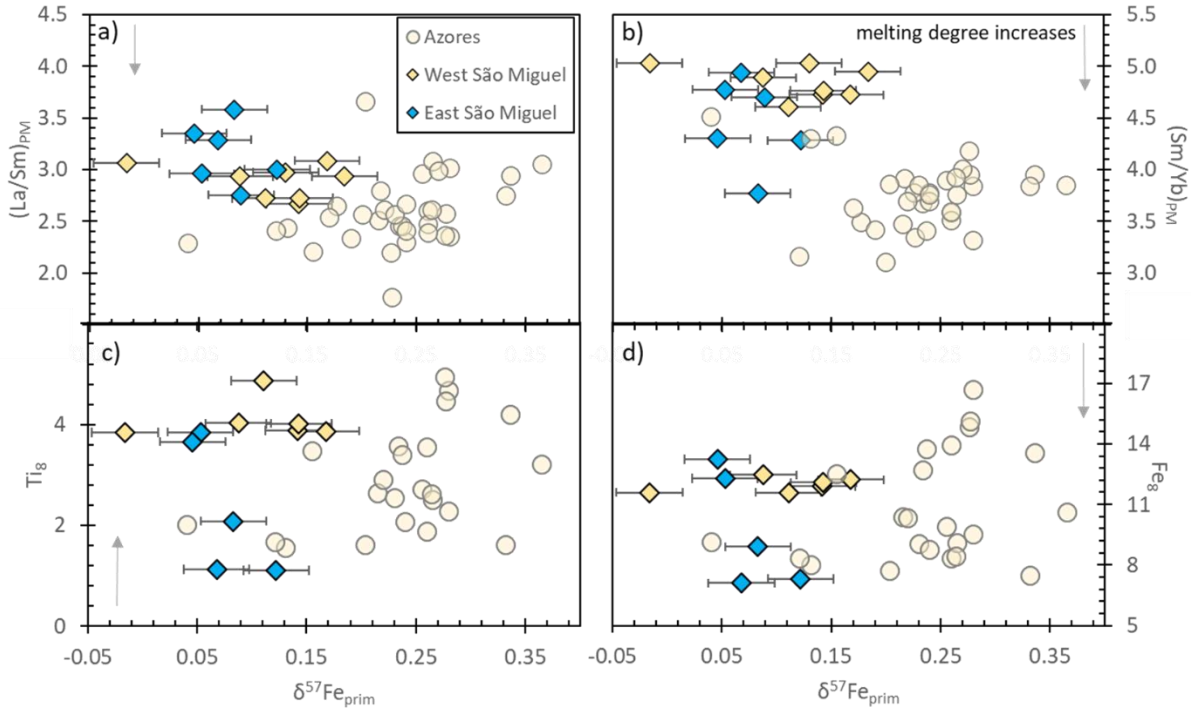

Figure S2. $\delta^{57}Fe_{prim}$ vs a) $(La/Sm)_{PM}$ and b) $(Sm/Yb)_{PM}$. Both $(La/Sm)_{PM}$ and $(Sm/Yb)_{PM}$ are primitive mantle normalised Rare Earth Element (REE) ratios (Sun and McDonough, 1989). For western São Miguel sample SM0140 with $\delta^{57}Fe_{prim}$ = +0.16‰ La, Sm and Yb have not been analysed. $\delta^{57}Fe_{prim}$ vs c) $Na_{8.0}$ and d) $Ti_{8.0}$, with Na_2O and TiO_2 crystal fractionation corrected to 8 wt. % MgO after Plank and Langmuir (1992) and Taylor and Martinez (2003). The FeO contents increase with increasing pressure and TiO_2 increases with decreasing melting degree (Taylor and Martinez, 2003; Plank and Langmuir, 1992). Data for the rest of the Azores islands (São Jorge, Pico, Faial, Terceira, João de Castro and Graciosa) are from (Soderman et al., 2021).

Discussion – mantle metasomatism

The radiogenic isotopic signature of Sr-Nd-Pb of western São Miguel is similar to those observed elsewhere for carbonatitic mantle components (Ernst, 2014; Hoernle et al., 2002; Castillo et al., 2018). Eastern São Miguel's radiogenic isotopic composition is unique among

OIB but does not exclude a carbonatitic component. Similar high Rb/Sr, low Sm/Nd and enhanced Th/U and U/Pb ratios have been stated for continental carbonatites in East Africa (Simonetti and Bell, 1994; Grünenfelder et al., 1986). We apply a carbonatite melt-mantle mixing model with the ratio mantle-melt of 99:1 (Grassi et al., 2012) to quantify the influence of a carbonatitic component or the contact with a carbon-rich mantle reservoir in São Miguel. The model shows the radiogenic Nd, Sr and Pb isotopic evolution of DMM, when interacting with a carbonatitic component, generated at 1.5 Ga and consisting of 94 wt.% pelagic material with an initial $^{87}Sr/^{86}Sr$ of 0.7074 (Rehkamper and Hofmann, 1997) and 6 wt.% marine carbonate with an initial $^{87}Sr/^{86}Sr$ of 0.7060 (Mirota and Veizer, 1994). Kelley et al. (2005) and Bach et al. (2003) suggest that during subduction-driven dehydration, the fractionation of Pb and U is large and can cause Pb- and U-loss ranging from 54 – 98% for Pb and from 25 – 50% for U. In our model we adopt a Pb- and U-loss of 65% and 25%, respectively (Kelley et al., 2005). We assume that carbonate was introduced into the mantle during subduction and is partially molten at depth during subduction (Rohrbach and Schmidt, 2011). The applied melting pressures of 13 and 22 GPa show that a source (here DMM from Salters and Stracke (2004)) interacting with 0.5 – 1.0% of a carbonatitic component can create the Nd, Sr and Pb radiogenic isotope trajectory formed by eastern São Miguel (Fig. S3). The melting pressure of 13 and 22 GPa were adapted from Grassi et al. (2012) and represent pressure conditions at the transition zone at 660 km, suggesting an interaction of mantle plume material and a carbonatitic component at great depth (Spandler et al., 2010). Our calculated percentage of a 0.5 – 1.0% carbonatitic component is, however, not coherent with Beier et al. (2013), who calculated that a mixing of 20% carbonated component with volatile free garnet peridotite can generate lavas from Santa Maria.

We assume that the small percentage of < 1.0% contamination by a carbonatitic component preserves the radiogenic isotopic signature of any additional mixing with an enriched component. However, element fractionation strongly affects the Pb isotopic signature leading to more radiogenic Pb ratios than we observe in OIB (Grassi et al., 2012) that are coherent with eastern São Miguel lavas. The effect of carbonate recycling at small melting degrees on radiogenic Pb isotopes within the mantle concomitant with elevated U relative to Pb and Th has been recognised by several studies (Castillo, 2016; Castillo, 2015; Castillo et al., 2018; Dasgupta et al., 2009; Bell and Tilton, 2001). Notably, a recent study

discusses radiogenic Pb isotopic signatures of OIB in combination with ancient seawater, which leads to enriched U but unchanged Th concentrations (Pettke et al., 2018). Ancient seawater can impart a radiogenic Sr isotopic signature with $^{87}Sr/^{86}Sr > 0.704$ and cannot be excluded as a possible factor causing alteration or contamination of a carbonatitic component (Veizer, 1989; Veizer et al., 1989; Shields and Veizer, 2002).

The sum of observations, including the low melting degree of São Miguel's lavas, indicate that a contribution of a small degree carbonatitic component cannot explain the $\delta^{57}Fe_{prim}$ of eastern or western São Miguel's lavas.

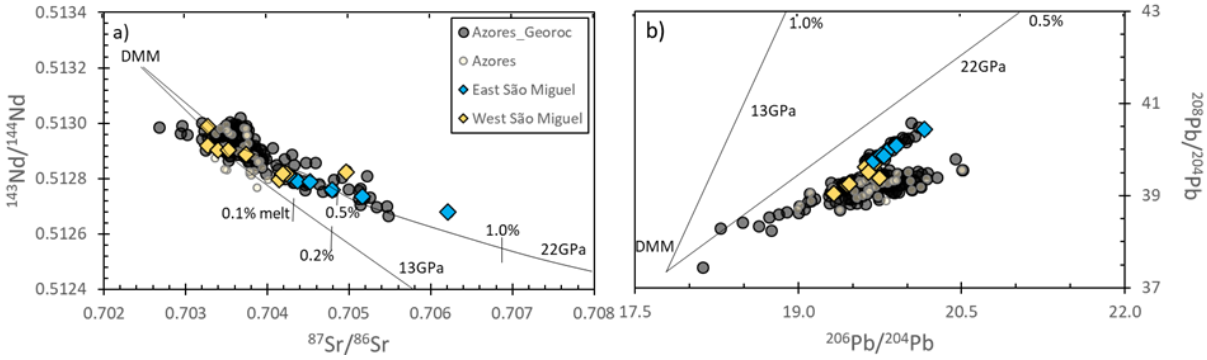

Figure S3. a) $^{87}Sr/^{86}Sr$ vs $^{143}Nd/^{144}Nd$ and b) $^{206}Pb/^{204}Pb$ vs $^{208}Pb/^{204}Pb$ of eastern and western São Miguel as well as Azores. Eastern and western São Miguel data from (Beier et al., 2007; Turner et al., 1997; Prytulak et al., 2014), Azores data from Soderman et al. (2021) and additional data obtained from GEOROC (http://georoc.mpch-mainz.gwdg.de/georoc/). Mixing line represents mixing of DMM with a carbonatitic component evolved at 1.5 Ga (for details of experimental data and modelling see Grassi et al., (2012)). Composition of present day DMM from Salters and Stracke (2004). Two mixing lines of a carbonatitic component generated at 13 GPa and 22 GPa are shown. Eastern São Miguel follows the mixing line between DMM and a carbonatitic component at 22 GPa and shows that an addition of 0.5 – 1.0% of a carbonatitic component to DMM produces the range of eastern São Miguel lavas in Nd and Sr system and a similar range in Pb systems.

Phlogopite or high K-hollandite indicators vs radiogenic isotopic ratios

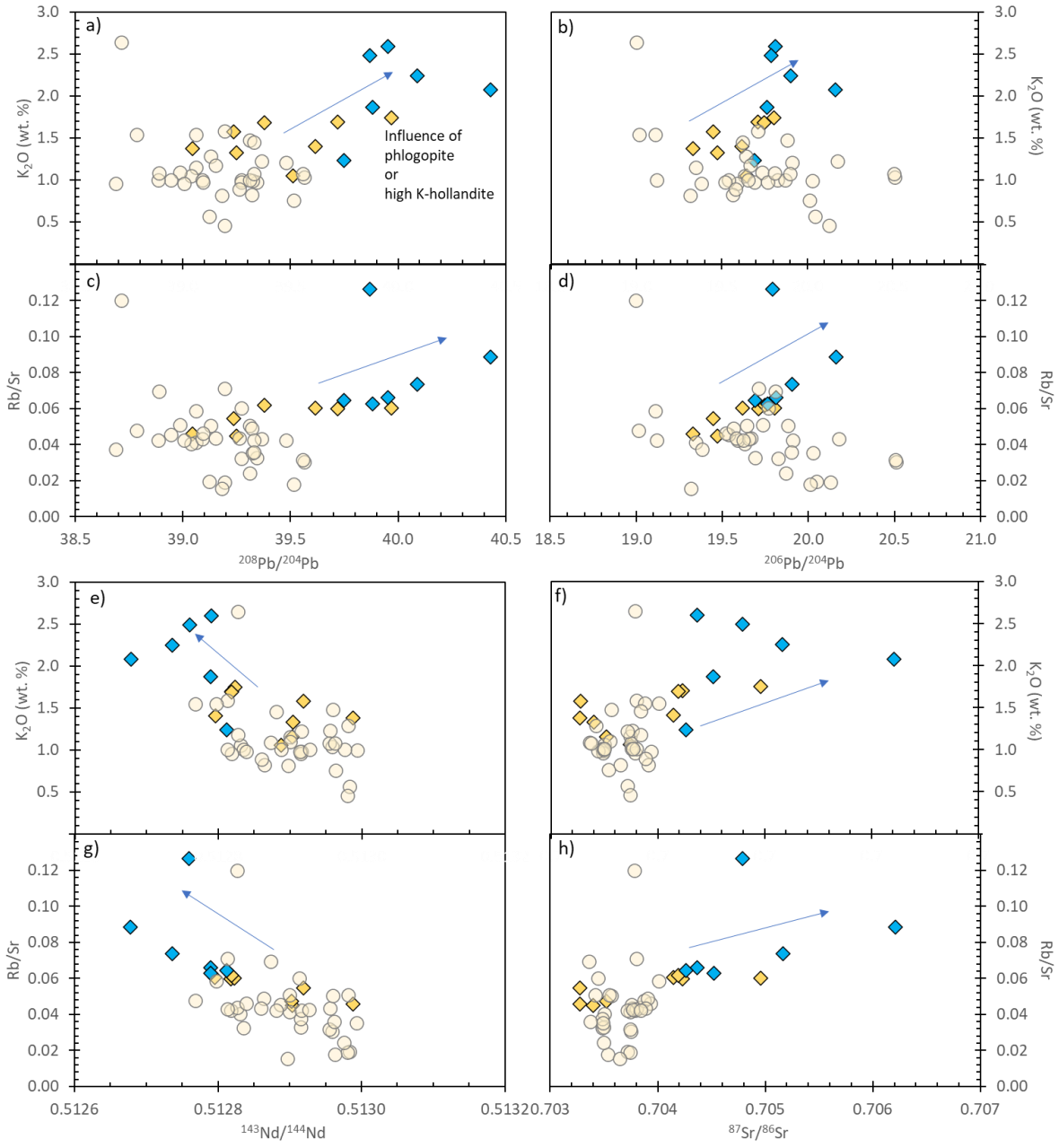

Figure S3. a) $^{208}Pb/^{204}Pb$ vs K_2O, b) $^{206}Pb/^{204}Pb$ vs K_2O, c) $^{208}Pb/^{204}Pb$ vs Rb/Sr, d) $^{206}Pb/^{204}Pb$ vs Rb/Sr, e) $^{143}Nd/^{144}Nd$ vs K_2O, f) $^{87}Sr/^{86}Sr$ vs K_2O, g) $^{143}Nd/^{144}Nd$ vs Rb/Sr, h) $^{87}Sr/^{86}Sr$ vs Rb/Sr.

References

Bach, W., Peucker-Ehrenbrink, B., Hart, S.R. and Blusztajn, J.S. (2003) Geochemistry of hydrothermally altered oceanic crust: DSDP/ODP Hole 504B - Implications for

seawater-crust exchange budgets and Sr-and Pb-isotopic evolution of the mantle. *Geochemistry, Geophysics, Geosystems* **4**, 8904.

Beier, C., Haase, K.M. and Hansteen, T.H. (2006) Magma Evolution of the Sete Cidades Volcano, São Miguel, Azores. *Journal of Petrology* **47**, 1375-1411.

Beier, C., Stracke, A. and Haase, K.M. (2007) The peculiar geochemical signatures of Sao Miguel (Azores) lavas: Metasomatised or recycled mantle sources? *Earth and Planetary Science Letters* **259**, 186-199.

Bell, K. and Tilton, G.R. (2001) Nd, Pb and Sr Isotopic Compositions of East African Carbonatites: Evidence for Mantle Mixing and Plume Inhomogeneity. *Journal of Petrology* **42**, 1927-1945.

Castillo, P.R. (2015) The recycling of marine carbonates and sources of HIMU and FOZO ocean island basalts. *Lithos* **216-217**, 254-263.

Castillo, P.R. (2016) A proposed new approach and unified solution to old Pb paradoxes. *Lithos* **252-253**, 32-40.

Castillo, P.R., Macisaac, C., Perry, S. and Veizer, J. (2018) Marine Carbonates in the Mantle Source of Oceanic Basalts: Pb Isotopic Constraints. *Scientific Reports* **8**, 14932.

Dasgupta, R., Hirschmann, M.M., McDonough, W.F., Spiegelman, M. and Withers, A.C. (2009) Trace element partitioning between garnet lherzolite and carbonatite at 6.6 and 8.6 GPa with applications to the geochemistry of the mantle and of mantle-derived melts. *Chemical Geology* **262**, 57-77.

Elliott, T., Blichert-Toft, J., Heumann, A., Koetsier, G. and Forjaz, V. (2007) The origin of enriched mantle beneath São Miguel, Azores. *Geochimica et Cosmochimica Acta* **71**, 219-240.

Ernst, R.E. (2014) Geochemistry of LIPs, in: Ernst, R.E. (Ed.), Large Igneous Provinces. Cambridge University Press, *Cambridge*, pp. 277-338.

Grassi, D., Schmidt, M.W. and Günther, D. (2012) Element partitioning during carbonated

pelite melting at 8, 13 and 22GPa and the sediment signature in the EM mantle components. *Earth and Planetary Science Letters* **327-328**, 84-96.

Grünenfelder, M.H., Tilton, G.R., Bell, K. and Blenkinsop, J. (1986) Lead and strontium isotope relationships in the Oka carbonatite complex, Quebec. *Geochimica et Cosmochimica Acta* **50**, 461-468.

Hoernle, K., Tilton, G., Le Bas, M., Duggen, S. and Garbe-Schoenberg, D. (2002) Geochemistry of oceanic carbonatites compared with continental carbonatites: mantle recycling of oceanic crustal carbonate. *Contributions to Mineralogy and Petrology* **142**, 520-542.

Kelley, K.A., Plank, T., Farr, L., Ludden, J. and Staudigel, H. (2005) Subduction cycling of U, Th, and Pb. *Earth and Planetary Science Letters* **234**, 369-383.

Le Bas, M.J., Le Maitre, R.W., Streckeisen, A. and Zanettin, B.A. (1986) A Chemical Classification of Volcanic Rocks Based on the Total Alkali-Silica Diagram. *Journal of Petrology* **27**, 745-750.

Le Maître, R. (1989) A classification of igneous rocks and glossary of terms. Recommendations of the IUGS Subcommission on the Systematics of Igneous Rocks. Ed. IUGS. Blackwell Publications, 193p.

Mirota, M.D. and Veizer, J. (1994) Geochemistry of precambrian carbonates: VI. Aphebian albanel formations, Quebec, Canada. *Geochimica et Cosmochimica Acta* **58**, 1735-1745.

Pettke, T., Kodolányi, J. and Kamber, B.S. (2018) From ocean to mantle: new evidence for U-cycling with implications for the HIMU source and the secular Pb isotope evolution of Earth's mantle. *Lithos* **316-317**, 66-76.

Plank, T. and Langmuir, C.H. (1992) Effects of the melting regime on the composition of the oceanic crust. *Journal of Geophysical Research: Solid Earth* **97**, 19749-19770.

Prytulak, J., Avanzinelli, R., Koetsier, G., Kreissig, K., Beier, C. and Elliott, T. (2014) Melting versus contamination effects on U-238-Th-230-Ra-226 and U-235-Pa-231 disequilibria

in lavas from Sao Miguel, Azores. *Chemical Geology* **381**, 94-109.

Rehkamper, M. and Hofmann, A. (1997) Recycled ocean crust and sediment in Indian Ocean MORB. *Earth and Planetary Science Letters* **147**, 93-106.

Rohrbach, A. and Schmidt, M.W. (2011) Redox freezing and melting in the Earth's deep mantle resulting from carbon-iron redox coupling. *Nature* **472**, 209.

Salters, V.J.M. and Stracke, A. (2004) Composition of the depleted mantle. *Geochemistry, Geophysics, Geosystems* **5**, Q05B07.

Shields, G. and Veizer, J. (2002) Precambrian marine carbonate isotope database: Version 1.1. *Geochemistry, Geophysics, Geosystems* **3**, 1 of 12-12 of 12.

Simonetti, A. and Bell, K. (1994) Nd, Pb and Sr isotopic data from the Napak carbonatite-nephelinite centre, eastern Uganda: an example of open-system crystal fractionation. *Contributions to Mineralogy and Petrology* **115**, 356-366.

Soderman, C.R., Matthews, S., Shorttle, O., Jackson, M.G., Ruttor, S., Nebel, O., Turner, S., Beier, C., Millet, M.-A., Widom, E., Humayun, M. and Williams, H.M. (2021) Heavy δ57Fe in ocean island basalts: a non-unique signature of processes and source lithologies in the mantle. *Geochimica et Cosmochimica Acta* **292**, 309-332.

Spandler, C., Yaxley, G., Green, D. and Scott, D. (2010) Experimental phase and melting relations of metapelite in the upper mantle: implications for the petrogenesis of intraplate magmas. *Contributions to Mineralogy and Petrology* **160**, 569-589.

Sun, S.-S. and McDonough, W.F. (1989) Chemical and isotopic systematics of oceanic basalts: implications for mantle composition and processes. *Geological Society, London, Special Publications* **42**, 313-345.

Taylor, B. and Martinez, F. (2003) Back-arc basin basalt systematics. *Earth and Planetary Science Letters* **210**, 481-497.

Turner, S., Hawkesworth, C., Rogers, N. and King, P. (1997) U-Th isotope disequilibria and

ocean island basalt generation in the Azores. *Chemical Geology* **139**, 145-164.

Veizer, J. (1989) Strontium Isotopes in Seawater through Time. *Annu. Rev. Earth Planet. Sci.* **17**, 141-167.

Veizer, J., Hoefs, J., Lowe, D.R. and Thurston, P.C. (1989) Geochemistry of Precambrian carbonates: II. Archean greenstone belts and Archean sea water. *Geochimica et Cosmochimica Acta* **53**, 859.

II. Supplementary data II

Table S1. Major element (wt. %) and trace element (ppm) data of lavas from São Miguel compiled from Beier et al. (2006), Beier et al. (2007), Prytulak et al. (2014), Turner et al. (1997), and Elliott et al. (2007).

Sample No.	LATI-TUDE	LONGI-TUDE	SiO_2	TiO_2	AL_2O_3	FEO_T	CAO	MGO	MNO	K_2O	NA_2O	P_2O_5	SC	V	CR	CO	NI	CU
West																		
SM0140	37.80	-25.70	44.31	2.79	10.79	11.18	12.78	12.41	0.18	1.15	2.25	0.45	n.d.	283.90	1056.00	n.d.	365.00	n.d.
SM0133	37.52	-25.52	47.09	3.40	13.33	10.45	11.03	8.60	0.17	1.58	2.83	0.57	28.14	297.13	449.49	44.92	121.78	67.80
SM0102	37.90	-25.82	45.17	2.82	10.44	10.45	10.99	14.26	0.17	1.41	2.02	0.47	29.05	228.99	705.03	59.72	311.23	74.87
513DS-1 Wr	37.88	-25.94	46.95	2.74	12.33	10.73	10.97	12.13	0.17	1.38	2.56	0.48	24.10	n.d.	996.00	44.60	319.00	70.50
SM9704A	37.75	-25.71	45.71	3.44	12.76	10.73	11.14	9.81	0.17	1.06	2.55	0.52	19.90	n.d.	670.00	48.60	185.00	25.90
S1	37.80	-25.50	45.31	4.09	14.11	12.38	10.41	7.76	0.17	1.70	3.16	0.58	24.83	289.77	269.94	47.32	94.55	67.41
SM7	37.80	-25.50	45.80	3.45	13.60	11.07	11.70	8.56	0.17	1.33	2.72	0.54	n.d.	319.00	n.d.	n.d.	153.00	n.d.
S10	37.80	-25.50	45.12	3.76	14.02	11.76	10.81	8.33	0.17	1.75	2.87	0.66	27.51	313.01	314.97	50.43	112.31	82.39
SP2	37.80	-25.50	45.53	4.07	13.89	12.23	10.36	7.93	0.18	1.69	3.09	0.59	24.97	299.13	297.50	49.15	103.20	79.86
East																		
SM0170	37.77	-25.48	48.70	3.10	16.57	9.87	7.79	4.41	0.18	2.60	4.16	0.84	10.78	141.67	26.24	23.82	17.60	18.43
SM0128	37.60	-25.40	48.77	3.55	15.31	10.60	8.11	4.03	0.16	2.25	3.44	0.69	13.71	218.28	1.61	29.28	21.44	41.79
SM9716	37.77	-25.16	48.33	3.92	14.69	11.95	8.80	5.52	0.16	2.08	2.98	0.54	19.20	n.d.	152.00	40.00	95.00	28.10
SM0204	37.80	-25.50	44.63	3.54	11.84	11.84	11.90	10.41	0.17	1.24	1.92	0.41	n.d.	n.d.	27.00	n.d.	5.00	n.d.
S3	37.80	-25.50	46.43	3.59	14.22	11.59	9.47	8.34	0.17	1.87	3.24	0.64	21.23	260.66	280.79	46.29	149.10	67.66
SP8	37.80	-25.50	48.09	2.94	13.49	10.70	8.69	9.10	0.17	2.49	3.17	0.43	21.63	230.89	358.13	51.61	158.83	75.86
Excluded data																		
SM0106	37.53	-25.47	61.23	0.72	17.64	2.72	1.46	0.48	0.17	5.17	6.85	0.09	1.91	10.44	1.07	0.58	0.26	1.53
SM0134	37.52	-25.52	54.56	1.92	17.35	6.60	4.86	2.41	0.19	3.61	5.63	0.62	5.63	95.00	1.38	8.28	0.39	3.42
515DS-1	37.86	-25.99	59.29	1.28	18.69	5.34	3.53	1.58	0.19	4.32	5.99	0.38	3.16	40.58	2.25	4.95	1.75	3.29

Table S2a. Trace element (ppm) data of lavas from São Miguel compiled from Beier et al. (2006), Beier et al. (2007), Prytulak et al. (2014), Turner et al. (1997), and Elliott et al. (2007).

Sample No.	ZN	RB	SR	Y	ZR	NB	MO	CS	BA	LA	CE	PR	ND	SM	EU	GD	TB	DY
West																		
SM0140	84.00	24.00	505.00	29.00	204.00	47.00	n.d.	n.d.	544.00	n.d.	n.d.	n.d.	n.d.	n.d.	n.d.	n.d.	n.d.	n.d.
SM0133	98.70	39.04	714.64	28.21	305.45	60.71	2.02	0.23	517.84	42.45	88.33	11.02	44.05	8.82	2.67	7.54	1.08	5.57
SM0102	84.32	32.27	533.57	19.54	226.44	44.82	1.84	0.28	348.39	33.55	71.42	8.85	35.54	7.17	2.13	6.04	0.86	4.51
513DS-1 Wr	90.00	28.50	622.00	19.30	259.00	48.00	1.90	0.32	404.00	36.60	75.50	9.51	38.30	7.93	2.43	6.70	0.96	5.16
SM9704A	82.60	22.60	615.00	23.20	207.00	45.70	1.86	0.05	359.00	30.50	64.60	8.04	33.50	7.13	2.22	6.61	0.92	4.97
S1	112.49	45.60	760.95	30.90	330.55	70.65	n.d.	0.34	493.97	41.80	91.78	12.12	48.99	9.96	3.11	9.00	1.35	6.90
SM7	n.d.	31.40	699.00	25.60	242.00	59.90	n.d.	n.d.	449.00	39.00	90.00	9.80	38.00	8.04	n.d.	7.33	1.09	5.42
S10	109.08	45.75	759.40	27.97	331.79	68.78	n.d.	0.35	485.07	42.15	89.77	11.60	46.18	9.15	2.86	8.21	1.24	6.27
SP2	116.71	47.34	766.27	30.60	345.95	74.39	n.d.	0.38	486.76	42.34	92.60	12.10	48.79	9.89	3.05	8.87	1.34	6.84
East																		
SM0170	109.84	65.72	995.33	36.49	443.96	89.64	3.14	0.61	767.35	73.39	153.39	18.91	73.88	14.20	4.19	11.91	1.70	8.84
SM0128	107.40	54.72	743.59	38.29	403.92	71.76	2.78	0.16	773.00	60.77	126.46	15.73	62.31	12.90	3.76	11.45	1.68	8.96
SM9716	99.50	55.30	624.00	38.80	389.00	62.40	2.41	0.16	487.00	59.10	112.00	13.60	53.00	10.50	3.04	9.75	1.34	7.67
SM0204	88.00	35.52	549.86	25.85	252.66	42.88	n.d.	0.36	372.64	32.21	67.73	8.59	35.09	7.44	2.30	6.65	0.97	5.12
S3	116.06	51.37	819.27	30.98	373.73	77.86	n.d.	0.50	530.78	47.51	101.74	13.24	51.83	10.22	3.16	9.07	1.37	6.92
SP8	101.49	67.82	536.56	27.93	377.68	72.66	n.d.	0.60	353.16	44.82	93.13	11.58	43.74	8.51	2.42	7.61	1.17	6.04
Excluded data																		
SM0106	92.09	132.83	313.47	39.69	807.93	166.11	2.06	0.29	1397.96	98.80	190.21	18.96	63.42	10.28	2.88	7.92	1.23	6.65
SM0134	112.85	86.08	814.11	41.78	572.38	129.82	2.57	0.62	1008.24	81.26	163.93	19.09	71.58	13.45	3.98	11.17	1.62	8.81
515DS-1	92.08	1090.07	543.18	33.71	607.16	130.14	0.97	0.26	n.d.	89.48	172.91	19.36	68.03	11.84	3.32	9.65	1.44	7.76

Table S2b. Trace element (ppm) data of lavas from São Miguel compiled from Beier et al. (2006), Beier et al. (2007), Prytulak et al. (2014), Turner et al. (1997), and Elliott et al. (2007).

Sample No.	HO	ER	TM	YB	LU	HF	TA	PB	TH	U	$^{143}ND/^{144}ND$	$^{87}SR/^{86}SR$	$^{206}PB/^{204}PB$	$^{207}PB/^{204}PB$	$^{208}PB/^{204}PB$
West															
SM0140	n.d.	n.d.	n.d.	n.d.	n.d.	n.d.	n.d.	n.d.	n.d.	n.d.	0.5129	0.7035	n.d.	n.d.	n.d.
SM0133	0.98	2.45	0.31	1.93	0.27	6.33	3.64	2.04	4.57	1.24	0.5129	0.7033	19.45	15.58	39.24
SM0102	0.80	1.97	0.26	1.57	0.22	5.95	2.94	n.d.	n.d.	n.d.	0.5128	0.7041	19.62	15.64	39.61
513DS-1 Wr	0.93	2.28	0.29	1.76	0.24	5.98	3.34	2.05	3.82	1.14	0.5130	0.7033	19.33	15.56	39.05
SM9704A	0.89	2.19	0.28	1.7	0.24	5.36	3.04	1.93	3.67	1.08	0.5129	0.7037	19.65	15.63	39.51
S1	1.19	2.98	n.d.	2.31	0.33	7.76	4.25	2.66	4.54	1.25	0.5128	0.7042	19.71	15.65	39.72
SM7	0.97	2.42	n.d.	1.87	0.27	5.83	3.76	2.07	3.75	1.08	0.5129	0.7034	19.47	15.59	39.25
S10	1.07	2.70	n.d.	2.06	0.30	6.99	3.97	2.90	4.84	1.27	0.5128	0.7050	19.81	15.70	39.97
SP2	1.17	2.94	n.d.	2.28	0.33	7.58	4.27	2.66	4.57	1.27	0.5128	0.7042	19.75	15.65	39.38
East															
SM0170	1.57	3.95	0.52	3.16	0.45	11.72	6.08	3.96	n.d.	n.d.	0.5128	0.7044	19.81	15.70	39.95
SM0128	1.61	4.07	0.54	3.31	0.46	10.65	4.85	3.85	7.25	1.79	0.5127	0.7052	19.90	15.73	40.09
SM9716	1.43	3.69	0.50	3.06	0.44	8.99	4.18	3.46	6.98	1.59	0.5127	0.7062	20.16	15.80	40.43
SM0204	0.90	2.23	0.29	1.74	0.24	5.68	2.72	1.42	3.95	1.03	0.5128	0.7043	19.69	15.68	39.75
S3	1.19	3.02	n.d.	2.35	0.33	8.04	4.48	3.04	5.04	1.44	0.5128	0.7045	19.76	15.67	39.88
SP8	1.05	2.70	n.d.	2.17	0.32	7.82	4.09	3.91	6.43	1.77	0.5128	0.7048	19.79	15.67	39.87
Excluded data															
SM0106	1.26	3.52	0.51	3.42	0.50	14.42	8.28	7.13	15.25	3.49	0.5129	0.7036	19.51	15.60	39.35
SM0134	1.62	4.23	0.57	3.54	0.50	12.41	7.62	4.44	10.96	2.84	0.5129	0.7035	19.43	15.58	39.23
515DS-1	1.44	3.81	0.54	3.49	0.50	15.15	8.73	6.13	13.46	1.76	0.5129	0.7036	19.50	15.61	39.37

CHAPTER 4

4. Iron isotope systematics during igneous differentiation in Kea- vs. Loa-trend lavas, Hawai'i

Saskia Ruttor[1*], Oliver Nebel[1], Yona Nebel-Yacobsen[1], Marc D. Norman[2], Mark A. Kendrick[3], Angus Rogers[1]

[1] School of Earth, Atmosphere and Environment, Monash University, Melbourne, 3800 Clayton, Australia, saskia.ruttor@monash.edu

[2]Research School of Earth Sciences, The Australian National University, Canberra ACT 2601, Australia

[3]School of Earth and Environmental Sciences, The University of Queensland, St Lucia, Queensland 4072, Australia

Abstract

The Big Island of Hawai'i is currently the most active site of magmatic activity in the Hawaiian chain of volcanoes that are associated with a mantle plume in the Pacific Ocean. Mantle source variability and magmatic processes have both been proposed to significantly affect lava chemistry at the Big Island, which is most prominently illustrated in a radiogenic isotope dichotomy of the so-called 'Kea-' and 'Loa-trend'. Here, we present stable Fe isotopes (δ^{57}Fe), complemented by radiogenic ^{176}Hf/^{177}Hf, in lavas from the Pu'u 'Ō'ō vent on the East Rift Zone of Kīlauea (Kea trend) and from the Southwest Rift Zone from Mauna Loa (Loa trend). In Hf isotopic space, Pu'u 'Ō'ō lavas range from ε_{Hf} = +9 to +13, aligning with published values of lavas from the 'Kea-trend'. Mauna Loa basalts and picrites presented here, have values ranging from ε_{Hf} = +8 to +11, which coincide with reported ε_{Hf} values of the Loa-trend. The Pu'u 'Ō'ō lavas with an average δ^{57}Fe of +0.15 ‰ at MgO ~ 7 wt. % fall on a crystal fractionation trend dominated by olivine crystallisation identical to that represented by lavas from the Kilauea Iki lava lake. Mauna Loa basalts and picrites define an overlapping trend that extends to lighter δ^{57}Fe of +0.06 ‰ at MgO ~ 16 wt. %, being affected by both, olivine crystallisation and accumulation. Pu'u 'Ō'ō and Mauna Loa lavas show outliers in δ^{57}Fe that tend towards δ^{57}Fe < +0.05 ‰, that is lighter than primitive mantle or mid ocean ridge basalts. On a three-isotope plot it is evident that the samples, have undergone multiple processes that erased the inherited Fe isotopic signature of these lavas. This suggests that there is no closed magma chamber present underneath both Pu'u 'Ō'ō and Mauna Loa but rather an open

magmatic system, which can experience re-charging events, masking processes that influence Fe isotopes, i.e., source inheritance or melting degree. The similar Fe isotopic variations of Mauna Loa and Pu‘u ‘Ō‘ō suggest that both lava suites have undergone similar fractionation processes during partial melting. Both lava suites show heavy Fe isotopic compositions, with Pu‘u ‘Ō‘ō showing the heaviest at δ^{57}Fe +0.30 ‰. An inherently heavy Fe isotopic signature (> 0.15 ‰) in addition to fractionation processes is required to explain some of the high values measured here for which no geochemical proxy can be identified. With our new stable Fe isotope data, we show that lavas which travel through a plumbing system undergo multiple fractionation processes. Crystal fractionation and accumulation results in small changes and can be corrected for. Source inheritance and melting degree are, however, masked by possible re-charging events of the plumbing system.

Keywords: Hawai’i, Fe isotopes, source inheritance, magmatic processes, crystal fractionation

4.1 Introduction

Hawaii’s big island is the most voluminous expression of a mantle plume on Earth and one of the most productive magmatic systems with an average annual lava production of > 25 million m^3. During the past 5 Myrs, ocean island basalts (OIB) from Hawai’i formed two geochemically distinct, parallel chains of volcanoes, the ‘Kea-’ and ‘Loa-trend’ (Jackson et al., 1975). The ‘Kea-trend’ is characterised by less radiogenic isotopes (hereafter referred to as ‘depleted’) and exemplified by lavas erupting from Kīlauea, whereas the ‘Loa-trend’ displays more radiogenic isotopes (termed ‘enriched’ hereafter) and sampled by lavas erupting from Mauna Loa (e.g., Abouchami et al., 2005; Tatsumoto, 1978; Weis et al., 2011).

Global OIB are characterised by a range of enriched vs depleted isotope systematics that are associated with variable crustal components that have supposedly resurfaced in a complex, deep mantle recycling. Stable Fe isotopes have been used to trace the character of some of these enriched components (e.g., Ruttor et al., 2021; Soderman et al., 2021; Nebel et al., 2019; Konter et al., 2016). However, the Fe isotopic composition of erupting lavas is also affected by complex crystal fractionation and accumulation (Teng et al., 2008; Sossi et al., 2016; McCoy-West et al., 2018; Teng et al., 2011; Schuessler et al., 2009; Weyer and Ionov, 2007). This effect was illustrated by crystal fractionation trends in samples from the Kilauea Iki lava lake with progressively heavier Fe isotope values along the liquid line of descent prior

to magnetite fractionation (Teng et al., 2008). From these variations, it is clear that petrogenetic processes can sometimes mask inherited, source related Fe isotopic compositions.

To understand and quantify such petrogenetic processes that lead to masked Fe isotopic signatures, we will compare enriched vs depleted lavas that have not experienced mixing and homogenisation processes and cover a wide range in MgO to ensure lavas show olivine fractionation and accumulation. Such lavas can be found on Kīlauea and Mauna Loa. The Pu‘u ‘Ō‘ō vent in the East Rift Zone of Kīlauea was active for ~35 years from 1983 – 2018 and was continuously geochemically monitored throughout this time (e.g., Garcia et al., 1996; Marske et al., 2008; Poland et al., 2012; Garcia et al., 2021). It has been suggested that the magmatic eruption at Pu‘u ‘Ō‘ō bypasses the summit magma storage beneath Kīlauea, avoiding mixing processes and homogenisation (Garcia et al., 2000; Garcia et al., 1996; Shamberger and Garcia, 2007; Pietruszka et al., 2006). The plumbing system beneath Mauna Loa, is not as well constrained (Robinson and Eakins, 2006). Mauna Loa’s magma reservoir is presumably located at a depth of 3 – 4 km beneath the summit, similar to Kīlauea (Poland et al., 2014). Comparable with interpretations of Pu‘u ‘Ō‘ō and based on major and trace element data of glasses in olivine-rich basalts, it is suggested that the magma erupted along the Southwest Rift Zone of Mauna Loa bypasses Mauna Loa’s summit magma reservoir (Garcia et al., 1995). Therefore, Pu‘u ‘Ō‘ō and Mauna Loa lavas may provide more direct insights into Hawai’ian source material and melting processes and associated Fe isotope systematics.

In this contribution, we aim to investigate the nature and origin of the Fe isotopic composition of tholeiitic, shield-building basalts from representative Loa and Kea Hawai’ian volcanoes. For this, we combine published major and trace element compositions, radiogenic Sr data (Garcia et al. 2021) and new Hf isotope data with stable Fe isotopes of submarine lavas from Mauna Loa’s Southwest Rift Zone and Pu‘u ‘Ō‘ō lavas from Kīlauea’s East Rift Zone.

4.2 Geological setting and samples

Hawai’ian islands form an age progressive chain of subaerial and submarine volcanoes in the central Pacific Ocean. The island of Hawai’i (Big Island) is the largest island of this so-called hotspot track, situated at the south-eastern end of the chain. Mauna Loa and Kīlauea

represent the currently active manifestations of the Loa and Kea trends on the Big Island of Hawai'i. The whole-rock samples studied here are tholeiitic basalts (Supplementary data I Fig. S1; Le Bas et al., 1986; Le Maitre et al., 1989) from the submarine Southwest flank of Mauna Loa and from the subaerial Pu'u 'Ō'ō vent, located on the East Rift Zone of Kīlauea (Fig. 1).

The submarine Mauna Loa samples were collected during a cruise of the *Moana Wave* in 1999 (Davis et al., 2003). The geological settings of samples analysed for this study include radial vent (number of samples; n = 1), rift zone (n = 7), flank (n = 3) and landslides (n = 3). The location of collection of the landslide samples is known, however, their primary location of eruption is less clear. Given this uncertainty, the landslide samples will be highlighted in the following and discussed separately. Radial vent and flank samples will be grouped together. The Mauna Loa basalts analysed here are aphanitic to glassy and slightly vesicular with variable proportions of olivine phenocrysts (Davis et al., 2003). The rift zone basalts consist of 11 – 30 % modal olivine and have calculated normative olivine of 1 to 30 vol%. In comparison, basalts from the radial vent, and flank have lower normative olivine of 0 – 17 vol%, and landslide samples have normative olivine of 0 – 39 vol%. The MgO contents of rift zone samples range from 11.7 to 23.8 wt.%, radial vent and slope basalts range from 6.93 to 18.2 wt.%. Landslide samples show MgO of 6.89 – 25.3 wt.% (Table 1).

The subaerial samples of Pu'u 'Ō'ō are labelled according to the date the rock was collected (e.g., day/month/year: 19/09/03), with samples covering eruptions between 2003 – 2005, 2010 and 2012 – 2014. Samples were collected mostly within one day after eruption in a molten state and were quenched in water (Garcia et al., 2021). These artificially quenched samples are aphyric to weakly phyric with small crystals of olivine and occasional clinopyroxene and plagioclase within a glassy to cryptocrystalline matrix (Garcia et al., 2021). MgO contents of the analysed samples range from 6.61 to 7.61 wt.% (Garcia et al., 2021).

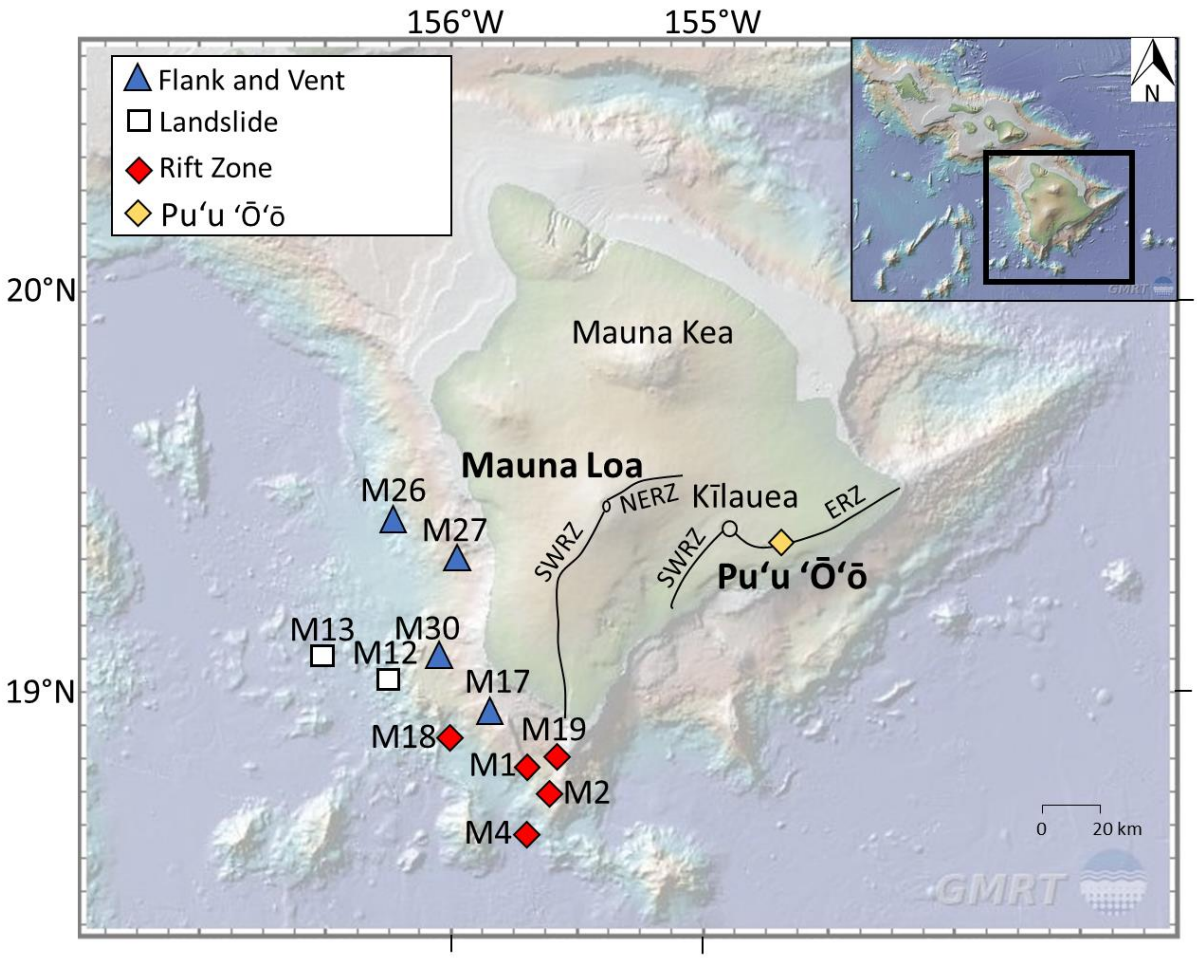

Figure 1. Dredged locations for Mauna Loa samples (M-) and Pu'u 'Ō'ō. SWRZ = Southwest Rift Zone, NERZ, Northeast Rift Zone, ERZ = East Rift Zone indicated with black lines. The maps were made with GeoMapApp (www.geomapapp.org; Ryan et al., 2009).

4.3 Analytical methods

Stable Fe and radiogenic Hf isotopes were analysed in a total of 23 whole-rock powders representing 14 submarine lavas from Mauna Loa and nine subaerial lavas from Pu'u 'Ō'ō. Major and trace element, as well as Sr isotopic data are taken from Prichard (2020) for the Mauna Loa samples and Garcia et al. (2021) for the Pu'u 'Ō'ō lavas. The data is summarized here for convenience (Supplementary data II). In addition, two samples from Pu'u 'Ō'ō (09/19/2003 and 10/15/2004) and three samples from Mauna Loa (M4-9, M19-24 and M1-26) have been analysed for Sr isotopic data as part of this study to complement the existing dataset.

For Sr analyses, the chemical separation is outlined by Pin et al. (2014) and will be briefly described here. Rock powder (~10 mg) was dissolved in a 1:1 mixture of concentrated HF-HNO_3 at 180°C over 3 days in 15mL Savillex® beakers. After evaporation at 120°C, the samples were treated three times with a drop of concentrated HNO_3 + 0.5M HCl and to break down CaF bonds. For chromatographic extraction, the resin Eichrom® Sr-Spec (100 – 150 µm) was preconditioned with 0.1mL of 1M HNO_3 containing 50mg/mL of ascorbic acid. After introducing the sample solution onto the resin, the resin was rinsed with 0.5mL of 1M HNO_3 containing 50mg/mL of ascorbic acid. The Sr-Spec was washed with 7M HNO_3 to get rid of unwanted elements (e.g., Barium). Strontium elution was achieved with 0.05M HNO_3. Samples were left on a hotplate at 55°C until dryness was achieved.

Chromatographic extraction and isotope analyses of stable Fe isotopes and radiogenic Hf isotopes were carried out on the same sample aliquots following the analytical procedures described in detail by Cheng et al. (2014) and Sossi et al. (2015). Rock powders (~25 mg) were weighed into Savillex® beakers and dissolved with 2mL concentrated HF:HNO_3 (ratio 1:2). After drying on a hotplate at 120°C, samples were treated with 16M HNO_3 and taken up with 9M HCl to be pipetted onto the AG-MP-1 anion resin, which was preconditioned with 9M HCl (Cheng et al., 2014). The resin is used to separate Fe from the matrix, which was achieved by rinsing the resin with 9M HCl and 5M HCl. The matrix was collected into a Teflon beaker for Hf analysis (see below). Iron was washed from the resin using 1M HCl, collected in a Teflon beaker and placed on a hotplate at 90°C.

The chromatographic extraction of Hf is described in Nebel et al. (2009) and Cheng et al. (2014). The matrix was collected as explained above (removed matrix during chromatographic extraction of Fe) and dissolved in 3M HCl. The matrix was then loaded onto the preconditioned Eichrom® Ln spec resin. The resin was rinsed with 3M HCl, 6M HCl and MQ water (18mΩ). For Ti elution a mixture of citric acid and 0.4M HNO_3 and 1% H_2O_2 (60ml; Münker et al, 2001) was used. With 0.5M HF (10ml) Hf was extracted and dried at 60°C. The samples prepared for Fe analyses were taken up in 2% HNO_3.

The Sr, Hf and Fe isotope analyses were undertaken at the Isotopia Laboratory, Monash University, Melbourne, using the ThermoFisher™ Scientific Neptune*Plus* multi-collector inductively coupled plasma mass spectrometer (MC-ICP-MS). For Sr and Fe analyses, the

samples were introduced via a low flow quartz cyclonic spray chamber and a PFA® nebuliser. Strontium isotopes were analysed in low and Fe in medium resolution mode. For Hf analysis, the samples were introduced via a Teledyne Cetac® Technologies Aridus II to create dry plasma conditions. Hf isotopes were measured in low resolution mode. To ensure data accuracy, BHVO2 (Hf and Sr reference material; Supplementary data II) was analysed and agrees with literature values (Weis et al., 2005).

For Fe analyses, each sample was analysed two or three times from a single dissolution. The average of these analyses is presented as the isotope ratio for each sample. A Ni standard solution was added to each dissolution to normalise the instrumental mass bias effects (Sossi et al., 2015). Fe isotopic compositions are reported relative to the IRMM-524a external standard, which is isotopically identical to IRMM-014 (Craddock and Dauphas, 2011) with ^{5x}Fe being either ^{56}Fe or ^{57}Fe:

$$\delta^{5x}Fe = \left[\frac{^{5x}Fe/^{54}Fe_{Sample}}{^{5x}Fe/^{54}Fe_{IRMM-524a}} - 1\right] x\ 1000 \quad (1)$$

The reproducibility of the IRMM524a standard on δ^{57}Fe is ± 0.03 ‰ (n=94, 2S.D.). As a measure of data accuracy, the USGS reference basalt BCR-2 was analysed. The data are presented in Table 1 and Supplementary data II. The results for reference materials are consistent with previously published literature values (e.g., BCR-2 literature δ^{57}Fe +0.14 ± 0.02 ‰ (2S.E.; Sossi et al., 2015) and δ^{57}Fe +0.13 ± 0.02 ‰ (2S.E.; Craddock and Dauphas, 2011) vs analysed value of δ^{57}Fe +0.15 ± 0.00 ‰ (2S.E.)).

4.4 Results

The δ^{57}Fe of Mauna Loa's rift zone, slope, and radial vent basalts range from -0.06 to +0.19 ‰ (Fig. 2a). In ε_{Hf} values, rift zone samples range from +5.5 to +7.6, whereas radial vent and slope samples span from +6.0 to +10.7 (Fig. 2b). In ^{87}Sr/^{86}Sr, the three rift zone samples analysed range from 0.70366 to 0.70375. The landslide samples present δ^{57}Fe and ε_{Hf} spanning +0.00 to +0.20 ‰ and +5.9 to +10.1, respectively. With regards to stable Fe and radiogenic Hf isotopes, radial vent, slope and rift samples overlap, with rift zone samples tending towards slightly heavier Fe isotopic compositions and more depleted Hf signatures. Based on ε_{Hf} and ^{87}Sr/^{86}Sr, Mauna Loa lavas, including landslide samples, are comparable to

other volcanoes ascribed to the Loa trend (data from GEOROC database (georoc.mpch-mainz.gwdg.de/georoc/), including Mauna Loa, Hualalai, Kahoolawe and Lanai (Fig. 2b).

The Pu'u 'Ō'ō lavas analysed here range in $\delta^{57}Fe$ from +0.09 to +0.18 ‰ and in ε_{Hf} from +9.3 to +13.1, with no significant differences in these parameters between the 2004 – 2005 and 2012 – 2014 eruptions. Two samples from Pu'u 'Ō'ō (19/09/2003 and 25/06/2010) deviate by having lighter $\delta^{57}Fe$ (-0.02 ‰) and heavier $\delta^{57}Fe$ (+0.30 ‰), respectively. In the radiogenic isotope system of $^{87}Sr/^{86}Sr$ vs $^{176}Hf/^{177}Hf$, Pu'u 'Ō'ō lavas are comparable to volcanoes ascribed to the Kea trend (data from GEOROC database (georoc.mpch-mainz.gwdg.de/georoc/), including Kohala, Mauna Kea, and Kīlauea (Fig. 2b). The two samples analysed for $^{87}Sr/^{86}Sr$ range from 0.70363 to 0.70365.

The primary Fe isotopic compositions of basaltic magmas can be modified by crustal processes such as fractional crystallization or accumulation of phases such as olivine and magnetite, and surficial or submarine alteration and weathering. For the samples studied here, alteration and weathering are unlikely to be an important factor because the Pu'u 'Ō'ō samples were collected as live lava or within a few hours of eruption and the Mauna Loa samples show no geochemical signatures of alteration such as fractionated K_2O/P_2O_5, Ba/Rb, or U/Th ratios (Supplementary data I Fig. S2 & S3). Magnetite fractionation is also unlikely to be an important process here because none of the magmas are sufficiently evolved to have crystallized magnetite (typically MgO < 4 wt. % for Hawaiian tholeiites). None of the lavas show signs of sulfide saturation (Cu vs Y; McCoy-West et al., 2018).

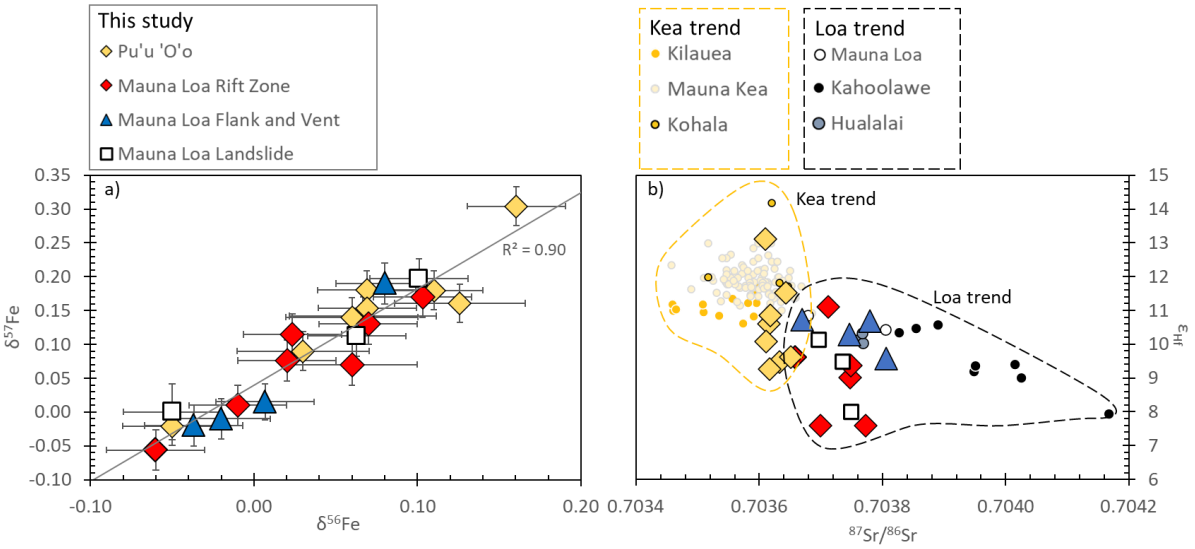

Figure 2. a) $\delta^{56}Fe$ vs $\delta^{57}Fe$, with grey line representing the linear regression (R^2=0.90). b) $^{87}Sr/^{86}Sr$ vs ε_{Hf}, yellow line highlights data points associated with the Kea trend and pink line highlights data points associated with the Kea trend. Data from Mauna Kea from Bryce et al. (2005) and Blichert-Toft et al. (2003), Kilauea from Tanaka et al. (2008), Kohala from Hanano et al. (2010) and Stille et al. (1986), Mauna Loa from Weis et al. (2011), Kahoolawe from Huang et al. (2005), Lanai from Gaffney et al. (2005) and Frey et al. (2016). Hualalai from Yamasaki et al. (2009). For calculation of ε_{Hf}, the $^{176}Hf/^{177}Hf$ value for Chondrite Uniform Reservoir (CHUR; $^{176}Hf/^{177}Hf$ = 0.282785) from Bouvier et al. (2008) was used.

Table 1. Iron isotopic compositions of submarine Mauna Loa and subaerial Pu'u 'Ō'ō lavas analysed in this study. MgO values from Prichard (2020). 2 S.E. = 2 S.D./ $\sqrt{n}$, n for number of Fe isotope analyses, after Sossi et al. (2015), 2S.D. for two-standard deviation, 2S.E. for two-standard error. Each sample has been analysed 2-3 times (n=2-3). $\delta^{57}Fe_{prim}$ calculated from $\Delta^{57}Fe_{ol\text{-}melt} = -0.4*10^6/T^2$ to correct for olivine accumulation or fractionation as described in the text. See Supplementary data II for major element, trace element and radiogenic isotopic compositions.

Volcano	Sample#	location	MgO (wt.%)	$\delta^{56}Fe$ (‰)	±2 S.E.	$\delta^{57}Fe$ (‰)	±2 S.E.	$\delta^{57}Fe_{prim}$ (‰)	n
Mauna Loa	M1-1	Rift Zone	23.77	+0.07	0.03	+0.13	0.02	+0.13	3
	M1-16	Rift Zone	16.71	+0.10	0.02	+0.17	0.02	+0.17	3
	M1-26	Rift Zone	22.14	+0.02	0.02	+0.08	0.02	+0.08	3
	M2-10	Rift Zone	11.71	-0.01	0.02	+0.01	0.03	-0.01	5
	M4-9	Rift Zone	21.42	+0.02	0.02	+0.11	0.01	+0.11	3
	M18-31	Rift Zone	18.27	-0.06	0.01	-0.06	0.02	-0.06	2
	M19-24	Rift Zone	12.88	+0.06	0.04	+0.07	0.04	+0.04	3
	M12-17	Landslide	6.89	+0.10	0.02	+0.20	0.03	+0.13	3
	M13-25	Landslide	25.23	-0.05	0.03	+0.00	0.04	+0.00	3
	M13-38	Landslide	21.11	+0.06	0.01	+0.11	0.02	+0.11	2
	M17-2	Flank	7.06	+0.08	0.01	+0.19	0.02	+0.12	3
	M26-44	Flank	15.44	-0.02	0.01	-0.01	0.03	-0.01	2
	M30-1	Flank	18.13	+0.01	0.02	+0.02	0.03	+0.02	3
	M27-11	Radial Vent	6.93	-0.04	0.00	-0.02	0.01	-0.08	2
Pu'u 'Ō'ō	19/09/2003	Rift Zone	7.44	-0.05	0.02	-0.02	0.03	-0.08	3
	23/04/2004	Rift Zone	7.13	+0.11	0.02	+0.18	0.05	+0.11	3
	15/10/2004	Rift Zone	7.24	+0.07	0.05	+0.14	0.04	+0.08	3
	08/08/2005	Rift Zone	6.91	+0.06	0.03	+0.14	0.03	+0.07	2
	20/06/2012	Rift Zone	6.97	+0.03	0.03	+0.09	0.03	+0.02	3
	25/07/2012	Rift Zone	6.61	+0.16	0.01	+0.30	0.02	+0.23	2
	08/06/2013	Rift Zone	7.61	+0.07	0.00	+0.18	0.03	+0.12	3
	18/11/2013	Rift Zone	7.12	+0.13	0.02	+0.16	0.01	+0.09	2
	27/06/2014	Rift Zone	6.93	+0.07	0.01	+0.15	0.01	+0.08	2
	BCR-2			0.08	0.02	0.15	0.00		5

4.5 Discussion

Ocean island basalts present heterogeneous stable Fe isotopic compositions (Fig. 3; e.g., Nebel et al., 2019; Soderman et al., 2021; Konter et al., 2016; Williams et al., 2005; Williams and Bizimis, 2014; Teng et al., 2008; Teng et al., 2013; Chen et al., 2019). This substantial heterogeneity within and among OIB cannot be explained by one single process, but requires several processes that can add to or negate each other to various degrees: (1) kinetic and equilibrium fractionation processes during partial melting (Weyer and Ionov, 2007) and crystallisation (Teng et al., 2008), (2) alteration processes within the mantle (e.g., diffusion during peridotite-melt interaction or mantle metasomatism by silicate or carbonate melt (Teng et al., 2011; Poitrasson et al., 2013; Weyer and Ionov, 2007; Williams et al., 2005; Beard et al., 2003), and (3) Fe isotope heterogeneity within the source material generating OIB (Nebel et al., 2019, Konter et al., 2016). Each of these processes will be discussed in the following.

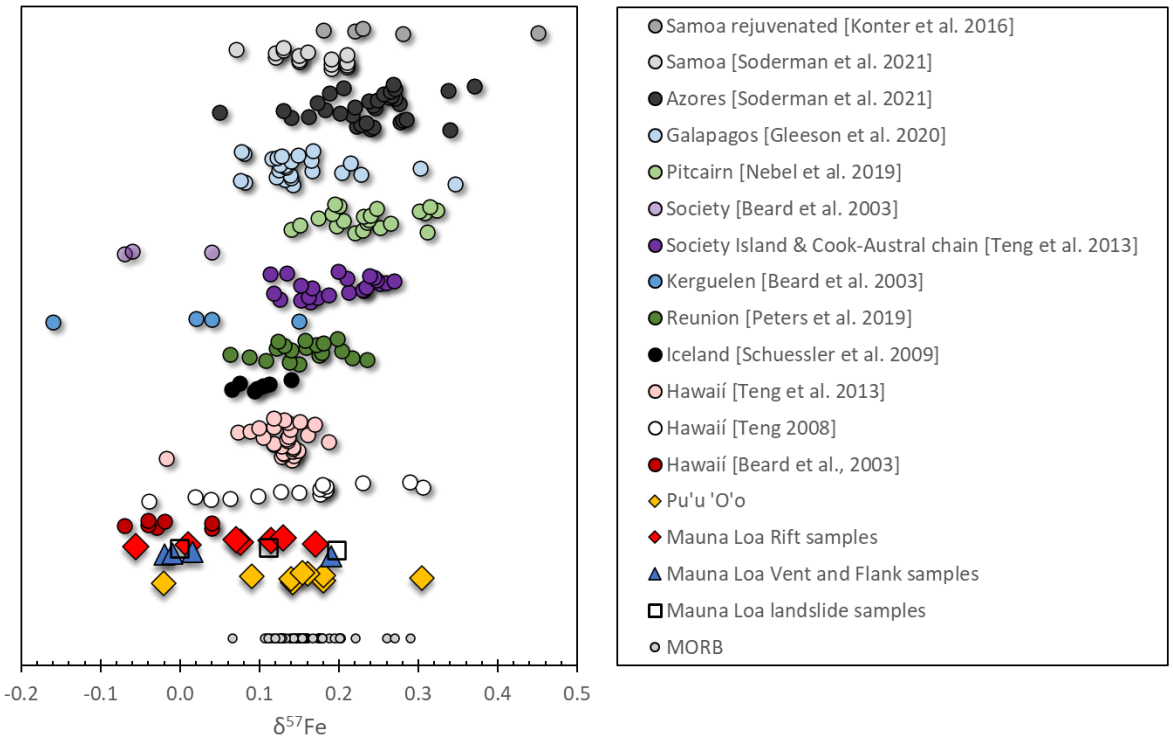

Figure 3. Compilation of Fe isotope data from OIB (see legend for references) and MORB (compilation from Chen et al. (2019)). BSE at $\delta^{57}Fe$ = +0.05 ± 0.01‰ (2S.E.; Sossi et al., 2016).

4.5.1 Olivine control on Fe isotopic compositions

During ascent, cooling of tholeiitic magmas leads to crystallization of olivine, which enriches the melt in heavier Fe isotopes (e.g., Teng et al., 2008; Teng et al., 2013). This mass dependent, mineral-melt isotopic fractionation is due to differences of the bonding environment of Fe^{2+} and Fe^{3+}, e.g., olivine has weak Fe-O bonds and hence concentrates light Fe in its structure (Dauphas et al., 2014; Teng et al., 2013; Sossi et al., 2012; Sossi and O'Neill, 2017; McCoy-West et al., 2018; Rabin et al., 2021).

To illustrate olivine fractionation and accumulation, we compared Mauna Loa and Pu'u 'Ō'ō lavas to the crystal fractionation trend represented by lavas from Kīlauea Iki lava lake. Here, the most differentiated melts (low MgO) have heavy Fe isotopic compositions and the most primitive melts (high MgO) tend towards lighter Fe isotopes (Fig. 4a; Teng et al., 2008).

The Pu'u 'Ō'ō basalts show a narrow range in MgO from 6.6 – 7.6 wt. % but have δ^{57}Fe ranging from -0.02 to +0.30 ‰ defining a cluster of data at +0.15 ‰ that lies just beneath Kīlauea Iki lava lake samples (Fig. 4a).. Such deviation has also been recognised for Koolau lavas (Teng et al., 2013). Teng et al. (2013) suggest that this deviation indicates the effect of both crystal fractionation and a parental melt that is heterogeneous in its Fe isotopic composition. Heterogeneities in the parental melt might also explain the variation in δ^{57}Fe of the Pu'u 'Ō'ō samples investigated here. One sample from Pu'u 'Ō'ō (19/09/2003 with δ^{57}Fe = -0.02 ‰) represents an outlier in the Pu'u 'Ō'ō sample suite when compared to the crystal fractionation trend as well as other OIB, such as the Tasmantid Seamounts (Ruttor et al. 2021), Samoa and the Azores (Soderman et al., 2021), Galapagos (Gleeson et al., 2020), Pitcairn (Nebel et al., 2019) and Baffin Island (McCoy-West et al., 2018; Fig. 4d-f).

Lavas from Mauna Loa range in MgO from 6.9 – 25.2 wt. %. Six samples (one Mauna Loa Vent and Flank sample and five Mauna Loa Rift samples) follow the crystal fractionation trend defined by the Kīlauea Iki lava lake samples. However, one Mauna Loa rift sample (M18-31 with δ^{57}Fe = -0.06 ‰) and three Mauna Loa vent and flank samples (M26-44 with δ^{57}Fe = -0.01 ‰, M27-11 with δ^{57}Fe = -0.02 ‰ and M30-1 with δ^{57}Fe = +0.02 ‰) deviate towards lighter Fe isotopic values. Additionally, these outliers show the lightest Fe isotopic compositions when compared to other OIB at similar MgO values, e.g., picrites from Baffin Island (further discussed below; McCoy-West et al., 2018) or basalts from Samoa (Soderman

et al., 2021). Mauna Loa landslide samples follow the crystal fractionation trend represented by Kīlauea Iki lava lake.

Strong deviations from the crystal fractionation towards light Fe isotopes have been associated with mantle metasomatism (Poitrasson et al., 2013; Weyer and Ionov, 2007). In the following, we will first estimate the primary melt Fe isotopic composition $\delta^{57}Fe_{prim}$ of the magma by applying a correction for olivine fractionation and accumulation followed by discussing if mantle metasomatism can explain $\delta^{57}Fe_{prim}$ variations.

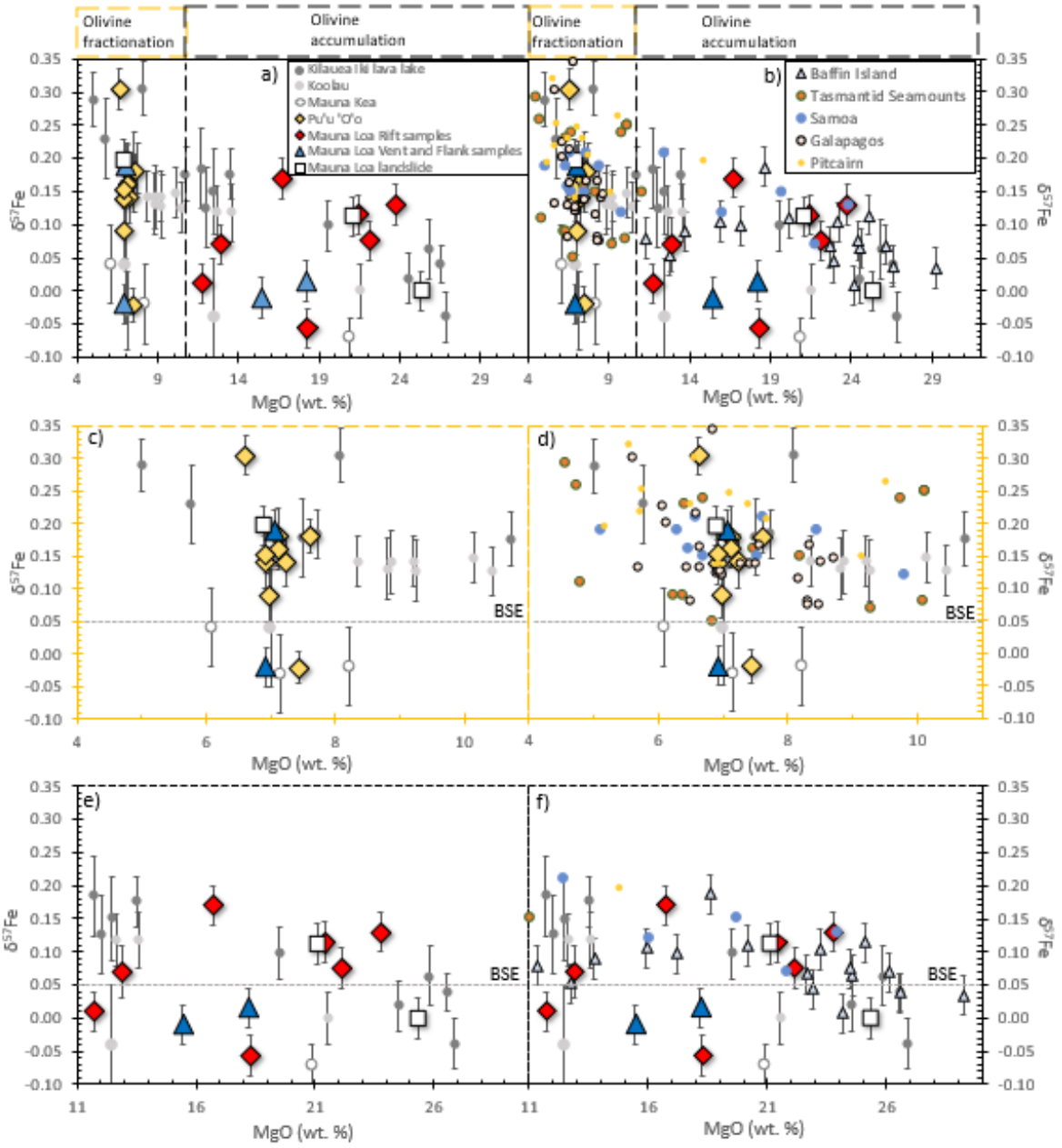

Figure 4. a) – f) MgO vs δ^{57}Fe. Lavas from Koolau and Mauna Kea (Beard et al., 2003), Kīlauea Iki are from Teng et al. (2008), Koolau from Teng et al. (2013), Tasmantid Seamounts (Ruttor et al. 2021), Samoa and the Azores (Soderman et al., 2021), Galapagos (Gleeson et al., 2020), Pitcairn (Nebel et al., 2019) and Baffin Island from (McCoy-West et al., 2018). Black dotted line in a) represents most magnesian melt from Kīlauea Iki lava lake from 1959 with MgO = 10.7 wt.%, which defines olivine fractionation for basalts with MgO < 10.7 wt.% and olivine accumulation for lavas with MgO > 10.7 wt.%. BSE at δ^{57}Fe = +0.05 ± 0.01‰ (2S.E.; Sossi et al., 2016).

With MgO > 10.7 wt. %, most of the Mauna Loa samples show olivine accumulation (Rhodes, 1995; Teng et al., 2008; Rhodes and Hart, 1995), when the interpretation of Teng et al. (2008) is followed. The Baffin Island picrites have been interpreted to show olivine accumulation at MgO > 21.0 wt. % (Fig. 5). A parental melt composition of 21.0 wt. % is supported on a log-log plot of incompatible vs compatible elements (e.g., MgO vs Y and Yb (Nebel et al., 2014); Supplementary data I Fig. S5) for Mauna Loa lavas.. For comparison, Falloon et al. (2007) calculated a parental melt composition of MgO 17.5 wt.% for Mauna Loa lavas using olivine geothermometry. It is thus suggested that olivine accumulation starts presumably at more primitive MgO values (i.e., MgO 17.5 – 21.0 wt.%) for Mauna Loa lavas contrary to lavas from Kīlauea Iki lava lake with MgO = 10.7 wt.%. This suggests that lavas from Mauna Loa can be corrected for olivine crystallisation at MgO < 17.5 - 21.0 wt. % (Fig. 5 & 6).

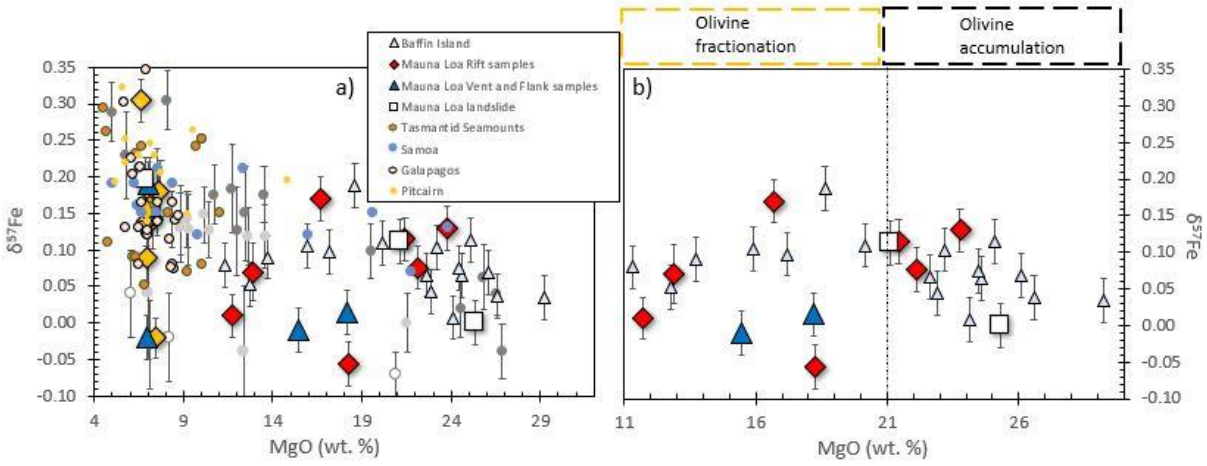

Figure 5. a) and b) MgO vs δ^{57}Fe. Lavas from Koolau and Mauna Kea (Beard et al., 2003), Kīlauea Iki are from Teng et al. (2008), Koolau from Teng et al. (2013), Tasmantid Seamounts (Ruttor et al. 2021), Samoa and the Azores (Soderman et al., 2021), Galapagos (Gleeson et al., 2020), Pitcairn (Nebel et al.,

2019) and Baffin Island from (McCoy-West et al., 2018). Black dotted line defines olivine accumulation for lavas with MgO > 21.0 wt.%.

To correct for fractional crystallization of olivine, we followed the method outlined in Sossi et al. (2016). We added equilibrium olivine to a melt composition ($Fe^{3+}/\sum Fe$ = 0.15; Nebel et al., 2019; Sossi et al., 2016) for samples with < 21.0 wt.% MgO until an equilibrium with the primitive mantle Mg#=90 is reached. The magnitude of correction increases with decreasing MgO value. For the Pu‘u ‘Ō‘ō lavas with 6.6 – 7.6 wt.% MgO, this correction reduced the measured $\delta^{57}Fe$ value by 0.06 to 0.08‰, expressed here as $\Delta^{57}Fe$. As noted above, the Mauna Loa samples have a wide range of MgO (6.9 – 25.3 wt.%), reflecting variable extents of olivine fractionation and accumulation. Four Mauna Loa Rift samples, three Mauna Loa Vent and Flank samples and one Mauna Loa landslide sample show olivine fractionation with a correction of 0.001 to 0.07‰ $\Delta^{57}Fe$ (Fig. 6).

Our model uses a temperature dependent fractionation factor $\Delta^{57}Fe_{Ol\text{-}Melt} *10^6/T^2 = -0.4$, where $\Delta^{57}Fe_{Ol\text{-}Melt}$ is the difference between the Fe isotopic composition of the melt $\delta^{57}Fe_{Melt}$ and olivine $\delta^{57}Fe_{Ol}$ (Sossi et al., 2016). For Hawai’ian lavas, a $\Delta^{57}Fe_{Ol\text{-}Melt} *10^6/T^2 = -0.15$ has been suggested (Teng et al., 2008). Applying the smaller fractionation factor leads to corrected values that are unresolvable from the measured data, whereas a fractionation factor of $-0.4*10^6/T^2$ could show an over-correction. We thus corrected our data with both, a more conservative fractionation factor of $-0.15*10^6/T^2$ and with $-0.4*10^6/T^2$ and compare the results in the Supplementary data I Fig. S4. The calculated primary melt Fe isotopic compositions ($\delta^{57}Fe_{prim}$) with the more extreme $\Delta^{57}Fe_{Ol\text{-}Melt} *10^6/T^2 = -0.4$ are shown in Fig. 6 and will be compared with radiogenic isotopic ratios as well as to the primitive mantle normalised trace element ratios in the following. Choosing $\Delta^{57}Fe_{Ol\text{-}Melt} *10^6/T^2 = -0.4$ to compare $\delta^{57}Fe_{prim}$ to radiogenic isotopic data has no implications on the interpretation, because both fractionation factors of $-0.4*10^6/T^2$ and $-0.15*10^6/T^2$ show the same distribution of $\delta^{57}Fe_{prim}$ vs Sr or Hf isotopic ratios (Supplementary Data I Fig. S9). The extent of the applied olivine fractionation correction is illustrated in Figure 6a and b. As a trace element in olivine, Ni is independent of our corrections and thus a good measure to validate accountability of our corrections.

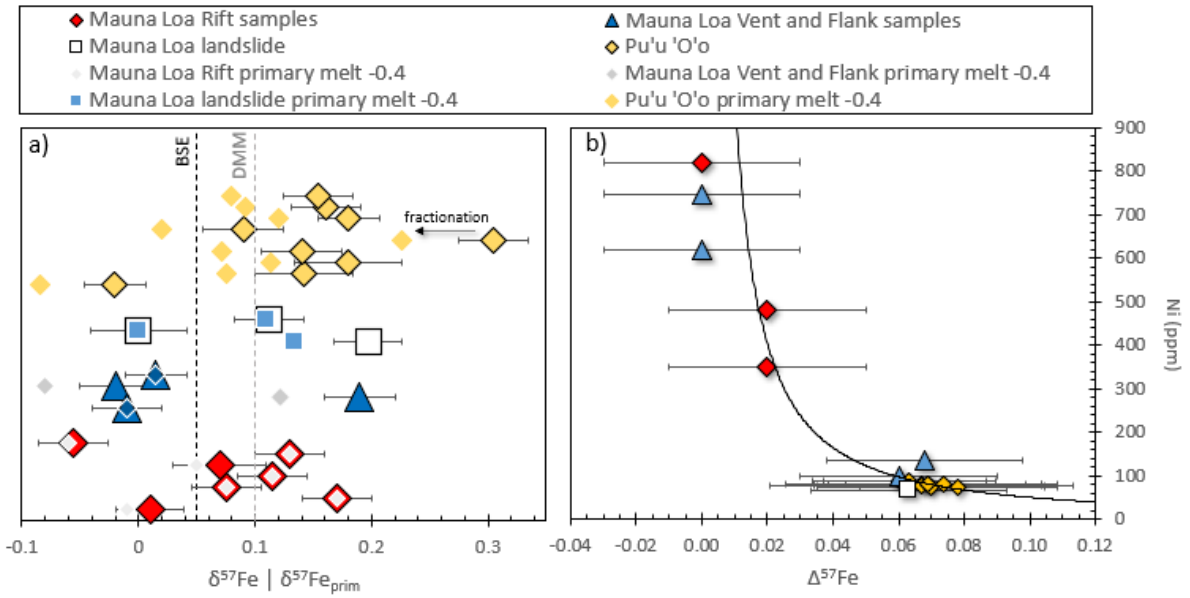

Figure 6. a) shows measured $\delta^{57}Fe$ and olivine fractionation corrected samples $\delta^{57}Fe_{prim}$, bulk silicate earth (BSE) at $\delta^{57}Fe$ = +0.05 ± 0.01‰ (2S.E.; Sossi et al., 2016), depleted MORB mantle (DMM) at $\delta^{57}Fe$ = +0.10 ± 0.01‰ (2S.E.; Sossi et al., 2016). b) degree of correction $\Delta^{57}Fe = \delta^{57}Fe_{meas} - \delta^{57}Fe_{prim}$ vs Ni (ppm), which is independent to our applied correction and a measure of olivine fractionation. Black curve illustrates exponential average through data. Samples with MgO ≤ 21.0 wt. % have been corrected for olivine fractionation.

Olivine accumulation should result in lighter $\delta^{57}Fe$ compared to the primary melt Fe isotopic composition. Olivine accumulation can be corrected for (McCoy-West et al., 2018; Nebel et al., 2014) when re-equilibrated with the melt (Teng et al., 2011) by treating olivine accumulation as a simple linear addition process. In this case, it is unlikely that accumulated olivine was in equilibrium with the final bulk composition. Therefore, we have not applied this correction to the samples analysed here as it would result in unreliable data. We note that the poor trend of MgO vs $\delta^{57}Fe$ for lavas that show olivine accumulation could result from the variation of olivine population of each sample (i.e., 17 – 30% modal olivine; Supplementary data I Fig. S6).

Whereas olivine fractionation can account for small variations in Fe isotopic compositions ($\Delta^{57}Fe = \delta^{57}Fe - \delta^{57}Fe_{Prim} \leq +0.08‰$), the missing trend in MgO vs $\delta^{57}Fe$ suggests that lavas of Pu‘u ‘Ō‘ō and Mauna Loa have experienced more than one process that fractionates its Fe isotopes. In first order, this missing co-variation argues, as expected (see Introduction), against the presence of a closed magma chamber. If a closed magma chamber would be

present, the lavas would have been not or only minimally exposed to other processes than fractional crystallisation and would correlate in MgO vs δ^{57}Fe (Chen et al., 2021; Teng et al., 2008). The strongest deviation from the crystal fractionation and accumulation trend (created by Kilauea Iki lava lake lavas) is represented by outliers of Pu'u 'Ō'ō and Mauna Loa, which tend towards δ^{57}Fe < BSE of δ^{57}Fe +0.05 ± 0.01‰ (2S.E.; Sossi et al., 2016). In the following, we will investigate additional processes or phases that lead to the light Fe isotopic compositions of these outliers.

4.5.2 Kinetic vs equilibrium fractionation

An additional process that can alter the Fe isotopic composition of OIB and eventually explain the deviation of outliers of Mauna Loa and Pu'u 'Ō'ō lavas from the crystal fractionation trend is kinetic isotope fractionation, a process that can be associated with fluid or melt percolation through the lithospheric mantle (e.g., Poitrasson et al., 2013; Weyer and Ionov, 2007). To understand if kinetic (e.g., diffusion) or equilibrium fractionation dominates the fractionation of Fe isotopes of Mauna Loa and Pu'u 'Ō'ō lavas, a three-isotope diagram can be used (Young and Galy, 2004; McCoy-West et al., 2018). The three-isotope diagram uses the different mass dependent fractionation laws for kinetic and equilibrium fractionations to identify single processes as well as multi-stage processes of fractionation in olivine crystals as well as whole rock data (Young and Galy, 2004; McCoy-West et al., 2018). Young et al. (2002) describe the difference of kinetic to equilibrium fractionation as follows: *"(…) kinetic fractionation results from motions that can often be ascribed classically using effective masses whereas equilibrium exchange is purely a quantum phenomenon that depend on atomic masses alone."* This difference results in the following equation:

$$\alpha(^{57}Fe/^{54}Fe) = (\alpha(^{56}Fe/^{54}Fe))^{\beta} \quad (1)$$

With α being the fractionation factor and β describing equilibrium fractionation with:

$$\beta = \frac{\frac{1}{m1} - \frac{1}{m3}}{\frac{1}{m1} - \frac{1}{m2}} \quad (2)$$

m1 is the atomic mass of ^{54}Fe with 53.93961, *m2* the atomic mass of ^{56}Fe with 55.93494, *m3* the atomic mass of ^{57}Fe with 56.93540. Whereas the kinetic fractionation law differs with:

$$\beta = \frac{\ln(\frac{M1}{M3})}{\ln(\frac{M1}{M2})} \quad (3)$$

with *M1*, *M2* and *M3* representing the masses in motion during kinetic processes. Following McCoy-West et al. (2018), this results in β = 1.475 for equilibrium and β = 1.4484 for kinetic mass-dependent fractionation of Fe isotopes. To accommodate for this difference in β, $\Delta(^{57}Fe/^{54}Fe)'$ defined as a linear form of δ, δ' is used:

$$\Delta(^{57}Fe/^{54}Fe)' = \delta(^{57}Fe/^{54}Fe)' - 1.475 * \delta(^{56}Fe/^{54}Fe)' \quad (4)$$

With δ' using the measured δ values:

$$\delta' = 10^3 \ln\left(\frac{(\delta+10^3)}{10^3}\right) \quad (5)$$

Figure 7a shows that Fe isotope fractionation caused by multistage processes dominates the Fe isotopic compositions of outliers from Mauna Loa and Puʻu ʻŌʻō lavas. Kinetic fractionation, e.g., the process of diffusion during melt percolation, should result in an enrichment of light Fe isotopes in the melt (McCoy-West et al., 2018; Richter et al., 2003; Weyer and Ionov, 2007). However, diffusion during peridotite-melt interaction could explain only in parts the light Fe isotopic composition of outliers from Mauna Loa and Puʻu ʻŌʻō lavas. Disequilibrium processes, such as diffusion induced metasomatism (Weyer and Ionov, 2007) have been suggested for lavas deviating from the crystal fractionation trend represented by Kīlauea Iki lava lake lavas (e.g., Fig. 4), which have experienced equilibrium fractionation processes only (Fig. 7a, b).

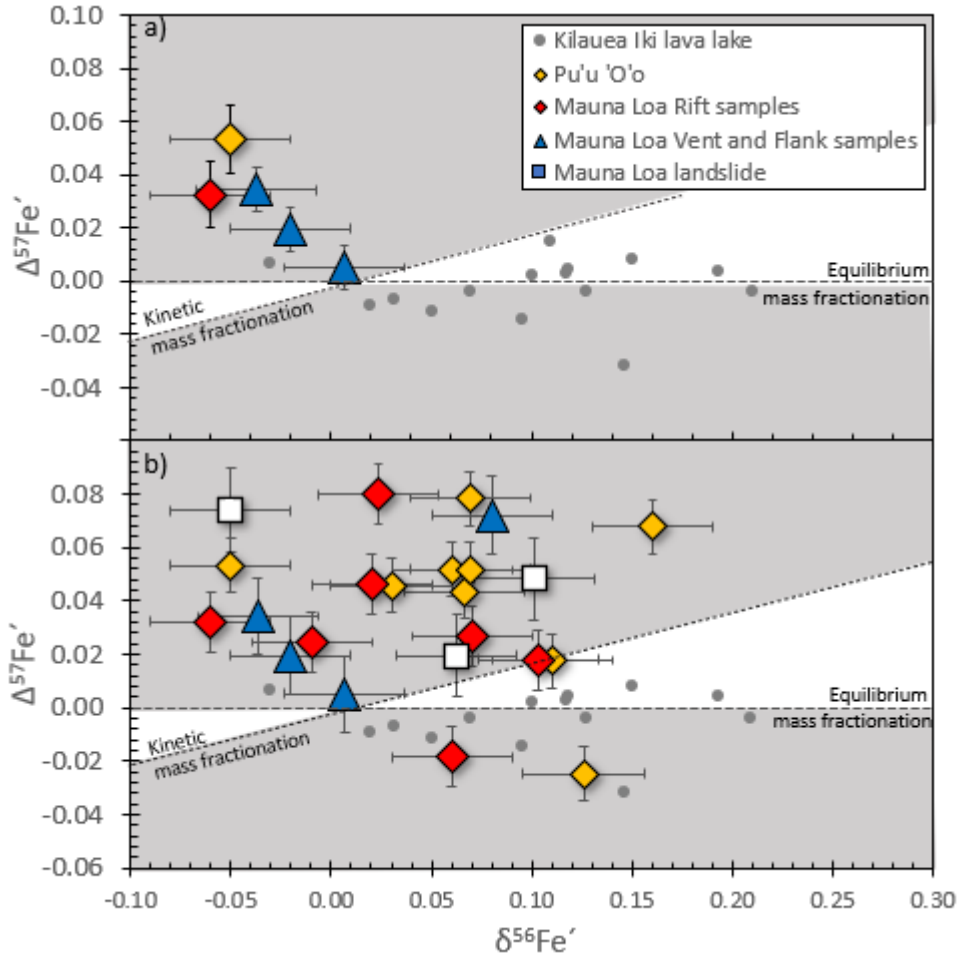

Figure 7. a) Outliers and b) complete data set of Mauna Loa and Pu‘u ‘Ō‘ō in $\delta^{56}Fe'$ vs $\Delta^{57}Fe'$ showing mass dependent fractionation of Fe isotopes. $\delta^{x}Fe' = 1000\ln((\delta^{x}Fe+1000)/1000)$ with $\delta^{x}Fe$ = measured $\delta^{57}Fe$ or $\delta^{56}Fe$, and $\Delta^{57}Fe' = \delta^{57}Fe' - 1.475 \times \delta^{56}Fe'$ (McCoy-West et al., 2018). Kinetic and equilibrium trends (dotted lines) represent single stage processes. Equilibrium fractionation shows a slope of 0 (β = 1.475) and of ~0. 027 (β = 1.4881). Samples that plot into the grey area are the product of multistage scenarios (grey field). Error bars for Kīlauea Iki lava lake lavas (Teng et al., 2008) have not been plotted to maintain overview.

Because outliers of Mauna Loa and Pu‘u ‘Ō‘ō plot within the area that describes multistage processes, we suggest that equilibrium mass fractionation in combination or in exchange with processes causing disequilibrium Fe isotope fractionation need to be considered to explain their light Fe isotopic composition. Interestingly, the rest of the Mauna Loa and Pu‘u ‘Ō‘ō lava suit does not follow the equilibrium fraction trend indicated by lavas from Kīlauea Iki lava lake but can only be explained by multiple processes that cause Fe isotopic fractionation (Fig. 7b).

This interpretation supports our assumption that these lavas have experienced more than one process that affected their Fe isotopic compositions.

Other processes that can alter the Fe isotopic composition of lavas is the melting degree. Considering the inter-mineral equilibrium fractionation of Fe (see olivine fractionation correction; Macris et al., 2015; Beard and Johnson, 2004), a melt that experienced high melting degrees is expected to show a relatively small Fe isotope fractionation compared to low degree melts (Williams and Bizimis, 2014). This can be seen, for example, in Figure 3, where Hawai'ian tholeiitic lavas show lighter Fe isotopic compositions compared to alkali lavas from the Azores (Soderman et al., 2021) and Pitcairn (Nebel et al., 2019). Estimates regarding the melting degree of Hawai'ian lavas suggest *F* = 4-10%, with Kīlauea representing lower degrees of melting than Mauna Loa (Norman and Garcia, 1999). Melting models have shown that melting degrees of 4-10% can account for a small fractionation with Δ^{57}Fe 0.02 – 0.10 ‰ of the residual source (Williams and Bizimis, 2014; Foden et al., 2018; Sossi et al., 2016; Dauphas et al., 2014). Thus, the fractionation of Fe isotopes caused by the melting degree is not large enough to account for the range in Fe isotopes here (if outliers are excluded). Additionally, comparing proxies for degrees of melting with stable Fe isotopes (e.g., δ^{57}Fe vs TiO_2, Supplementary data I S7) show no correlations, indicating that the melting degree does not or only to a small degree affect the Fe isotopic composition of lavas from Mauna Loa and Pu'u 'Ō'ō.

Another process that can influence the Fe isotopic composition of OIB is melting in the garnet stability field. The tholeiitic shield stage magmas sourcing Pu'u 'Ō'ō lavas are thought to have molten at a depth of 70 – 130 km based on numeric modelling and SiO_2 contents (Watson and McKenzie, 1991; Garcia et al., 2021) and show, similar to Mauna Loa, a garnet signature (O'Neill, 2016). Indices for a garnet signature (e.g., $(Gd/Yb)_{PM}$ vs $\delta^{57}Fe_{prim}$; Supplementary data I Fig. S8) indicate that the pronounced residual garnet signature is not affecting the Fe isotopic composition of Pu'u 'Ō'ō and Mauna Loa lavas. By systematically excluding melting degree and the garnet signature, we now evaluate if the mantle source of Mauna Loa and/or Pu'u 'Ō'ō shows a heterogeneous inherited Fe isotopic composition. An inherited isotopic heterogeneity can be identified by comparing radiogenic isotopic ratios with stable Fe isotopes of the primary melt.

4.5.3 Fe isotopic signature of the source

In radiogenic isotopic space (Sr, Nd, Pb, Hf), lavas exhibit a radiogenic isotopic signature reflecting the parent-daughter ratio of crustal material at time of subduction (White, 1985). Subducted, recycled crustal material is generally associated with radiogenic $^{87}Sr/^{86}Sr$ and $^{176}Hf/^{177}Hf$ isotopes as well as heavy Fe isotopic compositions of $\delta^{57}Fe > +0.15$ ‰ (Williams and Bizimis, 2014; Konter et al., 2016; Nebel et al., 2019; Stracke et al., 2005; Soderman et al., 2021), whereas the depleted mantle shows less radiogenic $^{87}Sr/^{86}Sr$ and $^{176}Hf/^{177}Hf$ isotopes and presumably a light Fe isotopic composition with $\delta^{57}Fe$ +0.05 ± 0.01‰ (2S.E.; Sossi et al. 2016). For our Hawai'ian lava suite, we would have expected that the depleted radiogenic isotopic signature of Pu'u 'Ō'ō lavas results in lighter $\delta^{57}Fe_{prim}$ compared to Mauna Loa. Figure 8 shows that such a distinction cannot be clearly made.

The Mauna Loa lavas do not show heavier Fe isotopes with more radiogenic isotopic signatures. When isolating Mauna Loa Rift and Mauna Loa Vent and Flank samples, one might argue for a distinction with Mauna Loa Rift samples showing a less radiogenic Sr isotopic signature at heavier Fe isotopic compositions, whereas Mauna Loa Vent and Flank samples show lighter Fe isotopic compositions at more radiogenic Sr isotopic compositions. However, such distinction does not hold true when ε_{Hf} is compared to $\delta^{57}Fe_{prim}$. Similar for lavas from Pu'u 'Ō'ō, with more radiogenic isotopic ε_{Hf} the lavas (excluding outlier with $\delta^{57}Fe_{prim}$ -0.08‰) increase towards heavier Fe isotopes. However, such distinction cannot be made by comparing $^{87}Sr/^{86}Sr$ vs $\delta^{57}Fe_{prim}$.

We note that lavas from Mauna Loa and Pu'u 'Ō'ō analysed in this study, tend towards heavier Fe isotopic compositions than the BSE and MORB (Sossi et al., 2016). This suggests that a component enriched in heavy Fe isotopes was involved in generating these lavas. This enriched (in heavy Fe isotopes) component can, however, not be ascribed to a crustal component *per se*, because a crustal component would show a more radiogenic isotopic signature tending towards heavy Fe isotopic compositions (Nebel et al., 2019). Such heavy Fe isotopic compositions have been ascribed to a pyroxenitic component in the plume source (Konter et al., 2016; Nebel et al., 2019) or in the lithosphere (Sun et al., 2020; Zhao et al., 2012). However, the heaviest $\delta^{57}Fe_{prim}$ +0.23 ‰ would require a purely pyroxenitic melt. A pyroxenitic source has been ascribed to Hawai'i based on olivine compositions (Herzberg,

2011; Sobolev et al., 2005) and cannot be excluded here. Following modelling, partial melting processes of peridotite do not exceed values of $\delta^{57}Fe_{prim}$ +0.15 ‰ for a melt fraction < 0.1 (Foden et al., 2018). Thus, a pyroxenitic melt is not needed to explain $\delta^{57}Fe_{prim} \leq$ +0.15 ‰ of Pu'u 'Ō'ō and Mauna Loa lavas.

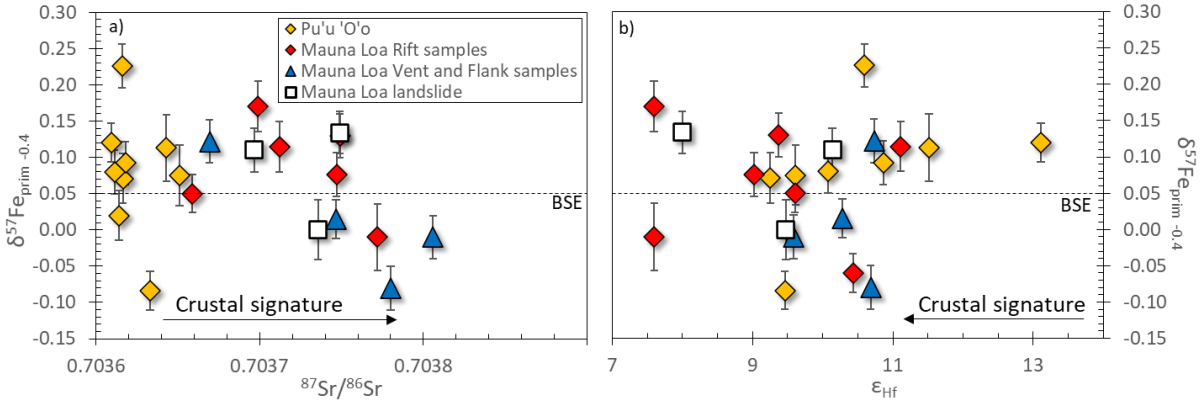

Figure 8. a) $^{87}Sr/^{86}Sr$ and b) ε_{Hf} vs $\delta^{57}Fe_{prim}$. For calculation of ε_{Hf}, the $^{176}Hf/^{177}Hf$ value for Chondrite Uniform Reservoir (CHUR; $^{176}Hf/^{177}Hf$ = 0.282785) from Bouvier et al. (2008) was used. No radiogenic Sr isotope data are available for Pu'u 'Ō'ō sample 15/10/2004 with +0.08‰ $\delta^{57}Fe_{prim}$). BSE at $\delta^{57}Fe$ = +0.05 ± 0.01‰ (2S.E.; Sossi et al., 2016).

4.6 Summary

We compared tholeiitic shield building lavas from Mauna Loa and Pu'u 'Ō'ō to identify magmatic processes underneath the Big Island of Hawai'i. Lavas from Mauna Loa and Pu'u 'Ō'ō bypass the summit magma reservoir. The absence of a closed magma chamber has been identified by comparing Mauna Loa and Pu'u 'Ō'ō to Kīlauea Iki lava lake lavas. The latter have undergone equilibrium fractionation processes only, e.g., crystallisation and accumulation of olivine (Teng et al., 2008). Mauna Loa and Pu'u 'Ō'ō were corrected for olivine crystallisation , which can account for a small variance in Fe isotopes. However, the missing co-variation of, i.e., MgO vs $\delta^{57}Fe$ and a three-isotope plot suggest that these lavas have experienced multiple processes that define their deviation from the crystal fractionation trend.

After olivine fractionation correction, Pu'u 'Ō'ō lavas and Mauna Loa lavas show similar Fe isotopic compositions to MORB with an average of $\delta^{57}Fe_{Prim}$ = +0.10‰ and +0.12‰, respectively, excluding outliers. These averaged $\delta^{57}Fe_{Prim}$ values are heavier than the BSE. Melting degree, source inheritance or the presence of a component heavy in Fe isotopes need to be considered to account for such heavy Fe isotopes. However, the high melting degree

and melting in the garnet stability field have no resolvable effect on the Fe isotopic composition of the here studied lavas. Missing co-variations between radiogenic isotopes and stable Fe isotopes argue against a source dependency of Fe isotopes.

A high proportion of pyroxenite has been suggested to generate lavas that represent the 'Loa trend' (Jones et al., 2017). Jones et al. (2017) argue that the tilted plume sourcing Hawai'i allows for two melting localities, deep melting of peridotite that forms the 'Kea-trend' and shallow melting of peridotite accompanied with pyroxenite generating the 'Loa-trend'. Such clear distinction cannot be made with Fe isotopes in this case. However, a pyroxenitic component, which shows a heavy Fe isotopic signature, might be obscured by melting of ambient peridotite due to the high melting degree of Hawai'ian tholeiites. Considering that the lavas studied here bypass the magma summit and do not enter closed magma chambers (would result in predominantly olivine crystallisation and accumulation) nor experienced homogenisation, we suggest that equilibrium, i.e., crystal fractionation and accumulation, and kinetic fractionation, i.e., diffusion, can mask or even erase the source dependency of Fe isotopes. Scenarios that could account for multiple fractionation processes are recharging events of the plumbing system. In such a scenario, the equilibrium fractionation alone cannot take place but kinetic in combination or alternating with equilibrium fractionation can explain the variation in Fe isotopes of Mauna Loa and Puʻu ʻŌʻō.

4.7 Conclusion

Given that lavas from Mauna Loa and Puʻu ʻŌʻō bypassed magma reservoirs, we suggest that recharging events in the plumbing system underneath these volcanoes mask the inherited Fe isotopic composition as well as effects of melting degree. We further suggest that multiple processes such as crystal fractionation as well as disequilibrium kinetic processes, like diffusion, altered the Fe isotopic composition.

4.8 References

Abouchami, W., Hofmann, A.W., Galer, S.J.G., Frey, F.A., Eisele, J. and Feigenson, M. (2005) Lead isotopes reveal bilateral asymmetry and vertical continuity in the Hawaiian mantle plume. *Nature* **434**, 851.

Beard, B.L. and Johnson, C.M. (2004) Inter-mineral Fe isotope variations in mantle-derived rocks and implications for the Fe geochemical cycle. *Geochimica et Cosmochimica Acta* **68**, 4727-4743.

Beard, B.L., Johnson, C.M., Skulan, J.L., Nealson, K.H., Cox, L. and Sun, H. (2003) Application of Fe isotopes to tracing the geochemical and biological cycling of Fe. *Chemical Geology* **195**, 87-117.

Bouvier, A., Vervoort, J.D. and Patchett, P.J. (2008) The Lu-Hf and Sm-Nd isotopic composition of CHUR: Constraints from unequilibrated chondrites and implications for the bulk composition of terrestrial planets. *Earth and Planetary Science Letters* **273**, 48-57.

Chen, S., Niu, Y., Guo, P., Gong, H., Sun, P., Xue, Q., Duan, M. and Wang, X. (2019) Iron isotope fractionation during mid-ocean ridge basalt evolution: Evidence from lavas on the East Pacific Rise at 10°30'N and its implications. *Geochimica et Cosmochimica Acta* **267**, p 227-239.

Chen, Y., Niu, Y., Duan, M., Gong, H. and Guo, P. (2021) Fractional crystallization causes the iron isotope contrast between mid-ocean ridge basalts and abyssal peridotites. *Communications Earth & Environment* **2**, 1-9.

Cheng, T., Nebel, O., Sossi, P.A. and Chen, F. (2014) Refined separation of combined Fe-Hf from rock matrices for isotope analyses using AG-MP-1M and Ln-Spec chromatographic extraction resins. *MethodsX* **1**, 144-150.

Craddock, P.R. and Dauphas, N. (2011) Iron isotopic compositions of geological reference materials and chondrites. *Geostandards and Geoanalytical Research* **35**, 101-123.

Dauphas, N., Roskosz, M., Alp, E.E., Neuville, D.R., Hu, M.Y., Sio, C.K., Tissot, F.L.H., Zhao, J., Tissandier, L., Médard, E. and Cordier, C. (2014) Magma redox and structural controls on iron isotope variations in Earth's mantle and crust. *Earth and Planetary Science Letters* **398**, 127-140.

Davis, M.G., Garcia, M.O. and Wallace, P. (2003) Volatiles in glasses from Mauna Loa Volcano,

Hawai'i: implications for magma degassing and contamination, and growth of Hawaiian volcanoes. *Contributions to Mineralogy and Petrology* **144**, 570-591.

Falloon, T.J., Green, D.H. and Danyushevsky, L.V. (2007) Crystallization temperatures of tholeiite parental liquids: Implications for the existence of thermally driven mantle plumes. Special Papers Geological Society of America **430**, 235.

Foden, J., Sossi, P.A. and Nebel, O. (2018) Controls on the iron isotopic composition of global arc magmas. *Earth and Planetary Science Letters* **494**, 190-201.

Garcia, M.O., Hulsebosch, T.P. and Rhodes, J.M. (1995) Olivine-rich submarine basalts from the southwest rift zone of Mauna Loa volcano: Implications for magmatic processes and geochemical evolution. *GMS* **92**, 219-239.

Garcia, M.O., Petruszka, A.J., Norman, M.D. and Rhodes, J.M. (2021) Kilauea's Pu'u 'O'o Eruption (1983-2018): A Synthesis pf Magmatic Processes During a Prolonged Basaltic Event. *Chemical Geology* **581**, 12091.

Garcia, M.O., Pietruszka, A.J., Rhodes, J.M. and Swanson, K. (2000) Magmatic processes during the prolonged Pu'u'O'o eruption of Kilauea Volcano, Hawaii. *Journal of Petrology* **41**, 967-990.

Garcia, M.O., Rhodes, J., Trusdell, F.A. and Pietruszka, A.J. (1996) Petrology of lavas from the Puu Oo eruption of Kilauea Volcano: III. The Kupaianaha episode (1986–1992). *Bulletin of Volcanology* **58**, 359-379.

Gleeson, M.L.M., Gibson, S.A. and Williams, H.M. (2020) Novel insights from Fe-isotopes into the lithological heterogeneity of Ocean Island Basalts and plume-influenced MORBs. *Earth and Planetary Science Letters* **535**, 116114.

Jackson, E.D., Shaw, H.R. and Bargar, K.E. (1975) Calculated geochronology and stress field orientations along the Hawaiian chain. *Earth and Planetary Science Letters* **26**, 145-155.

Jones, T.D., Davies, D.R., Campbell, I.H., Iaffaldano, G., Yaxley, G., Kramer, S.C. and Wilson, C.R.

(2017) The concurrent emergence and causes of double volcanic hotspot tracks on the Pacific plate. *Nature* **545**, 472-477.

Konter, J.G., Pietruszka, A.J., Hanan, B.B., Finlayson, V.A., Craddock, P.R., Jackson, M.G. and Dauphas, N. (2016) Unusual δ56Fe values in Samoan rejuvenated lavas generated in the mantle. *Earth and Planetary Science Letters* **450**, 221-232.

Le Bas, M.J., Le Maitre, R.W., Streckeisen, A., Zanettin, B. and Rocks, I.S.o.t.S.o.I. (1986) A chemical classification of volcanic rocks based on the total alkali-silica diagram. *Journal of Petrology* **27**, 745-750.

Le Maitre, R., Bateman, P., Dudek, A., Keller, J., Lameyre, J., Le Bas, M., Sabine, P., Schmid, R., Sorensen, H. and Streckeisen, A. (1989) A classification of igneous rocks and glossary of terms. Recommendations of the IUGS Subcommission on the Systematics of Igneous rocks. *London: Blackwell Scientific Publications*.

Macris, C.A., Manning, C.E. and Young, E.D. (2015) Crystal chemical constraints on inter-mineral Fe isotope fractionation and implications for Fe isotope disequilibrium in San Carlos mantle xenoliths. *Geochimica et Cosmochimica Acta* **154**, 168-185.

Marske, J.P., Garcia, M.O., Pietruszka, A.J., Rhodes, J.M. and Norman, M.D. (2008) Geochemical variations during Kīlauea's Pu ʻu ʻŌ ʻō eruption reveal a fine-scale mixture of mantle heterogeneities within the Hawaiian plume. *Journal of Petrology* **49**, 1297-1318.

McCoy-West, A.J., Fitton, J.G., Pons, M.-L., Inglis, E.C. and Williams, H.M. (2018) The Fe and Zn isotope composition of deep mantle source regions: Insights from Baffin Island picrites. *Geochimica et Cosmochimica Acta* **238**, 542-562.

Münker, C., Weyer, S., Scherer, E. and Mezger, K. (2001) Separation of high field strength elements (Nb, Ta, Zr, Hf) and Lu from rock samples for MC-ICPMS measurements. *Geochemistry, Geophysics, Geosystems* **2**, 2001GC000183.

Nebel, O., Campbell, I.H., Sossi, P.A. and Van Kranendonk, M.J. (2014) Hafnium and iron

isotopes in early Archean komatiites record a plume-driven convection cycle in the Hadean Earth. *Earth and Planetary Science Letters* **397**, 111-120.

Nebel, O., Morel, M.L.A. and Vroon, P.Z. (2009) Isotope Dilution Determinations of Lu, Hf, Zr, Ta and W, and Hf Isotope Compositions of NIST SRM 610 and 612 Glass Wafers. *Geostandards and Geoanalytical Research* **33**, 487-499.

Nebel, O., Sossi, P.A., Bénard, A., Arculus, R.J., Yaxley, G.M., Woodhead, J.D., Rhodri Davies, D. and Ruttor, S. (2019) Reconciling petrological and isotopic mixing mechanisms in the Pitcairn mantle plume using stable Fe isotopes. *Earth and Planetary Science Letters* **521**, 60-67.

O'Neill, H.S.C. (2016) The Smoothness and Shapes of Chondrite-normalized Rare Earth Element Patterns in Basalts. *Journal of Petrology* **57**, 1463-1508.

Pietruszka, A.J., Hauri, E.H., Carlson, R.W. and Garcia, M.O. (2006) Remelting of recently depleted mantle within the Hawaiian plume inferred from the 226Rb-230Th-238U disequilibria of Pu'u 'O'o eruption lavas. *Earth and Planetary Science Letters* **244**, 155-169.

Pin, C., Gannoun, A. and Dupont, A. (2014) Rapid, simultaneous separation of Sr, Pb, and Nd by extraction chromatography prior to isotope ratios determination by TIMS and MC-ICP-MS. *Journal of Analytical Atomic Spectrometry* **29**, 1858-1870.

Poitrasson, F., Delpech, G. and Gregoire, M. (2013) On the iron isotope heterogeneity of lithospheric mantle xenoliths: implications for mantle metasomatism, the origin of basalts and the iron isotope composition of the Earth. *Contributions to Mineralogy and Petrology* **165**, 1243-1258.

Poland, M.P., Miklius, A., Sutton, A.J. and Thornber, C.R. (2012) A mantle-driven surge in magma supply to Kīlauea Volcano during 2003–2007. *Nature Geoscience* **5**, 295-300.

Prichard, J. (2020) Geochemical Modelling of Shallow Fractionation and Deep Mantle Melting Below Mauna Loa Volcano, Hawaii. *Australian National University*.

Rabin, S., Blanchard, M., Pinilla, C., Poitrasson, F. and Gregoire, M. (2021) First-principles calculation of iron and silicon isotope fractionation between Fe-bearing minerals at magmatic temperatures: The importance of second atomic neighbors. *Geochimica et Cosmochimica Acta* **304**, 101-118.

Rhodes, J. (1995) The 1852 and 1868 Mauna Loa picrite eruptions: Clues to parental magma compositions and the magmatic plumbing system. *GMS* **92**, 241-262.

Rhodes, J. and Hart, S. (1995) Episodic trace element and isotopic variations in historical Mauna Loa lavas: implications for magma and plume dynamics. *Mauna Loa Revealed: Structure, Composition, History, and Hazards* **92**, 263-288.

Richter, F.M., Davis, A.M., DePaolo, D.J. and Watson, E.B. (2003) Isotope fractionation by chemical diffusion between molten basalt and rhyolite. *Geochimica et Cosmochimica Acta* **67**, 3905-3923.

Robinson, J.E. and Eakins, B.W. (2006) Calculated volumes of individual shield volcanoes at the young end of the Hawaiian Ridge. *Journal of Volcanology and Geothermal Research* **151**, 309-317.

Ruttor, S., Nebel, O., Nebel-Jacobsen, Y., Cohen, B., Eggins, S. (2021) Alkalinity of ocean island lavas decoupled from source components: a case study from the EM1-PREMA Tasmantid mantle plume. *Geochmimica et Cosmochimica Acta* **314**, 140-158.

Ryan, W.B., Carbotte, S.M., Coplan, J.O., O'Hara, S., Melkonian, A., Arko, R., Weissel, R.A., Ferrini, V., Goodwillie, A. and Nitsche, F. (2009) Global multi-resolution topography synthesis. *Geochemistry, Geophysics, Geosystems* **10**.

Schuessler, J.A., Schoenberg, R. and Sigmarsson, O. (2009) Iron and lithium isotope systematics of the Hekla volcano, Iceland - Evidence for Fe isotope fractionation during magma differentiation. *Chemical Geology* **258**, 78-91.

Shamberger, P.J. and Garcia, M.O. (2007) Geochemical modeling of magma mixing and magma reservoir volumes during early episodes of Kīlauea Volcano's Pu ʻu ʻŌ ʻō eruption.

Bulletin of Volcanology **69**, 345-352.

Soderman, C.R., Matthews, S., Shorttle, O., Jackson, M.G., Ruttor, S., Nebel, O., Turner, S., Beier, C., Millet, M.-A., Widom, E., Humayun, M. and Williams, H.M. (2021) Heavy δ57Fe in ocean island basalts: a non-unique signature of processes and source lithologies in the mantle. *Geochimica et Cosmochimica Acta* **292**, 309-332.

Sossi, P., Foden, J. and Halverson, G. (2012) Redox-controlled iron isotope fractionation during magmatic differentiation: an example from the Red Hill intrusion, S. Tasmania. *Contributions to Mineralogy and Petrology* **164**, 757-772.

Sossi, P.A., Halverson, G.P., Nebel, O. and Eggins, S.M. (2015) Combined separation of Cu, Fe and Zn from rock matrices and improved analytical protocols for stable isotope determination. *Geostandards and Geoanalytical Research* **39**, 129-149.

Sossi, P.A., Nebel, O. and Foden, J. (2016) Iron isotope systematics in planetary reservoirs. *Earth and Planetary Science Letters* **452**, 295-308.

Sossi, P.A. and O'Neill, H.S.C. (2017) The effect of bonding environment on iron isotope fractionation between minerals at high temperature. *Geochimica et Cosmochimica Acta* **196**, 121-143.

Stracke, A., Hofmann, A.W. and Hart, S.R. (2005) FOZO, HIMU, and the rest of the mantle zoo. *Geochemistry, Geophysics, Geosystems* **6**, Q05007.

Sun, P., Niu, Y., Guo, P., Duan, M., Chen, S., Gong, H., Wang, X. and Xiao, Y. (2020) Large iron isotope variation in the eastern Pacific mantle as a consequence of ancient low-degree melt metasomatism. *Geochimica et Cosmochimica Acta* **286**, 269-288.

Tatsumoto, M. (1978) Isotopic composition of lead in oceanic basalt and its implication to mantle evolution. *Earth and Planetary Science Letters* **38**, 63-87.

Teng, F.-Z., Dauphas, N. and Helz, R.T. (2008) Iron isotope fractionation during magmatic differentiation in Kilauea Iki lava lake. *Science (New York, N.Y.)* **320**, 1620.

Teng, F.-Z., Dauphas, N., Helz, R.T., Gao, S. and Huang, S. (2011) Diffusion-driven magnesium and iron isotope fractionation in Hawaiian olivine. *Earth and Planetary Science Letters* **308**, 317-324.

Teng, F.-Z., Dauphas, N., Huang, S. and Marty, B. (2013) Iron isotopic systematics of oceanic basalts. *Geochimica et Cosmochimica Acta* **107**, 12-26.

Weis, D., Kieffer, B., Maerschalk, C., Pretorius, W. and Barling, J. (2005) High-precision Pb-Sr-Nd-Hf isotopic characterization of USGS BHVO-1 and BHVO-2 reference materials. *Geochemistry, Geophysics, Geosystems* **6**, Q02002.

Weyer, S. and Ionov, D.A. (2007) Partial melting and melt percolation in the mantle: The message from Fe isotopes. *Earth and Planetary Science Letters* **259**, 119-133.

White, W.M. (1985) Sources of oceanic basalts: Radiogenic isotopic evidence. *Geology* **13**, 115-7613-7613-7612-7115-11989.

Williams, H.M. and Bizimis, M. (2014) Iron isotope tracing of mantle heterogeneity within the source regions of oceanic basalts. *Earth and Planetary Science Letters* **404**, 396-407.

Williams, H.M., Peslier, A.H., McCammon, C., Halliday, A.N., Levasseur, S., Teutsch, N. and Burg, J.P. (2005) Systematic iron isotope variations in mantle rocks and minerals: The effects of partial melting and oxygen fugacity. *Earth and Planetary Science Letters* **235**, 435-452.

Young, E.D., Galy, A. and Nagahara, H. (2002) Kinetic and equilibrium mass-dependent isotope fractionaion laws in nature and their geochemical and cosmochemical significance. *Geochimica et Cosmochimica Acta* **66**, 1095-1104.

Young, E.D. and Galy, A. (2004) The isotope geochemistry and cosmochemistry of magnesium. *Reviews in Mineralogy and Geochemistry* **55**, 197-230.

Zhao, X., Zhang, H., Zhu, X., Tang, S. and Yan, B. (2012) Iron isotope evidence for multistage melt–peridotite interactions in the lithospheric mantle of eastern China. *Chemical Geology* **292**, 127-139.

SUPPLEMENTARY DATA

I. Supplementary data I

The analysed samples analysed for this study comprise tholeiitic lavas of Mauna Loa and Pu‘u ‘Ō‘ō (Fig. S1.).

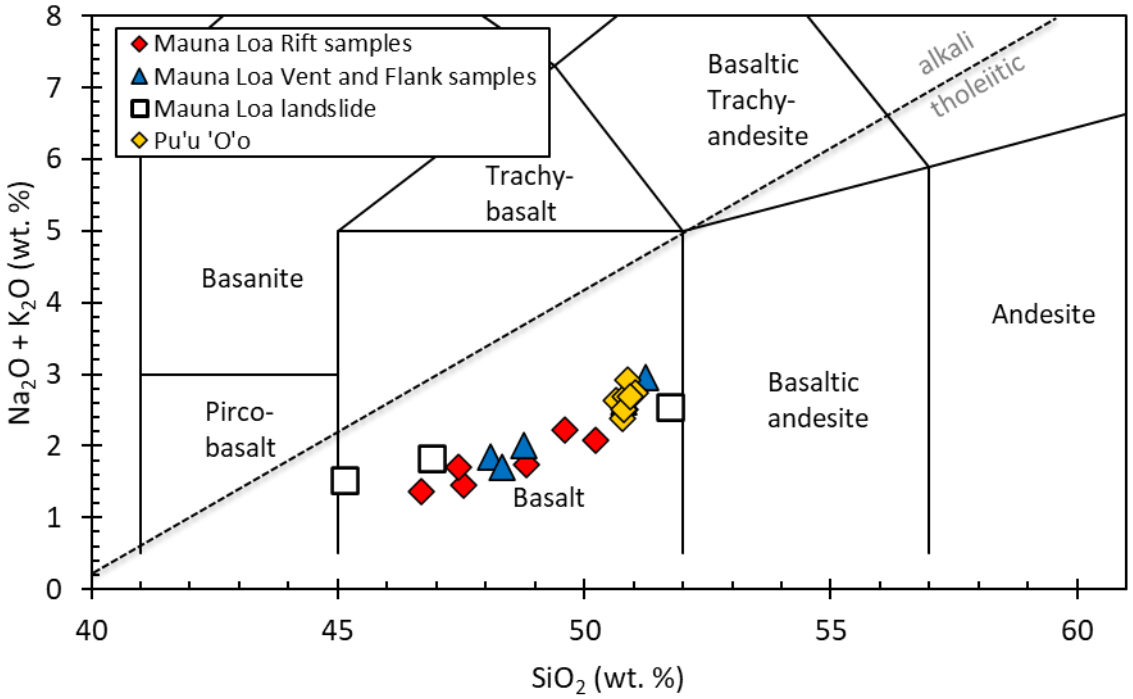

Figure S1. Total alkali-silica diagram (TAS diagram) after Le Bas et al. (1986b) and division lines after Le Maître (1989) for classification of the whole rock suit of Mauna Loa and Pu‘u ‘Ō‘ō.

The measured $\delta^{57}Fe$ of the samples is not correlated with K_2O/P_2O_5 or any other ratio involving fluid mobile elements, suggesting that the measured $\delta^{57}Fe$ values have not been influenced by post-magmatic alteration processes (Fig. S2).

Samples with MgO < 4.0 wt. % can show magnetite fractionation, which leads to the removal of heavy Fe isotopes from the remaining melt (Sossi et al., 2012; Nebel et al., 2015). None of the samples analysed here show magnetite alteration and MgO values of both basalt suits are > 6.0 wt.% MgO (Fig. S2b, c).

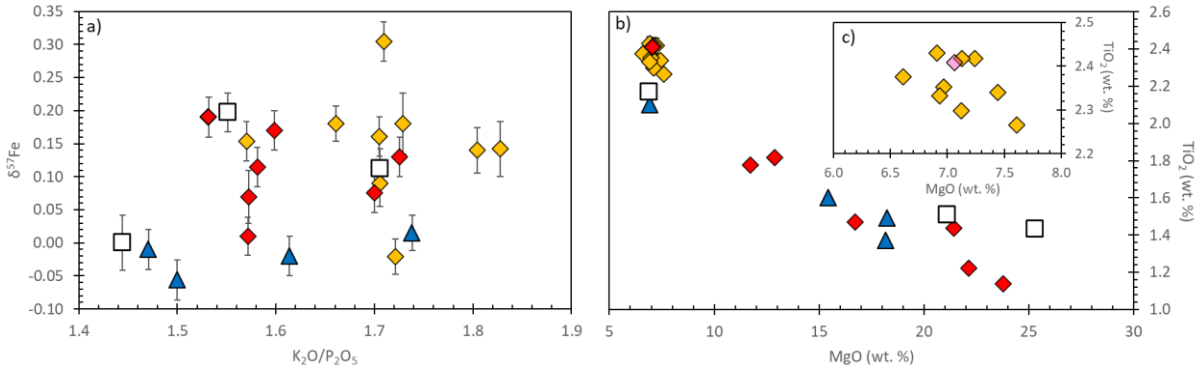

Figure S2. a) K_2O/P_2O_5 vs $\delta^{57}Fe$ shows that submarine Mauna Loa and subaerial Pu'u 'Ō'ō samples are not affected by post-magmatic alteration, b) MgO vs TiO_2 and c) enlarged MgO vs TiO_2 shows that none of the analysed samples show magnetite saturation.

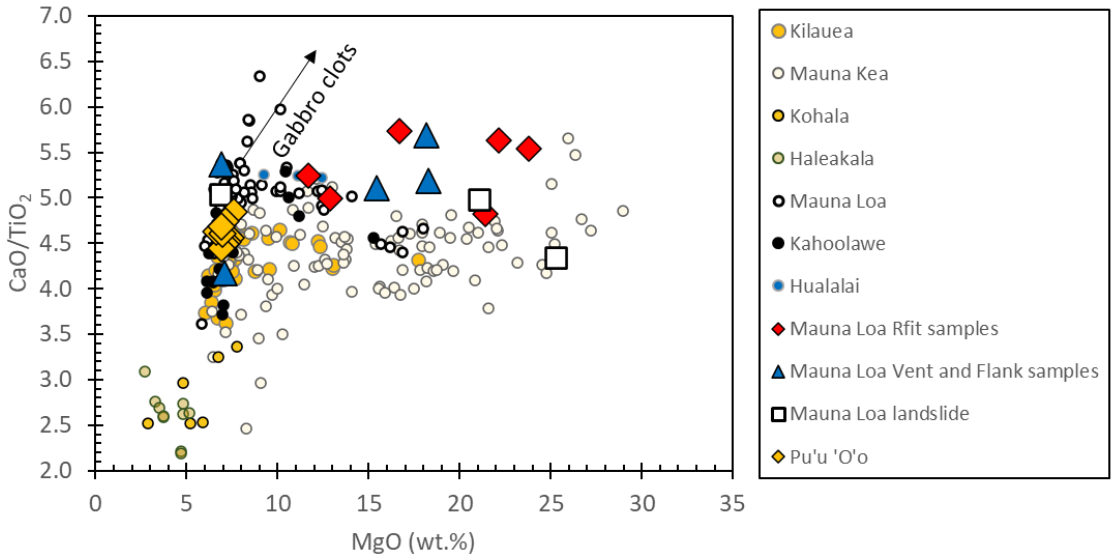

Figure S3. Indicator for gabbro clots indicated by CaO/TiO2 > 5.0 (Garcia et al., 2021).

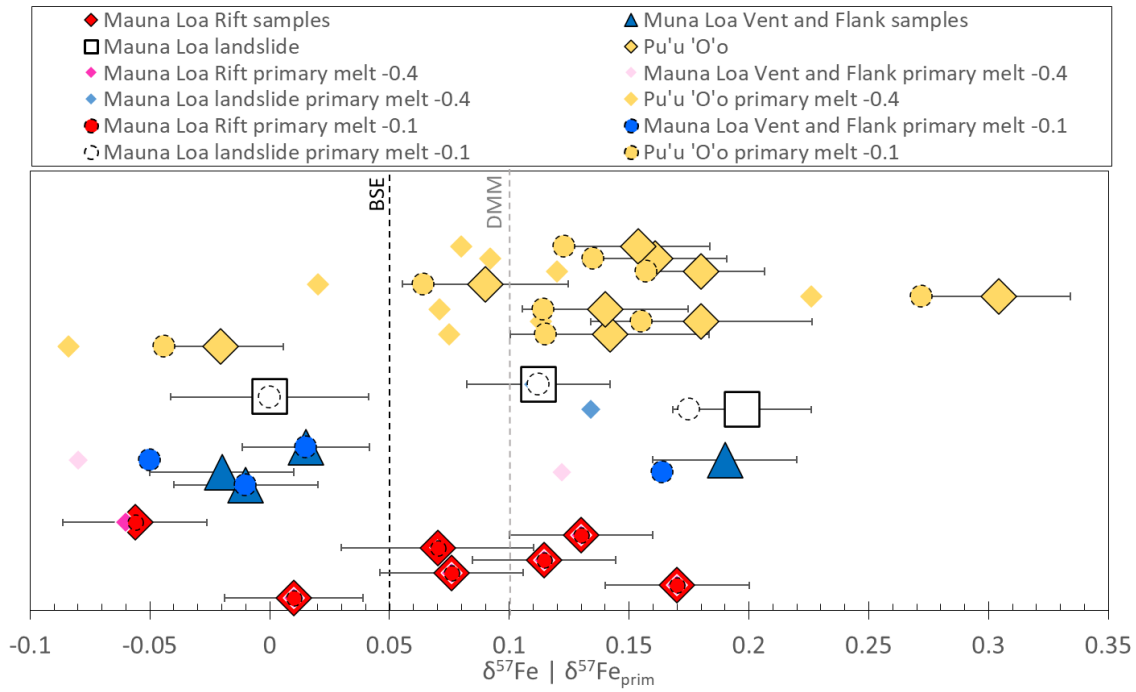

Figure S4. Measured $\delta^{57}Fe$ and olivine fractionation corrected samples as $\delta^{57}Fe_{prim\text{-}0.4}$ and $\delta^{57}Fe_{prim\text{-}0.15}$. Bulk silicate earth (BSE) at $\delta^{57}Fe$ = +0.05 ± 0.01‰ (2S.E.; Sossi et al., 2016), depleted MORB mantle (DMM) at $\delta^{57}Fe$ = +0.10 ± 0.01‰ (2S.E.; Sossi et al., 2016).

The primary melt MgO composition can be identified in log-log plots of compatible vs incompatible elements (McCoy-West et al., 2018). At 21.0 wt. % MgO, Mauna Loa lavas show a break in slope, which identifies the primary melt composition.

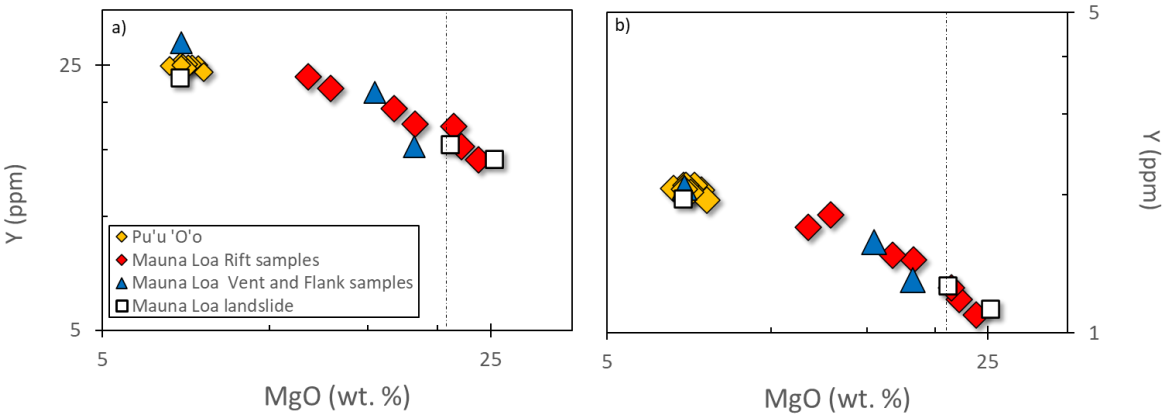

Figure S5. a) MgO vs Y and c) MgO vs Yb, plotted on a logarithmic scale. Grey dotted line indicates break in slope, which marks the primary melt composition at MgO 21.0 wt. %.

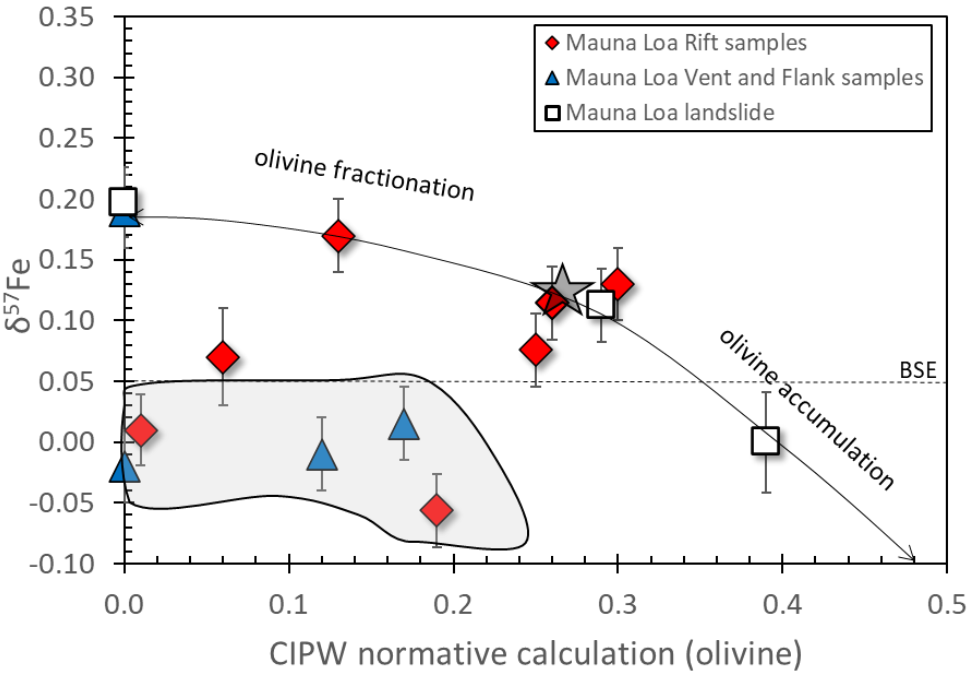

Figure S6. CIPW normative calculation of olivine vs. δ^{57}Fe. Black arrows show olivine fractionation and accumulation pathway, grey field indicates outliers. Black star shows parental melt at δ^{57}Fe +0.12‰

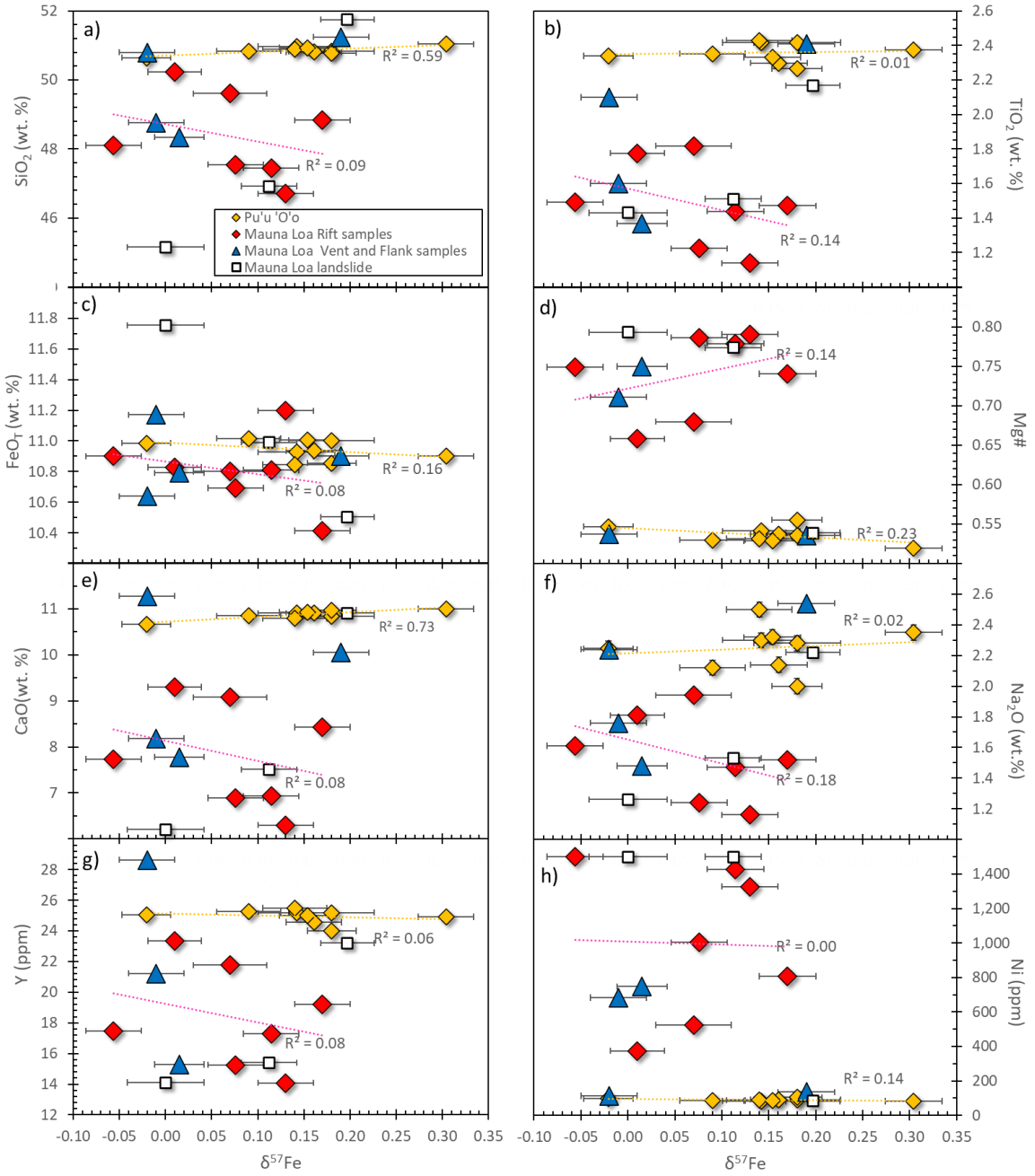

Figure S7. $\delta^{57}Fe$ vs a) SiO_2, b) TiO_2, c) FeO_T, d) Mg#, e) CaO, f) Na_2O, g) Y and h) Ni. R^2 reflects correlation coefficient of the best fit.

Basalts that form at such depths can show a garnet signature, which can be identified by comparing middle rare earth element (MREE) with heavy rare earth element (HREE) such as $(Gd/Yb)_{PM}$ (Lassiter and DePaolo, 1997; Sossi and O'Neill, 2017; Norman and Garcia, 1999). Compared to Mauna Loa, Pu'u 'Ō'ō lavas show higher values in $(Gd/Yb)_{PM}$ with an average value of 2.21 (Mauna Loa $(Gd/Yb)_{PM}$ = 2.25), indicating a higher signature of residual garnet. The missing co-variation between $(Gd/Yb)_{PM}$ and $\delta^{57}Fe_{prim}$ (Fig. S8) indicates that the

pronounced residual garnet signature is not causing the wide range in Fe isotopes from Pu‘u ‘Ō‘ō and Mauna Loa lavas. Therefore, we suggest that the mantle source of Mauna Loa as well as Pu‘u ‘Ō‘ō lavas shows an *a priori* heterogeneous Fe isotopic composition.

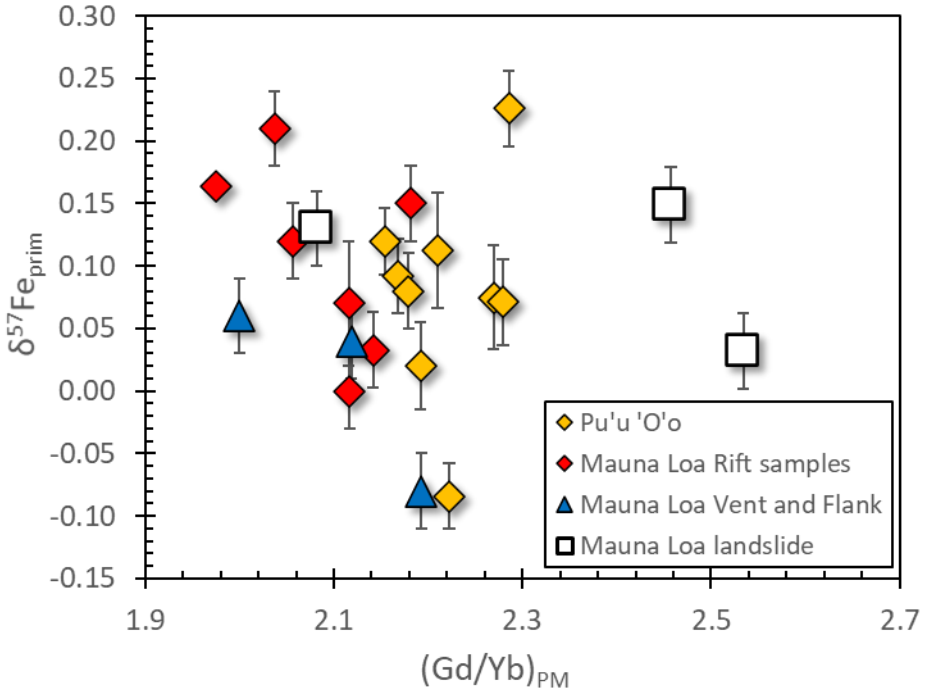

Figure S8. a) $(Gd/Yb)_{PM}$ vs $\delta^{57}Fe_{prim}$.

We corrected our Hawai’ian lavas with a fractionation factor of $-0.4*10^6/T^2$ and $-0.15*10^6/T^2$. To compare $\delta^{57}Fe_{prim}$ with radiogenic isotopic data, we chose the primary Fe isotopic composition that has been corrected with a fractionation factor of $-0.4*10^6/T^2$. Choosing this factor has no implications on the interpretation of the comparison as shown in Fig S9. Independent of the fractionation factor applied, the samples show the same distribution in a plot of $\delta^{57}Fe_{prim}$ vs $^{87}Sr/^{86}Sr$ and ε_{Hf}.

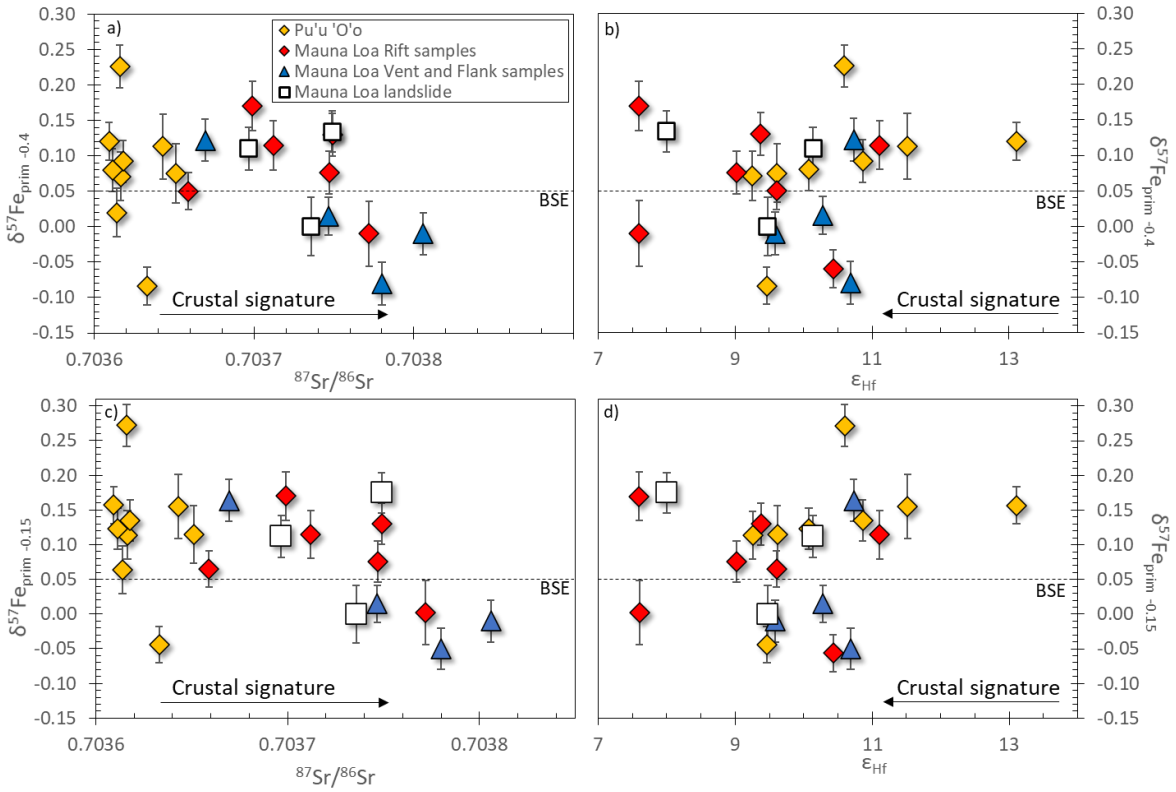

Figure S9. a) $^{87}Sr/^{86}Sr$ and b) ε_{Hf} vs $\delta^{57}Fe_{prim\ -0.4}$ and c) $^{87}Sr/^{86}Sr$ and d) ε_{Hf} vs $\delta^{57}Fe_{prim\ -0.15}$. For calculation of ε_{Hf}, the $^{176}Hf/^{177}Hf$ value for Chondrite Uniform Reservoir (CHUR; $^{176}Hf/^{177}Hf$ = 0.282785) from Bouvier et al. (2008) was used. No radiogenic Sr isotope data are available for Pu‘u ‘Ō‘ō sample 15/10/2004 with +0.08‰ $\delta^{57}Fe_{prim}$). BSE at $\delta^{57}Fe$ = +0.05 ± 0.01‰ (2S.E.; Sossi et al., 2016).

References

Garcia, M.O., Petruszka, A.J., Norman, M.D. and Rhodes, J.M. (2021) Kilauea's Pu'u 'O'o Eruption (1983-2018): A Synthesis pf Magmatic Processes During a Prolonged Basaltic Event. *Chemical Geology* **581**, 12091.

Le Bas, M.J., Le Maitre, R.W., Streckeisen, A. and Zanettin, B.A. (1986) A Chemical Classification of Volcanic Rocks Based on the Total Alkali-Silica Diagram. *Journal of Petrology* **27**, 745-750.

Le Maître, R. (1989) A classification of igneous rocks and glossary of terms. Recommendations of the IUGS Subcommission on the Systematics of Igneous Rocks. Ed. IUGS. Blackwell Publications, 193p.

McCoy-West, A.J., Fitton, J.G., Pons, M.-L., Inglis, E.C. and Williams, H.M. (2018) The Fe and Zn

isotope composition of deep mantle source regions: Insights from Baffin Island picrites. *Geochimica et cosmochimica acta* **238**, 542-562.

Nebel, O., Sossi, P.A., Bénard, A., Wille, M., Vroon, P.Z. and Arculus, R.J. (2015) Redox-variability and controls in subduction zones from an iron-isotope perspective. *Earth and Planetary Science Letters* **432**, 142-151.

Sossi, P., Foden, J. and Halverson, G. (2012) Redox-controlled iron isotope fractionation during magmatic differentiation: an example from the Red Hill intrusion, S. Tasmania. *Contributions to Mineralogy and Petrology* **164**, 757-772.

Sossi, P.A., Nebel, O. and Foden, J. (2016) Iron isotope systematics in planetary reservoirs. *Earth and Planetary Science Letters* **452**, 295-308.

II. Supplementary data II

Table S1. Radiogenic isotopic ratios of lavas from Hawai'i.

Sample No.		$^{87}Sr/^{86}Sr$	$^{176}Hf/^{177}Hf$
Mauna Loa			
M1-1	Rift Zone	0.7037	0.2831
M1-16	Rift Zone	0.7037	0.2830
M1-26	Rift Zone	0.7037	0.2830
M2-10	Rift Zone	0.7038	0.2830
M4-9	Rift Zone	0.7037	0.2831
M18-31	Rift Zone		0.2831
M19-24	Rift Zone	0.7037	0.2831
M12-17	Landslide	0.7037	0.2830
M13-25	Landslide	0.7037	0.2831
M13-38	Landslide	0.7037	0.2831
M17-2	Flank	0.7037	0.2831
M26-44	Flank	0.7038	0.2831
M30-1	Flank	0.7037	0.2831
M27-11	Radial Vent	0.7038	0.2831
Kilauea Pu'u O'o			
19/09/2003	Rift Zone	0.7036	0.2831
15/10/2004	Rift Zone	0.7037	0.2831
23/04/2004	Rift Zone	0.7036	0.2831
8/08/2005	Rift Zone	0.7036	0.2830
25/07/2010	Rift Zone	0.7036	0.2831
20/06/2012	Rift Zone	0.7036	0.2831
8/06/2013	Rift Zone	0.7036	0.2832
18/11/2013	Rift Zone	0.7036	0.2831
27/06/2014	Rift Zone	0.7036	0.2831
BCR2			0.2829
BHVO2			0.2831

CHAPTER 5

5. Summary, Conclusion and Outlook

5.1 Summary

The aim of this thesis is to understand magmatic processes and source composition of OIB by using stable Fe isotopes in combination with radiogenic isotopic systems. As outlined in the introduction, the fractionation of Fe isotopes can depend on (1) source heterogeneity, (2) melting conditions and crystal fractionation, (3) magmatic processes, e.g., mixing processes and (4) alteration processes like mantle metasomatism. These processes have been discussed in each chapter.

To evaluate if source inheritance influences the Fe isotopic composition of OIB, radiogenic isotopic systems have been compared to stable Fe isotopes. Out of the three hotspot locations, only São Miguel's Fe isotope data covaries with radiogenic isotopic ratios of Sr, Nd and Pb. Interestingly, the enriched radiogenic isotopic component of eastern São Miguel shows a light Fe isotopic composition compared to the depleted component (in radiogenic isotopes) of western São Miguel with a heavy Fe isotopic composition. When compared to locations that show such covariations, e.g., Pitcairn, it becomes apparent that enriched radiogenic isotopic values are usually associated with heavy Fe isotopes. Thus, we suggest that source heterogeneity needs to be further assessed when interpreting covariations of Fe isotopes with radiogenic isotope data for São Miguel. To explain the conundrum of an enriched component showing a light Fe isotopic signature, Fe isotope data in conjunction with major and trace element ratios revealed that low degree mantle metasomatism causes the light Fe isotopic composition of eastern São Miguel's lavas. Such interpretation is strengthened by the presence of phlogopite or high potassium (K)-hollandite, a mineral associated with mantle metasomatism. For the Tasmantid Seamounts and Hawai'i, the missing covariation between proxies for source variability and Fe isotopes suggests that other processes need to be considered to explain their Fe isotopic composition. Each ocean island needs to be assessed individually to identify whether Fe isotopes can be associated with the source inheritance. Such dependency seems irrespective of tectonic setting, e.g., the presence of a rift, magma supply, temperature and pressure conditions or melting degree.

Additional to source inheritance, melting degrees need to be considered when interpreting Fe isotopes of OIB. This study shows that different melting degrees of tholeiitic and alkali lavas result in different Fe isotopic values. For example, the Azores, and with this São Miguel, show on average heavier Fe isotopic compositions at lower melting degrees than Hawai'ian tholeiitic lavas at higher melting degrees. Such differences between alkali and tholeiitic lavas can also be identified for the Tasmantid Seamounts, with alkali basalts showing heavier Fe isotopic compositions at larger melting degrees compared to tholeiitic lavas. For the Tasmantid Seamounts, comparisons of radiogenic and stable isotopes as well as trace elements show that rather than pressure, temperature is determining the different melting degrees of the Tasmantid tholeiitic and alkali lavas.

Contrary to MORB, OIB, among others the three locations studied in this thesis, show a wide range in Fe isotopic compositions. In addition to the melting degree, olivine crystallisation and accumulation can account for some of this variance in stable Fe isotopes. In general, more evolved basalts with MgO < 10 wt.% show a heavier Fe isotopic composition compared to primitive basalts with MgO > 10 wt.% (Teng et al., 2008). Lavas from the Kīlauea Iki lava lake (Teng et al., 2008) and picrites from the Baffin Island (McCoy-West et al., 2018) describe such trend and illustrate the effect of olivine fractionation and accumulation. For basalts that deviate from this trend, e.g., Chapter 4, multiple processes must have taken place that altered the Fe isotopic composition.

A process that has been suggested to account for such deviation is mantle metasomatism (Poitrasson et al., 2013; Sun et al., 2020; Weyer and Ionov, 2007). In fact, all three locations, the Tasmantid Seamounts, São Miguel and Hawai'ian lavas have undergone mantle metasomatism. Mantle metasomatism is complex and for each location a variety of metasomatizing agents need to be considered. For example, eastern São Miguel's lavas show co-variations between proxies for low degree silicic, K-rich metasomatism and Fe isotopes. This silicic K-rich melt led to a light Fe isotopic signature of eastern São Miguel's lavas.

In addition to the processes listed above, tectonic settings need to be considered when interpreting Fe isotope data. This is not only valid for basalts from the Tasmantid Seamounts, which are situated on an extinct rift setting but also for basalts of western São Miguel, which

is characterised by the run through of the Terceira Rift. In both cases, melting at a rift setting altered the Fe isotopic composition towards heavy Fe isotopes.

To summarise, the Fe isotopic compositions of the Tasmantid Seamounts, São Miguel and Hawai'ian OIB cannot be explained by one single process. Multiple processes need to be considered when interpreting the Fe isotopic composition of OIB.

In the following, aims that have been outlined in the introduction will be addressed:

(1) *identifying the isotopic characteristics of OIB (with focus on the Tasmantid Seamounts, São Miguel and Kīlauea and Mauna Loa)*: mantle components have been identified by comparing radiogenic isotope data of the Tasmantid Seamounts and Hawai'i to other OIB. In Fe isotopes, the Tasmantid Seamounts, São Miguel and Hawai'i cover a wide range but lie within the Fe isotopic compositions known for OIB with δ^{57}Fe -0.16 to +0.45‰. To understand the heterogeneity of Fe isotopes in OIB more hotspot locations need to be analysed in their Fe isotopic composition. This thesis added three locations to this list and contributed to a better understanding of processes that influence the Fe isotopic composition of OIB.

(2) *identifying petrogenetic processes that led to the formation of OIB*: this thesis showed that several processes need to be considered to understand the range in Fe isotopes as well as in radiogenic isotopic compositions of OIB. Whereas crystal fractionation and accumulation play a role, only small variations in stable Fe isotopes can be explained by such processes. Melting conditions and source inheritance as well as mixing processes of, for example, peridotite with metasomatising agents dominate the Fe isotopic composition of OIB. Focusing on the three locations studied here, these processes have been identified by using stable Fe isotopes in conjunction with radiogenic isotopic and trace element ratios.

(3) *distinguishing whether enriched (subducted and recycled) and depleted mantle components remain as distinct lithological units (with different Fe isotopic composition) in the mantle*: Analysing Fe isotopes in OIB from the Tasmantid Seamounts, São Miguel and Hawai'i showed that enriched mantle components cannot always be ascribed to a pyroxenitic lithological unit nor can a depleted component always be ascribed to peridotitic lithological unit. Such ascription is complex and several processes as well as mass balance calculations need to be considered before identifying possible lithological units or the mixing of such.

Focusing on the three locations discussed in this study and on heavy Fe isotopic compositions, we showed that peridotite can mix with pyroxenitic veins (at rift settings) or metasomatising agents that enrich the melt in heavy Fe isotopes. Light Fe isotopic compositions can be associated with peridotite mixing with metasomatising agents that cause a light Fe isotopic composition in melts. Such metasomatising agents are, for example, low degree silicic melts or processes like diffusion.

5.2 Conclusion

Examining the generation of OIB systematically demonstrates the unknown processes that might influence Fe isotopic compositions: With the subduction and recycling of oceanic crust (δ^{57}Fe +0.15‰; Chen et al., 2019; Teng et al., 2013) small amounts of sediment get transported into the mantle (Chase, 1981; Hofmann and White, 1982; Stracke et al., 2003; Weaver, 1991). Sediments can show a heavy Fe isotopic signature (δ^{57}Fe < +0.9‰; Du et al., 2017) or a light Fe isotopic signature (i.e., hydrous silicic melt or carbonates with δ^{57}Fe < -0.13‰; Debret et al., 2020; Johnson et al., 2010). As subduction continues, oceanic/continental crust, lithosphere and sediment permeates through or stagnates at the transition zone (Agrusta et al., 2017; Dasgupta et al., 2004; Doucet et al., 2020; Goes et al., 2008). Subducted, recycled material that reaches the CMB might experience contribution of heavy Fe isotopes from core liquids (Lesher et al., 2020). As hot rock reaches the upper mantle, fluids or melts of stagnated slabs in the upper mantle might interact with the hot buoyant rock, increase the melting degree and alter its Fe isotopic signature (Debret et al., 2020; Williams et al., 2004; Williams et al., 2005). Metasomatising agents, e.g., silicate or carbonatitic melts and/or fluids might alter the Fe isotopic composition of a melt towards a light or heavy Fe isotopic composition. This study strengthened the assumption that Fe isotopes are excellent proxies in identifying mantle metasomatism (Poitrasson et al., 2013; Weyer and Ionov, 2007). We were able to show that metasomatising agents and mixing processes can be tracked with stable Fe isotopes. Furthermore, we identified that, depending on melting conditions, e.g., elevated temperature at the centre of a plume, the Fe isotopic composition of a melt is either enriched in heavy Fe isotopes (low melting degree) or depleted in heavy Fe isotopes (high melting degree; Chapter 2). During magma cooling and the crystallisation of olivine and pyroxene the melt becomes heavier in Fe isotopes (Chapter

4; Sossi and O'Neill, 2017; Teng et al., 2008; Weyer, 2008). As the magma approaches the surface, the tectonic setting in which the lava erupts influences the Fe isotopic composition of OIB (Chapter 2 and 3). We were able to show that melting at rift settings alters the Fe isotopic composition of melts and can result in a heavy Fe isotopic composition.

This study shows that Fe isotopes in conjunction with radiogenic isotopes, trace elements and major elements can be a powerful tool in identifying and interpreting magmatic processes. Additionally, stable Fe isotopes can identify the material that is melting, e.g., peridotite mixed with a metasomatising agent. Such classification of mantle material is not possible with radiogenic isotopes, major or trace elements.

5.3 Outlook

The heterogeneity in stable Fe isotopes of OIB is dependent on many factors. Comparing Fe isotopes with radiogenic isotopes and major and trace elements provides detailed information about composition and magmatic processes of the Earth's mantle. Such information needs to be included in experimental petrology and geodynamic modelling. Questions like, how does a plume interact with an ancient rift, what material can act as a metasomatising agent and how does this agent influence the Fe isotopic composition of the melt need to be addressed in further research. This study sets a starting point by identifying the interaction of peridotite with metasomatising agents such as low degree silicic melts and metasomatising agents that are enriched in heavy Fe isotopes. However, other metasomatising agents, e.g., carbonatitic melts, and their influence on Fe isotopes need to be studied further. As such topic is very complex, an interdisciplinary approach is suggested. For example, island arc settings can provide insights into material that escapes from subducting slabs during descent into the deep mantle. Geochemical studies on island arc settings combined with experimental petrology focusing on the escape of fluids during subduction could provide further knowledge of the stagnated material at the mantle transition zone and on the material that can interact or mix with hot, upwelling mantle material.

5.4 References

Agrusta, R., Goes, S., van Hunen, J. (2017) Subducting-slab transition-zone interaction: Stagnation, penetration and mode switches. *Earth and Planetary Science Letters* **464,** 10-23. https://doi.org/10.1016/j.epsl.2017.02.005.

Chase, C.G. (1981) Oceanic island Pb: two-stage histories and mantle evolution. *Earth and Planetary Science Letters* **52**(2), 277-284.

Dasgupta, R., Hirschmann, M.M., Withers, A.C. (2004) Deep global cycling of carbon constrained by the solidus of anhydrous, carbonated eclogite under upper mantle conditions. *Earth and Planetary Science Letters* **227**(1-2), 73-85. 10.1016/j.epsl.2004.08.004.

Debret, B., Reekie, C., Mattielli, N., Savov, I., Beunon, H., Ménez, B. & Williams, H. (2020) Redox transfer at subduction zones: insights from Fe isotopes in the Mariana forearc. *Geochemical Perspectives Letters* **12**, 46-51.

Doucet, L., Zheng-Xiang, L., Brendan, M., Collins, W., Spencer, C. & Mitchell, R. (2020) Distinct formation history for deep-mantle domains reflected in geochemical differences. *Nature Geoscience* **13**(7)**,** pp 511-515.

Goes, S., Capitanio, F.A., Morra, G., (2008) Evidence of lower-mantle slab penetration phases in plate motions. *Nature* **451**(7181): 981-984.

Hofmann, A.W., White, W.M., (1982) Mantle plumes from ancient oceanic crust. *Earth and Planetary Science Letters* **57**(2): 421-436. 10.1016/0012-821X(82)90161-3.

Johnson, C., Bell, K., Beard, B., Shultis, A., (2010) Iron isotope compositions of carbonatites record melt generation, crystallization, and late-stage volatile-transport processes. *Mineralogy and Petrology* **98**(1), 91-110. 10.1007/s00710-009-0055-4.

Lesher, C. E., Dannberg, J., Barfod, G. H., Bennett, N. R., Glessner, J. J., Lacks, D. J. & Brenan, J. M. (2020) Iron isotope fractionation at the core–mantle boundary by thermodiffusion. *Nature Geoscience* **13**(5)**,** pp 382-386.

McCoy-West, A.J., Fitton, J.G., Pons, M.-L., Inglis, E.C., Williams, H.M., (2018) The Fe and Zn isotope composition of deep mantle source regions: Insights from Baffin Island picrites. *Geochimica et Cosmochimica Acta* **238,** 542-562. 10.1016/j.gca.2018.07.021.

Poitrasson, F., Delpech, G., Gregoire, M., (2013) On the iron isotope heterogeneity of lithospheric mantle xenoliths: implications for mantle metasomatism, the origin of basalts and the iron isotope composition of the Earth. *Contributions to Mineralogy and Petrology* **165**(6), 1243-1258. 10.1007/s00410-013-0856-7.

Sossi, P.A., O'Neill, H.S.C., (2017) The effect of bonding environment on iron isotope fractionation between minerals at high temperature. *Geochimica et Cosmochimica Acta* **196**, 121. 10.1016/j.gca.2016.09.017.

Stracke, A., Bizimis, M., Salters, V.J.M., (2003) Recycling oceanic crust: Quantitative constraints. *Geochemistry, Geophysics, Geosystems* **4**(3). 10.1029/2001GC000223.

Sun, P., Niu, Y., Guo, P., Duan, M., Chen, S., Gong, H., Wang, X. & Xiao, Y. (2020) Large iron isotope variation in the eastern Pacific mantle as a consequence of ancient low-degree melt metasomatism. *Geochimica et Cosmochimica Acta* **286**, 269-288.

Teng, F.-Z., Dauphas, N., Helz, R.T., (2008) Iron isotope fractionation during magmatic differentiation in Kilauea Iki lava lake. *Science* (New York, N.Y.) **320**(5883), 1620. 10.1126/science.1157166.

Weaver, B.L., (1991) The origin of ocean island basalt end-member compositions: trace element and isotopic constraints. *Earth and Planetary Science Letters* **104**(2-4), 381-397.

Weyer, S., (2008) Geochemistry. What drives iron isotope fractionation in magma? *Science* (New York, N.Y.) **320**(5883), 1600. 10.1126/science.1160204.

Weyer, S., Ionov, D.A., (2007) Partial melting and melt percolation in the mantle: The message from Fe isotopes. *Earth and Planetary Science Letters* **259**(1-2), 119-133. 10.1016/j.epsl.2007.04.033.

Williams, H. M., McCammon, C. A., Peslier, A. H., Halliday, A. N., Teutsch, N., Levasseur, S. & Burg, J.-P. (2004) Iron isotope fractionation and the oxygen fugacity of the mantle. *Science* **304**(5677)**,** pp 1656-1659.

Williams, H. M., Peslier, A. H., McCammon, C., Halliday, A. N., Levasseur, S., Teutsch, N. & Burg, J. P. (2005) Systematic iron isotope variations in mantle rocks and minerals: The effects of partial melting and oxygen fugacity. *Earth and Planetary Science Letters* **235**(1)**,** pp 435-452.

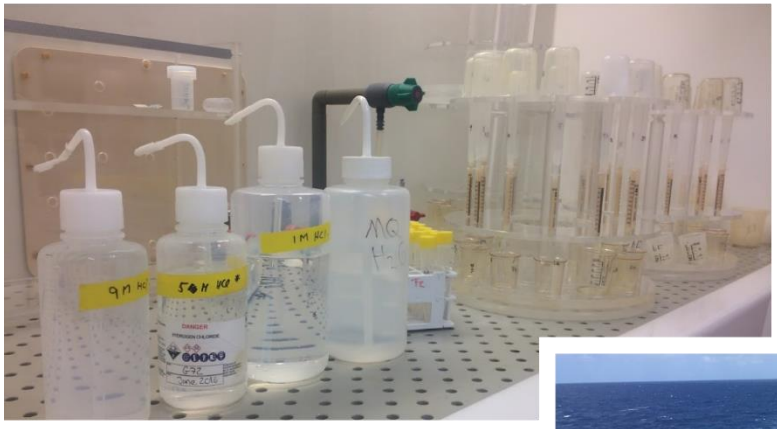

Top and bottom right pictures taken by me 2019, bottom left picture taken by Marianne Richter 2018. Collage shows all the great things that my PhD included.

"Ends are not really a bad thing, they just mean that something else is about to begin."

(C. JoyBell C.)

The End.